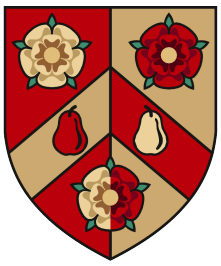


Investigations of Evaporated and Hybrid Organic Solar Cells with Engineered Förster Resonance Energy Transfer

Ming Zhu

Wolfson College



University of Oxford

A thesis submitted for the degree of

Doctor of Philosophy

Michaelmas 2025

This thesis is dedicated to my parents and grandparents,

who have always supported me unconditionally

and encouraged me pursue what I love.

Acknowledgements

I still cannot quite believe that my PhD is finally coming to an end after four years. I've had a wonderful time with so many amazing people during this journey. Some I only met once, and others have since moved on to different places, but without crossing paths with each of them, my PhD experience would not have been complete. The emotional support of my cat, Steve, during countless late nights of thesis writing has also been invaluable.

First of all, I would like to thank my parents for their immense financial support. Without them, I would not have been able to begin my PhD journey. I am also grateful to Wolfson College and Dr Andrew Prentice for awarding me the Andrew Prentice Physics Bursary. This generous support eased the financial burden on my parents and made it possible for me to visit them more often. I would also like to acknowledge Beamline B07 at Diamond Light Source for granting me access to the facilities I needed to carry out parts of my research. Special thanks to the beamline staff for their excellent support.

I would like to thank everyone who helped me or shared good times with me here, I know it is impossible to name everyone individually. I am especially grateful to my supervisor, Prof Moritz Riede, for his guidance and support throughout my PhD. I truly appreciate the encouragement and freedom he gave me to explore and develop skills beyond my research. I would also like to thank Dr Pascal Kaienburg and Dr Anna Jungbluth for so many research discussions, helpful feedback, and their support when they were in the group. Many thanks as well to all my colleagues and friends in the AFMD and Snaith groups, for always being willing to try my baking and for making the office such a fun and friendly place. Special thanks go to my friend Dr Andreas E. Lauritzen for his bi-weekly online "sanity checks" during thesis-writing period. I already miss working alongside such wonderful people: Olivia, Zhongcheng, Ruohan, Zhenlong, Kate, Fengning, Xinyu, Shuaifeng, Heon, Akash, and many others. I will miss our lunches, coffee breaks, and office chats. I also want to thank Prof Feng Gao and his

lovely group members at Linköping University, where I had the opportunity to visit and learn a great deal for my research.

I am also deeply grateful to my friends back home, Coco, Chancy, Dingding, Xiaohou, Meimei, and Menglei, for always supporting me on lousy days. Finally, I want to thank my husband, Xinze, who always picks up my calls when I need, and my grandparents for their unwavering love and support throughout this journey.

Abstract

Recent advances in non-fullerene acceptor (NFA) materials have enabled power conversion efficiencies (PCEs) exceeding 20% in solution-processed (SP) organic solar cells (OSCs). However, vacuum-thermal-evaporated (VTE) OSCs, despite offering advantages in reproducibility and commercial scalability, have largely plateaued at lower PCEs (∼10%), primarily relying on fullerene-based electron acceptors and exhibiting significant open-circuit voltage (V_{oc}) losses (typically ∼0.7-1.1 V, defined as the difference between V_{oc} and device photovoltaic gap E_g^{PV}/e). Motivated by design strategies established in high-efficiency SP NFA OSCs, this thesis investigates whether and how similar principles can be applied to VTE OSCs employing non-fullerene electron acceptors, through systematic molecular screening and device studies across planar (PHJ) and bulk heterojunction (BHJ) configurations. A central focus is on systems that enable efficient Förster Resonance Energy Transfer (FRET) between the electron donor and acceptor, forming a two-step exciton dissociation pathway that mimics that of SP NFA OSCs. This work explores both all-VTE and hybrid OSC systems (comprising VTE donors and SP NFAs). The first part of the thesis involves screening six candidate molecules, SubNc, SubPc, DTDCTB, HB194, DCV3T, and FBR, through comprehensive optical and electronic characterisation. SubNc/DCV3T and SubNc/FBR are identified as promising molecular pairs, satisfying key criteria: high absorption coefficients (>10^5 cm^{-1}), high photoluminescence quantum yields for high-gap molecule (ideally also for low-gap molecule), efficient FRET from high-gap to low-gap molecule, and sufficiently large ionisation energy (IE) /electron affinity (EA) offsets (>0.4–0.5 eV) to support dominant charge transfer. In the second part, these pairs are investigated in PHJ and BHJ device architectures. A SubNc/DCV3T bilayer PHJ achieves a PCE above 3.5% with a record-low voltage loss, which is comparable to leading SP NFA OSCs, of 0.60 V. The BHJ counterpart delivers a functional device with PCE of 2.5% and a low voltage loss of 0.64 V. The lower PCE is primarily attributed to low charge carrier mo-

bility in the active-layer films and unfavourable edge-on molecular orientation. Further study of a trilayer PHJ based on FRET-supporting pair SubNc/HB194, characterised by near-zero EA offset, identifies general molecular design criteria for introducing a second electron acceptor via FRET to enhance device performance without compromising V_{oc}. Specifically, this second electron acceptor should (i) possess an EA similar to that of the original acceptor, (ii) enable efficient FRET to the original acceptor, and (iii) exhibit electron mobility comparable to, or greater than, that of the original acceptor. Finally, studies on PHJ hybrid OSC systems and their C_{60} references, enabling various CT state visibility, reveal a linear correlation between $\Delta E_{S1,CT}$ and radiative voltage loss ΔV_{oc}^{rad}, enabling estimation of $\Delta E_{S1,CT}$ in PHJ systems where CT state features are obscured by S_1 emission. Overall, this thesis confirms that several molecular design rules from SP NFA OSCs can be successfully extended to VTE systems and introduces new methodologies for CT state characterisation in challenging ultra-low $\Delta E_{S1,CT}$ regimes. These results highlight the need for new evaporable NFAs with optimised optical, electronic, and morphological properties to bridge the performance gap between VTE and SP OSCs.

Contents

Abstract iii

List of Figures x

List of Tables xviii

List of Abbreviations xx

List of Publications xxiv

1 Introduction 1

1.1 Global Warming and Renewable Energies 1

1.2 Development and Challenges of OSCs 3

1.3 Thesis Outline 6

2 The Physics of Organic Solar Cells 9

2.1 Organic Semiconducting Molecules 10

2.1.1 Energy Levels of a Molecule 10

2.1.2 Absorption and Emission 13

2.2 Organic Thin Films 17

2.2.1 Energy Levels in Solids 17

2.2.2 Excitons 19

2.2.3 Exciton Transport 20

2.3 Organic Solar Cells 22

2.3.1 Electron Donor and Acceptor Configuration 22

2.3.2 Charge Generation and Recombination 25

2.3.3 Current Density-Voltage Characteristics 28

2.3.4 External Quantum Efficiency and Electroluminescence . . . 31
2.3.4.1 Reciprocity . . . 31
2.3.4.2 Determination of CT State Energy . . . 32
2.3.4.3 Urbach Energy . . . 36
2.3.5 Voltage Loss . . . 38
2.3.5.1 Reference Energies . . . 38
2.3.5.2 Radiative Limit . . . 39
2.3.5.3 Detailed Balance Picture . . . 41

3 The Physics of Förster Resonance Energy Transfer 44
3.1 FRET Theory . . . 45
3.1.1 Transfer Mechanisms . . . 45
3.1.2 FRET Radius and Transfer Rate . . . 48
3.1.3 Experimental Determination of FRET . . . 50
3.2 Applications of FRET in Organic Solar Cells . . . 52

4 Materials & Methods 55
4.1 Materials . . . 56
4.2 Sample Fabrication . . . 58
4.2.1 Substrate Preparation . . . 58
4.2.2 Vacuum Thermal Deposition . . . 59
4.2.3 Solution Preparation, Spin Coating and Annealing . . . 60
4.2.4 Solar Cell Device Encapsulation . . . 63
4.2.5 Solar Cell Device Architecture . . . 63
4.3 Thin Film Characterization . . . 65
4.3.1 Steady-state and Time-resolved PL Spectroscopy . . . 65
4.3.2 Photoluminescence Quantum Yield . . . 65
4.3.3 Absorption Measurements . . . 66
4.3.4 Spectroscopic Ellipsometry . . . 66
4.3.5 Ultraviolet Photo-electron Spectroscopy and Inverse Photo-Emission Spectroscopy . . . 67

4.3.6 Transient Absorption Spectroscopy . . . 68
4.3.7 Grazing Incidence Wide Angle X-Ray Scattering . . . 69
4.4 Solar Cell Characterisation . . . 71
4.4.1 Current Density-Voltage Measurements . . . 71
4.4.2 External Quantum Efficiency Measurements . . . 71
4.4.3 Electroluminescence Spectroscopy . . . 72
4.5 Computational Methods . . . 72
4.5.1 Transfer Matrix Modelling . . . 72

5 Identifying FRET Donor-Acceptor Pair Suitable for OSCs 74
5.1 Introduction . . . 76
5.2 Pristine Film Optical Characteristics . . . 78
5.2.1 Background Spectra . . . 78
5.2.2 SubNc . . . 79
5.2.3 SubPc . . . 80
5.2.4 DTDCTB . . . 82
5.2.5 HB194 . . . 83
5.2.6 DCV3T . . . 84
5.2.7 FBR . . . 85
5.3 Pristine Film Electronic Characteristics . . . 86
5.3.1 Ionisation Energy and Electron Affinity . . . 86
5.3.2 Charge Carrier Mobility . . . 89
5.4 Photoluminescence Quenching Measurements and Candidate Selections for Solar Cells . . . 91
5.4.1 Film Stacks . . . 91
5.4.2 Blocking Layer CBP . . . 93
5.4.3 Fully Evaporated Molecules . . . 96
5.4.3.1 SubNc and HB194 . . . 96
5.4.3.2 SubNc and DCV3T . . . 98
5.4.3.3 DTDCTB and DCV3T . . . 99

5.4.3.4 SubPc and DCV3T . . . 101
5.4.3.5 HB194 and DCV3T . . . 102
5.4.4 Half Solution-Processed and Half Evaporated . . . 104
5.4.4.1 SubNc and FBR . . . 104
5.4.4.2 DTDCTB and FBR . . . 105
5.4.4.3 SubPc and FBR . . . 107
5.5 Conclusions . . . 108

6 Exploiting FRET in Evaporated OSCs 111
6.1 Introduction . . . 113
6.2 Application of FRET in Bi-Layer Planar Heterojunction OSCs . . . 116
6.2.1 Materials and Devices . . . 116
6.2.2 TAS Analysis . . . 117
6.2.2.1 FRET Pairs . . . 117
6.2.2.2 Non-FRET Pairs . . . 121
6.2.3 Device Performance . . . 124
6.2.4 Charge Transfer Characteristics . . . 131
6.2.5 Voltage Losses . . . 136
6.2.6 Conclusions . . . 140
6.3 Application of FRET in Tri-Layer Planar Heterojunction OSCs . . . 142
6.3.1 Materials and Devices . . . 142
6.3.2 Device Performance . . . 142
6.3.2.1 SubNc|HB194 Bilayer PHJ . . . 142
6.3.2.2 α-6T|SubNc|HB194 Trilayer PHJ . . . 145
6.3.3 Voltage Losses . . . 149
6.3.4 Conclusions . . . 151
6.4 Application of FRET in Bulk Heterojunction OSCs . . . 152
6.4.1 Materials and Devices . . . 152
6.4.2 Device Performance . . . 153
6.4.3 GIWAXS Study on Molecular Orientation and Packing . . . 158

6.4.4 Conclusions . . . 162

7 Exploiting FRET in Half-solution Processed Half-evaporated OSCs 164

7.1 Introduction . . . 165

7.2 Materials and Devices . . . 167

7.3 Device Performance . . . 168

7.3.1 Current Density-Voltage . . . 168

7.3.2 External Quantum Efficiency . . . 172

7.4 Charge Transfer Characteristics and Voltage Loss . . . 175

7.5 Conclusions . . . 179

8 Conclusion and Outlook 181

A Computation Code 218

A.1 Spectral Overlap Integral J Calculation . . . 218

A.2 Spectroscopic Ellipsometry Fitting . . . 218

A.3 Voltage Loss Calculation . . . 218

A.4 Parameters Extracted from EQE . . . 218

A.4.1 Determination of E_g^{PV} . . . 218

A.4.2 Determination of E_U^{app} . . . 219

A.5 Reduced EL and EQE . . . 219

List of Figures

1.1 Annual global CO_2 emissions from fossil fuels and land-use change and average temperature anomalies. . . . 2

1.2 Best certified research solar cell efficiencies of emerging photovoltaic (PV) technologies over time. . . . 4

2.1 Schematics of atomic s and p orbitals and sp, sp^2, and sp^3 hybrid orbitals. . . . 10

2.2 Schematics of formation of ethane from six hydrogen atoms and two sp^3-hybridised carbon atoms and ethene from four hydrogen atoms and two sp^2-hybridised carbon atoms. . . . 11

2.3 Energy level diagram illustrating the energy levels of σ and π bonds formed between carbon atoms for ethene and benzene. . . . 12

2.4 Jablonski diagram showing singlet (S) and triplet (T) states, along with their corresponding vibrational manifolds. . . . 14

2.5 Schematic of a diatomic molecule showing the difference in interatomic distance between the excited state (r^*) and ground state (r_0) and absorption and fluorescence emission spectra between the vibrational ground states and vibrational manifolds of S_0 and S_1. . . . 16

2.6 Schematic diagram illustrating the energy levels of molecular states in the isolated molecule and molecular solid forms. . . . 18

2.7 Schematics of *Frenkel* excitons, *Charge transfer* excitons and *Wannier* excitons. 19

2.8 Schematics of *Förster* Resonance Energy Transfer and *Dexter* Energy Transfer. . 21

2.9 Energy levels of ground-state donor, charge transfer (CT) state, and ground-state acceptor in solid films. . . . 23

2.10 Schematics of different donor–acceptor heterojunction architectures for solar cell applications. . . . 24

2.11 Jablonski diagram illustrating charge generation and recombination processes in organic solar cells (OSCs) in a 5-state model picture. 27
2.12 Example current density–voltage (J–V) curve modelled with the ideal Shockley diode equation under illumination and in the dark. 29
2.13 Schematic Marcus energy diagram for a charge-transfer transition 33
2.14 Schematic of $E_U^{\mathrm{app}}(E)$ for donor:acceptor blends with large, medium, and small $\Delta E_{S1,CT}$. 36
2.15 Example of E_g^{PV} extraction from the EQE spectrum. 39
2.16 Schematic of relevant energy levels and corresponding voltage loss terms in the detailed balance (DB) picture. 41

3.1 Schematic illustrating the *Dexter* (contact) zone and near field around an energy donor molecule. 45
3.2 Simplified schematic of an energy donor molecule with radius R_D, and an acceptor molecule with radius R_A, separated by distance r_{DA} and their equivalent dipole–dipole coupling. 47

4.1 Molecular structure of the molecules for active layer (evaporable and soluble), interface modifying layer and wide-gap blocking layer used in this thesis. All chemical name are listed in Table 4.1 and 4.2. 56
4.2 Schematic of the evaporation chamber of The National Thin-Film Cluster Facility for Advanced Functional Materials (NTCF) used in this thesis. 60
4.3 Schematic of the spin-coating process for thin-film fabrication. 62
4.4 Schematic of the multilayer PHJ device stacks (standard architecture) used in this thesis. 64
4.5 Schematic of the bulk heterojunction (BHJ) device stack (standard architecture) used in this thesis. 64
4.6 Schematic of the bilayer hybrid planar heterjunction (PHJ) device stack (inverted architecture) with an inverted architecture used in this thesis. 65

5.1 Molecular structures and name of the organic molecules investigated. 77

5.2 Photoluminescence (PL) background spectra recorded with the laser off at integration times of 0.2, 0.3, and 0.5 s. 79
5.3 Extinction coefficient κ and normalised photoluminescence (PL) spectra of SubNc film on glass. 80
5.4 Extinction coefficient κ and normalised photoluminescence (PL) spectra of SubPc film on glass. 81
5.5 Extinction coefficient κ and normalised photoluminescence (PL) spectra of DTDCTB film on glass. 82
5.6 Extinction coefficient κ and normalised photoluminescence (PL) spectra of HB194 film on glass. 83
5.7 Extinction coefficient κ and normalised photoluminescence (PL) spectra of DCV3T film on glass. 84
5.8 Extinction coefficient κ and normalised photoluminescence (PL) spectra of FBR film on glass. 85
5.9 Ultraviolet photo-electron spectroscopy (UPS) and inverse photo-emission spectroscopy (IPES) spectra of HB194, DCV3T and SubNc. 86
5.10 Schematic energy levels of SubNc, SubPc, DTDCTB, HB194, DCV3T, and FBR. 88
5.11 Schematic of film stacks used for photoluminescence (PL) quenching experiments to indirectly verify *Förster* Resonance Energy Transfer (FRET) from the energy donor to acceptor molecule. 91
5.12 Steady-state photoluminescence (PL) spectra of multilayer thin-film samples with stack configurations shown in Figure 5.11a-d for HB194, SubNc, DTDCTB, SubPc, DCV3T and FBR. 95
5.13 Schematic energy levels, extinction coefficient (κ) spectra, steady-state photoluminescence (PL) spectra of pristine or stacked SubNc, CBP, and HB194 films. . 97
5.14 Schematic energy levels, extinction coefficient (κ) spectra, steady-state photoluminescence (PL) spectra of pristine or stacked SubNc, CBP, and DCV3T films. . 99
5.15 Schematic energy levels, extinction coefficient (κ) spectra, steady-state photoluminescence (PL) spectra of pristine or stacked DTDCTB, CBP, and DCV3T films. 100

5.16 Schematic energy levels, extinction coefficient (κ) spectra, steady-state photoluminescence (PL) spectra of pristine or stacked SubPc, CBP, and DCV3T films. . 101
5.17 Schematic energy levels, extinction coefficient (κ) spectra, steady-state photoluminescence (PL) spectra of pristine or stacked HB194, CBP, and DCV3T films. 103
5.18 Schematic energy levels, extinction coefficient (κ) spectra, steady-state photoluminescence (PL) spectra of pristine or stacked SubNc, CBP, and FBR films. . . 105
5.19 Schematic energy levels, extinction coefficient (κ) spectra, steady-state photoluminescence (PL) spectra of pristine or stacked DTDCTB, CBP, and FBR films. 106
5.20 Schematic energy levels, extinction coefficient (κ) spectra, steady-state photoluminescence (PL) spectra of pristine or stacked SubPc, CBP, and FBR films. . . 107

6.1 Normalised extinction coefficient spectra of SubNc and DCV3T, and DTDCTB and DCV3T, with the excitation wavelengths used for transient absorption spectroscopy (TAS) measurements indicated. 117
6.2 Transient absorption spectra of the SubNc:DCV3T (1:1 by vol) blend at various time delays upon DCV3T and SubNc photoexcitation with 500 nm and 700 nm pulses, respectively, at an absorbed pump fluence 2.7 μJ/cm^2. 118
6.3 Transient absorption spectra of the DTDCTB:DCV3T (1:1 by vol) blend at various time delays upon DCV3T and DTDCTB photoexcitation with 500 nm and 700 nm pulses, respectively, at an absorbed pump fluence 2.7 μJ/cm^2. . . . 120
6.4 Normalised extinction coefficient spectra of SubPc and DCV3T, and HB194 and DCV3T, with the excitation wavelengths used for transient absorption spectroscopy (TAS) measurements indicated. 121
6.5 Transient absorption (TA) spectra of SubPc:DCV3T (1:1 by vol) and HB194:DCV3T (1:1 by vol) blends at various time delays upon photexcitation at different wavelength at an absorbed pump fluence 2.7 μJ/cm^2. 123
6.6 Current density–voltage characteristics of planar heterojunction devices using SubNc, DTDCTB, SubPc, and HB194 as electron donors (20 nm) and DCV3T as the electron acceptor (20 nm). 125

6.7 Time-resolved photoluminescence (TRPL) dynamics of SubNc, DTDCTB, SubPc, HB194, DCV3T pristine films excited by 510 nm laser (635 nm for DTDCTB) at or near the wavelength of steady-state PL peak, with intensity normalised. . . 128
6.8 Sensitive external quantum efficiency spectra of the best performing planar heterojunction devices using SubNc, DTDCTB, SubPc, and HB194 as electron donors (20 nm) and DCV3T as the electron acceptor (20 nm). 130
6.9 Measured absorptance and calculated number of absorbed photons (under AM1.5 g solar illumination) for the best planar heterojunction devices using SubNc, DTDCTB, SubPc, and HB194 as electron donors (20 nm) and DCV3T as the electron acceptor (20 nm). 131
6.10 Apparent Urbach energy (E_U^{app}) spectra of the best planar heterojunction devices with SubNc, DTDCTB, SubPc, and HB194 as electron donors (20 nm) and DCV3T as the electron acceptor (20 nm). 132
6.11 Normalised reduced electroluminescence (EL) and external quantum efficiency (EQE) spectra of the best planar heterojunction devices using SubNc, SubPc, and HB194 as electron donors (20 nm) and DCV3T as the electron acceptor (20 nm) 134
6.12 Reduced electroluminescence (EL) spectra of the HB194|DCV3T PHJ device with Marcus theory fits for a possible CT state. 135
6.13 Open-circuit voltage loss decomposition for the best planar heterojunction devices using SubNc, DTDCTB, SubPc, and HB194 as electron donors (20 nm) and DCV3T as the electron acceptor (20 nm). 137
6.14 External quantum efficiency spectra, Reduced electroluminescence spectra and apparent Urbach energy (E_U^{app}) spectra of the best planar heterojunction (PHJ) 20 nm SubNc|20 nm DCV3T and 20 nm HB194|20 nm DCV3T devices. 139
6.15 Current density-Voltage characteristics and Sensitive external quantum efficiency spectra of the best SubNc|HB194 bilayer PHJ device along with its single-component reference SubNc. 143

6.16 Heat maps showing the dependence of short-circuit current J_{sc}, open-circuit voltage V_{oc}, fill factor, FF, and power conversion efficiency, PCE, on thicknesses of SubNc and HB194. 145
6.17 Schematic showing the respective highest occupied molecular orbital (HOMO) and lowest unoccupied molecular orbital (LUMO) levels and normalized extinction coefficient spectra of the molecules. Schematic of the stacking of α-6T|SubNc|HB194 triplelayer PHJ device. 146
6.18 Current density-Voltage characterization and sensitive external quantum efficiency spectra of α-6T|SubNc|HB194 triple-layer PHJ devices along with its references. 147
6.19 Measured sensitive external quantum efficiency and calculated internal quantum efficiency spectra based on TMM simulated device absorptance. 148
6.20 Voltage loss breakdown showing ΔV_{oc}^{sc}, ΔV_{oc}^{rad}, ΔV_{oc}^{nr} of devices with active layer being pristine SubNc (24 nm), SubNc (10 nm)|HB194 (14 nm), α-6T (20 nm)|SubNc (24 nm), α-6T (20 nm)|SubNc (12 nm)|SubPc (18 nm), and α-6T (20 nm)|SubNc (10 nm)|HB194 (14 nm). 149
6.21 Current density-voltage characteristics and external quantum efficiency of SubNc:DCV3T bulk heterojunction (BHJ) devices with 1:0.5, 1:1, 1:1.5, 1:3, 1:5 donor-to-acceptor ratios by vol. 153
6.22 The dependence of short-circuit current (J_{sc}), voltage loss in Detail Balance picture ΔV_{oc}^{DB}, fill factor (FF) and power conversion efficiency (PCE) on DCV3T concentration in SubNc:DCV3T BHJ devices. 154
6.23 Sensitive External Quantum Efficiency spectra and voltage losses breakdown of SubNc:DCV3T 1:1 by vol and 1:5 by vol BHJ devices. 155
6.24 Apparent Urbach energy (E_U^{app}) of (a) SubNc:DCV3T bulk heterojunction (BHJ) 1:1 (b) 1:5 by vol solar cell devices. 157
6.25 Extinction coefficients of SubNc, DCV3T , SubNc:DCV3T (1:1 by vol), and SubNc:DCV3T (1:5 by vol) and absorptance (A) and numbers of absorbed photons spectra of SubNc:DCV3T 1:1 by vol and 1:5 by vol bulk heterojunction solar cell devices. 158

6.26 Normalised integrated in-plane (IP) and out-of-plane (OoP) GIWAXS profiles and GIWAXS 2D images of pure DCV3T and SubNc films. 159
6.27 Normalised integrated in-plane (IP) and out-of-plane (OoP) GIWAXS profiles and GIWAXS 2D images of SubNc:DCV3T blend films at 1:1 and 1:5 (by vol). . 160

7.1 Summary of device performance parameters: short-circuit current J_{sc}, open-circuit voltage V_{oc}, fill factor FF, power conversion efficiency PCE for planar heterojunction devices in inverted stack using SubNc, DTDCTB and SubPc as electron donors (20 nm) and FBR as electron acceptor (20 nm). 168
7.2 Summary of device performance parameters: short-circuit current J_{sc}, open-circuit voltage V_{oc}, fill factor FF, power conversion efficiency PCE for planar heterojunction devices (C_{60} reference devices) in inverted stack using SubNc, DTDCTB and SubPc as electron donors (20 nm) and C_{60} as electron acceptor (20 nm). 169
7.3 Current density-voltage characteristics of planar heterojunction devices using SubNc, DTDCTB and SubPc as electron donors (20 nm) and FBR (C_{60}) as electron acceptor (20 nm). 171
7.4 Transfer-Matrix simulated and measured device absorptance spectra for best performing planar heterojunction devices using SubNc, DTDCTB, SubPc as electron donors (20 nm) and FBR as the electron acceptor (20 nm). 173
7.5 Sensitive external quantum efficiency (EQE) spectra of the best performing planar heterojunction devices using SubNc, DTDCTB, SubPc as electron donors (20 nm) and FBR (C_{60}) as the electron acceptor (20 nm). 174
7.6 Sensitive external quantum efficiency (EQE) spectra of the best performing planar heterojunction (PHJ) devices using SubNc, SubPc as electron donors (20 nm) and FBR (C_{60}) as the electron acceptor (20 nm) with Marcus theory fits for S_1 and CT states. Apparent Urbach energy (E_U^{app}) spectra of PHJ device with SubNc|FBR as active layer. 176

7.7 Open-circuit voltage loss decomposition in DB picture for the best planar heterojunction devices using SubNc and SubPc as electron donors (20 nm) and FBR (C_{60}) as the electron acceptor (20 nm). Radiative voltage loss (ΔV_{oc}^{rad}) plotted as a function of the energy difference between the S_1 and CT states ($\Delta E_{S1,CT}$). . 177

7.8 $\Delta E_{S1,CT}$ as a function of $\Delta Q_{\pi,D-A}$ for SubNc|FBR (C_{60}) and SubPc|FBR (C_{60}) material systems. 178

List of Tables

4.1 Acronyms, chemical names, densities, purities and suppliers for the vacuum thermal deposited molecules used in this thesis. 57

4.2 Acronyms, chemical names, molecular weight, purities and suppliers for the solute or dispersive molecules used in this thesis. 58

4.3 Chemical names, chemical formula, molecular weight, purities and suppliers for the solvents and solutions used in this thesis. 58

4.4 Spin-coating parameters for the films used in this thesis. 63

5.1 Reported photoluminescence quantum yields (ϕ_{PL}) of SubPc in different solvents. 81

5.2 Work function (WF), ionisation energy (IE), electron affinity (EA), and fundamental gap (E_{fund}) determined from ultraviolet photo-electron spectroscopy (UPS) and inverse photo-emission spectroscopy (IPES) measurements on pristine films of HB194, DCV3T, and SubNc deposited on silicon wafers. 87

5.3 Ionisation energy (IE), electron affinity (EA) and fundamental gap (E_{fund}) taken from literature measured on solid films of SubPc, DTDCTB, and FBR. 87

5.4 Electron (μ_e) and hole (μ_h) mobilities of pristine films of SubNc, SubPc, DTDCTB, HB194, DCV3T, and FBR, as reported in the literature. 90

5.5 Summary of the ionisation energy difference (IE_D–IE_A), electron affinity difference (EA_D–EA_A), spectral overlap integral J, and whether efficient FRET was observed via photoluminescence quenching for the studied electron donor–acceptor molecular pairs. 109

6.1 Summary of open-circuit voltage (V_{oc}), short-circuit current density (J_{sc}), fill factor (FF), and power conversion efficiency (PCE) for 20 nm electron donor|20 nm electron acceptor planar heterojunction devices. 124

6.2 Summary of the photovoltaic gap (E_g^{PV}), open-circuit voltage (V_{oc}), total voltage loss ($\Delta V_{oc} = E_g^{PV}/e - V_{oc}$), short-circuit current (J_{sc}), fill factor (FF), and power conversion efficiency (PCE) for the best-performing planar heterojunction devices using SubNc, DTDCTB, SubPc, and HB194 as electron donors (20 nm) and DCV3T as the electron acceptor (20 nm). 127

6.3 Summary of voltage loss relative to Shockley-Queisser limit (ΔV_{oc}^{SQ}), voltage loss due to imperfect photocurrent collection (ΔV_{oc}^{sc}), radiative voltage loss (ΔV_{oc}^{rad}), and non-radiative voltage loss (ΔV_{oc}^{nr}) for the best 20 nm SubNc|20 nm HB194 (DCV3T) planar heterojunction devices. 138

6.4 Active layer thickness, device photovoltaic gap (E_g^{PV}), open-circuit voltage (V_{oc}), total voltage loss, short-circuit current (J_{sc}), fill factor (FF) and power conversion efficiency (PCE) for the reported devices. 144

6.5 Performance characteristics of the best-performing pixels for solar cell devices with 40 nm SubNc:DCV3T active layers in 1:0.5, 1:1, 1:1.5, 1:3 and 1:5 donor-to-acceptor ratios (by vol). 154

6.6 Morphology parameters extracted from the GIWAXS measurements of 40 nm films of DCV3T pristine films deposited on Si wafers. 159

6.7 Morphology parameters extracted from the GIWAXS measurements of 40 nm films of SubNc:DCV3T blend 1:1 (by vol) and 1:5 (by vol) deposited on Si substrates. 161

7.1 Summary of open-circuit voltage (V_{oc}), short-circuit current (J_{sc}), fill factor (FF), and power conversion efficiency (PCE) for the best-performing planar heterojunction devices using SubNc, DTDCTB, SubPc as electron donors (20 nm) and FBR (C_{60}) as the electron acceptor (20 nm). 170

7.2 Summary of device photovoltaic gap (E_g^{PV}), open-circuit voltage (V_{oc}), voltage loss relative to Shockley-Queisser limit (ΔV_{oc}^{SQ}), voltage loss due to imperfect photocurrent collection (ΔV_{oc}^{sc}), radiative voltage loss (ΔV_{oc}^{rad}) and ΔV_{oc}^{nr} (V) for the best 20 nm SubNc (SubPc)|20 nm FBR (C_{60}) planar heterojunction devices. 177

List of Abbreviations

A	Acceptor
A	Absorptance
a-Si	Amorphous Silicon
AM1.5 g	Air Mass 1.5 Global
BHJ	Bulk Heterojunction
BCT	Back Charge Transfer
c-Si	Crystalline Silicon
CCD	Charge-coupled Device
CdTe	Cadmium Telluride
CIGS	Copper Indium Gallium Selenide
CT	Charge Transfer
CV	Cyclic Voltammetry
D	Donor
DB	Detailed Balance
DLS	Diamond Light Source
DFT	Density Functional Theory
DSSC	Dye-sensitised Solar Cell
EA	Electron Affinity
EL	Electroluminescence
EN	Energetic State
EQE	External Quantum Efficiency
E_B	Exciton Binding Energy

E_{CT}	Charge Transfer State Energy
E_{fund}	Fundamental Gap
E_g^{PV}	Photovoltaic Gap
E_{OPT}	Optical Gap
E_{S1}	Lowest Excited Singlet State Energy
E_{trans}	Transport Gap
E_U	Urbach Energy
E_U^{app}	Apparent Urbach Energy
FRET	Förster Resonance Energy Transfer
FF	Fill Factor
FWHM	Full-width at Half-Maximum
GaAs	Gallium Arsenide
GHG	Greenhouse Gas
GIWAXS	Grazing-Incidence Wide-Angle X-ray Scattering
GSB	Ground-state Bleaching
HBEC	High-binding-energy Cut-off
HOMO	Highest Occupied Molecular Orbital
HWHM	Half-width at Half-Maximum
IE	Ionisation Energy
IEA	International Energy Agency
IDA	Ideal Dipole Approximation
ILC	Injection-limited Current
IP	In-Plane
IPCC	Intergovernmental Panel on Climate Change
IPES	Inverse Photoelectron Spectroscopy
IQE	Internal Quantum Efficiency
ISC	Intersystem Crossing
J-V	Current Density–Voltage
J_{sc}	Short-circuit Current Density
LCOE	Levelised Cost of Electricity

LED	Light-emitting Diode
LUMO	Lowest Unoccupied Molecular Orbital
L	Crystal Coherence Length
L_D	Exciton Diffusion Length
MPP	Maximum Power Point
NFA	Non-Fullerene Acceptor
NIR	Near-Infrared
NTCF	National Thin-Film Cluster Facility for Advanced Functional Materials
OLED	Organic Light-emitting Diode
OoP	Out-of-Plane
OPA	Optical Parametric Amplifier
OPV	Organic Photovoltaic
OSC	Organic Solar Cell
OFET	Organic Field-effect Transistor
PA	Photoinduced Absorption
P	Power Density
PCE	Power Conversion Efficiency
PHJ	Planar Heterojunction
PL	Photoluminescence
PLQY	photoluminescence quantum yield
PSC	Perovskite Solar Cell
PV	Photovoltaic
QCM	Quartz Crystal Microbalance
Q	Quadrupole Moment
R_0	Förster Radius
S_0	Singlet Ground State
S_1	Lowest Excited Singlet State
S_n	n^{th} Excited Singlet State
SCLC	Space-charge0limited Current
SQ	Shockley–Queisser

SP	Solution Processing
SOMO	Singly Occupied Molecular Orbital
T_1	Lowest Triplet Excited State
T_n	n^{th} Excited Triplet State
TAS	Transient Absorption Spectroscopy
TCSPC	Time-corrected Single-photon Counting
TMM	Transfer Matrix Modelling
TOF	Time-of-flight
TRPL	Time-Resolved Photoluminescence
UPS	Ultraviolet Photoelectron Spectroscopy
UHV	Ultra-high-vacuum
UV	Ultraviolet
VTE	Vacuum Thermal Evaporation
V_{oc}	Open-circuit Voltage
WF	Work Function
$\Delta E_{S1,CT}$	Energy Difference Between Singlet Excited State and Charge Transfer State
ϵ	Dielectric Constant
f	Oscillator Strength

List of Publications

Published Peer-Reviewed Articles

1. I. Habib, P. Kaienburg, D. Xia, O. Gough, **M. Zhu**, J. Spruce, W. Li, M. Riede, Vacuum deposited organic solar cells with BTIC-H as A–D-A non-fullerene acceptor. *APL Mater.* 1 June 2023; 11 (6): 061128.

2. A. Jungbluth, L. M. Hanauske, **M. Zhu**, G. Christoforo, P. Kaienburg, and M. Riede, An open source sensitive external quantum efficiency setup for characterising optoelectronic devices. *Journal of Open Hardware*, vol. 9, no. 1, 2025.

Submitted Articles

1. **M. Zhu**, D. Tsokkou, O. Gough, K. Trinkaus, N. Evans, P. Kaienburg, K. Meerholz, S. Olthof, N. Banerji, M. Riede, Low-Voltage-Loss Vacuum-Deposited BHJ Organic Solar Cells with DCV3T. Under review. *Journal of Physics D: Applied Physics*, 2025

Conference Presentations

1. **M. Zhu**, P. Kaienburg, Z. Li, N. Evans, M. Riede, "Investigating FRET Involved Non-Fullerene All-Small-Molecule Organic Solar Cells," *Sustainable Advanced Materials for Solar Energy Conversion (SAMSEC)*, 2023, Swansea, UK. **(Oral Presentation)**

2. **M. Zhu**, N. Evans, P. Kaienburg, M. Riede, "Exploiting Förster Resonance Energy Transfer in Evaporated Organic Solar Cells," *Interface Properties in Organic and Hybrid Electronics (IPOE)*, 2024, Barcelona, Spain. **(Oral Presentation)**

1 | Introduction

1.1 Global Warming and Renewable Energies

Since the 20th century, greenhouse gas (GHG) emissions, particularly carbon dioxide (CO_2), resulting from human activities have increased dramatically, driving global climate change [1,2]. By 2025, the annual global CO_2 emissions are estimated to be approximately seven times higher than those at the beginning of the 20th century, with the majority originating from fossil fuel combustion (Figure 1.1a). Climate change, driven by excessive GHGs, is now recognised as a major threat to humanity. From the early 21st century, global average temperature anomalies have risen rapidly above 0 °C (Figure 1.1b), contributing to more frequent natural disasters and extreme weather events worldwide [3]. According to the Intergovernmental Panel on Climate Change (IPCC), global warming is projected to reach the critical threshold of 1.5 °C by the early 2030s, even under the most optimistic scenarios [3], which assume unified global action beginning in 2020 and a 60% reduction in GHG emissions by 2035 [4]. However, as of early 2025, the remaining carbon budget to limit global warming to 1.5 °C with 50% probability corresponds to less than four years of emissions at current rate [5]. Urgent action is therefore needed, particularly in the energy sector, which is the primary source of global GHG emissions.

To mitigate climate change, renewable energy sources, including solar, wind, hydro, geothermal, and biomass, are critical for replacing fossil fuels and enabling a global transition to low-carbon energy systems. Recognising this, many nations have increasingly prioritised renewables, leading to a significant surge in capacity over the past decade [6]. Solar and wind energy, in particular, have emerged as the fastest-growing sources, projected by the International Energy Agency (IEA) to supply 10% of global energy by 2030, up from 6% in 2022 [7]. Solar energy is especially attractive due to its abundance, one-hour of the solar radiation

reaching Earth exceeds the world's annual energy demand [8].

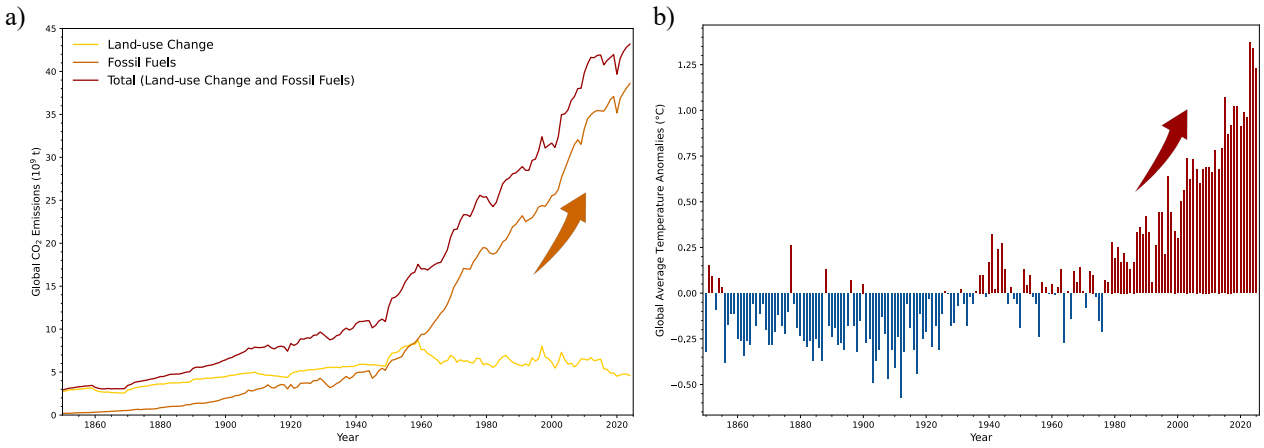


Figure 1.1: (a) Annual global CO_2 emissions from fossil fuels and land-use change. Data obtained with permission under CC BY 4.0 from Our World in Data [1]. (b) Annual global average temperature anomalies. Data obtained from National Centers for Environmental Information at NOAA [2].

Solar energy can be harnessed in two main ways: solar thermal and solar photovoltaic (PV) technologies. Solar thermal systems collect and convert solar heat for electricity generation or direct heating applications. Large-scale thermal power generation typically requires solar concentrators and thermal engines, as seen in installations like the Ivanpah Solar Electric Generating System in the United States. Solar thermal technologies have been deployed for over a century [9]. In contrast, photovoltaic technologies directly convert sunlight into electricity via the photovoltaic effect. The first commercial PV modules emerged in the 1950s and 60s, with power conversion efficiencies (PCEs) around 10% [10]. Since then, materials such as crystalline silicon (c-Si), amorphous silicon (a-Si), gallium arsenide (GaAs), cadmium telluride (CdTe), and copper indium gallium selenide (CIGS) have been developed for PV applications [11].

Among these, c-Si dominates the commercial PV market, accounting for 98% of global PV module production as of 2024 [12]. In 2025, the best-performing commercial c-Si single-junction cell achieved PCE exceeding 27% [13]. Improved efficiency, reduced material costs, and expanded manufacturing have made silicon PV the most cost-effective source of electricity in history, with the global weighted average levelised cost of electricity (LCOE) reaching \$0.043/kWh in 2024 [14]. While c-Si benefits from material abundance, cost-effectiveness, and high performance, its production still results in substantial GHG emissions, up to 4 kg CO_2e

for per kg of silicon, and the estimated carbon footprint for electricity generated by c-Si PVs is 50 g CO_2e/kWh [15, 16].

To further reduce the carbon footprint of solar-based electricity and to open vast new market beyond rigid modules, alternative PV materials have been extensively researched. Emerging PV technologies such as organic photovoltaics (OPVs), dye-sensitised solar cells (DSSCs), and perovskite solar cells (PSCs) offer promising alternatives. Among them, OPVs, also referred to as organic solar cells (OSCs), are particularly attractive for their sustainability and commercial potential. OSC manufacturer Heliatek reported a life cycle assessment compliant with DIN EN ISO 14040:2009 and 14044:2018, estimating a remarkably low carbon footprint of only 5–7 g CO_2e/kWh for their modules [17]. This is significantly lower than that of c-Si PVs and comparable to wind and hydro power [16]. OSCs, based on organic semiconductors, exhibit unique physical and optoelectronic properties and have attracted substantial research interest. They are the focus of this thesis and will be discussed in detail in the following chapters.

1.2 Development and Challenges of OSCs

The advantages of OSCs extend beyond their ultra-low carbon footprint. OSCs benefit from chemically tunable structures of organic semiconducting molecules, allowing their optoelectronic properties to be tailored for various applications. In addition, OSCs are composed of abundant and non-toxic raw materials. Owing to the high absorption coefficients of organic semiconductors, efficient light harvesting can be achieved with active material quantities as low as 1 g/m^2, and the devices can be processed at relatively low temperatures using scalable, cost-effective fabrication methods [16, 18]. Typical active layer thicknesses are on the order of hundreds of nanometres, and OSCs can be fabricated on flexible substrates with flexible electrodes, making them especially attractive compared to conventional, rigid, and heavy c-Si PVs. Because of these unique characteristics, OSCs have the potential to become the cheapest source of electricity, potentially surpassing Si PVs [16].

Despite these advantages in sustainability, weight, flexibility, and optical absorption, a key limitation of OSCs remains their relatively low PCEs. Figure 1.2 shows the certified PCEs of emerging PV technologies measured under standard test or reporting conditions, with OSCs

indicated by orange solid circles. The highest certified power conversion efficiency (PCE) for a single-junction OSC is 19.2% [19], and the highest reported (non-certified) value is 20.8% [20]. These efficiencies remain significantly lower than those of other emerging PVs such as PSCs (certified PCE = 27.0% [21]) and conventional inorganic technologies like GaAs (certified PCE = 29.1% [22]).

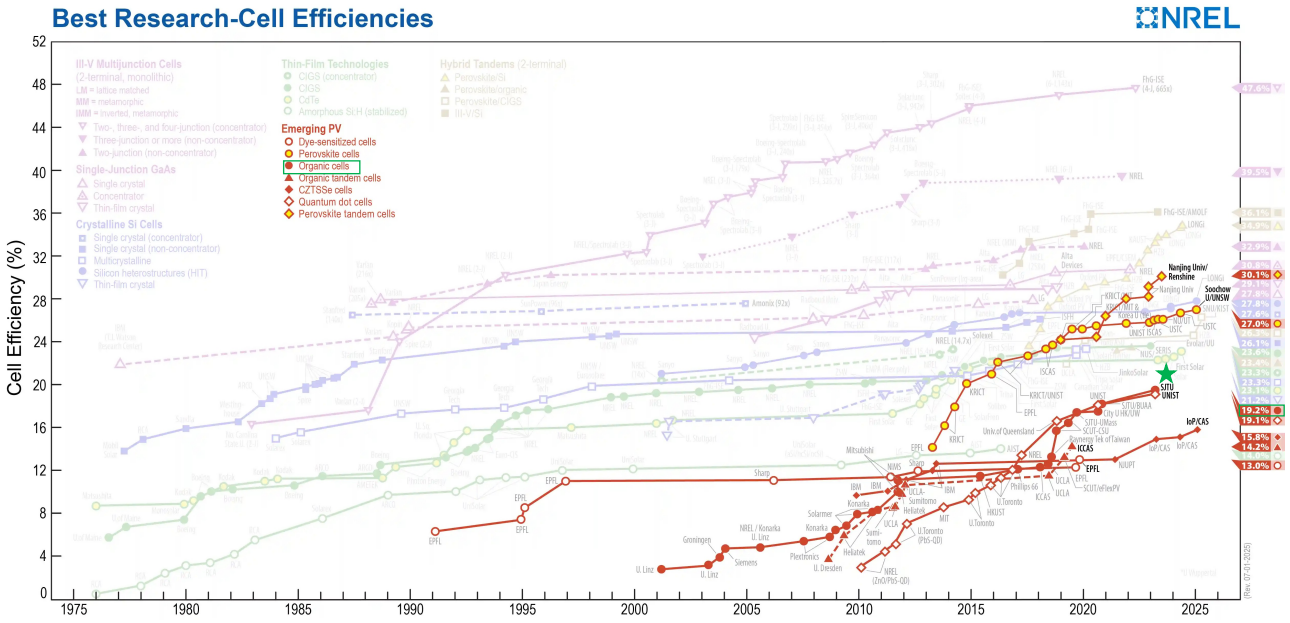


Figure 1.2: Best certified research solar cell efficiencies of emerging photovoltaic (PV) technologies over time. Efficiencies for organic PV are shown as solid circles, with the highest reported efficiency highlighted by a green star to be 19.2%. Data are based on OSCs measured under standard test or reporting conditions, defined by the global reference spectrum for flat-plate devices and the direct reference spectrum for concentrator devices, as specified in IEC 60904-3:2019 RLV and ASTM G173. The solar cell temperature is 25 °C, and efficiencies are based on either the total cell area or the aperture-defined area. This plot is courtesy of the National Renewable Energy Laboratory, Golden, CO and was downloaded from National Laboratory of the Rockies [23]. The data in the plot were last updated on 6$^{\text{th}}$ December 2025.

The relatively low PCEs of OSCs are largely attributed to significant energy losses within the light-absorbing organic semiconductor layers, which result in lower open-circuit voltages (V_{oc}) than expected from the optical gap (E_{OPT}) of the material. These energy losses include both radiative (photon) and non-radiative (thermal) contributions. Non-radiative losses in OSCs can easily exceed 100 mV and are a major factor limiting performance. Even the best-performing OSCs exhibit total voltage losses of ∼0.55 V, nearly double that of GaAs PVs (∼0.31 V), and significantly higher non-radiative losses (0.23 V vs. 0.027 V) [24, 25]. These losses are

believed to be partially intrinsic, arising from the coupling of excited states to intramolecular vibrational modes of organic molecules [16, 26]. Researchers in this field are still trying to understand the origin of high non-radiative losses in OSCs, with the aim of further improving their power conversion efficiencies.

In addition, the fundamental charge generation mechanism in OSCs differs from inorganic semiconductors: it requires two molecules, an electron acceptor (A), to facilitate exciton dissociation from the electron donor (D), introducing further voltage loss [27]. Organic semiconductors generally possess low dielectric constants (ϵ ~3–5) [28], much lower than those of inorganic materials (ϵ ~10–15) [29], resulting in high exciton binding energies (E_B) that prevent thermal dissociation. Therefore, additional driving force, typically provided by a second molecule with suitable energy levels, is required to separate excitons into free charges, at the cost of energy losses. Compounding this, organic semiconductors typically exhibit low charge carrier mobilities (10^{-10} to 10^{1} cm^2 V^{-1} s^{-1}), several orders of magnitude lower than their inorganic counterparts (10^{2}–10^{4} cm^2 V^{-1} s^{-1}) [30, 31]. This leads to enhanced charge trapping and recombination. Early OSCs addressed some of these limitations using fullerene-based acceptors, such as C_{60}, which offer relatively high electron mobility (up to ~1 cm^2 V^{-1} s^{-1}) [32] and deep-lying energy levels that promote efficient exciton dissociation and electron transport. However, the limited tunability of fullerene derivatives constrained further optimisation, with state-of-art fullerene OSCs achieving efficiencies capped around 11%, accompanied by high voltage losses of 0.89 V [33].

In response, significant efforts have been devoted to developing new non-fullerene acceptor (NFA) molecules and their corresponding donor materials. There are two major fabrication approaches: solution processing (SP) and vacuum thermal evaporation (VTE). Depending on the fabrication technique, different types of molecules can be processed. SP can accommodate large polymers and complex molecules (>1000 g/mol) and uses ambient-pressure techniques such as spin-coating and blade-coating. Because of the ease and wide use of SP in lab, the majority of NFA molecules developed to date have been optimised for this processing method. In contrast, VTE is limited to small molecules with thermally stable chemical structures and requires specialised equipment, but offers superior reproducibility and batch consistency. VTE is also considered to have stronger commercial prospects, as demonstrated by its success in

organic light-emitting diode (OLED) manufacturing. During the fullerene era, performance differences between SP and VTE OSCs were minimal, with VTE-based devices achieving PCEs over 10%, with only ∼1% lower than their SP counterparts [34].

However, with the development of novel "A-D-A" and "A-DA'D-A" type NFAs, most notably Y6 in 2019 [35], SP OSCs made a significant leap forward. The benchmark PM6:Y6 system achieved a PCE of 15.7% with the voltage loss cut to 0.56 V [36], and continued advances in molecular design and morphology control have pushed their PCEs beyond 20% [20]. Despite their impressive efficiency, SP-based OSCs face challenges related to long-term stability [16, 37] and scalable manufacturing [38]. As a result, VTE remains the more commercially viable route for OSC deployment.

Due to the high up-front research costs, VTE OSCs have long remained under-represented in the field. Most of the newly developed high-performance NFAs are either too large to be evaporated or thermally unstable, decomposing during the evaporation process. As a result, they cannot be directly employed in VTE OSCs. Consequently, high energy losses and low PCEs continue to challenge VTE OSCs, especially given that comparatively little attention has been paid to designing new NFA molecules tailored for evaporation, in contrast to the extensive development seen for SP systems. As understanding of high-performing NFAs in SP OSCs has advanced, several key designing criteria and the underlying charge generation mechanisms have been identified as central to achieving low voltage losses and high PCEs [39–43]. This raises the important question of whether these strategies can also be applied to VTE systems using non-fullerene molecules as electron acceptors. Investigating this possibility could offer a pathway to generalise performance-enhancing design principles and provide meaningful guidance for the development of evaporable NFAs. The ultimate goal is to bridge the performance gap between VTE and SP OSCs and unlock the full commercial potential of OSCs.

1.3 Thesis Outline

This thesis focuses on investigating a series of all-VTE and hybrid OSC systems with non-fullerene electron acceptors, the latter comprising VTE electron donors and SP electron acceptors. The selected molecular pairs possess several key characteristics identified in state-of-art SP

NFA-based OSCs. One major characteristic, related to free charge generation pathways, is the presence of efficient Förster Resonance Energy Transfer (FRET) from the electron donor to the acceptor upon donor photoexcitation, followed by efficient hole transfer back to the donor [39]. In this thesis, OSC systems based on some key designing strategies summarised from SP NFA-based OSCs are developed. And these systems are investigated regarding free charge generation routes, device performance, charge transfer characteristics, and voltage losses. To establish a solid foundation for understanding the performance of systems under study, comprehensive characterisations of the pristine molecular films, focusing on their optical and electronic properties, are also included.

Chapter 2 introduces the fundamental physics of OSCs, including the optoelectronic properties of organic semiconducting molecules and molecular solids. It explains the underlying working principles and common characterisation methods of OSC devices. In particular, the chapter outlines key approaches for probing charge transfer (CT) states and presents the primary analytical framework used in this thesis, the detailed balance (DB) picture, for evaluating voltage losses. Chapter 3 covers the principles of FRET, including its mechanism, quantitative evaluation, and experimental determination, with a focus on its relevance to OSC applications. Chapter 4 summarises the materials used in this thesis and details the experimental and computational techniques employed.

Chapter 5 presents comprehensive optical and electronic characterisations of the pristine films of all studied molecules (SubNc, SubPc, DTDCTB, HB194, DCV3T and FBR). It also reports a series of photoluminescence (PL) quenching measurements, based on solid films, for verifying the occurrence of FRET between selected electron donor and acceptor molecules. These molecular pairs comprise VTE molecules serving as electron donors, and VTE (or SP) NFA molecules serving as electron acceptors. The electron donor–acceptor pairs of interest are those expected to support electron transfer from the donor following FRET from the acceptor, mimicking charge generation pathways in high-performing SP NFA OSCs. Comparison systems include those that do not support efficient electron transfer or FRET.

Chapter 6 comprises three sub-chapters that investigate selected molecular pairs in different device configurations.

1. Sub-chapter 6.2 examines bilayer planar heterojunction (PHJ) devices incorporating the

selected molecular pairs. The primary aims are to assess the influence of ionisation energy (IE) and electron affinity (EA) offsets on free charge generation when FRET is present, to determine how these offsets affect the energetic separation between CT and lowest excited singlet (S_1) states, and to identify possible origin of non-radiative voltage losses, other from CT state.

2. Sub-chapter 6.3 investigates trilayer PHJ devices using a FRET-enabled molecular pair with minimal EA offset (i.e. limited electron transfer efficiency). This chapter explores the potential of using FRET to enhance the performance of a previously established bilayer PHJ system.

3. Sub-chapter 6.4 explores the best-performing system identified in Sub-chapter 6.2, re-configured as a bulk heterojunction (BHJ). This system demonstrates low voltage losses comparable to those in leading SP NFA OSCs but with a much lower PCE. The focus here is to understand what are the key limitations that prevent it from reaching higher efficiencies.

Chapter 7 investigates hybrid systems comprising SP NFAs and VTE electron donors, along with their C_{60} references, in bilayer PHJ configuration. This chapter aims to identify a universal and simple approach to estimate CT state energy in PHJ systems with small energetic difference between CT and S_1 states ($\Delta E_{S1,CT}$).

Chapter 8 summarises the key findings of the thesis and outlines potential directions for future research. The appendix provides the codes used for data processing, calculations, and fitting.

2 | The Physics of Organic Solar Cells

In this chapter, the fundamentals of organic semiconducting molecules are discussed, including their molecular origins, effective energy bands, electronic transitions, and excitonic properties in both isolated molecules and solid-state cases. The primary sources consulted include books such as [27, 44]. The main pathways for exciton generation and transport within organic semiconductor films are introduced. Building upon this foundation, the underlying working principles of organic solar cells are explained. In particular, the donor–acceptor configuration, free charge generation mechanisms, and common device characterisation methods are explained. In addition, key approaches for probing charge transfer states and quantifying energetic disorder are presented. Finally, the origin of open-circuit voltage losses in organic solar cells are described within the framework of detailed balance model, with reference to the work of Rau et al. [45, 46]. This framework are used to outline how voltage losses can be quantified, forming the basis for the voltage loss analysis carried out in this thesis.

2.1 Organic Semiconducting Molecules

2.1.1 Energy Levels of a Molecule

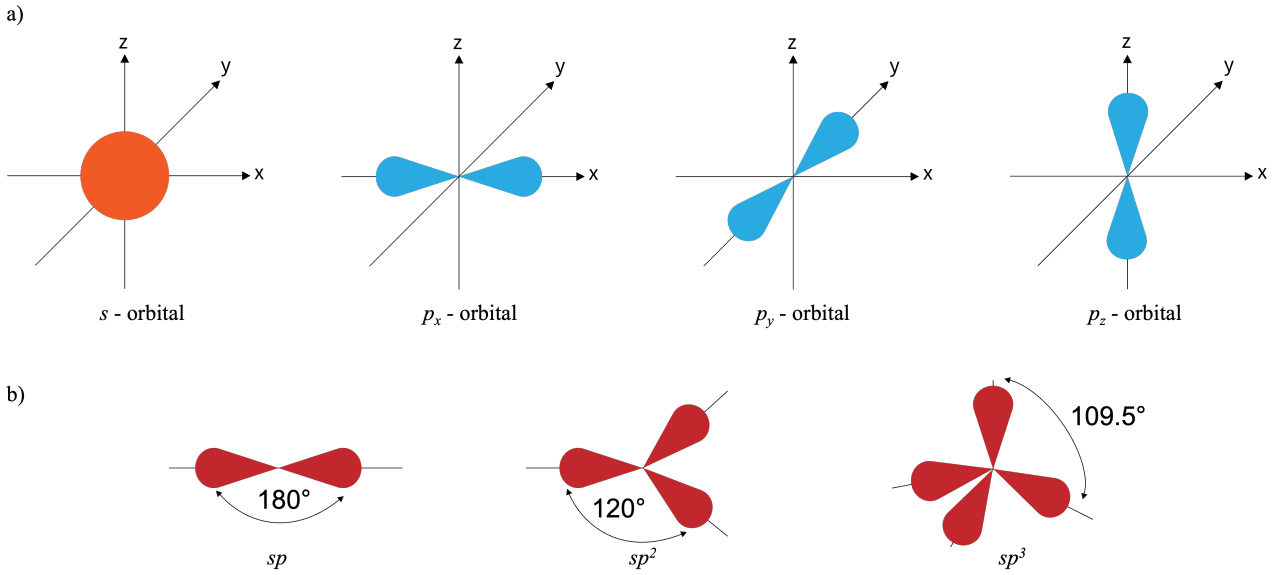


Figure 2.1: (a) Atomic s and p orbitals. The orange (s) and blue (p_x, p_y, p_z) regions represent the spatial distributions where electrons can be found. (b) sp, sp^2, and sp^3 hybrid orbitals. sp forms two equivalent orbitals oriented linearly. sp^2 forms three equivalent orbitals arranged in a trigonal planar geometry (120° bond angle). sp^2 forms four equivalent orbitals with a tetrahedral arrangement (109.5° bond angle). Redrawn and adapted from Reference [44].

Organic semiconducting molecules are carbon-based molecules. In its ground state, atomic carbon has six electrons, including four valence electrons. In the simplest Bohr model, these electrons are distributed in discrete shells around the nucleus. In the more advanced quantum mechanical model, however, electrons are described by wave functions and orbitals, which are solutions to the *Schrödinger equation* and reflect their wave-like behaviour [27]. Carbon has the electronic configuration $1s^2 2s^2 2p^2$, where the 1st and 2nd s-orbitals are fully occupied. Two of the three degenerate p-orbitals ($2p_x$, $2p_y$, $2p_z$) (Figure 2.1a) are singly occupied. When a carbon atom forms covalent bonds with other atoms, such as hydrogen or other carbon atoms, new hybrid orbitals are formed through linear combinations of the $2s$ and $2p$ orbitals, in order to minimise the total energy of the bonded system. Depending on the number of $2p$ orbitals mixed with the $2s$ orbital, the resulting hybrid orbitals are classified as sp, sp^2, or sp^3 (Figure 2.1b).

In sp hybridisation, one $2p$ orbital is combined with one $2s$ orbital, while in sp^3 hybridisation, all three $2p$ orbitals are combined with the $2s$ orbital. For organic semiconductors, the most commonly encountered hybridisations are sp^2, and sp^3, which are discussed in detail below through the examples of methane, ethane, ethene, and benzene.

In the case of methane (CH_4), the carbon atom forms four C–H bonds through sp^3 hybridisation, resulting in four equivalent sp^3 orbitals. These orbitals point toward the four corners of a tetrahedron, with bond angles of 109.5° between them (Figure 2.1b, sp^3). In ethane (C_2H_6), each carbon atom also has four sp^3 hybrid orbitals. When one electron in a carbon sp^3 orbital pairs with an electron from either another carbon's sp^3 orbital or a hydrogen's $1s$ orbital, a σ-bond is formed (Figure 2.2a).

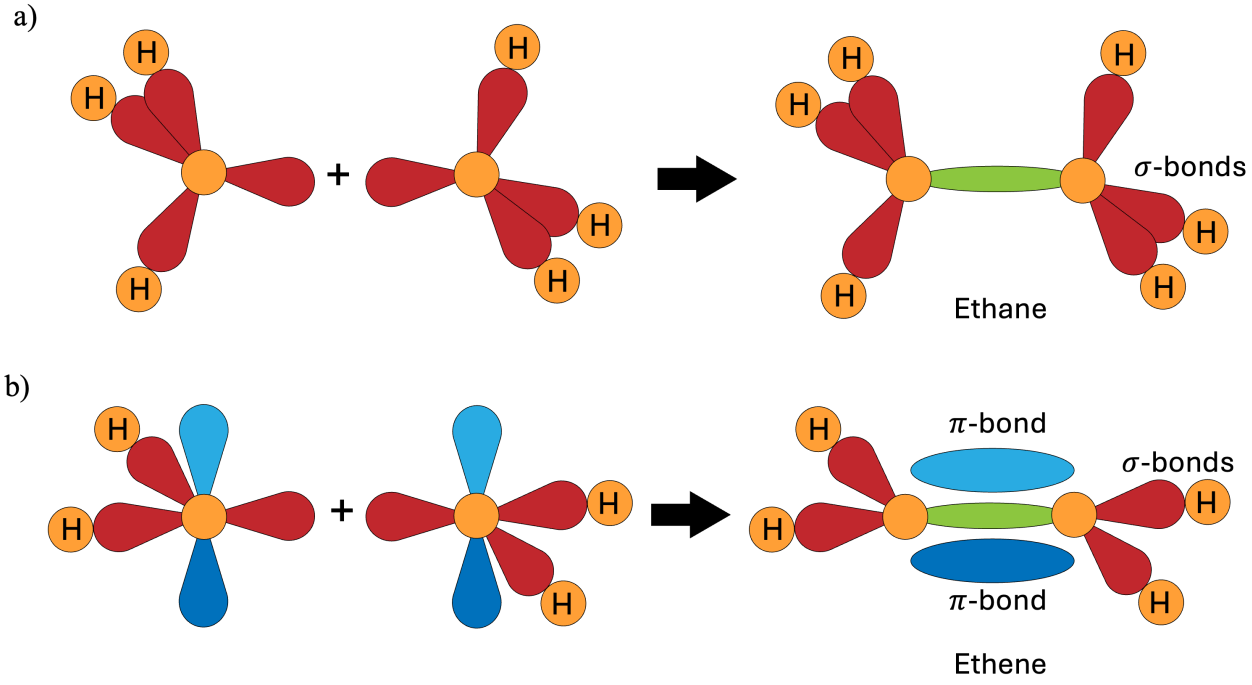


Figure 2.2: (a) Formation of ethane from six hydrogen atoms and two sp^3-hybridised carbon atoms. (b) Formation of ethene from four hydrogen atoms and two sp^2-hybridised carbon atoms. The hybridised orbitals are shown in red and the s-orbitals in orange. The σ-bonds are shown in green, while the two different phases of the π-bond are indicated by light and dark blue. The σ-bonds result from the overlap of sp^2 orbitals, and the π-bond arises from the out-of-plane overlap of p_z orbitals. Redrawn and adapted from Reference [44].

For ethene (C_2H_4), each carbon atom forms two C–H σ-bonds and one C–C σ-bond via overlap of sp^2 hybrid orbitals, leaving one unhybridised $2p_z$ orbital per carbon. These remaining $2p_z$ orbitals overlap out of the molecular plane to form a π-bond (Figure 2.2b). The π-bonding

orbitals are further classified as bonding (π) or anti-bonding (π^*) depending on their spin configuration, with the bonding state having lower energy (Figure 2.3, Ethene). Similarly, σ-bonds are classified into bonding (σ) and anti-bonding (σ^*) orbitals.

When more sp^2-hybridised carbon atoms are involved, as in the case of benzene (C_6H_6), the π-bonds can become delocalised across the entire molecule, resulting in a system of conjugated π-bonds. As additional π and π^* orbitals are formed, the energy spacing between the respective bonding and anti-bonding states decreases (Figure 2.3, Benzene) [27, 44].

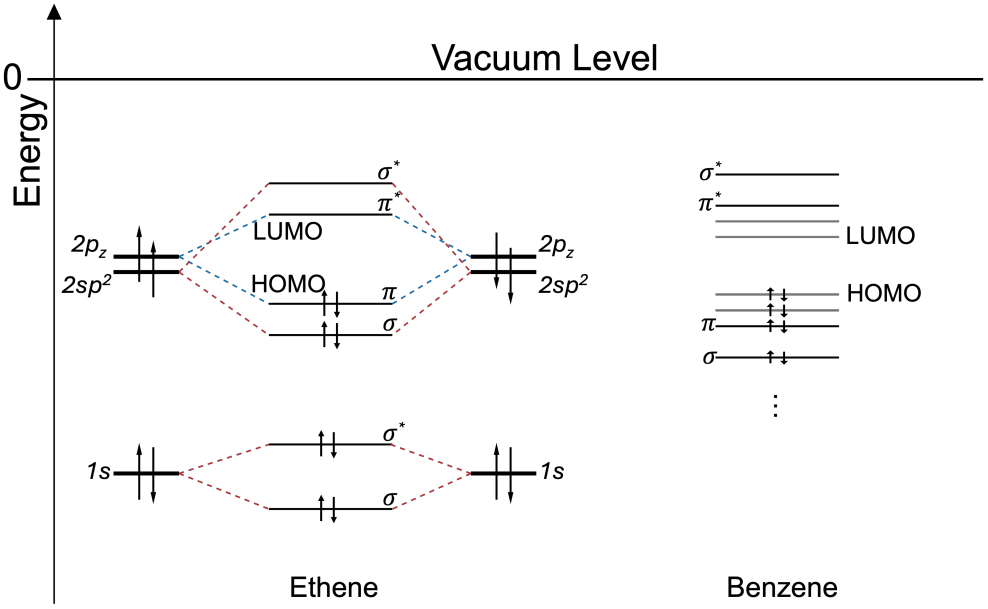


Figure 2.3: Energy level diagram illustrating the energy levels of σ and π bonds formed between carbon atoms for ethene and benzene. The formation of these bonds from atomic orbitals are shown for ethene. σ-bonds formed between carbon and hydrogen atoms are not included. Redrawn and adapted from Reference [44]

Electrons occupy molecular orbitals from lowest to highest energy, filling the bonding states first. The highest occupied bonding orbital is known as the highest occupied molecular orbital (HOMO), while the lowest unoccupied anti-bonding orbital is referred to as the lowest unoccupied molecular orbital (LUMO). These frontier orbitals are analogous to the valence and conduction bands in inorganic semiconductors. The energetic difference between HOMO and LUMO, can be analogous to the transport gap (E_{trans}) in inorganic semiconductors. However, in organic semiconductors, charge mobilities are typically lower, and the energy levels exhibit greater disorder [47, 48]. This contrasts with those ordered inorganic semiconductors (e.g c-Si) , where strong interactions in periodic crystal lattices give rise to well-defined bands with high

electrical conductivity [27].

2.1.2 Absorption and Emission

Absorption and emission of light by a molecule are fundamentally electronic transitions between ground and excited states. For organic semiconductors, E_{OPT} is typically large, ranging from approximately 1.7 to 3 eV. Only recently have narrow-gap molecules been reported, such as F8IC (1.27 eV), IEICO-4F (1.24 eV), and PBDT-TP (1.19 eV) [49]. In the absorption and emission spectra of molecular solids, $\pi - \pi^*$ transitions are typically not observed as sharp lines but rather as broadened peaks, due to the presence of vibrational, rotational, and translational manifolds [27]. Vibrational manifolds typically exhibit characteristic spacings around 200 meV, which are further overlaid by rotational and translational manifolds with spacings on the order of 10 meV [27].

Excited states are categorised as either singlet states (with spin-paired electrons) or triplet states (with electrons of same spin direction), as illustrated in Figure 2.4. Spin-paired electrons have opposite spins and therefore exhibit an overall spin of zero. The singlet ground state (S_0) of a molecule is typically a singlet [27].

Figure 2.4 presents the energy levels of ground, excited states and the possible transitions between them for a molecule's valence electrons. Upon photon absorption, an electron is promoted from S_0 to an excited singlet state (S_1, S_2, etc.). Electrons in higher singlet states (S_2, S_3, ...) undergo rapid non-radiative internal conversion to the lowest excited singlet state S_1 within picoseconds [27]. And then, relaxation can occur either radiatively via fluorescence or non-radiatively back to the ground state.

Triplet excited states, in contrast, are spin-forbidden therefore not directly populated via optical transitions from singlet states such as S_0 or S_1. However, they can still be accessed via a process called intersystem crossing (ISC), facilitated by spin–orbit coupling. The probability of ISC can be enhanced by incorporating heavy atoms into the molecular structure [50]. In this case, electrons in the lowest triplet excited state (T_1) can then directly decay to the S_0 states radiatively through phosphorescence. Because this process is spin-forbidden and thus less probable, the T_1 state typically exhibits a much longer exciton lifetime (on the order of milliseconds) compared to the S_1 state (typically in the microsecond to nanosecond range) [27].

Having introduced the possible transitions between different electronic states, we now consider how these transitions and states can be described with vibrational sublevels incorporated, within a quantum mechanical framework, specifically in the context of organic molecules.

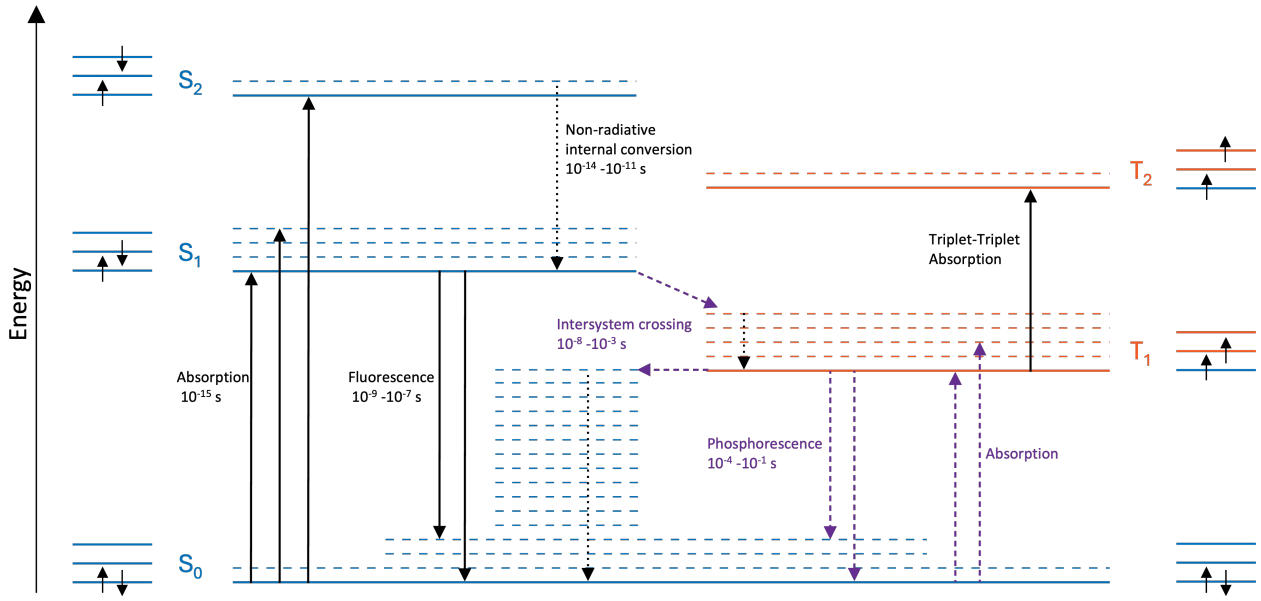


Figure 2.4: Jablonski diagram showing singlet (S) and triplet (T) states, along with their corresponding vibrational manifolds (dashed horizontal lines). Example optical transitions between these states are indicated by black solid arrows. Non-radiative internal conversion processes are shown as black dotted arrows, while spin-forbidden transitions (intersystem crossing) are shown as purple dashed arrows. Triplet-state radiative emission and absorption pathways are labelled separately. Typical timescales for each process are indicated. The electron spin configuration for each state is shown next to the respective energy levels. Redrawn and adapted from Tress [27] and Reference [51].

Under the *Born–Oppenheimer approximation*, where the coupling between electronic and nuclear vibrations is assumed to be weak, the total wavefunction of a molecular state can be approximated as the product of the electronic wavefunction Ψ_{el}, the spin wavefunction Ψ_{spin}, and the vibrational wavefunction Ψ_{vib}:

$$\Psi_{total} = \Psi_{el} \cdot \Psi_{spin} \cdot \Psi_{vib}, \tag{2.1}$$

where Ψ_{el} depends on the positions of the electrons and nuclei, Ψ_{spin} depends on the individual spin state of the electrons, and Ψ_{vib} depends on the positions of the nuclei [44]. The probability of finding the electrons, their spins, and the nuclei at specific positions in space is given by the square of the total wavefunction, $|\Psi_{total}|^2$.

After knowing total wavefunction of molecular states, electronic transitions from an initial state Ψ_i to a final state Ψ_j can be described. The intensity of light absorption or emission is expressed by the transition rate k_{ij}, defined as the number of transition events occurring per second (i.e. $k = \mathrm{d}n/\mathrm{d}t$) [44]. In the case of weak electronic coupling between states, where the transition is driven by a perturbing Hamiltonian $\hat{H}'$, k_{ij} can be described by *Fermi's golden rule*:

$$k_{ij} = \frac{2\pi}{\hbar}|\langle\Psi_j|\hat{H}'|\Psi_i\rangle|^2\rho \tag{2.2}$$

where ρ is the density of final states. By substituting the wavefunction Ψ (from Equation 2.1), the expression becomes:

$$k_{ij} = \frac{2\pi}{\hbar}|\langle\Psi_{el,j}\cdot\Psi_{spin,j}\cdot\Psi_{vib,j}|\hat{H}'|\Psi_{el,i}\cdot\Psi_{spin,i}\cdot\Psi_{vib,i}\rangle|^2\rho \tag{2.3}$$

For light–matter interactions, $\hat{H}'$ is related to the properties of the electromagnetic field and is expressed as $\hat{H}' = e\hat{\mathbf{r}}$, where $e\hat{\mathbf{r}}$ is the electric dipole operator [44]. This operator acts only on the electronic wavefunction Ψ_{el}, since the incident electromagnetic wave can only displace electrons resonantly [44]. The nuclei, being significantly heavier, cannot respond on the timescale of the oscillating electric field, and the spin wavefunctions are unaffected by the field [44, 52]. Hence, Equation 2.3 is derived to:

$$k_{ij} = \frac{2\pi}{\hbar}\rho|\langle\Psi_{el,j}|e\hat{\mathbf{r}}|\Psi_{el,i}\rangle|^2|\langle\Psi_{vib,j}|\Psi_{vib,i}\rangle|^2|\langle\Psi_{spin,j}|\Psi_{spin,i}\rangle|^2 \tag{2.4}$$

If the spin states of the initial and final states are the same, i.e. the transition is spin-allowed (e.g. $S_1 \rightarrow S_0$ or $T_2 \rightarrow T_1$), then the spin integral $\langle\Psi_{spin,j}|\Psi_{spin,i}\rangle$ equals 1. In contrast, for spin-forbidden transitions such as $T_1 \rightarrow S_0$, the integral is zero. Although these transitions can still occur via spin–orbit coupling, they cannot be described by this form of k_{ij}.

The electronic integral $\langle\Psi_{el,j}|e\hat{\mathbf{r}}|\Psi_{el,i}\rangle$ is non-zero only for dipole-allowed transitions [44]. Its value increases when the wavefunctions of the initial and final states have substantial overlap, and it ultimately governs the intensity of the electronic transition [44].

The final term, the vibrational integral $\langle\Psi_{vib,j}|\Psi_{vib,i}\rangle$, governs the spectral shape of absorp-

tion and emission. Figure 2.5a illustrates the potential energy curves of a diatomic molecule in the ground and first excited singlet states, based on Morse potential model. In the excited state, the potential energy curve is often displaced along the interatomic distance coordinate by $r^* - r_0$ (Figure 2.5a). This right-shift from r_0 to r^* arises because promoting an electron into an anti-bonding orbital reduces internuclear electron density, weakening the bond and expanding the equilibrium geometry [44].

For organic molecules, vibrational level splitting is typically around 100-200 meV, associated with the vibrational modes of C-C or C-H bonds [53]. At room temperature, where the thermal energy is approximately 25 meV, electrons predominantly occupy the lowest vibrational levels.

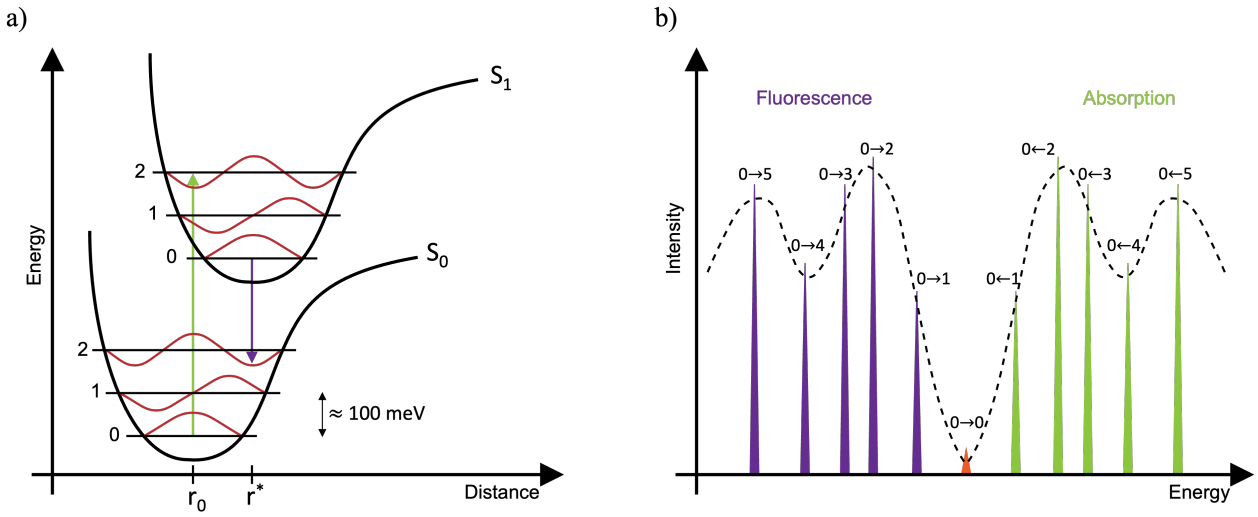


Figure 2.5: (a) Schematic of a diatomic molecule showing the difference in interatomic distance between the excited state (r^*) and ground state (r_0). Absorption and emission transitions are indicated by green and purple solid arrows, respectively. (b) Absorption and fluorescence emission spectra between the vibrational ground states and vibrational manifolds of S_0 and S_1, respectively. In solution or solid phase, the spectral peaks are broadened (dashed lines) compared to those in the gas phase. Redrawn and adapted from Tress [27] and Reference [51].

According to the *Franck–Condon principle*, the probability of an optical transition between two states increases with the degree of overlap between their vibrational wavefunctions at fixed molecular coordinates. Consequently, the intensity of vibrational transitions can be described using the overlap integral $\langle \Psi_{vib,m} | \Psi_{vib,0} \rangle$, representing the transition from the lowest (0 th) vibrational level of the ground state to the m th vibrational level of the excited state,. The probability of such a transition is given by the *Franck–Condon factor* $F = |\langle \Psi_{vib,m} | \Psi_{vib,0} \rangle|^2$. The transition is often denoted as $I_{0 \to m}$.

As shown in Figure 2.5b, the fluorescence emission spectrum is red-shifted (i.e. shifted to lower energy) compared to the absorption spectrum. This shift results from non-radiative energy losses associated with rapid internal conversion and molecular reorganisation to a new equilibrium geometry after excitation.

2.2 Organic Thin Films

2.2.1 Energy Levels in Solids

The energetic bands and optoelectronic transitions of isolated organic molecules have been discussed, and we now will revisit these concepts in the context of organic solids. When organic molecules are brought together to form amorphous or crystalline solid films, polarisation effects emerge. Weak *Van Der Waals* interactions arising from these polarisation effects alter the energy landscape relative to the vacuum level. These shifts are illustrated in Figure 2.6. Molecular properties such as absorption spectra and energy levels are shifted due to polarisation effects in molecular solids. To clearly distinguish between isolated-molecule and solid-state cases, subscripts 'g' and 'c' are used to denote the gas-phase (isolated molecule) and condensed-phase (molecular solid) values, respectively, when referring to LUMO, HOMO, EA, and IE.

Within the framework of *Koopmans' theorem*, the energy of the HOMO_g (LUMO_g) of a molecule is approximately equal to the negative of the ionisation energy IE_g (electron affinity EA_g), respectively [54]. This equivalent can also be extended to the solid state. In the solid state, shifts in IE_c and EA_c arise from two primary effects: (1) induction from surrounding molecules (U_{ind}), and (2) electrostatic interactions due to the environmental charge distribution (U_{el}) [51, 55]. These effects contribute to the electrostatic stabilisation energies for holes (P_c^+) and electrons (P_c^-), defined as:

$$P_c^+ = IE_c - E_{HOMO_g} = -U_{ind} + U_{el} \tag{2.5}$$

$$P_c^- = EA_c - E_{LUMO_g} = U_{ind} + U_{el} \tag{2.6}$$

Here, U_{ind} lowers IE_c and raises EA_c, thereby stabilising the energy levels, while U_{el} shifts both IE_c and EA_c equally in the same direction [56, 57].

When a molecule is placed in a static electric field, electric multipoles can be induced due to distortion of its charge distribution [55]. This effect is especially significant in organic molecules with large, delocalised π-electron clouds, where induction effects can result in energy level differences of 1–2 eV between the gas and solid phases [55, 58].

Electrostatic interactions arise from charge–charge, charge–dipole, dipole–dipole, and charge –quadrupole interactions, among others [55]. For neutral molecules with negligible dipole–dipole interactions or near-zero static dipole moments, charge–quadrupole interactions dominate [51, 55]. These interactions mainly affect the nearest neighbours, as their influence decays with $1/r^3$ [51]. Charge–quadrupole effects can significantly influence solid-state energy levels, as demonstrated by both modelling and experimental measurements in thin films and devices [39].

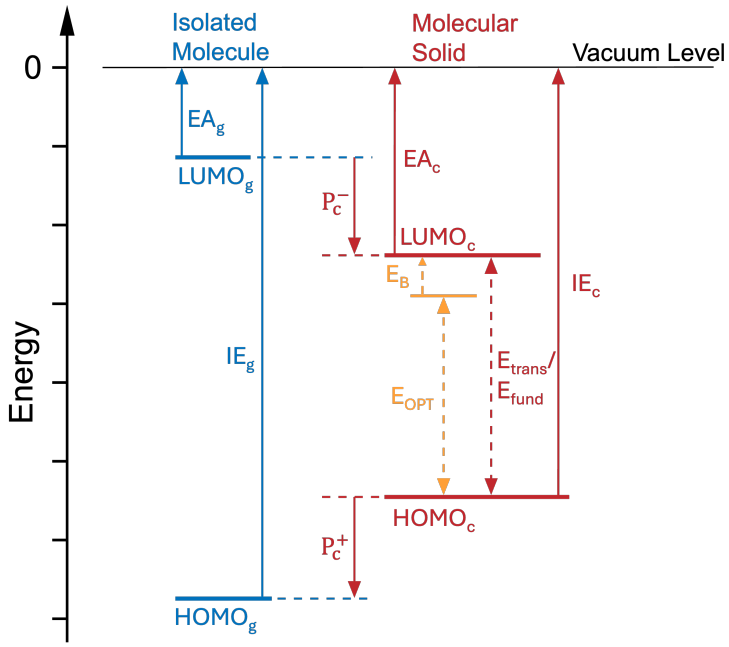


Figure 2.6: Schematic diagram illustrating the energy levels of molecular states in the isolated molecule (denoted with subscript 'g') and molecular solid (denoted with subscript 'c') forms. LUMO and HOMO represent the energies of molecular orbitals relative to the vacuum level, where LUMO is the lowest unoccupied molecular orbital, HOMO is the highest occupied molecular orbital. E_B is the exciton binding energy. EA, IE, and P denote the electron affinity, ionisation energy, and polarisation energy, respectively. E_{OPT} and E_{trans}/E_{fund} represent the optical and electrical transport/fundamental gaps. The energy level (orange solid line) labelled in graph for E_{OPT} does not represent physical energy level with respect to $HOMO_c$ and $LUMO_c$. Redrawn and adapted from Reference [59].

Returning to Figure 2.6, similar to the isolated molecule case, the energetic difference between $HOMO_c$ and $LUMO_c$ in molecular solids defines E_{trans} (also referred as the fundamental gap E_{fund}), where electron transport occurs in the $LUMO_c$ and hole transport occurs in the $HOMO_c$ [27, 51]. In organic semiconductor solids, E_{fund}/E_{trans} differs from E_{OPT} due to the presence of exciton binding energy. Here, E_{OPT} is defined as the first allowed optical transition between S_0 and the S_1, which equals $E_{fund} - E_B$ [27, 51].

2.2.2 Excitons

Upon photoexcitation, semiconducting molecules generate excitons, which are bound electron–hole pairs. The energy required to separate an electron–hole pair is defined as E_B. For molecular solids, E_B corresponds to the difference between E_{OPT} and E_{fund}/E_{trans}, as shown in Figure 2.6.

In highly crystalline inorganic semiconductor solids, where strong intermolecular interactions occur (i.e. $\epsilon \geq 10$), excitons are very weakly bound (with $E_B \approx k_B T$) and delocalised across many molecules. These are referred to as *Wannier* excitons (Figure 2.7c). Due to their loosely bound nature, *Wannier* excitons can easily dissociate into free holes and electrons, as their binding energy is typically lower than the thermal energy at room temperature [60].

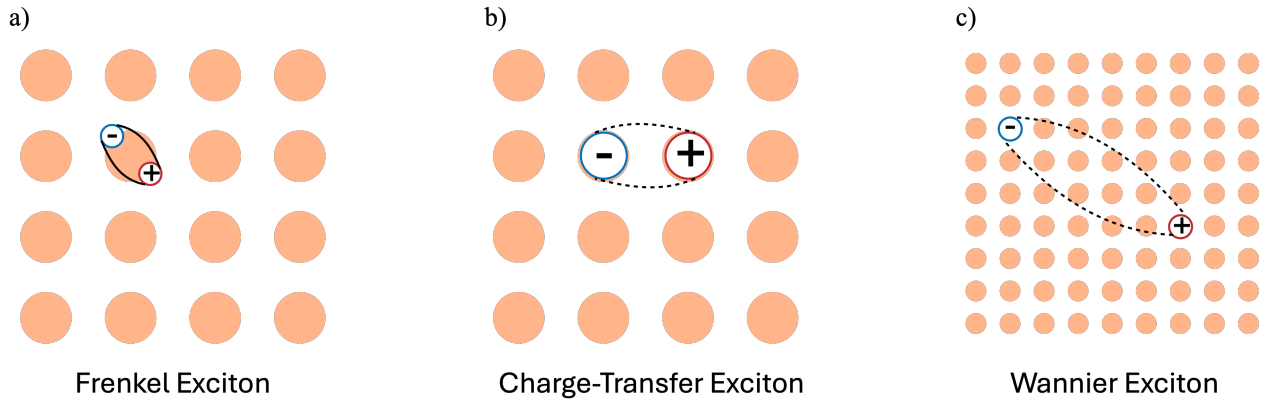


Figure 2.7: (a) *Frenkel* excitons, where tightly bound electron–hole pairs are located on a single molecule. (b) *Charge transfer* excitons, where weakly bound electron–hole pairs are localised across molecules. (c) *Wannier* excitons, where very weakly bound electron–hole pairs are highly delocalised across many molecules.

In contrast, organic semiconductors generate tightly bound excitons that are described by

Frenkel excitons, where the electron–hole pair is localised on a single molecule upon photon absorption (Figure 2.7a). Their E_B is typically on the order of hundreds of meV, and their solid films tend to have low dielectric constants ($\epsilon \approx$ 3-5) [27, 61].

Excitons that are localised across neighbouring molecules are classified as CT excitons (Figure 2.7b). These excitons are associated with an intermediate energetic state known as the CT state. CT states are typically found in bi-molecular solids, much less common in mono-molecular systems, as their absorption features can be indistinguishable from the $S_0 \rightarrow S_1$ transition in mono-molecular systems [51]. Exceptions include two single-component systems: α-6T and Y6. In α-6T, differences in HOMO and LUMO levels at the interface between molecules of differing orientation enable CT state formation, whereas in Y6, CT states arise from interactions between π-π stacked neighbouring molecules of the same orientation [62–65]. The importance and formation of CT states in the operation of organic solar cells will be discussed in further sections.

2.2.3 Exciton Transport

After *Frenkel* excitons are generated, they can migrate through solid to neighbouring molecules. Exciton transport lengths in organic semiconductor solids typically range from 5–20 nm, although some molecules exhibit unexpectedly long transport distances of 20–47 nm [66, 67].

There are generally two energy transfer mechanisms that facilitate exciton transport from an excited molecule to an ground-state molecule non-radiatively: *Förster* (Figure 2.8a) and *Dexter* (Figure 2.8b) [68–70]. Following energy transfer, the excited molecule returns to its ground state while the ground-state molecule is promoted to an excited state, effectively relocating the exciton.

The *Förster* mechanism is a dipole–dipole electromagnetic interaction that occurs when the absorption spectrum of the energy acceptor significantly overlaps with the emission spectrum of the excited energy donor. This is a non-radiative process, and it is often referred to as Förster Resonance Energy Transfer (FRET). Upon excitation of the energy donor, its transition dipole moment interacts with that of a nearby acceptor molecule, resulting in the promotion of one of the acceptor's electrons to excited state, while an electron on the donor returns to the ground state (Figure 2.8a). No actual exchange of electrons takes place. The efficiency of FRET

decreases with the distance r_{DA} between donor and acceptor as ${r_{DA}}^{-6}$ under ideal dipole approximation and in the weak electronic coupling regime, and is therefore only effective over certain ranges, typically 1–10 nm [66,70]. In general, only singlet excitons can be transferred via FRET, although triplet excitons can also be transferred if they are located on a phosphorescent donor [66,71,72].

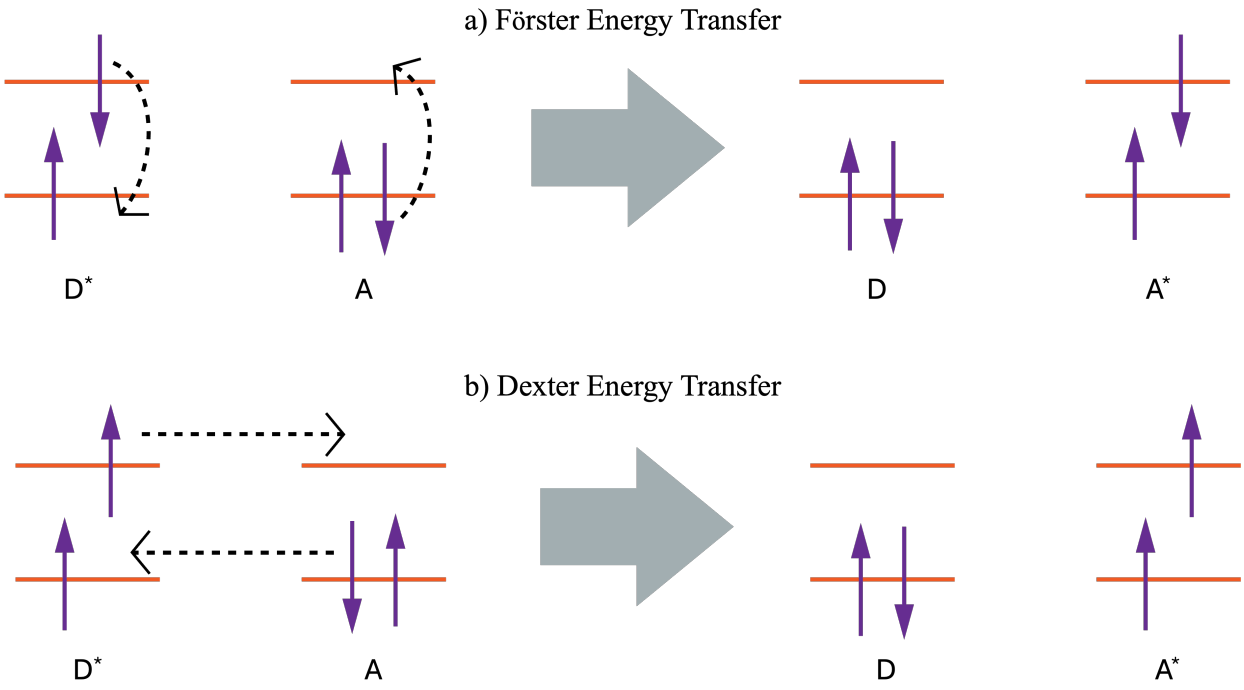


Figure 2.8: (a) *Förster* Resonance Energy Transfer. (b) *Dexter* Energy Transfer. The orange horizontal lines represent HOMO and LUMO energy levels of energy donor (D) and acceptor (A); the asterisk denotes excited states. The dashed arrows show simultaneous rearrangement of the electronic configuration. Redrawn and adapted from Reference [66].

In contrast, *Dexter* energy transfer involves actual electron exchange between the excited energy donor and acceptor and can only occur when their molecular orbitals significantly overlap (i.e. when the donor–acceptor separation r_{DA} is within 1 nm) [66,68,73]. During *Dexter* transfer, an electron from the excited energy donor molecule has a finite probability of going into an excited orbital of the ground-state acceptor, promoting the acceptor into an excited state while the donor returns to the ground state (Figure 2.8.b). The probability of *Dexter* transfer decays exponentially with distance r_{DA}, making it a short-range process ($\approx 1\ nm$), in contrast to the longer-range (1-10 nm) FRET. Both singlet and triplet excitons located at a non-phosphorescent excited donor can be transferred via *Dexter* mechanism, however singlet

excitons transfer more efficiently with FRET [66].

2.3 Organic Solar Cells

2.3.1 Electron Donor and Acceptor Configuration

As briefly discussed in previous sections, Frenkel excitons in organic semiconductors typically have an E_B on the order of hundreds of meV, which is significantly larger than the thermal energy k_BT (approximately 25 meV at room temperature) and thus strongly bound. Therefore, to generate free electrons and holes before decays occur, this binding energy must be overcome. The earliest generation of OSCs employed only one type of molecule in photoactive layer (e.g. CuPc, MgPc), which suffered from inefficient exciton dissociation, limiting their PCEs to around 1% [74]. To overcome this limitation, Tang introduced the concept of a bi-molecular heterojunction (later known as planar heterojunction, PHJ), closely resembling the inorganic p–n junction [75], where one molecule functions as an electron donor and the other as an electron acceptor .

By selecting electron donor and acceptor molecules with suitable energy level alignment for charge transfer, localised Frenkel excitons can delocalise at the electron donor-acceptor (D-A) interface and form CT excitons [27, 76]. When the donor molecule has a shallower LUMO (lower EA) than the acceptor (Figure 2.9a, Figure 2.9c), an electron in the excited electron donor state (S_1) can transfer to the acceptor's LUMO, resulting in a positively charged donor (D^+) and a negatively charged acceptor (A^-) (Figure 2.9.b). This electron transfer process is followed by molecular reorganisation, which lowers the total molecular energy and gives rise to singly occupied molecular orbitals (SOMOs) on both electron donor and acceptor molecules [27]. These SOMOs are slightly closer in energy than the original LUMO_c^A and HOMO_c^D levels (Figure 2.9b), and their energy difference defines the CT state energy E_{CT}, which is thus generally smaller than lowest excited singlet state energy (E_{S1}) of individual molecule. For some state-of-art NFA systems, the energy difference between E_{S1} and E_{CT} approaches zero [39, 41, 77–79], suggesting that the SOMOs at the CT interfaces may become significantly close and even overlap. CT states can be experimentally probed via absorption

and emission spectroscopy, as they are optically coupled to the ground state [80,81], which will be discussed in detail later.

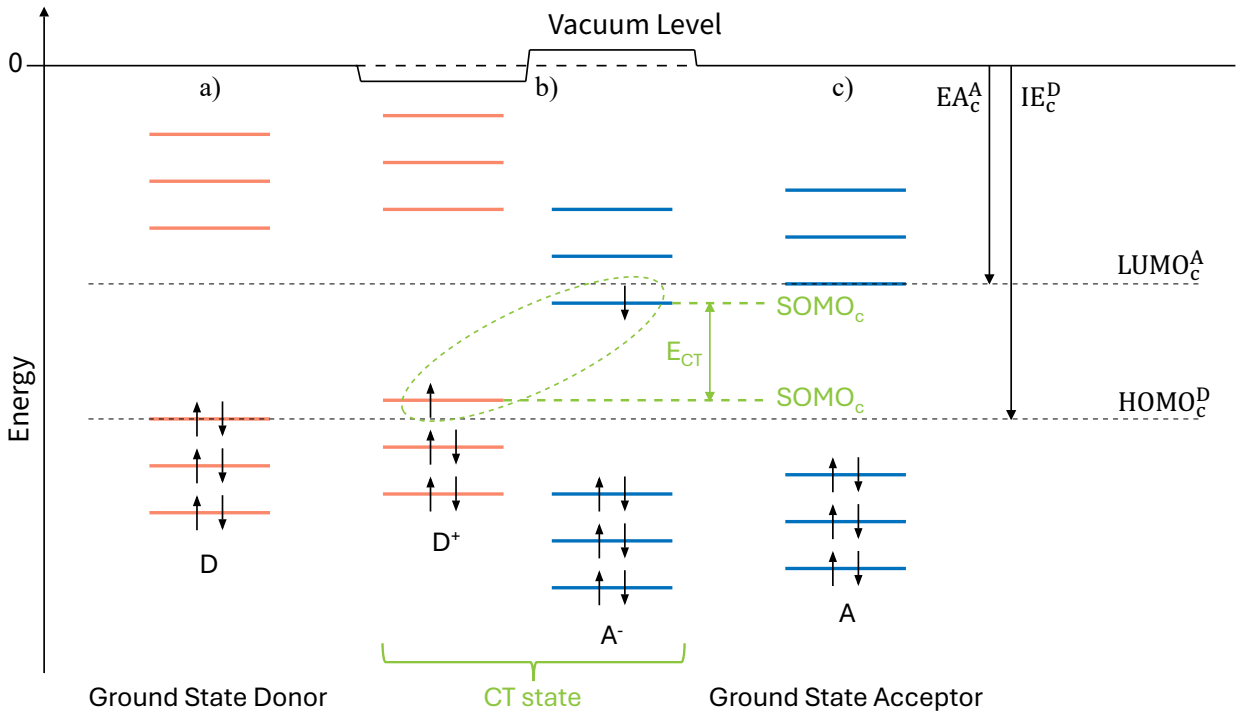


Figure 2.9: (a) Ground-state donor, (b) charge transfer (CT) state, and (c) ground-state acceptor energy levels in solid films. In the CT state, the ionised donor (cation, D^+) and acceptor (anion, A^-) undergo molecular reorganisation, which lowers the energy of the hole and electron on each molecule, respectively. This reorganisation gives rise to singly occupied molecular orbitals (SOMOs) on both the donor and acceptor. The energy difference between these two SOMOs defines the CT state energy (E_{CT}). The difference between the acceptor LUMO ($LUMO_c^A$) and donor HOMO ($HOMO_c^D$) is referred as the effective band gap. The difference between the $SOMO_c$–$SOMO_c$ gap and the $HOMO_c^D$–$LUMO_c^A$ gap corresponds to the CT-state exciton binding energy. Redrawn and adapted from Tress [27] and Reference [51].

Because CT excitons are more delocalised than Frenkel excitons, they have lower binding energies, which increases the probabilities of charge separation [27]. In the case of electron transfer from the electron donor, the LUMO offset (ΔLUMO) provides the driving force to overcome the Frenkel exciton binding energy $E_B^{Frenkel}$ [27, 41]. Similarly, when the electron acceptor is excited and $HOMO_c^D$ lies above $HOMO_c^A$ (i.e. ΔHOMO> 0), a hole can transfer from the excited acceptor to the donor, also forming a CT exciton at the D-A interface. This process is referred as hole transfer. While D-A heterojunctions significantly enhance exciton dissociation in OSCs, they also introduce recombination pathways [61, 81, 82], which will be discussed in subsequent sections.

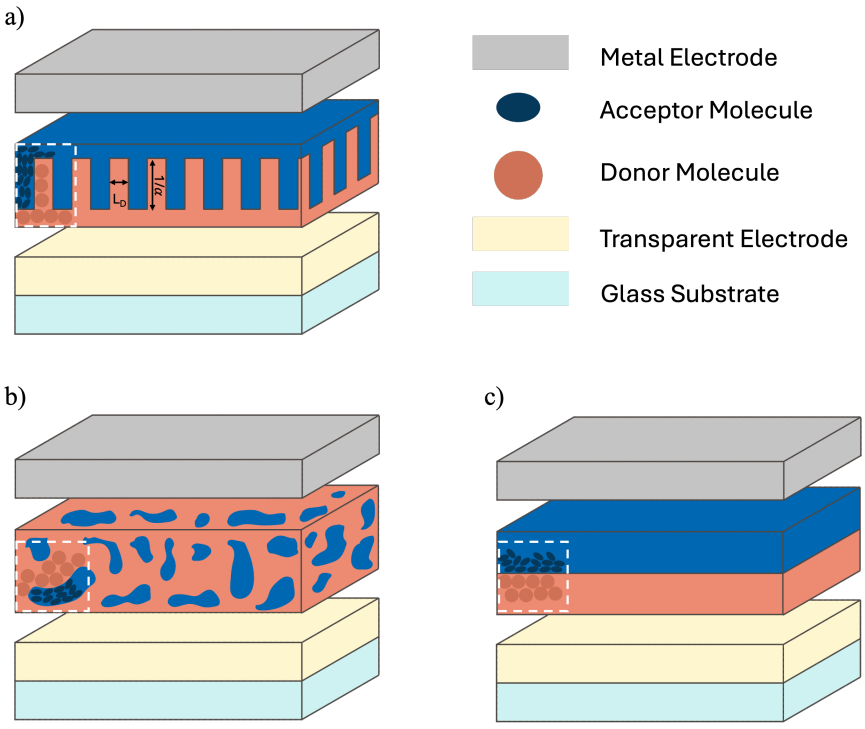


Figure 2.10: Schematics of different donor–acceptor heterojunction architectures for solar cell applications: (a) comb-like structure, (b) bulk heterojunction (BHJ), and (c) planar heterojunction (PHJ). The layers that consist of donor and acceptor molecules form the active layer. Simplified illustrations of molecular contact (random-lying molecules) at the donor|acceptor interface are shown in the white dashed boxes. In the ideal comb-like structure, the width of each 'tooth' equals the exciton diffusion length L_D, while the length is inversely proportional to the absorption coefficient α of the absorber molecules. Redrawn and adapted from Tress [27].

The first heterojunction solar cell featured vertically stacked electron donor and acceptor layers, forming the so-called PHJ configuration (Figure 2.10c) [75]. When favourable energetic offsets are at the interface, this structure provides good exciton dissociation pathways for those excitons that can reach it [83]. However, the efficiency of this configuration is fundamentally limited by the exciton diffusion length (L_D), which typically ranges from 5 to about 50 nm [66, 67]. This is considerably shorter than the typical absorption depth δ of organic semiconductors, which lies between 100–200 nm [84, 85]. As a result, although the PHJ architecture improves exciton dissociation efficiency at the interface, the limited free charge carriers generation constrains the overall photocurrent.

The ideal architecture is often thought to be a comb-like structure (Figure 2.10a), in which the 'tooth' of each material have a width equal to L_D and a length equal to the absorption depth ($\delta = 1/\alpha$, where α is the absorption coefficient) [27]. This design would enable both effi-

cient exciton separation and sufficient photon absorption. However, such a precisely controlled nanostructure is not easily achievable in reality. As a practical alternative, intermixed bulk heterojunctions (BHJs) were developed by blending the donor and acceptor molecules (Figure 2.10b) [86–88]. This approach enables the use of thicker active layers to around 100 nm [89], while maintaining efficient exciton dissociation, with D-A interfaces distributed throughout the film, allowing most excitons to reach an interface before recombining.

In addition to selection of molecules, the morphology and phase characteristics of donor and acceptor materials also influence solar cell performance [90–92]. Studies of dilute BHJs systems with donor or acceptor content $\leq$10% have shown that D-A interfaces can serve as additional recombination sites for electrons and holes [51, 93, 94]. An excessive number of D-A interfaces can lead to losses in both open-circuit voltage and photocurrent [93]. More recently, the introduction of a third component into binary BHJs has shown promise for enhancing light absorption, optimising film morphology, and mitigating recombination losses [95, 96].

2.3.2 Charge Generation and Recombination

Having discussed the D-A configuration and the formation of CT states at their interface, we now turn to the subsequent processes of free charge generation and recombination in these OSCs. Figure 2.11 summarises the major charge generation routes, recombination pathways, associated transition rates, and characteristic timescales.

CT states can form at D-A interface via either electron transfer or hole transfer from Frenkel excitons. In most OSCs employing fullerenes (e.g C_{60}) as the electron acceptor, the donor molecules dominate photon absorption, and CT states are primarily formed via electron transfer. However, in some fullerene systems, hole transfer plays a more prominent role. For example, in TAPC:C_{60} blends, where TAPC is a wide-gap, transparent molecule and C_{60} is the dominant absorber [97]. Depending on the absorption profiles of the electron donor and acceptor, both electron and hole transfer processes may occur and contribute to CT state formation. In some state-of-the-art NFA-based OSC systems, both donor and acceptor absorb strongly in distinct or minimally overlapping spectral regions. And it has been shown that electron donor excitons can first undergo FRET to the acceptor, followed by hole transfer back to donor to form CT states and subsequent charge separation [39].

The energetic offset in LUMO (or HOMO) between electron donor and acceptor was initially thought to provide the driving force for CT exciton formation. For a long time, it was believed that large energetic offset is essential for efficient exciton dissociation and later it was found for efficient systems, an offset of roughly 300 meV is required for efficient systems [98]. More recently, an alternative picture based on the lowest excited singlet/CT state energy difference has been proposed, where the driving force for CT state generation is the energy difference $\Delta E_{S1,CT} = E_{S_1} - E_{CT}$. In fullerene-based systems, $\Delta E_{S1,CT}$ of around 100 meV was suggested to be necessary for efficient charge separation [99, 100]. Ongoing research continues to explore which, offset in EA_c/IE_c or $\Delta E_{S1,CT}$, more accurately describe the driving force for CT state formation.

However, exciton dissociation driven by energetic offsets predominantly applies to low-energy CT states, denoted as CT^1 in Figure 2.11. In addition to these, a second class of CT excitons, so-called hot CT states, exists at higher energies and can also contribute to free charge carrier generation [101]. The excitons, which carry excess energy, may access delocalised and energetically elevated CT states, from which they can dissociate directly into free carriers via a rate constant k^*_{CS} (Figure 2.11 green dashed line). Nevertheless, numerous studies on fullerene-based OSCs have shown that hot CT-mediated dissociation is not the dominant charge generation pathway [102]. An exception is the DTDCTB/C_{60} system, which has been reported to rely primarily on hot CT dissociation for charge separation [103]. While some hypotheses suggest that low-offset NFA-based OSCs may also exploit hot CT pathways for efficient charge generation, this remains an debating question in the field.

Absorption and emission of photons are reciprocal processes involved in the optoelectronic transitions of individual molecules, typically accompanied by a Stokes shift toward lower energies for emission. This shift arises from non-radiative energy losses due to rapid internal conversion and molecular reorganisation as the molecule relaxes to a new equilibrium following excitation [27, 44]. After excitons are generated on electron donor (or acceptor) molecules, those that fail to reach the D-A interface follow the recombination pathways, ultimately relaxing back to the ground state S_0 (Figure 2.11a). For excitons that do reach the D-A interface, the interfacial energetic driving force promotes their entry into the CT state manifold at rate of $k_{CT,S1}$, where they relax to CT^1 on ultrafast timescales of 20–300 fs, as measured in fullerene

blends [102, 104].

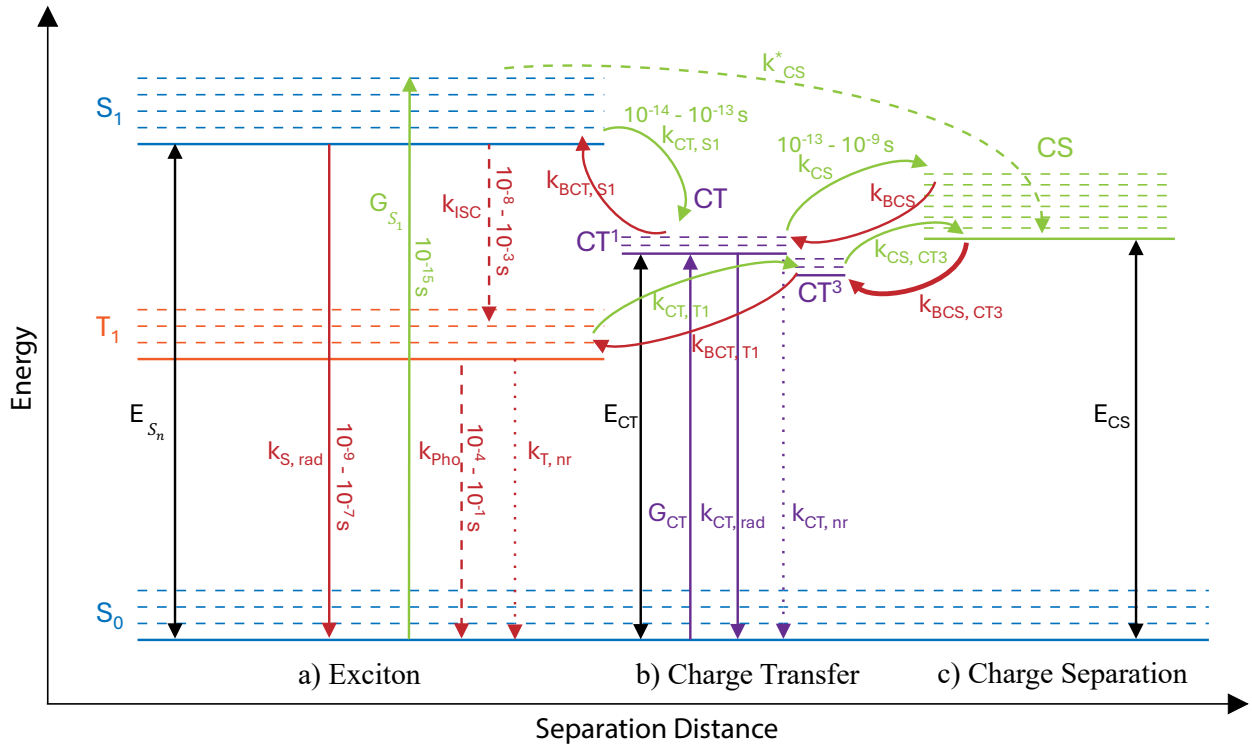


Figure 2.11: Jablonski diagram illustrating charge generation and recombination processes in organic solar cells (OSCs) in a 5-state model picture. (a) Upon photon absorption by an electron donor or acceptor molecule, electrons are promoted from the ground state (S_0) to the first singlet excited states (S_1), forming excitons at rate G_{S_1}. If these excitons reach electron donor–acceptor (D-A) interfaces, they can be converted into charge transfer (CT) states via electron or hole transfer at rate $k_{CT,S1}$. Alternatively, excitons may bypass the lowest energy CT state and dissociate directly into charge-separated (CS) states at a rate k^*_{CS} as 'hot' CT excitons. Excitons that do not reach a D-A interface may decay from S_1 radiatively ($k_{S,rad}$), undergo intersystem crossing (ISC) to the triplet state T_1 at rate k_{ISC}, and subsequently decay via phosphorescence (k_{Pho}) or non-radiatively ($k_{T,nr}$). b) The CT manifold is composed of singlet or triplet CT (CT^1 and CT^3) states, which are coupled via ISC. CT^1 states can also be directly photoexcited at rate G_{CT}. Once formed, CT^1 states may undergo back charge transfer (BCT) to the singlet states S_1 at rate $k_{BCT,S1}$, decay to the ground state S_0 non-radiatively ($k_{CT,nr}$) or radiatively ($k_{CT,rad}$), or dissociate into CS states at rate k_{CS}. T_1 triplets may also be transited back into CT^3 states at rate $k_{CT,T1}$ and then CS states at rate $k_{CS,CT3}$. (c) CS states may recombine to form CT^1 and CT^3 states at rate k_{BCS} and $k_{BCS,CT3}$, respectively. CT^3 states may further undergo BCT to triplet states T_1 and recombine. Solid arrows indicate optically allowed transitions, red dashed arrows represent spin-forbidden transitions, and dotted arrows indicate non-radiative decay pathways. Green arrows denote pathways leading from exciton generation to charge dissociation. The energy levels of singlet, CT, and CS states are labelled as E_{S_1}, E_{CT}, and E_{CS}, respectively. Typical timescales of major transitions were taken from References [27, 101, 104]. Redrawn and adapted from Tress [27], References [51] and [105].

Charge recombination processes can generally be categorised as geminate or non-geminate.

Geminate recombination is the recombination of an electron-hole pair that originated from the same exciton. Non-geminate recombination is the recombination of an electron and hole that come from different excitons. Once CT^1 states are formed, charge dissociation (k_{CS}) competes with recombination via radiative ($k_{CT,rad}$), non-radiative ($k_{CT,nr}$) decay or back transfer to S_1 states ($k_{BCT,S1}$). As CT states are optically coupled to S_0, they can decay radiatively to the ground state. In addition, they can relax non-radiatively through vibrational relaxation, similar to singlet exciton states (Figure 2.11b) [102]. Those CT^1 excitons that successfully dissociate enter the charge-separated (CS) state and can subsequently be extracted as free charge carriers if no other losses occur.

CT^1 excitons that enter CS state may also recombine to reform CT complexes, CT^1 and CT^3 at rate k_{BCS} and $k_{BCS,CT3}$ (Figure 2.11c). This bimolecular reformation results in singlet and triplet charactered CT excitons that are nearly degenerate in energy, separated by only a few tens of meV [106, 107]. Following spin statistics, 3/4 of the regenerated CT excitons are triplets (CT^3) and 1/4 are singlets (CT^1). The CT^3 excitons are spin-forbidden from directly decaying to the ground state S_0, and instead tend to undergo back charge transfer (BCT) to the lower-energy triplet state T_1 at rate $k_{BCT,T1}$. These long-lived CT^3 excitons are considered one of the main loss channels in OSCs [106]. However, with appropriate control over wavefunction delocalisation, it is possible to dissociate CT^3 excitons back into free charges at rate $k_{CS,CT3}$ rather than allowing them to decay into T_1 states [106].

2.3.3 Current Density-Voltage Characteristics

For every solar cell, its current density-voltage (J-V) characteristics provide a direct measure of device performance under known spectrum and intensity of incident light source. Shockley and Queisser proposed the detailed balance framework, which defines the maximum theoretical efficiency for a single p–n junction solar cell with a bandgap of E_g. Under this idealised model, it is assumed that no absorption occurs below E_g, each absorbed photon generates one electron–hole pair, and all recombination is radiative [108]. This framework establishes the so-called Shockley–Queisser (S-Q) limit of a device. Under this model, for an ideal inorganic semiconductor p–n junction under illumination, Shockley [109] derived the J–V characteristics

(shown in Figure 2.12) as

$$J(V,T) = J_0(e^{\frac{qV}{k_BT}} - 1) - J_{ph}(V), \tag{2.7}$$

where J_0 is the dark saturation current, q is the elementary charge, k_B is the Boltzmann constant, T is the temperature of device, J_{ph} denotes the photocurrent under illumination, and V is the applied external voltage. For many high-performance crystalline inorganic semiconductors, $J_{ph}(V)$ is independent of V, and thus the short-circuit current density (J_{sc}) is given as $J_{sc} = J_{ph}$. However, for organic semiconductors with low charge carrier mobilities, significant charge can be accumulated during operation, partially screening the applied external field [51]. As a result, a lot of OSCs exhibit strong voltage dependence in their photocurrent [27] i.e. the photocurrent increases with forward bias due to enhanced internal electric fields.

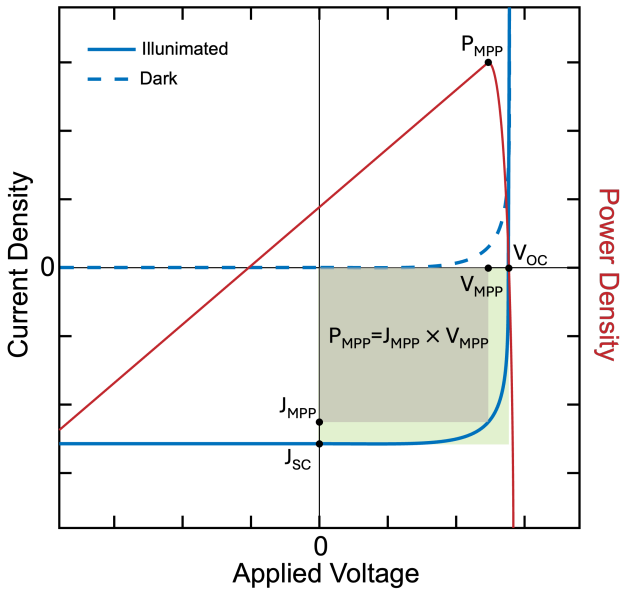


Figure 2.12: Example current density–voltage (J–V) curve modelled with the ideal Shockley diode equation (Equation 2.7) under illumination (solid blue line) and in the dark (dashed blue line). The power density $P = J \times V$ is shown as a red solid line. The grey shaded area represents the maximum power density $J_{MPP} \times V_{MPP}$, while the green shaded area corresponds to $J_{sc} \times V_{oc}$. The maximum power point P_{MPP}, current density and voltage at MPP (J_{MPP}, V_{MPP}), short-circuit current density J_{sc}, and open-circuit voltage V_{oc} are marked with black dots. Redrawn and adapted from Reference [51].

With Equation 2.7, one can derive the ideal open-circuit voltage V_{oc} (i.e. the voltage under illumination for which all charge carriers recombine and $J(V,T) = 0$) as

$$V_{oc} = \frac{k_BT}{q} \ln\left(\frac{J_{ph}}{J_0} + 1\right) \approx \frac{k_BT}{q} \ln \frac{J_{ph}}{J_0}. \tag{2.8}$$

In practice, real devices do not operate under idealised conditions. Losses from imperfect absorption, charge extraction, and non-radiative recombination must be considered. Therefore, Equation 2.7 is generalised into the non-ideal diode equation:

$$J(V,T) = J_0(e^{\frac{qV}{n \cdot k_B T}} - 1) - J_{ph}(V), \tag{2.9}$$

with the inclusion of an ideality factor n (typically between 1 and 2) to account for the dominant recombination pathways [27].

By definition, the power density P generated by a solar cell is given as $P = J \cdot V$, where J is the current density. On the J–V curve, the maximum power point (MPP) corresponds to the operating condition where the product $J_{MPP} \times V_{MPP}$ is maximised. The fill factor (FF), describing the squareness of the J–V curve, is defined as

$$FF = \frac{P_{MPP}}{J_{sc} \cdot V_{oc}}. \tag{2.10}$$

The power conversion efficiency (PCE) quantifies how effectively the incident light is converted into electrical power and is defined as

$$PCE = \frac{P_{MPP}}{P_{in}} = \frac{J_{sc} \cdot V_{oc} \cdot FF}{P_{in}}, \tag{2.11}$$

where P_{in} is the input power density from the incident light. Solar cell standard reporting conditions are defined as 1000 W m^{-2} irradiance, 25 °C cell temperature, Air Mass 1.5 Global (AM1.5 g) spectrum. This is the most commonly used standard to report PCE of solar cells. In practice, the J–V characteristics of OSCs may deviate significantly from the ideal model (e.g., S-shaped J–V curves), making it challenging to interpret key parameters such as V_{oc}, J_{sc}, FF, and the resulting PCE. In later chapters, these deviations and their possible physical origins in specific OSC systems will be discussed in detail.

2.3.4 External Quantum Efficiency and Electroluminescence

2.3.4.1 Reciprocity

In OSCs, absorbed photons in the active layer generate bound electron–hole pairs through photovoltaic effect. These excitons can dissociate into free charge carriers, which are subsequently extracted by the electrodes, provided they do not undergo recombination. External quantum efficiency (EQE) spectra describe the spectral dependence of the number of free charge electron-hole pairs generated per incident photon, and is defined as

$$EQE(E) = \frac{\text{number of } e^- - h^+ \text{ pairs}}{\text{number of incident photons}(E)} \tag{2.12}$$

where E is the photon energy. The measurement of EQE typically involves directing spectrally resolved light onto the device under test and recording the resulting photocurrent as a function of wavelength. Conversely, when charge carriers are injected into a solar cell by applying external voltage (current), the device can act as a light-emitting diode (LED) and emit photons that can be collected using a spectrometer [110]. This measurement is referred as electroluminescence (EL) spectroscopy.

Since absorption and emission are reciprocal processes, EQE and EL can therefore be related through Rau's optoelectronic reciprocity theorem [45], involving the black-body spectrum $\phi_{BB}(T, E)$ and a voltage-dependent factor:

$$\delta\phi_{em}(E) = EQE(E) \cdot \phi_{BB}(T, E) \cdot (e^{\frac{qV}{k_B T}} - 1), \tag{2.13}$$

where $\delta\phi_{em}(E)$ is the additional emission under an applied bias compared to the case without bias.

Equation 2.13 provides a direct approach to convert between EQE and EL spectra, which can be useful for validating EL measurements or extending the sensitivity of EQE into the sub-gap region. In practice, however, reciprocity may not be perfectly valid for OSCs due to effects such as low carrier mobilities [110] and optical interference [111, 112]. Therefore an alternative way to validate the EL measurement is by varying the applied voltage during acquisition and confirming that the emission peak positions do not shift within the wavelength range of interest.

In OSCs, CT states are generally regarded as emissive, and therefore spectrally resolved EL has been often used in conjunction with EQE to probe CT states [40, 41].

2.3.4.2 Determination of CT State Energy

Marcus theory was initially developed to describe chemical reactions in solutions, but it was later shown to be useful for describing, for instance, CT processes and exciton transport/hopping between semiconductors in thin films [82, 113–115]. The classical Marcus theory is based on three major assumptions:

1. CT is much faster than the motion of nucleus.
2. Electronic transitions generally occur between vibrational energy states that show wave function overlap.
3. Energy is conserved during the CT process.

Based on these assumptions and thermodynamic principles, the energetic barrier (ΔG^*) for a localised exciton to undergo CT from the lowest vibronic excited state D^*/A (electron donor excited) or D/A^* (electron acceptor excited) to the CT state (D^+/A^-) can be derived as

$$\Delta G^* = \frac{(\Delta G_0 + \lambda)^2}{4\lambda}, \tag{2.14}$$

where ΔG_0 denotes the energetic difference between the minima of the free energy curves of the initial and final states, and λ is the reorganisation energy [82]. The reorganisation energy is defined as the excess energy of one state at the minimum energy nuclear coordinate of another one. For simplicity, Figure 2.13 also visualises this transition.

In organic semiconductor blends, CT states formed between electron donor and acceptor molecules are demonstrated to be the lowest-energy absorbing and emitting states [80, 81, 116, 117]. As the direct absorption and emission between the ground state and CT state are also allowed, the same logic applies to describe direct transition between the ground and CT state. ΔG_0 now corresponds to the energetic difference and λ denotes the molecular reorganisation between the CT and ground state. Therefore, Fermi's golden rule can be applied

to describe the rate k_{ij} of CT transition, where the vibrational transition is accounted for by the Franck–Condon (FC) factor:

$$k_{ij} = \frac{2\pi}{\hbar}|I_{ij}|^2 \cdot FC, \tag{2.15}$$

with I_{ij} being the electronic coupling term. According to Boltzmann statistics, the transition rate of a process with an activation barrier ΔG is

$$k_{ij} \propto e^{(-\frac{\Delta G}{k_B T})}. \tag{2.16}$$

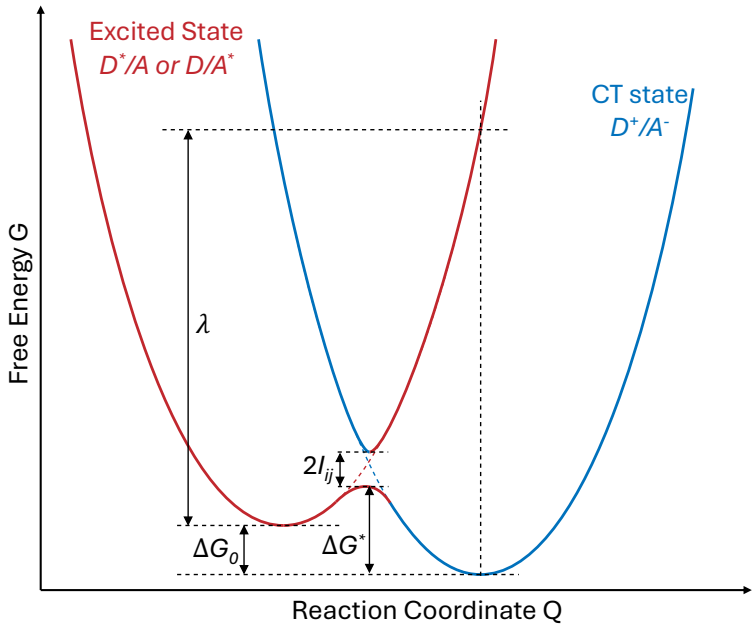


Figure 2.13: Schematic Marcus energy diagram for a charge-transfer transition from excited state D^*/A (D/A^*) to CT state D^+/A^-, with free energy (G) plotted against the collective nuclear reaction coordinate (Q). The red and blue parabolas represent the excited state D^*/A (D/A^*) and charge transfer (CT) state, respectively. ΔG^* is the energetic barrier for localised exciton from excited state D^*/A (D/A^*) to CT state D^+/A^-, ΔG_0 the free energy difference between state minima, λ the reorganisation energy, and $2I_{ij}$ the electronic coupling at the avoided crossing. Redrawn and adapted from Reference [51].

By combining Equations 2.14, 2.15, and 2.16, Marcus theory gives the final expression for the CT transition rate [27]:

$$k_{ij} = \frac{|I_{ij}|^2}{\hbar}\sqrt{\frac{\pi}{\lambda k_B T}} \cdot e^{(-\frac{(\Delta G_0 + \lambda)^2}{4\lambda k_B T})}, \tag{2.17}$$

where the FC is:

$$FC = \frac{1}{\sqrt{4\pi\lambda k_B T}} \cdot e^{(-\frac{(\Delta G_0+\lambda)^2}{4\lambda k_B T})}. \tag{2.18}$$

Thus, the CT state absorption cross-section σ_{CT} can be finally written, according to Marcus theory, as

$$\sigma_{CT}(E)E = \frac{f_{CT}}{\sqrt{4\lambda_{CT} k_B T}} \cdot e^{(-\frac{(E_{CT}+\lambda_{CT}-E)^2}{4\lambda_{CT} k_B T})}, \tag{2.19}$$

where E_{CT} is the CT state energy, λ_{CT} is the reorganisation energy between the CT and ground state, and f_{CT} denotes the oscillator strength describing the CT optical dipole transition.

When CT states are probed by EQE, the absorption cross-section needs to be linked to the EQE. Assuming negligible optical interference (i.e. when $d \ll \lambda/n$, n is the refractive index of the active layer) and weak absorption (i.e. when $\alpha(E)d \ll 1$) with reflective back electrodes, EQE can be approximated as

$$EQE(E) = \eta_a(E) IQE(E) \approx 2\alpha(E)d \cdot IQE(E), \tag{2.20}$$

where d is the absorber layer thickness, $\alpha(E)$ is the absorption coefficient, $\eta_a(E)$ is the absorption rate and $IQE(E)$ is the internal quantum efficiency [81]. The absorption coefficient in the CT region can be written as $\alpha = \sigma_{CT} N_{CT}$, with N_{CT} being the number of CT complexes. Substituting α in Equation 2.20 yields:

$$EQE_{CT}(E) = \frac{f}{E\sqrt{4\lambda_{CT} k_B T}} \cdot e^{(-\frac{(E_{CT}+\lambda_{CT}-E)^2}{4\lambda_{CT} k_B T})}, \tag{2.21}$$

where

$$f = 2d\eta_a N_{CT} f_{CT} \tag{2.22}$$

is an absorption pre-factor that depends on the CT state oscillator strength. Equation 2.21 can then be used to fit a Gaussian shape to the low energy tail to extract E_{CT}, reorganization energy λ_{CT} and oscillator strength f.

A similar expression can be derived for S_1 state by adapting Equation 2.21:

$$EQE_{S_1}(E) = \frac{f_{S_1}}{E\sqrt{4\lambda_{S_1}k_BT}} \cdot e^{(-\frac{(E_{S_1}+\lambda_{S_1}-E)^2}{4\lambda_{S_1}k_BT})}, \tag{2.23}$$

where f_{S_1} is the oscillator strength, λ_{S_1} is the reorganisation energy for the S_1 state, and E_{S_1} is the corresponding state energy. In practice, by first fitting the S_1 region in EQE spectra and then fitting the CT contribution to the residual, more accurate values for both sets of parameters can be extracted [82].

Absorption and emission processes are connected by reciprocity. Therefore, assuming reciprocity holds, the EL spectrum can be expressed analogously as:

$$EL_{CT}(E) = \frac{E \cdot f'}{\sqrt{4\lambda_{CT}k_BT}} \cdot e^{(-\frac{(E_{CT}+\lambda_{CT}-E)^2}{4\lambda_{CT}k_BT})}, \tag{2.24}$$

which allows EL spectra to be fitted to extract E_{CT} and λ_{CT} as well.

In cases where Gaussian fitting of E_{CT} and E_{S1} is not feasible, the combined use of reduced EL and EQE spectra can be used. Removing the energy dependence in the pre-factor, the reduced spectra are defined as:

$$EQE_R(E) = EQE_{CT}(E) \cdot E = \frac{f}{\sqrt{4\lambda_{CT}k_BT}} \cdot e^{(-\frac{(E_{CT}+\lambda_{CT}-E)^2}{4\lambda_{CT}k_BT})}, \tag{2.25}$$

$$EL_R(E) = \frac{EL_{CT}(E)}{E} = \frac{f'}{\sqrt{4\lambda_{CT}k_BT}} \cdot e^{(-\frac{(E_{CT}+\lambda_{CT}-E)^2}{4\lambda_{CT}k_BT})}. \tag{2.26}$$

By scaling the reduced EL to match the EQE amplitude such that $f = f'$, E_{CT} can be determined from the intersection of the two spectra [81]. This approach can also be applied to determine S_1 state energies.

While the classical Marcus theory provides reliable fits for systems where the CT state is spectrally distinct from the S_1 state, it has limitations. The theory assumes classical nuclear motion, neglects quantum effects, and assumes that transitions only occur between two states. In systems where CT and S_1 states are closely aligned, this approach fails. More advanced models, such as the Marcus–Levich–Jortner model or three-state models, are developed to address these issues and are discussed in Reference [82]. For the purpose of this thesis, however,

only the classical Marcus model is applied.

2.3.4.3 Urbach Energy

In crystalline semiconductors, static and structural energetic disorders are commonly quantified by Urbach energies E_U, acquired by applying an exponential-tail model to their absorption spectra. Their absorption coefficient (α) spectra typically display an exponential tail below the band edge, and generally follows the expression [118]:

$$\alpha(E,T) \propto \exp\left(\frac{E - E_{on}(T)}{E_U(T)}\right), \tag{2.27}$$

where E_{on} is the onset energy of the tail, and $E_U(T)$ quantifies the total energetic disorder of the system. It is generally accepted that lower E_U indicate reduced static disorder, which is expected to result in lower charge recombination and higher charge carrier mobilities in photovoltaic devices [119, 120].

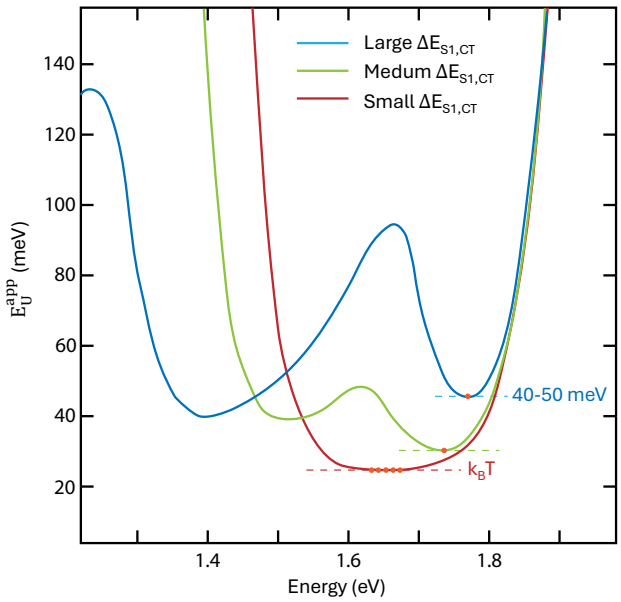


Figure 2.14: Schematic of $E_U^{\text{app}}(E)$ for donor:acceptor blends with large (solid blue line), medium (solid green line), and small (solid red line) $\Delta E_{S1,CT}$. $E_U^{\text{app}}(E)$ equal to k_BT (300 K) is shown as the horizontal red dashed line. Red, blue, and green dashed horizontal lines indicate the $E_U^{\text{app}}(E)$ minima in the sub-gap S_1 absorption region. For large and medium $\Delta E_{S1,CT}$ systems, the $E_U^{\text{app}}(E)$ minimum is taken as the lowest point of the parabolic curve and for small $\Delta E_{S1,CT}$ systems, it is taken as the averaged value within the plateau region.

In organic semiconductors, the sub-gap spectral features are more complex and can include

CT states (in systems compromising electron donor and acceptor molecules), excitonic features, and trap states [118]. In fullerene-based OSCs, CT states typically give rise to Gaussian-shaped sub-gap absorption tails in EQE spectra. Consequently, energetic disorder in such systems is often described using Gaussian picture [82, 121]. However, with the recent emergence of low-offset (low $\Delta E_{S1,CT}$) NFA-based OSCs, CT state features are no longer spectrally distinct from the lowest singlet excited state (S_1) in sub-gap region. In such cases, E_U have been increasingly used to probe disorder.

The spectral line-shapes of α and absorptance A in the sub-gap tail region can be related via a modified Beer–Lambert law, $A = \widetilde{f}\alpha d$, where d is the active-layer thickness and $\widetilde{f}$ is an energy-dependent correction factor (approximately unity in cases of negligible optical interference) [111, 122]. This allows EQE to be related to A, and thereby the spectral shape of EQE to follow that of α [118]. Rather than force fitting an exponential model to EQE spectra to extract intrinsic E_U, assessing the apparent Urbach energy (E_U^{app}) is a better approach to probe energetic disorder and can be obtained using:

$$E_U^{app}(E) = [\frac{\mathrm{d} \ln EQE(E)}{\mathrm{d}E}]^{-1}, \tag{2.28}$$

Figure 2.14 shows the dependence of E_U^{app} on photon energy, as $\Delta E_{S1,CT}$ increases from small to large. For a system with a true exponential EQE tail (Figure 2.14, red curve), E_U^{app} is constant across the sub-gap spectral region and equals E_U. However, E_U^{app} typically includes extrinsic contributions that broaden the absorption edge, such as CT states, optical interference, and mid-gap states [118]. In blends with large $\Delta E_{S1,CT}$, where CT state absorption dominates the sub-gap region, E_U^{app} exhibits strong energy dependence and can be approximated by $E_U^{app} \approx 2k_BT\lambda_{CT}/(E_{CT}+\lambda_{CT}-E)$, where E_{CT} and λ_{CT} are extracted from Gaussian fits of the CT-state features [118]. In such cases, E_U^{app} displays a narrow parabolic profile in the higher-energy region of the sub-gap S_1 absorption, with a distinct minimum around 40–50 meV, as it is shown as blue curve in Figure 2.14 [118].

As $\Delta E_{S1,CT}$ decreases, E_U^{app} maintains its parabolic shape but the minimum value drops sharply, approaching k_BT (Figure 2.14, green curve) [118]. In systems such as PM6:Y6 and PM6:ITIC, where $\Delta E_{S1,CT}$ is very small and CT states become indistinguishable from S_1

states, the sub-gap absorption tail is exponential and E_U^{app} saturates at a broad plateau with $E_U^{app} \approx k_B T$ (Figure 2.14, red curve) [118]. Small deviations around $k_B T$ can be present due to optical interference. A weak dependence on film thickness has been reported, leading to deviations ranging from +2.3 meV to –5.8 meV [118]. For large and medium $\Delta E_{S1,CT}$ systems, the E_U^{app} minimum is taken as the lowest point of the parabolic curve. For small $\Delta E_{S1,CT}$ systems, it is taken as the averaged value within the plateau region and in this thesis, five consecutive points (shown as orange circles on red curve in Figure 2.14) within the plateau region are used for this extraction.

2.3.5 Voltage Loss

For PV technologies, energy losses are recognised as a major contributor to non-ideal device performance. In particular, OSCs exhibit significantly higher voltage losses compared to high-performing inorganic PV technologies. Voltage loss is typically defined as the difference between a reference energy and the open-circuit voltage, expressed as $\Delta V_{oc} = E_{ref} - V_{oc}$, under standard test conditions [82]. The selection and definition of the reference energy E_{ref} critically influence the magnitude of ΔV_{oc}. Therefore, to ensure consistency and comparability across different systems, this thesis adopts a single methodology for determining the reference energy throughout the analysis.

2.3.5.1 Reference Energies

For OSCs, it is common to use the 'optical gap' as the reference energy in voltage loss analysis. This energy is typically extracted from the absorption edge. However, there are several approaches to determining the optical gap, as the value cannot be precisely defined in OSCs or other real solar cells [82, 123]. Common methods include linear extrapolation of the Ultraviolet (UV)-Vis absorption spectra in Tauc plots, extrapolation of EQE spectra to zero, or identifying the inflection point of the EQE spectral edge [82, 124, 125].

For voltage loss analysis, it is both physically meaningful and practically feasible to determine the reference energy E_{ref} from EQE spectra, as EQE data are widely measured and reported for solar cells [126, 127]. This makes it easier to re-analyse and compare voltage losses across the literature, especially when studies adopt different definitions of the reference

energy [46, 82, 123]. In this thesis, E_{ref} is determined from the inflection point of the EQE spectral edge, which can be interpreted as the 'photovoltaic gap' E_g^{PV}, a quantity that reflects device rather than intrinsic material properties [46, 82]. This method is relatively straightforward but typically carries an uncertainty of around 10 meV [82]. In some cases, averaging across the absorption edge [46] or fitting a sigmoid function to the EQE spectrum [128] has been recommended to reduce this uncertainty [82].

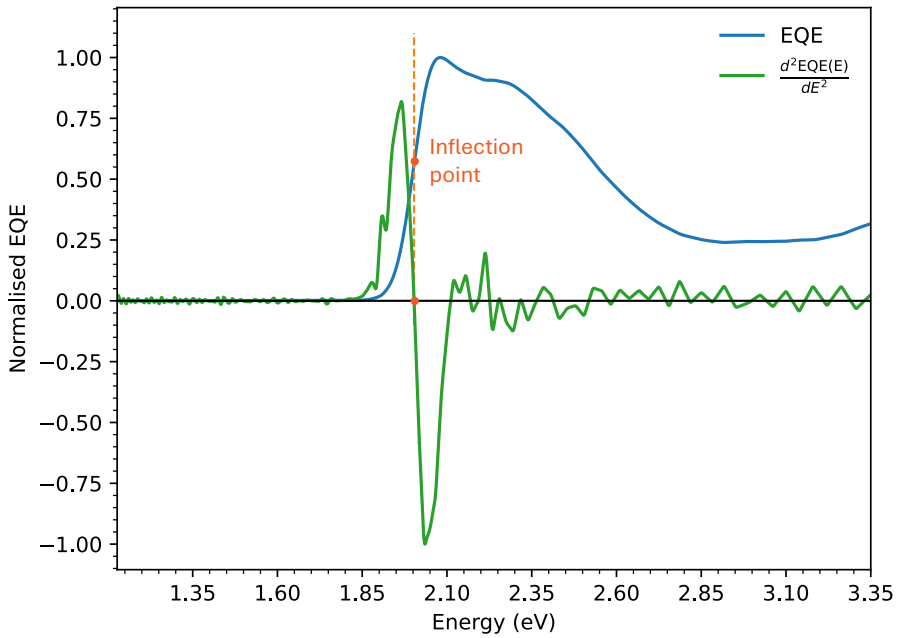


Figure 2.15: Example of E_g^{PV} extraction from the EQE spectrum. The blue curve shows the EQE of the device under investigation and the green curve its second derivative with respect to photon energy E. The orange circles mark the inflection points found on the EQE and $\frac{d^2\text{EQE}}{dE^2}$ spectra, from which E_g^{PV} is extracted.

Figure 2.15 demonstrates the method used in thesis to extract E_g^{PV} from the EQE spectrum, where E_g^{PV} is defined as the photon energy at the inflection point of the sub-gap EQE, identified via the zero crossing of $\frac{d^2\text{EQE}}{dE^2}$.

2.3.5.2 Radiative Limit

With EQE spectra, one can calculate the radiative saturation current density (J_0^{rad}) and J_{sc} as

$$J_0^{rad} = q \int_0^{\infty} EQE(E) \cdot \phi_{BB} \mathrm{d}E, \tag{2.29}$$

$$J_{sc} = q \int_0^{\infty} EQE(E) \cdot \phi_{AM1.5} \mathrm{d}E, \tag{2.30}$$

where ϕ_{BB} is the blackbody photon flux from the ambient environment at temperature T, and $\phi_{AM1.5}$ denotes the AM1.5 g solar spectrum at 1000 W m^{-2}. The J_{sc} value obtained from Equation 2.30 with measured EQE spectra often deviates from the experimentally measured value via J–V characterisation. This deviation can be attributed to several factors, including low charge carrier densities under low light intensity, imperfect optical alignment, and uncertainties in the calibrated spectral response of reference photodiodes [51]. As a result, measured EQE should generally be interpreted as a relative, rather than absolute, value.

For a non-ideal solar cell in which the EQE deviates from an ideal step function but only radiative recombination occurs, the radiative upper limit of the open-circuit voltage (V_{oc}^{rad}) can be determined from Equations 2.29 and 2.30 as

$$V_{oc}^{rad} = \frac{k_B T}{q} \ln(\frac{J_{sc}}{J_0^{rad}}). \tag{2.31}$$

It is worth noting that Equation 2.31 assumes that $J_{ph}(V_{oc}) = J_{ph}(0) \equiv J_{sc}$ at V_{oc}. While this assumption is valid for most inorganic diodes, it does not strictly hold for OSCs due to their voltage-dependent photocurrent $J_{ph}(V)$. Nevertheless, given the complexity of determining $J_{ph}(V)$ and its log dependence accurately, this approximation is still widely accepted and used in the literature [51].

To obtain meaningful values of V_{oc}^{rad} from this integral, it is crucial that all input quantities are measured with a sufficiently large dynamic range [51]. In practice, the integration limits are constrained by the spectral range and noise floor of the experimental setup. Therefore, the low-energy tail of the EQE spectrum is commonly extended using linear or Gaussian extrapolation. By plotting V_{oc}^{rad} as a function of the integral bounds, one can estimate the energy range over which V_{oc}^{rad} saturates.

The difference between the measured V_{oc} and the calculated V_{oc}^{rad} quantifies the non-radiative voltage losses (ΔV_{oc}^{nr}), which are thought to primarily arise from phonon-assisted or vibration-mediated electronic transitions [26, 129]. According to another form of the reciprocity theorem [45, 130], V_{oc}^{rad} can also be related to the external quantum efficiency of electrolumi-

nescence (Q_{LED}), which quantifies the proportion of injected charge carriers that are emitted as photons:

$$\Delta V_{oc}^{nr} = V_{oc}^{rad} - V_{oc} = \frac{k_B T}{q} \ln(Q_{LED}^{-1}) = \frac{k_B T}{q} \ln(\frac{J_0}{J_0^{rad}}) \tag{2.32}$$

2.3.5.3 Detailed Balance Picture

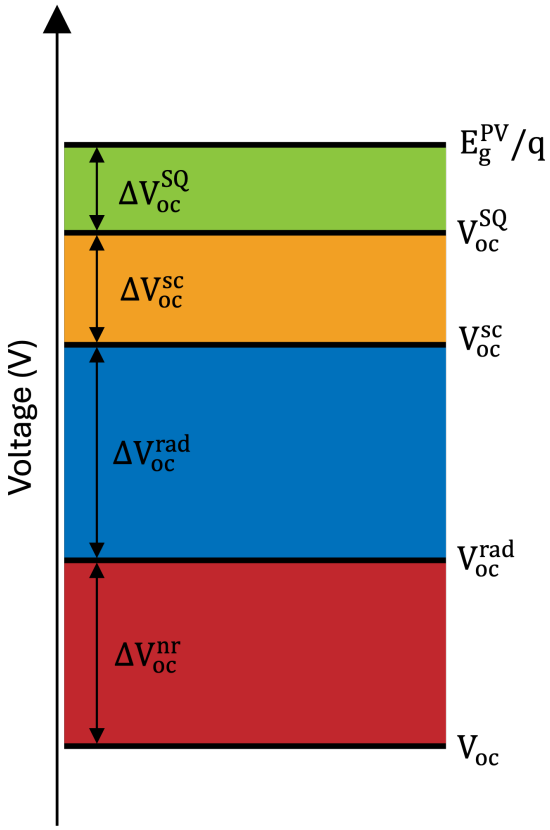


Figure 2.16: Schematic of relevant energy levels and corresponding voltage loss terms in the detailed balance (DB) picture. Voltage losses are calculated with respect to the photovoltaic gap (E_g^{PV}). The Shockley-Queisser (SQ) limit V_{oc}^{SQ} defines the maximum possible V_{oc}, introducing the first loss term ΔV_{oc}^{SQ}. Deviations in current collection lead to ΔV_{oc}^{sc}. The remaining loss terms, V_{oc}^{rad} and ΔV_{oc}^{nr}, describe radiative and non-radiative losses, respectively. Redrawn and adapted from Reference [82].

There are currently two common frameworks for describing voltage losses in OSCs: the DB picture and the energetic state (EN) picture. Both approaches define the same radiative limit. In the EN picture, voltage losses are calculated with respect to the energetic states present in OSCs, as $\Delta V_{oc}^{EN} = E_{S1}/q - V_{oc} = (E_{S1} - E_{CT})/q + (E_{CT}/q - V_{oc}^{rad}) + (V_{oc}^{rad} - V_{oc})$, where the

reference energy is defined as E_{S1} [61]. This framework emphasises the critical role of the CT state energy in determining the V_{oc} of OSCs, making it particularly suited for these systems. In contrast, the DB picture provides a more general description of voltage loss components applicable to all types of solar cells. However, the EN picture requires accurate determination of both E_{S1} and E_{CT}, and thus can only be applied when these values are experimentally accessible. For state-of-the-art low-offset NFA systems, where E_{CT} cannot be reliably extracted, the EN picture becomes impractical. In this thesis, the majority of systems investigated exhibit S_1-dominated EQE and EL spectra with no resolvable CT state features, rendering E_{CT} difficult to extract directly. Therefore, only the DB framework is applied throughout this work. Following the DB theory, Rau *et al.* provided a mathematically consistent and physically meaningful framework for decomposing voltage losses in photovoltaic devices [45,46], as shown in Figure 2.16:

$$\begin{aligned}\Delta V_{oc}^{DB} &= E_{ref}/q - V_{oc} \\ &= (E_g^{PV}/q - V_{oc}^{SQ}) + (V_{oc}^{SQ} - V_{oc}^{sc}) + (V_{oc}^{sc} - V_{oc}^{rad}) + (V_{oc}^{rad} - V_{oc}) \\ &= \Delta V_{oc}^{SQ} + \Delta V_{oc}^{sc} + \Delta V_{oc}^{rad} + \Delta V_{oc}^{nr}. \end{aligned} \tag{2.33}$$

Here, ΔV_{oc}^{DB} is the total voltage loss under the DB model. ΔV_{oc}^{SQ} represents the loss relative to the S-Q limit [108], ΔV_{oc}^{sc} accounts for losses due to incomplete photocurrent collection, ΔV_{oc}^{rad} corresponds to excess radiative losses, and ΔV_{oc}^{nr} denotes the remaining non-radiative loss. The full derivation of Equation 2.33 can be found in Reference [46], and only brief explanations are provided here.

The S-Q limit V_{oc}^{SQ} defines the maximum theoretical V_{oc} for a solar cell with gap E_g^{PV}, and can be determined as:

$$V_{oc}^{SQ}(E_g^{PV}) = \frac{k_B T}{q} \ln\left(\frac{J_{sc}^{SQ}(E_g^{PV})}{J_0^{SQ}(E_g^{PV})}\right), \tag{2.34}$$

where J_{sc}^{SQ} and J_0^{SQ} are reference saturation current densities determined by substituting $EQE(E)$ with a unit step function in Equations 2.29 and 2.30 [46]. Even in ideal solar

cells, ΔV_{oc}^{SQ} is non-zero due to unavoidable radiative recombination, typically ranging from 250–300 mV for $E_g^{PV} = 1.2$–1.3 eV [51].

The second loss term, ΔV_{oc}^{sc}, results from the deviation between the actual J_{sc} and the ideal J_{sc}^{SQ}:

$$\Delta V_{oc}^{sc} = \frac{k_B T}{q} \ln(\frac{J_{sc}^{SQ}}{J_{sc}}). \tag{2.35}$$

This contribution is usually small. For instance, a 20% reduction in J_{sc} relative to the S-Q limit leads to a loss of only around 6 mV [131]. Such reductions are commonly attributed to incomplete absorption or inefficient charge extraction.

The third term, ΔV_{oc}^{rad}, quantifies additional radiative losses due to absorption below the band edge:

$$\Delta V_{oc}^{rad} = \frac{k_B T}{q} \ln(\frac{J_{sc}^{rad}}{J_0^{SQ}}). \tag{2.36}$$

In OSCs, this loss is significantly affected by the value of $\Delta E_{S1,CT}$ and can range from tens to hundreds of millivolts [51, 132].

Finally, the non-radiative loss term ΔV_{oc}^{nr}, which tends to be the largest loss contribution in OSCs, often ranges from 200 to 500 mV [42]. Only very recently, some state-of-art NFA-based systems managed to lower this loss to 150 mV [133]. In comparison, inorganic solar cells typically exhibit much lower non-radiative losses between 20 and 100 mV [134]. Although the underlying mechanisms are not yet fully understood, studies on fullerene-based OSCs suggest an inverse correlation between ΔV_{oc}^{nr} and E_{CT}, in line with the energy gap law [26, 135]. Strategies to reduce this loss include employing molecules with high photoluminescence quantum yield (PLQY), engineering $\Delta E_{S1,CT}$ of the blend, and optimising blend morphology [134].

3 | The Physics of Förster Resonance Energy Transfer

This chapter provides a concise overview of Förster Resonance Energy Transfer (FRET) theory, including the underlying transfer mechanism, the definition of FRET efficiency, and its calculation based on Reference [70]. Experimental methods used to verify the presence of FRET in both solution and solid-state systems are also discussed. Finally, a brief summary of applications of FRET in organic solar cells is presented.

3.1 FRET Theory

3.1.1 Transfer Mechanisms

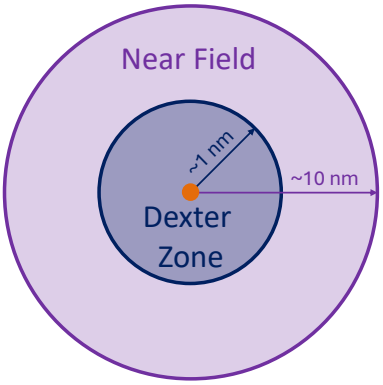


Figure 3.1: Schematic illustrating the *Dexter* (contact) zone and near field around an energy donor molecule. Further surrounding the molecule are the intermediate zone and the far field, which are omitted in the figure as they are not relevant to FRET. The orange sphere represents the energy donor at the centre of the *Dexter* zone (blue shaded), with a radius of about 1 nm (2-3 nm for larger molecules). Surrounding the *Dexter* zone is the near field (purple shaded), extending roughly 1-10 nm from the energy donor, within which *Förster* theory applies. Redrawn and adapted from Reference [70].

Förster Resonance Energy Transfer describes the radiationless transmission of an energy quantum (e.g a photon) from its site of absorption (e.g a excited-state chromophore) to its site of application (e.g. a nearby ground-state chromophore). This energy transfer can occur between two individual molecule or between two groups of molecules. This occurs via resonance interaction between energy donor and acceptor over distances significantly greater than interatomic separation, without conversion to thermal energy and without kinetic collision between the energy donor and acceptor [70]. The energy donor can be considered as a group of closely spaced electrical oscillators that generate an electric field in the surrounding space [136]. This space can be divided into four distinct zones according to distance, which in order from the closest to the farthest are: the *Dexter* zone (contact zone), the near field, the intermediate zone, and the far zone [70]. Figure 3.1 shows a schematic of the *Dexter* and near-field zones around an energy donor, which are most relevant for FRET. These zones are defined using a characteristic distance b [70]:

$$b = \frac{\lambda}{2\pi n}, \tag{3.1}$$

where λ is the fluorescence wavelength of the energy donor, and n is the refractive index of the surrounding medium. The approximate radii of the *Dexter* zone, near field, intermediate zone, and far field are $0.01b$, $0.1b$, $10b$, and infinite, respectively [68]. For energy donors emitting in the range 300-800 nm embedded in media with $n = 1.3 - 1.6$, b is typically 100 nm or less [70]. *Förster* theory does not apply at energy donor–acceptor distances below 1 nm due to two main reasons: (i) the breakdown of the ideal dipole approximation (IDA) [68], and (ii) the possible formation of an excited-state complex between the energy donor and acceptor [136]. At distances beyond ∼10 nm, the assumption of a negligible contribution of oscillating energy donor charges to the electric field also becomes invalid [70]. Therefore, FRET is restricted to the near-field region, approximately 1-10 nm from the energy donor.

Several mechanisms exist for excitation energy transfer from energy donor to acceptor, including resonance energy transfer, reabsorption, complex formation, and collisional quenching [70, 136]. Each mechanism exhibits distinct characteristics and can therefore be experimentally distinguished [136]. Notably, early *Förster* theory investigations were based on systems in solution, so many diagnostic features are solution-specific. FRET was found to exhibit the following key characteristics [136]:

1. Transfer efficiency does not change with increasing sample volume.
2. Transfer efficiency does not change with increasing viscosity.
3. Decreased energy donor lifetime.
4. Unchanged energy donor fluorescence spectrum.
5. Unchanged energy donor absorption spectrum.

Although reabsorption can produce similar spectral outcomes as FRET, it originates from a fundamentally different mechanism. In contrast to FRET, reabsorption shows increased transfer with increasing sample volume, no change in energy donor lifetime, and a shift in the energy

donor fluorescence spectrum [70]. For solid-state systems, parameters such as solution viscosity and sample volume are not physically meaningful. However, the remaining characteristic fingerprint phenomena still hold true. In later sections, experimental approaches to confirm the occurrence of FRET in solid films will be explored.

As discussed earlier, one of the key assumptions of *Förster* theory is the IDA. Figure 3.2 illustrates a simplified arrangement of energy donor and acceptor molecules where the IDA holds. The energy donor is treated as a sphere of radius R_D containing a group of coupled electrical oscillators, and similarly, the acceptor is modelled with radius R_A. Each oscillator comprises an electron oscillating in a specific direction, bound elastically to a stationary nucleus [70]. When the distance between the energy donor and acceptor centres, r_{DA}, is much larger than both R_D and R_A, higher-order multipole interactions become negligible, and the interaction reduces to a dipole–dipole coupling [70]. The equivalent donor dipole is located at the energy donor centre, with direction $\hat{d}$ and dipole moment $\vec{p_D} = q_e D_D \hat{d}$, where $D_D \hat{d}$ is the vector sum of fluctuating oscillators at multiple frequencies [70, 136]. Similarly, the energy acceptor has dipole moment $\vec{p_A} = q_e D_A \hat{a}$, where $D_A \hat{a}$ represents the vector sum of its oscillators [70, 136].

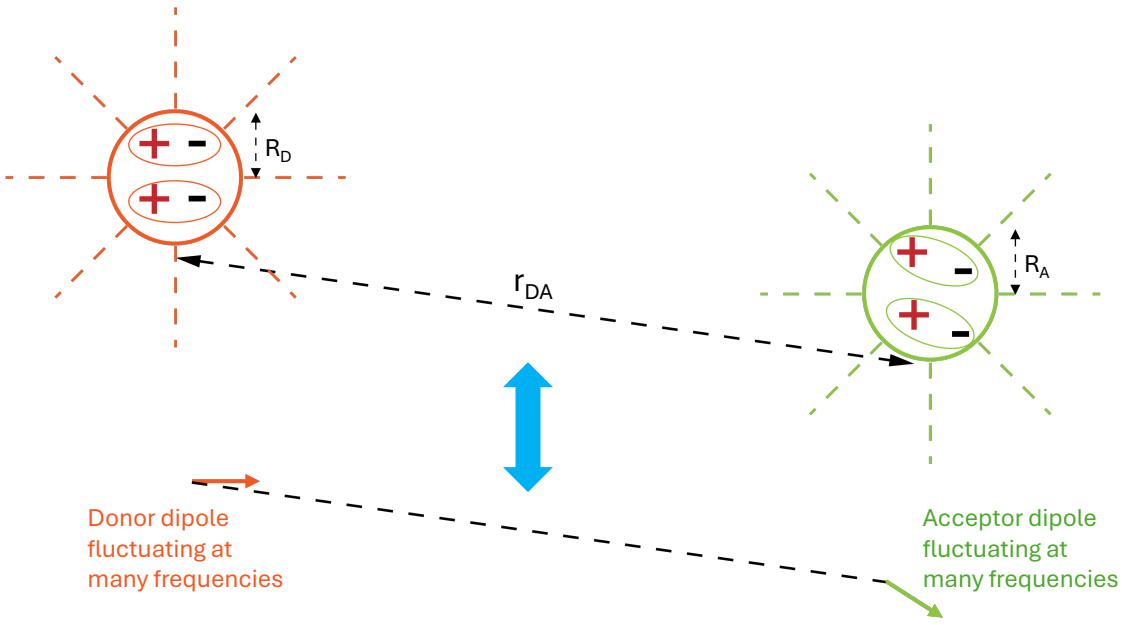


Figure 3.2: Simplified schematic (top) of an energy donor molecule on the left with radius R_D, and an acceptor molecule on the right with radius R_A, separated by distance r_{DA}. When $r_{DA} \gg R_D$ and $r_{DA} \gg R_A$, the interaction can be approximated to a dipole–dipole coupling as shown in the lower schematic. Redrawn and adapted from Reference [70].

Resonance arises when an oscillator with a natural frequency interacts with an external

system oscillating at or near the same frequency. Energy is transferred most efficiently when these frequencies match. In *Förster* theory, both energy donor and acceptor molecules are viewed as ensembles of coupled oscillators. Upon light excitation, the energy donor oscillators absorb energy and emit their own electromagnetic field (fluorescence). If the natural frequency of the energy acceptor oscillators, ν_A, matches the donor frequency, ν_D, resonance occurs, and the acceptor absorbs a significant amount of energy (W_A) from the donor. This is the mechanism by which energy is transferred from excited energy donor molecules to acceptor molecules via resonance.

3.1.2 FRET Radius and Transfer Rate

Fundamentally, FRET occurs via dipole–dipole interactions. Accordingly, a set of three fundamental equations can be derived from classical *Förster* theory and refined through quantum-mechanical considerations [70, 136]:

$$E_{\mathrm{FRET}} = \frac{k_{\mathrm{FRET}}}{k_{\mathrm{FRET}} + 1/\tau_D} = \frac{R_0^6}{R_0^6 + r_{DA}^6}, \tag{3.2}$$

$$k_{\mathrm{FRET}} = \frac{1}{\tau_D}\left(\frac{R_0^6}{r_{DA}^6}\right), \tag{3.3}$$

$$R_0^6 = \frac{9(\ln 10)\kappa^2 \Phi_D J}{128\pi^5 n^4 N_A}. \tag{3.4}$$

The key quantities are defined as follows:

E_{FRET} = efficiency of the transfer.

k_{FRET} = rate of energy transfer.

τ_D = excited state lifetime of the energy donor in the absence of acceptor.

R_0 = *Förster* radius, that is, the energy donor-acceptor distance at which $k_{\mathrm{FRET}} = 1/\tau_D$, so that the probability of the excited donor to fluoresce is equal to the probability of transfer of energy to the acceptor.

κ^2 = orientation factor.

J = overlap integral.

Φ_D = quantum yield of the energy donor fluorescence in the absence of acceptor.

n = refractive index of the medium that energy donor and acceptor are embedded in.

The full derivations can be found in Reference [70] and in the original work by Förster [136]. For organic semiconductors, the calculation of R_0 is a commonly used approach to quantify FRET strength when ϕ_D is available [39]. However, since R_0 is also linearly dependent on the spectral overlap integral J, the latter can be used as a comparative metric for FRET strength when comparing systems that share the same energy donor. Therefore, the practical calculation of J is discussed in detail in this thesis.

For systems where energy donor and acceptor dipoles are randomly oriented, as is the case in disordered solids such as BHJ and PHJ architectures, $\kappa^2 = 2/3$ is a reasonable approximation [70]. This assumption is valid when translational diffusion is slow compared to the FRET timescale, and energy transfer is effectively unidirectional (energy donor to acceptor). Moreover, since R_0 depends on κ^2 via the sixth root, small errors in κ^2 do not strongly influence the resulting R_0.

The spectral overlap integral, J, can be calculated using wavelength, wavenumber, or frequency domains. In this thesis, the wavelength-based form, J_λ, is used and defined as [70, 136]:

$$J = J_\lambda = \int_0^\infty \epsilon_A(\lambda)\lambda^4 F_D(\lambda)\mathrm{d}\lambda, \tag{3.5}$$

where $\epsilon_A(\lambda)$ is the molar extinction coefficient of the energy acceptor (M^{-1} cm^{-1}), λ is the wavelength in nm, and $F_D(\lambda)$ is the energy donor's normalised emission spectrum (area under the curve = 1, dimensionless). The resulting units for J are M^{-1} cm^{-1} nm^4. For films, $\epsilon_A(\lambda)$ is related to the absorption coefficient via [39]:

$$\epsilon_A(\lambda) = \frac{\alpha_A(\lambda) M_w^A}{1000 \cdot \rho_A}, \tag{3.6}$$

where $\alpha_A(\lambda)$ is the absorption coefficient (cm^{-1}), M_w^A is the acceptor molecular weight (g

mol^{-1}), and ρ_A is the thin-film density (g cm^{-3}). The absorption coefficient $\alpha_A(\lambda)$ can be calculated from the extinction coefficient $\kappa_A(\lambda)$ using:

$$\alpha_A(\lambda) = \frac{4\pi\kappa_A(\lambda)}{\lambda \times 10^{-7}}, \tag{3.7}$$

where the conversion factor accounts for units of λ in nm. The extinction coefficient $\kappa_A(\lambda)$ is typically obtained from spectroscopic ellipsometry. Substituting Equation 3.6 and 3.7 into Equation 3.5 gives the applied expression for J:

$$J = J_\lambda = 4\pi \times 10^4 \int_0^\infty \frac{\kappa_A(\lambda) M_w^A}{\rho} \lambda^3 F_D(\lambda) \mathrm{d}\lambda. \tag{3.8}$$

In practice, the refractive index n is also wavelength-dependent. Therefore, an effective value n_{eff} is often computed as a weighted average over the spectral overlap region [39]:

$$n = n_{\text{eff}} = \frac{\int_0^\infty \epsilon_A(\lambda) n(\lambda) \lambda^4 F_D(\lambda) \mathrm{d}\lambda}{J} \tag{3.9}$$

$$= \frac{4\pi \times 10^4 \int_0^\infty \frac{\kappa_A(\lambda) M_w^A}{\rho} n(\lambda) \lambda^3 F_D(\lambda) \mathrm{d}\lambda}{J}. \tag{3.10}$$

For BHJ systems, $n(\lambda)$ is measured for the energy donor–acceptor blend; for PHJ systems, it is taken from the energy donor material. In both cases, $n(\lambda)$ can be obtained by ellipsometry. Substituting the derived R_0^6 (Equation 3.4) and converting to nanometres, the *Förster* radius becomes:

$$R_0 = 0.0211 [\frac{\kappa^2 \Phi_D J}{n^4}]^{\frac{1}{6}}, \tag{3.11}$$

where κ^2 is approximated to be 2/3 in disordered solids.

3.1.3 Experimental Determination of FRET

It is now known that k_{FRET}, is closely related to the distance between energy donor and acceptor molecules, r_{DA}, and the *Förster* radius R_0, which itself depends on several parameters: the orientation factor κ^2, the quantum yield of energy donor emission Φ_D, and the spectral overlap

integral J. Therefore, FRET process which can be experimentally observed, the following conditions must be met by the energy donor and acceptor [70]:

1. The energy donor and acceptor must possess strong electronic transitions.
2. The energy donor–acceptor distance, r_{DA}, should fall within the range of approximately 1–10 nm, though this may vary depending on molecular size.
3. There must be spectral overlap between the donor emission and acceptor absorption spectra.
4. The orientation factor κ^2 should not be too small, i.e. not close to zero.
5. The energy donor quantum yield Φ_D should be reasonably high.

Experimentally, fluorescence quenching measurements are widely employed as an accessible mean to assess the occurrence of FRET [137–147]. Transient absorption spectroscopy (TAS) has also been used to directly probe FRET, as it provides information on excited-state dynamics over ultrafast timescales [39, 148–152]. TAS is particularly valuable for distinguishing FRET from competing processes such as CT and morphological quenching, detecting weak FRET, and extracting k_{FRET}, though it is less accessible due to more specialized equipment than fluorescence-based methods [149, 151, 153].

Fluorescence quenching measurements can be performed in solution, hybrid (solid–solution), or solids. For molecules soluble in organic solvents, FRET is typically assessed by preparing separate solutions of energy donor, acceptor, and donor–acceptor mixtures with varying acceptor concentrations. PL spectra are recorded upon excitation at a wavelength that selectively excites the energy donor. If FRET occurs, the energy donor emission decreases while acceptor emission increases with increasing acceptor concentration, as observed in References. [140, 141, 143, 144]. In hybrid states, similar measurements have been performed, with FRET evidenced by a decrease in energy donor PL intensity in the solid phase as the acceptor concentration increases [142]. In solid films, FRET is supported by quenched energy donor PL in donor–acceptor blends under selective donor excitation, as demonstrated for example in References [145, 147]. An alternative method involves preparing pristine energy donor, pristine

energy acceptor, and bilayer films with the donor and acceptor in a layer-by-layer vertical stacking. Quenching of the energy donor PL in the bilayer sample upon donor excitation indicates FRET [138].

However, PL quenching alone does not distinguish FRET from other quenching processes, such as CT. When energy donor and acceptor molecules form CT interfaces in blends or at molecular interfaces in vertical stacking, PL quenching may originate from CT rather than FRET. To mitigate this, a thin but closed wide-gap spacer layer can be introduced between the energy donor and acceptor to prevent CT states from forming. If energy donor PL quenching still occurs in the presence of the spacer, FRET is strongly supported. This approach was employed in Reference [146, 154]. Because FRET is a long-range (r_{DA} ∼1-10 nm), non-contacting energy transfer process, quenching can still be observed without direct energy donor–acceptor contact, although the efficiency decreases with increasing r_{DA}, as described by Equation 3.2.

TAS, on the other hand, offers a more robust and direct method to confirm FRET. It tracks the spectral evolution of excited-state species on femtosecond to nanosecond timescales, providing insights into both energy and charge transfer dynamics. Typically, pristine film of energy acceptor and blend film of energy donor–acceptor are prepared. Upon selective energy donor excitation, simultaneous ground-state bleaching (GSB) signals from both energy donor and acceptor at very early times (∼0.5 ps) are generally considered strong evidence of FRET or CT. To further distinguish between these, enhancement in the stimulated emission (SE) signal of the energy acceptor has been used as an indicator of FRET [150]. Different material systems may require system-specific signatures to differentiate between FRET and CT, as shown in References [39, 148, 149, 151, 152]. In all cases, TAS provides a powerful tool for robustly verifying the presence of FRET.

3.2 Applications of FRET in Organic Solar Cells

Originally, FRET found widespread applications in the study of biological systems due to its intrinsic sensitivity to small variations in intermolecular distance and orientation. With appropriate sample configurations, FRET enables both qualitative and quantitative distance measurements within molecular systems. Notably, it has been applied in areas such as signal

transduction, molecular *in vitro* diagnostics for medical sensing, and nanotechnology [70].

In OSCs, FRET has been considered as an alternative mechanism to *Dexter*-type exciton transfer for facilitating exciton transport, mainly responsible for short-lived (nanosecond-scale) singlet excitons. Long-lived (microsecond-scale) triplet excitons may also undergo FRET when located near phosphorescent organometallic energy acceptors [155]. In early fullerene-based BHJ OSCs, such as P3HT:PCBM systems, efficient FRET from P3HT to PCBM was reported, followed by hole transfer back to P3HT [154] And FRET was considered to be beneficial to draw excitons to electron donor and acceptor heterointerfaces where they can efficiently get dissociated across domain sizes of ∼10 nm. However, if subsequent charge transfer (e.g., hole extraction) is inefficient while FRET remains highly efficient, energy losses can result, as demonstrated in the IF8BT:PCBM system [156]. Nonetheless, these findings opened up the possibility of incorporating a third photoactive component (e.g., a dye) into a two-material photoactive blend to expand spectral absorption [154, 157].

Building on this concept, several systems with three photoactive materials have been proposed to exploit FRET from different perspectives. Huang *et al.* introduced squaraine dye (SQ-dye) into a P3HT:PCBM BHJ, enabling efficient FRET from SQ-dye to P3HT and enhancing light harvesting [141]. Their optimised device containing 1 wt% SQ-dye achieved a PCE of 4.5%, with increased J_{sc} and FF compared to the P3HT:PCBM reference (PCE=3.3%), while maintaining V_{oc}. The increase in J_{sc} was attributed to additional exciton generation from SQ-dye, and the improved FF to a lower series resistance and higher shunt resistance introduced by the small amount of SQ-dye.

With continued material development, fullerene-free systems have also demonstrated FRET functionality. In VTE OSCs, Cnops *et al.* proposed a three-layer PHJ cascade device composed of α-6T|SubNc|SubPc, in which efficient FRET occurs from SubPc to SubNc, followed by hole transfer at the α-6T/SubNc interface to α-6T [146]. By carefully aligning the LUMO levels of the energy donor (SubPc) and acceptor (SubNc), they enabled efficient energy harvesting without sacrificing V_{oc}. Their optimised trilayer device achieved a high PCE of 8.4%, with simultaneous improvements in FF, J_{sc}, and V_{oc} relative to the bilayer reference (containing only α-6T and SubNc, PCE=6.0%). In this system, FRET facilitates long-range exciton transfer without introducing additional voltage loss.

Similar strategies have been applied in solution-processed NFA OSCs by incorporating a third component to broaden light harvesting. For example, Mohapatra *et al.* introduced PCDTBT (PBDB-T) into PTB7-Th:IT4F BHJ systems [150], and Wang *et al.* added DB-1 (DB-2) into PM6:Y6 blends [152]. In the latter case, a so-called 'dual FRET' was reported, whereby DB-1 (DB-2) transferred energy to both PM6 and Y6. Additionally, these third components prevented excessive self-aggregation of Y6, thereby promoting optimal phase separation in ternary blends. It was further observed that the presence of FRET from a third component improved the exciton diffusion length in the Y6:PY-IT BHJ system [145], with diffusion length positively correlated with FRET efficiency. This may also partly explain the improved performance in the work by Wang *et al.*.

FRET has also been observed in state-of-the-art binary solution-processed NFA OSCs [39]. In such systems, a two-step exciton dissociation mechanism dominates: first, FRET occurs from the electron donor to the acceptor, followed by hole transfer back to the donor. This mechanism requires a sizeable IE offset of approximately 0.5 eV to ensure efficient hole transfer. Although the explicit benefit of FRET was not highlighted, previous work on ternary blends may suggest that efficient FRET improves exciton diffusion lengths in binary systems as well.

This raises the question of whether engineering electron donor–acceptor pairs to support efficient FRET in binary OSCs could improve performance. This is not yet fully explored in VTE systems, where the best-performing fullerene-based devices typically lack FRET and exhibit efficiencies capped at approximately half those of solution-processed NFA OSCs. In this thesis, several all-VTE and hybrid (solution-processed electron acceptor with evaporated electron donor) systems are therefore investigated to explore whether FRET contributes to device performance enhancements in binary OSCs, and if so, which device parameters (e.g J_{sc}, FF and voltage losses) are influenced and how they are influenced.

4 | Materials & Methods

This chapter provides a detailed overview of the materials and experimental methods utilized in this thesis. First, the chemical names, molecular structures and supplier information of molecules used are presented. Then, detailed methods for sample fabrication based on vacuum thermal deposition and spin-coating via solutions are described, and all OSC device architectures used are presented. Finally, the different experimental and computational characterization techniques used for studying solid film samples and full devices are illustrated.

4.1 Materials

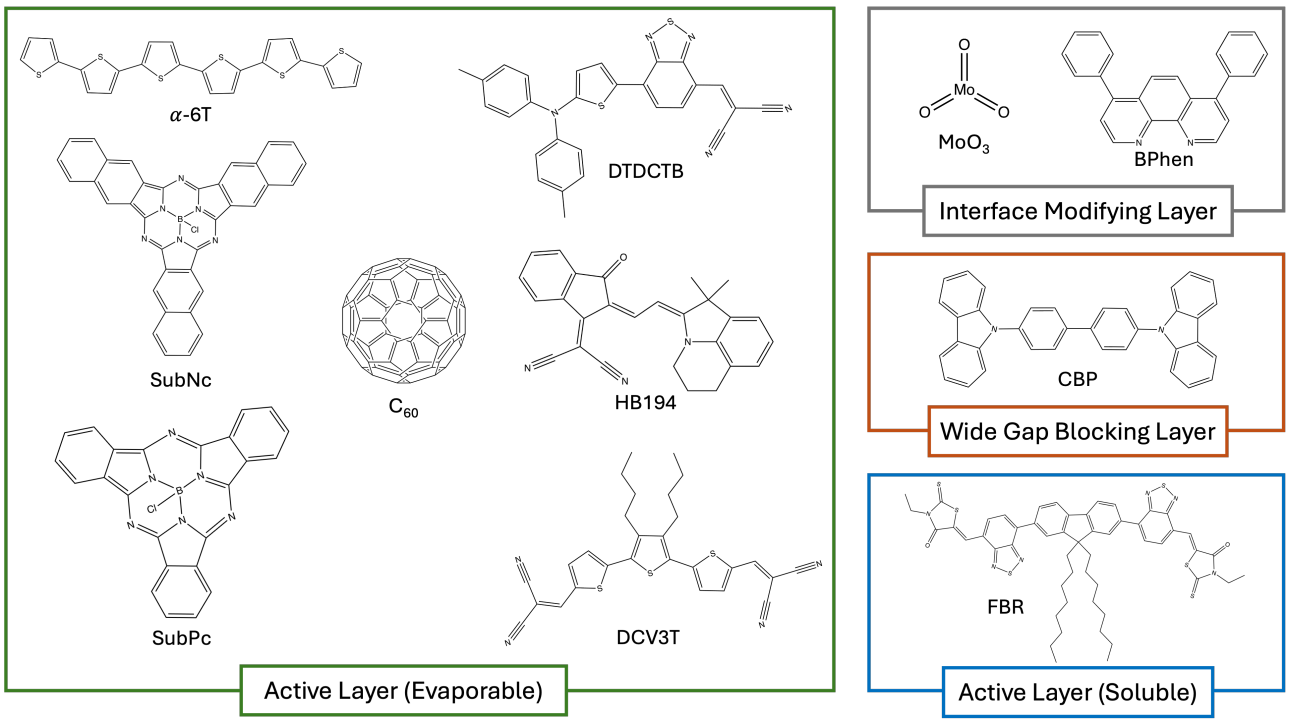


Figure 4.1: Molecular structure of the molecules for active layer (evaporable and soluble), interface modifying layer and wide-gap blocking layer used in this thesis. All chemical name are listed in Table 4.1 and 4.2.

Figure 4.1 shows the molecular structures of the materials used in this thesis, which are either evaporable in vacuum or solution-processable. The acronyms, chemical names, molecular weight and supplier information of relevant materials can be found in Table 4.1 and 4.2. All materials were used as received. The evaporable small molecules were purchased in sublimation-purified form. Table 4.1 also lists the molecular densities used during the vacuum evaporation process.

Table 4.2 also includes information on PEDOT:PSS, the electron transport layer water-based dispersion, and zinc acetate dihydrate, which is used as the precursor for the solution processed hole transport layer. Table 4.3 summarizes the chemical formulas, molecular weights, and supplier details of the solvents used for the solution-processed layers, as well as the cleaning solution used for substrate preparation. All solvents and solutions were used as received

and stored appropriately, either in a glovebox or in a sealed cabinet, following the handling instructions provided by the manufacturer.

Table 4.1: Acronyms, chemical names, densities[a], purities and suppliers for the vacuum thermal deposited molecules used in this thesis.

Acronym	**Chemical Name**	**Density (g/cm^3)**	**Purity**	**Supplier**
α-6T	α-Sexithiophene	1.40	Sublimed, >99 %	Luminescence Technology Corp.
HB194	2-((Z)-2-((E)-2-(1,1-Dimethyl-5,6-dihydro-1H-pyrrolo[3,2,1-ij]quinolin-2(4H)-ylidene)ethylidene)-3-oxo-2,3-dihydro-1H-inden-1-ylidene)malononitrile	1.40	Sublimed, >99 %	Luminescence Technology Corp.
SubNc	Boron sub-2,3-naphthalocyanine chloride	1.62	Sublimed, >99 %	Luminescence Technology Corp.
SubPc	Boron subphthalocyanine chloride	1.40	Sublimed, >99 %	Luminescence Technology Corp.
DTDCTB	2-((7-(5-(Di-p-tolylamino)thiophen-2-yl)benzo[c][1,2,5]thiadiazol-4-yl)methylene)malononitrile	1.36	Sublimed, >99 %	Luminescence Technology Corp.
C_{60}	Buckminsterfullerene C60	1.65	Multiple sublimed, >99.95 %	Creaphys GmbH
DCV3T	3',4'-Dibutyl-5,5"-bis(dicyanovinyl)-2,2':5',2"-terthiophene	1.45	Sublimed, >99 %	Luminescence Technology Corp.
BPhen	4,7-diphenyl-1,10-phenanthroline	1.22	Sublimed, >99.5 %	Luminescence Technology Corp.
MoO_3	Molybdenum trioxide	4.69	Sublimed, >99.998 %	Luminescence Technology Corp.
CBP	4,4'-Bis(carbazol-9-yl)biphenyl	1.19	Sublimed, >99.8 %	Luminescence Technology Corp.
Ag	Silver	10.5	99.99 %	Kurt J. Lesker Company

[a] The densities were taken directly from literature, manufacturer's data-sheet or estimated from tooling evaporations.

Table 4.2: Acronyms, chemical names, molecular weight, purities and suppliers for the solute or dispersive molecules used in this thesis.

Acronym	**Chemical Name**	**Molecular Weight (g/mol)**	**Purity**	**Supplier**
FBR	5,5'-[(9,9-Dioctyl-9H-fluorene-2,7-diyl)bis(2,1,3-benzothiadiazole-7,4-diylmethylidyne)]bis[3-ethyl-2-thioxo-4-thiazolidinone]	1001.44	>98.5 %	1-Material Inc.
Zinc Acetate Dihydrate	Zinc Acetate Dihydrate	219.51	>99.999 %	Sigma-Aldrich
PEDOT:PSS	Poly(2,3-dihydrothieno-1,4-dioxin)-poly(styrenesulfonate)	N/A	Aqueous dispersion	Heraeus Epurio GmbH

Table 4.3: Chemical names, chemical formula, molecular weight, purities and suppliers for the solvents and solutions used in this thesis.

Chemical Name	**Chemical Formula**	**Molecular Weight (g/mol)**	**Purity**	**Supplier**
Chlorobenzene	C_6H_5Cl	112.56	anhydrous, 99.8 %	Sigma-Aldrich
2-Methoxyethanol	$C_3H_8O_2$	76.09	anhydrous, 99.8 %	Sigma-Aldrich
Ethanolamine	C_3H_7NO	61.08	ACS reagent, 99.0 %	Sigma-Aldrich
2-propanol	C_3H_8O	61.10	puriss., meets analytical specifications of Ph. Eur., BP, USP, ≥99.5 % (GC)	Sigma-Aldrich
Acetone	C_3H_6O	58.08	puriss., meets analytical specifications of Ph. Eur., BP, NF, ≥99 % (GC)	Sigma-Aldrich
Hellmanex® III	N/A	N/A	N/A	Hellma®

4.2 Sample Fabrication

4.2.1 Substrate Preparation

Prior to thin-film deposition or spin-coating, all substrates are cleaned sequentially in ultrasonic baths containing Hellmanex® solution, deionised water, acetone, and isopropanol. Each sonication step is carried out for 10 minutes at a bath temperature of 55 °C. Following this, the substrates are treated with an O_3 plasma for 10 minutes before coating. Thin-film samples

are prepared on plain glass[1], fused quartz[2] or silicon wafers[3]. Full device stacks are fabricated on pre-patterned indium tin oxide (ITO)-coated glass substrates[4].

4.2.2 Vacuum Thermal Deposition

Figure 4.2 presents a schematic of co-deposition of two molecular species using the evaporation chamber[5] in the National Thin-Film Cluster Facility for Advanced Functional Materials (NTCF). The chamber is attached to a nitrogen-filled glovebox and is isolated from air exposure. Prior to deposition, material powders are loaded into ceramic crucibles and transferred into the chamber under N_2 atmosphere. With the aid of a dry pump[6] and a cryogenic pump[7] connected to a He compressor[8], the system reaches a base pressure of 10^{-7}–10^{-8} mbar. The ceramic crucibles, located approximately 40 cm below the substrates, are heated by tungsten coils and enclosed in a stainless steel shield. A pre-set heating program is used to gradually increase the temperature until the materials sublime at the target evaporation rate.

To prevent premature deposition of material onto the substrate, a substrate shutter is positioned below the substrate and remains closed until the desired rate is achieved. Deposition rates are monitored via quartz crystal microbalances (QCMs), and during this work, maintained between 0.1–1 Å/s. Common layers such as BPhen were evaporated at a nominal rate of 0.1 Å/s, and Ag was deposited at a nominal rate of 0.5 Å/s for the initial 50 nm and 1 Å/s thereafter. Once the set rate is reached, the substrate shutter opens automatically, allowing the molecules to deposit onto the substrate. Substrate temperatures during deposition were maintained at room temperature.

The exact deposition area on the substrate is defined using various shadow masks. The evaporation rates and film thicknesses are controlled and based on pre-programmed processes. According to the manufacturer specifications, the recorded deposition rates have an uncertainty of ±5 %. Upon completion, the substrates are transferred back into N_2-filled glovebox without

[1]Biotain Crystal Co., Ltd., soda-lime glass
[2]Knight Optical Ltd., Type WHQ
[3]Inseto Ltd., W-Si Wafer 04/005
[4]Biotain Crystal Co., Ltd., patterned, 135 nm ITO film on soda-lime glass
[5]Angstrom Engineering Inc., Nebula Cluster Series
[6]Ebara Technologies Inc., EV-A10-2
[7]Edwards Vacuum Ltd., Cryo Torr Cryopump 8F
[8]Edwards Vacuum Ltd., CTI-CRYOGENICS 9600

air exposure for subsequent encapsulation and/or further characterisations.

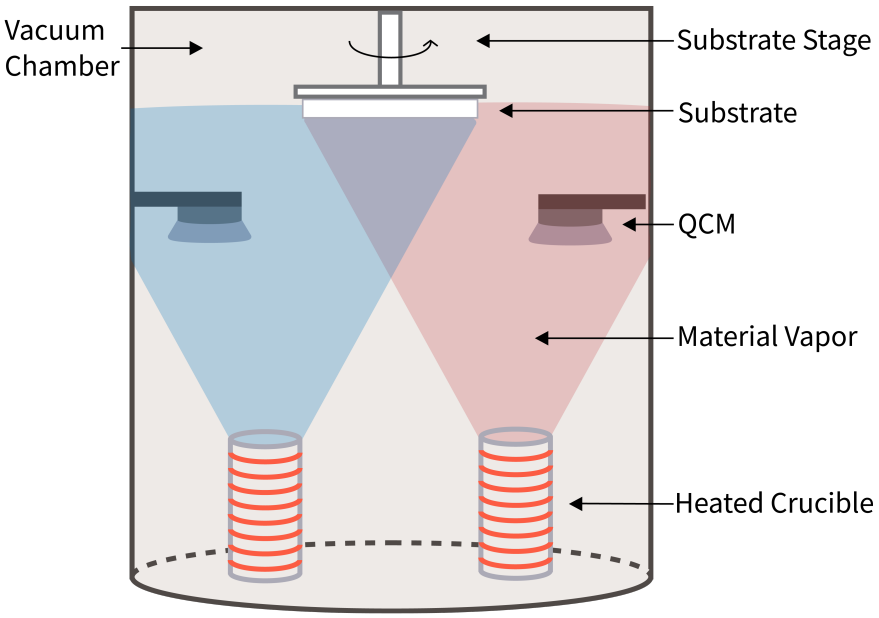


Figure 4.2: Schematic of the evaporation chamber of The National Thin-Film Cluster Facility for Advanced Functional Materials (NTCF) used in this thesis. This vacuum deposition system operates at a base pressure of 10^{-7}–10^{-8} mbar. Ceramic crucibles, filled with material powders, are heated via surrounding coils until sublimation occurs. The evaporation rate is monitored and regulated using quartz crystal microbalances (QCMs), allowing the deposition rate and eventual thickness of each material to be monitored. With knowledge of the respective film densities, the mixing ratio between different molecules in the deposited film can be tuned. The sublimed molecules condense onto the substrate, with thickness controlled to nanometre precision. The substrates are fixed onto a stage that is rotating to improve homogeneity to better than 5 %. By employing shadow masks (not shown), the deposition area can be spatially defined. Once the target thickness is achieved, a shutter (not shown), located just below the substrate, is closed to prevent further deposition onto the substrate.

4.2.3 Solution Preparation, Spin Coating and Annealing

All organic solutes are stored in a dry, nitrogen-filled (N_2) glovebox that contains no solvents. The scale used for weighing has an uncertainty of ± 0.1 mg. After weighing materials into vials under the specific conditions described below, the materials are transferred to either a 'wet' (contains solvents and as such potentially their vapour residues) N_2-filled glovebox or a fumehood for solvent addition. The solvents are stored in these respective environments.

ZnO – The preparation of zinc oxide sol–gel solution and settings for film annealing is described. To prepare the solution, 100 mg of zinc acetate dihydrate is dissolved in 1 ml of 2-methoxyethanol (solvent) along with 28 μl of ethanolamine, which acts as a stabiliser. The

solution is then sealed and stirred at room temperature overnight. All solutions are stored in air at room temperature and used the following day. Weighing, mixing, and stirring are carried out in air, and the final solution is deposited in a fumehood. The ZnO processing follows reported procedure in Reference [158]. Film annealing is carried out on a pre-heated hotplate[9] in fumehood at 150 °C for 45 minutes. After annealing, the film is removed from the hotplate and left to cool down to room temperature in the fumehood.

PEDOT:PSS – The preparation of diluted PEDOT:PSS water dispersion and settings for film annealing is described. To prepare the dispersion, equal volumes of PEDOT:PSS aqueous solution [10] and deionised water are mixed. The mixture is then shaken for several minutes to ensure homogenisation and stored in a refrigerator at 5 °C for later use. The dispersion is used within two weeks. Weighing, mixing, and shaking are performed in air, and the final dispersion is deposited in a fumehood. Final annealing is carried out on a pre-heated hotplate in a fumehood at 150 °C for 10 minutes. After annealing, the film is removed from the hotplate and left to cool down to room temperature in the fumehood.

FBR – The preparation of FBR solutions and settings for film annealing is described. In this thesis, two concentrations, 2.5 mg/ml and 10 mg/ml, are used to produce films of approximately 3 nm and 20 nm thickness, respectively. For the 2.5 mg/ml solution, 2.5 mg of FBR is dissolved in 1 ml of chlorobenzene (CB, solvent); for the 10 mg/ml solution, 10 mg of FBR is used. The solution is then sealed and stirred at room temperature overnight for use the next day. Apart from the weighing step, which is carried out in air, all other operations are conducted in a N_2-filled 'wet' glovebox. The FBR processing follows reported procedures in the literature [159]. Final annealing is carried out on a pre-heated hotplate[11] in N_2-filled glovebox at 110 °C for 5 minutes. After annealing, the film is removed from the hotplate and left to cool in the glovebox.

Figure 4.3 illustrates the static spin-coating process used in this thesis. Spin-coating involves depositing a material solution onto a stationary substrate resting on a chuck, which is subsequently rapidly rotated. The centrifugal force spreads the solution across the surface, leading to an approximately uniform distribution and the formation of a thin film. As the ro-

[9] Stuart®, SD160
[10] Heraeus Epurio GmbH, CLEVIOS P VP.AI 4083
[11] Stuart®, CD162

tation starts to accelerate, most of the solution is expelled from the substrate. The remaining liquid gradually matches the rotational speed of the substrate, allowing the film to level out. During this process, solvent evaporation continues, and the solute condenses into a solid film.

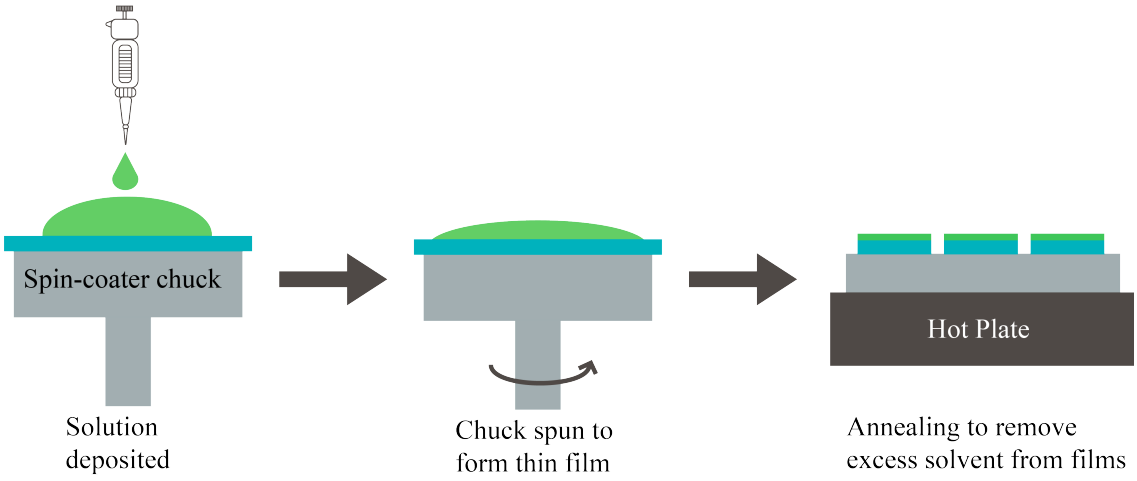


Figure 4.3: Schematic of the spin-coating process for thin-film fabrication. After dispensing the solution onto a cleaned substrate using a pipette, the chuck spins (2000-4000 rpm) to facilitate solvent evaporation and film formation. Subsequently, the samples are annealed to remove any residual solvent. Adapted from the thesis of Dr Nicky Evans [160].

The thickness of a film produced by spin-coating is generally inversely proportional to the square of the spin speed [161]. However, the exact thickness also depends on the solution concentration and the solvent evaporation rate, which is influenced by factors such as solvent viscosity, ambient pressure, ambient temperature, local humidity, and the deposition atmosphere. In addition, film thickness uniformity may be affected by the substrate shape, surface roughness, cleanliness, solvent polarity, and substrate hydrophobicity. Consequently, optimal spin-coating conditions are typically determined empirically. In this thesis, the thickness of spin-coated films is measured using spectroscopic ellipsometry. Spin speed and solution concentration are adjusted accordingly to achieve the desired film thickness.

All the spin-coating for the films detailed in this thesis was done via static spin-coating. The spin-coating parameters used for each material are listed in Table 4.4 below:

Table 4.4: Spin-coating parameters for the films used in this thesis.

Material Name	Filtering	Spin Speed (rpm)	Acceleration (rpm/s)	Duration (s)	Film Thickness (nm)	Casting Environment
ZnO	N/A	4000	2000	30	~30	Fumehood (in air)
PEDOT:PSS	PES filter[a]	2000	2000	30	~25	Fumehood (in air)
FBR (2.5 mg/ml)	N/A	4000	2000	40	~3	Glovebox (N_2)
FBR (10 mg/ml)	N/A	4000	2000	40	~20	Glovebox (N_2)

[a] Gilson Scientific Ltd., 0.45 μm pore size

4.2.4 Solar Cell Device Encapsulation

After solar cell fabrication, the devices are transferred under a N_2 atmosphere into another N_2-filled glovebox for encapsulation via transfer tubes. The active-layer region on each substrate is encapsulated using a custom-designed gapped glass cover[12]. A UV-curable sealant [13] is applied to the edges of the cover glass using a dispensing robot[14], ensuring that the active-layer region remain isolated from the glue. The substrates are then placed into a custom-designed holder and cured under UV light, with the active-layer region masked using black masking tape.

4.2.5 Solar Cell Device Architecture

Two general classes of device stacks are fabricated in this thesis: the conventional and the inverted architectures. The conventional stack follows the structure ITO|Hole Transport Layer| Electron Donor:Electron acceptor (Electron Donor|Electron acceptor)|Electron Transport Layer| Metal Electrode, as illustrated in Figures 4.4 and 4.5. In contrast, the inverted stack swaps the positions of the hole and electron transport layers, as shown in Figure 4.6. Note that the layer thicknesses in these schematics are not drawn to scale.

For conventional stacks, all solar cells apart from differences in active layers, are fabricated with nominally identical hole transport layers, electron transport layers and electrodes. The fabrication sequence involves sequential deposition of PEDOT:PSS (~ 25 nm, spin-coated at 2000 rpm), active layers (composition and thickness varied; individual component deposition

[12] AMG Inc., Encap Glass 28.0*21.5*0.7t, Cavity 25.0*18.5*0.3t
[13] Everlight Chemical Industrial Corporation, Eversolar AB-341
[14] Fisnar Europe Ltd., F4200N.2 Compact Benchtop Robot

rates ranging from 0.1 – 1 Å/s), BPhen (8 nm, 0.1 Å/s), and Ag (120 nm, 0.5 – 1 Å/s), as shown in Figures 4.4 and 4.5. For BHJ devices, electron donor and acceptor molecules were co-evaporated for blend films as active layers.

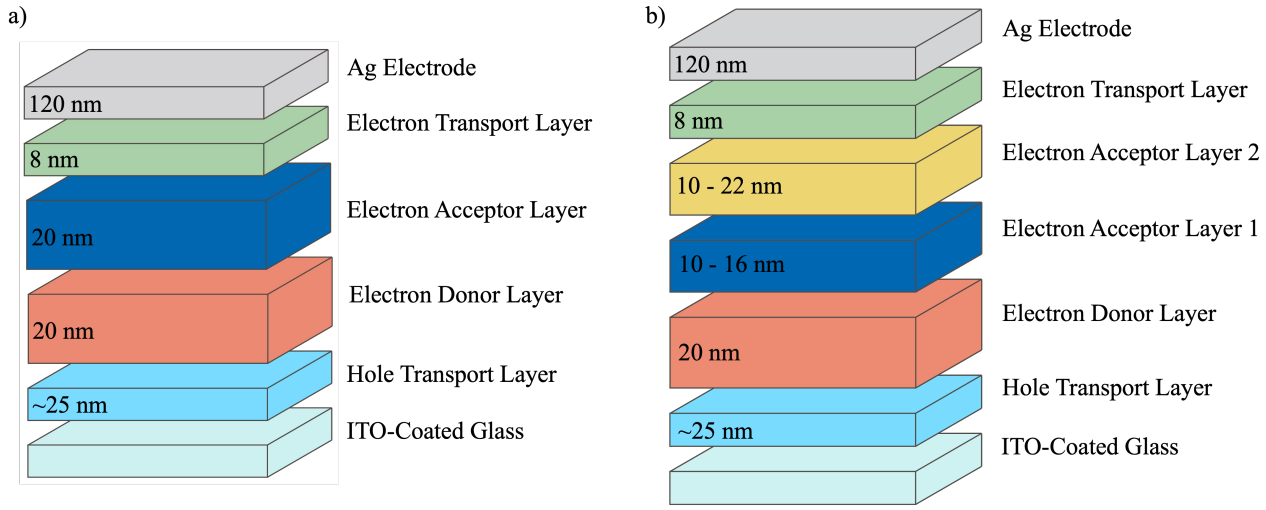


Figure 4.4: Schematic of the multilayer PHJ device stacks (standard architecture) used in this thesis. (a) Bilayer PHJ device structure. (b) Trilayer PHJ device structure. The thicknesses of all other layers were nominally kept constant across all fabricated devices.

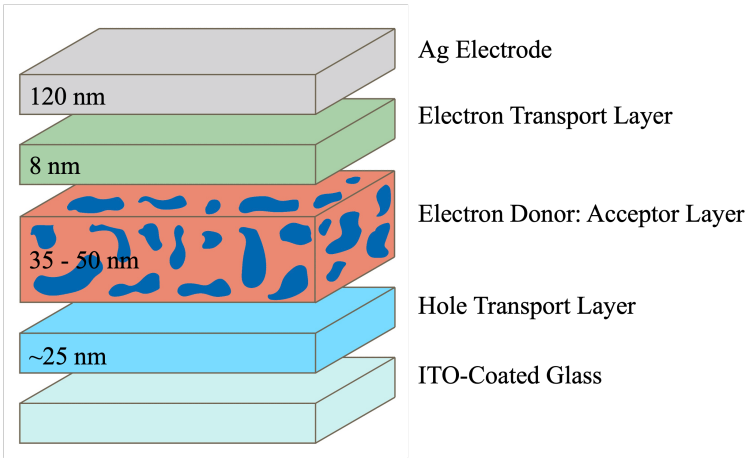


Figure 4.5: Schematic of the bulk heterojunction (BHJ) device stack (standard architecture) used in this thesis. The thicknesses of all other layers were nominally kept constant across all fabricated devices.

Figure 4.6 shows the inverted stack used in the fabrication of hybrid solar cells combining SP and VTE layers. Except for the electron donor layer, all other layers are the same and are fabricated via successive deposition of ZnO (∼ 30 nm, spin-coated at 4000 rpm), FBR (∼ 20 nm, spin-coated at 4000 rpm), electron donor layer (various molecules, 20 nm, 0.20–0.25 Å/s), MoO_3 (10 nm, 0.1 Å/s), and Ag (100 nm, 0.5–1 Å/s).

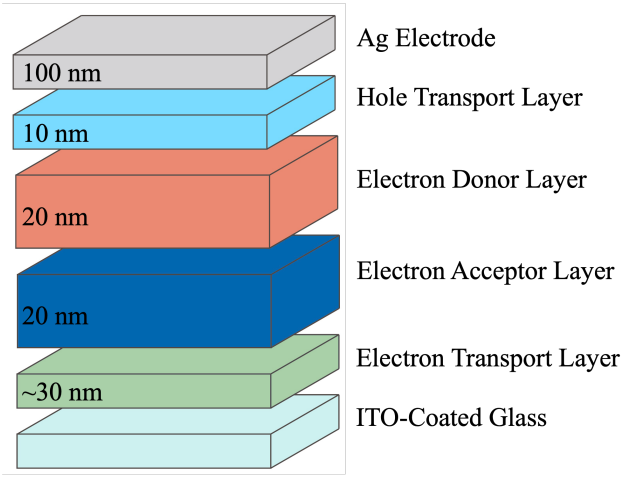


Figure 4.6: Schematic of the bilayer hybrid planar heterjunction (PHJ) device stack (inverted architecture) with an inverted architecture used in this thesis. The thicknesses of all layers were nominally kept constant across all fabricated devices.

4.3 Thin Film Characterization

4.3.1 Steady-state and Time-resolved PL Spectroscopy

In steady-state and time-resolved PL measurements the thin-film samples on glass are photoexcited from the sample side, or from the glass side in the case of hybrid films, using either a 510 nm diode laser[15] or a 635 nm diode laser[16], operating at a frequency of 10 MHz. The emitted photoluminescence is coupled into a grating spectrometer[17]. The spectrally dispersed PL signal is then directed to a time-correlated single-photon counting (TCSPC) setup[18], with photon counting performed using a accumulating processor, PicoHarp 300[19]. For each sample, at least two different positions were measured to ensure that the final spectrum selected was among those with consistent spectral shape and intensity.

4.3.2 Photoluminescence Quantum Yield

PLQY measurements of the thin-film samples on glass are performed by photoexciting the samples from the thin-film side using a 532 nm continuous-wave laser[20], with a spot size of

[15]PicoQuant GmbH, LDH-P-C-510
[16]PicoQuant GmbH, LDH-635
[17]Princeton Instruments, SP-2558
[18]PicoQuant GmbH, FluoTime 300
[19]PicoQuant GmbH, PicoHarp 300
[20]Roithner Lasertechnik GmbH, RTLMLL-532-1.5-3W

approximately 0.15 cm^2. The laser intensity is adjusted according to the optical gap of the material under investigation, such that the resulting photon flux corresponded to that under one-sun illumination conditions. The emitted photoluminescence is collected using an integrating sphere and transferred via a fibre bundle[21], coupled to a calibrated grating spectrometer[22]. The PLQY (ϕ_{PL}) is calculated using the three-measurement de Mello method [162, 163]. For each sample, measurements were taken at three different positions to ensure the representativeness of the resulting ϕ_{PL} values.

4.3.3 Absorption Measurements

The absorption measurements were carried out by Katherine Trinkaus (Oxford). The absorptance of the solar cell devices is measured using a custom-built fibre-optic UV–Vis setup. Incident light is directed onto the samples via a bifurcated optical fibre[23] connected to a Ultraviolet-Vis-Near-Infrared (UV-Vis-NIR) light source[24], and the reflected light is collected through the same fibre, which is connected to a spectrometer[25]. Reflectance spectra are acquired and analysed using the OceanView software[26].

Device absorptance is calculated using the relation $A = 1 - R$, where R is the measured reflectance. For each measurement, the 100% reflectance baseline is calibrated using the bare evaporated aluminium electrode regions on each device pixel, ensuring a consistent distance between the sample and the fibre. The 0% reflectance baseline is obtained when the shutter of the light source is closed.

4.3.4 Spectroscopic Ellipsometry

Spectroscopic ellipsometry (SE) measurements are performed using a spectroscopic ellipsometer[27] at incidence angles of 45°, 55°, 65°, and 75°. The recorded Ψ and Δ values are fitted using B-spline or anisotropic B-Splines models in the CompleteEASE software [28] to determine the

[21] Ocean Optics, QR600-7-SR125BX
[22] Ocean Optics, QEPRO-XR300-slitsize
[23] Ocean Optics, QR600-7-SR125BX
[24] Ocean Optics, DH-2000-BAL
[25] Ocean Optics, Maya 2000 Pro
[26] Ocean Optics, OceanView 1.6.7 Lite
[27] J.A. Woollam Co., Inc., RC2 Spectroscopic Ellipsometer
[28] J.A. Woollam Co., Inc., CompleteEASE Version 6.61

thickness of the films and to extract the optical constants, n and κ. The modelling was carried out by Katherine Trinkaus (Oxford) where stated and all other modelling was performed by the author.

4.3.5 Ultraviolet Photo-electron Spectroscopy and Inverse Photo-Emission Spectroscopy

The measurements and analyses are carried out by Nicky Evans (Oxford) and Dr Selina Olthof at the University of Cologne[29]. Ultraviolet photoelectron spectroscopy (UPS) measurements are performed using a custom-designed multi-chamber Ultra-high-vacuum (UHV) system. Samples are measured at a base pressure on the order of 1×10^{-8} mbar (He atmosphere) using a PHOIBOS 100 hemispherical analyzer[30], positioned normal to the sample. UPS measurements are conducted with a monochromatic helium discharge lamp[31] using HeI radiation at an excitation energy of 21.22 eV. The sample bias is set to -8 V, and the pass energy is set to 2 eV. The energy resolution of the detector is 110 meV, as determined by the width of the Fermi edge. The position of $E_\mathrm{b} = 0$ eV corresponds to the Fermi level of the system and is calibrated using sputter-cleaned metal foils (Au, Ag, Cu).

The value for the work function is determined by subtracting the high-binding-energy cut-off (HBEC) from the excitation energy, while the ionisation energy is calculated as the sum of the work function and the HOMO onset energy. An additional uncertainty of ±100 meV is assigned to the HOMO onset position, in addition to the ±110 meV energy resolution of the analyser (as determined from the Fermi edge width).

Inverse photoelectron spectroscopy (IPES) measurements are performed in the same UHV system, under pressure of approximately 1×10^{-8} mbar. A Kimball ELG-2 electron source is used to emit electrons at an emission current of 2 μA. A UV bandpass photon detector, comprising a SrF_2 window and a NaCl solid-state detector[32], is used to collect counts. The energy resolution is limited by the broad transmission profile of the bandpass detector to approximately ±450 meV.

[29]Faculty of Mathematics and Natural Sciences, University of Cologne, Cologne
[30]SPECS Group., PHOIBOS 100
[31]Scienta Omicron, VUV5000
[32]Omnivac, IPES 2000

This technique allows determination of the LUMO onset energy with respect to the Fermi level. Using the work function obtained from the prior UPS measurement, the electron affinity is calculated by subtracting the difference between the LUMO onset energy and the HBEC from the excitation energy.

4.3.6 Transient Absorption Spectroscopy

The measurements and analyses were carried out by Dr Demetra Tsokkou at the University of Bern[33]. TA spectra are acquired using a custom-built setup based on output pulses from a regeneratively amplified Ti:sapphire laser system[34]. The fundamental laser beam is split into two parts: the pump and the probe beams. The pump beam is directed into an optical parametric amplifier (OPA) to generate tunable wavelengths ranging from the ultraviolet to the infrared, and is then focused onto the sample. The probe beam is focused onto a 5 nm-thick sapphire crystal to generate broadband white light covering the visible and near-infrared spectral regions. This probe beam is subsequently split into two paths: the signal probe beam, which is directed and focused onto the sample, and the reference probe beam, which is sent directly to the detector. The pump and signal probe beams are spatially and temporally overlapped at the sample position.

The time delay between the pump and probe pulses is controlled by adjusting the optical path length of the probe using a computer-controlled motorised micrometer translation stage, enabling time-resolved measurements up to 1.5 ns. The transmitted signal probe and the reference probe are directed into a spectrograph for detection.

Two spectrographs[35] are used in the setup, each comprising a home-built prism spectrometer equipped with either two back-thinned silicon CCDs[36] or two InGaAs arrays[37], allowing simultaneous detection of both the signal and reference beams and improving the signal-to-noise ratio.

Spectra are recorded separately in the visible (450–750 nm) and near-infrared (800–1300 nm)

[33]Department of Chemistry, Biochemistry and Pharmaceutical Science (DCBP), University of Bern, Switzerland
[34]Coherent Corp., Astrella, 1 kHz, 35 fs, 6 mJ, 800 nm pulse
[35]Assembled by Entwicklungsbüro Stresing, Berlin
[36]Hamamatsu Photonics K.K., S07030-0906 for VIS
[37]Hamamatsu Photonics K.K., S07030-0906 for NIR

ranges. To ensure consistency across the full spectral window, the data are scaled to provide a continuous spectrum between the visible and near-infrared regions. The pump pulses are modulated at 500 Hz using a mechanical chopper, and the probe signals are recorded on a shot-to-shot basis. All measurements are performed with the pump beam polarisation set at the magic angle relative to the probe to eliminate contributions from polarisation-dependent effects. At each time delay, the spectra are averaged to achieve a sufficient signal-to-noise ratio.

4.3.7 Grazing Incidence Wide Angle X-Ray Scattering

All Grazing Incidence Wide-Angle X-ray Scattering (GIWAXS) data are acquired by the author, and all analyses presented in this thesis are performed by Olivia Gough (Oxford). GIWAXS measurements presented in this thesis were performed at the Surface and Interface Diffraction beamline (I07) of the Diamond Light Source (DLS)[38]. Each image is taken with an exposure time of 10 s at the incidence angle of 0.15°, which notably is above the critical angle for organic materials. Images were collected using a Pilatus 2M detector[39] and subsequent images calibrated with a silver behenate (AgBeh) standard, using the library pyFAI-calib2 [164] in Python.

GIWAXS enables structural characterisation of thin films on molecular length scales. It is particularly powerful for probing molecular packing, orientation, and crystallinity in films that are not X-ray transparent. Constructive interference of incident X-rays diffracted from atomic or molecular planes appears as bright spots on the detector. The diffraction angle is related to the interplanar spacing, while the direction of diffraction corresponds to the orientation of those planes. According to Bragg's law:

$$d = \frac{2\pi}{q} \tag{4.1}$$

where q is the magnitude of the scattering vector, defined by the incident X-ray wavelength λ and the scattering angle θ as:

$$q = \frac{4\pi}{\lambda} \sin\theta \tag{4.2}$$

[38]Beam energy: 20 keV (0.62 Å), beamtime number SI36456-2
[39]DECTRIS Ltd., Pilatus 2M Detector System

In the resulting 2D GIWAXS patterns, scattering along the q_z direction corresponds to diffraction from planes parallel to the substrate, while scattering along the q_{xy} direction corresponds to diffraction from planes perpendicular to the substrate.

The 2D images are converted into reciprocal space maps using custom Python scripts using the specialised library `pyFAI` [164], with polarisation and solid angle corrections applied as described in Reference [165]. The reciprocal space maps shown in this thesis are presented on a linear colour scale, with intensity limits chosen to enhance visualisation of scattering features.

Peak positions are extracted from radial line profiles of the reciprocal space maps using Lorentzian peak fitting with a first-degree polynomial background:

$$I(q) = I_L \cdot \frac{\Gamma^2}{(q - q_0)^2 + \Gamma^2} + a \cdot q + b \tag{4.3}$$

where I is the measured intensity, q_0 is the peak centre, Γ is the half-width at half-maximum (HWHM), and a, b, and I_L are fitting constants.

Stacking Distances (d) of reflections with peak at q_0 are calculated from equation:

$$d = \frac{2\pi}{q_0} \tag{4.4}$$

Crystal coherence lengths (L_{hkl}) are estimated using an adapted Scherrer equation [166]:

$$L_{hkl} = \frac{2\pi K}{\Delta q_{hkl}} \tag{4.5}$$

where $\Delta q_{hkl} = 2\Gamma$ is the full width at half maximum (FWHM) of the peak, and K is a shape factor set to 1.047, corresponding to spherical grains [167]. This simplified analysis does not account for additional peak broadening contributions (e.g. from detector resolution or beam divergence), and therefore the calculated values should be interpreted as relative estimates of grain size, valid only for comparisons between samples measured under identical conditions.

4.4 Solar Cell Characterisation

4.4.1 Current Density-Voltage Measurements

Current density–voltage (J–V) measurements are performed in ambient environment under simulated AM1.5 g light[40] illumination and in the dark, with applied voltage from a Keithley 2400 sourcemeter[41]. The active area of the solar cell is defined by a black-anodized metal aperture to 0.25 cm^2, held within a light-tight sample holder. The reported values for J_{sc} are corrected for spectral mismatch and adjusted to an intensity equivalent of 100 mW/cm^2 after measurement. The devices shown for each material system represent the best-performing samples, selected from a set of at least 24 devices. The exact voltage sweep range is adapted depending on device performance. However, measurements are generally conducted using both forward and reverse scans between -2 V and +2 V, with voltage step of 0.03 V.

4.4.2 External Quantum Efficiency Measurements

Sensitive EQE measurements are conducted on a custom-built setup [168]. The probing light is generated by a tungsten–halogen light source[42], and diffracted by wavelength using a monochromator[43]. Stray light and higher-order diffraction components are eliminated using two sets of optical filters[44]. The light beam is modulated by a chopper wheel[45] at a frequency of approximately 330 Hz, and then focused onto the device under test. The resulting photocurrent is pre-amplified[46] and recorded using a lock-in amplifier[47]. Si[48] and InGaAs[49] photodiodes with calibrated spectral responses are used to calculate the EQE values.

[40] WAVELABS Solar Metrology Systems GmbH, SINUS-220
[41] Keithley Instruments, LLC., 2400 Source Measure Unit
[42] Princeton Instruments, TS-428, 250 W
[43] Teledyne Vision Solutions, Spectra-Pro HRS300, Triple Grating Imaging Spectrograph
[44] Thorlabs Inc., hard-coated edge-pass and long-pass filters
[45] Stanford Research Systems, SR450, Optical Chopper
[46] Zürich Instruments, HF2TA Current Amplifier
[47] Zürich Instruments, HF2LI Lock-In Amplifier
[48] Thorlabs, FDS100
[49] Thorlabs, FGA21

4.4.3 Electroluminescence Spectroscopy

The EL measurements presented in this thesis were performed by Dr Zhongcheng Yuan (Oxford) [50]. EL measurements of the solar cells are conducted using a custom-built setup housed in a N_2-filled glovebox at room temperature. A Keithley 2400 sourcemeter[51] is used to apply voltage and record current from the device under test. An integrating sphere, coupled with a QE Pro spectrometer[52], is used to collect the EL spectra. The integrating sphere–spectrometer system is calibrated using a vis-NIR radiometric calibration source for absolute light intensity, and an HG-1 calibration source[53] for wavelength accuracy.

The applied voltage is ramped from 0 V up to the point where the current density exceeds the device's short-circuit current, with voltage steps of 0.01 – 0.015 V. Spectral signals are integrated over 200 – 1000 ms at each voltage step, depending on device performance, to ensure stabilisation and reliable measurement. The spectra at each applied voltage and the corresponding current are collected and processed using custom-written LabVIEW software for further analysis.

4.5 Computational Methods

4.5.1 Transfer Matrix Modelling

Transfer matrix modelling (TMM) is performed using the methodology and code published in Reference [169]. TMM is a computational approach used to model the propagation of electromagnetic waves through multilayer structures. It describes the complex interplay of reflection and transmission at each interface by treating the incident light as a combination of forward and backward propagating waves, which are mathematically linked via transmission and propagation matrices. In the context of solar cell research, TMM is particularly valuable for analysing the wavelength-dependent interference effects within the device stack. Moreover, it enables estimation of the short-circuit current density under different charge collection conditions by

[50] Snaith Group, Department of Physics, University of Oxford, Oxford
[51] Keithley Instruments, LLC., 2400 Source Measure Unit
[52] Ocean Optics, QEPRO-XR300-slitsize
[53] Ocean Optics, HG-1 Mercury Argon Calibration Light Source

adjusting the entered IQE. Here in this thesis, IQE is assumed to be 100 % in all simulations. In particular, for PHJ solar cells, TMM allows estimation of the individual contribution to the short-circuit current from each active layer. The method requires the complex refractive index, $\tilde{n} = n + i\kappa$, as input. The values of $\tilde{n}$ used in this study are obtained either from literature sources (e.g. Reference [169]) or from experimental measurements using SE described previously.

5 | Identifying FRET Donor-Acceptor Pair Suitable for OSCs

This chapter presents comprehensive characterisations of the pristine films of the molecules used in this thesis. Detailed optical characterisations, including spectroscopic ellipsometry (SE), steady-state photoluminescence (PL) spectroscopy, photoluminescence quantum yield (PLQY) measurements, alongside surface energetics characterisation by ultraviolet photoelectron spectroscopy (UPS) and inverse photoelectron spectroscopy (IPES), performed by Dr Nicky Evans (Oxford). Charge carrier mobility values and additional IE/EA data compiled from the literature are also provided. Molecules were selected on the basis of high absorption coefficients and, where possible, high charge carrier mobilities and PLQY, and categorised into electron donors and acceptors. Electron acceptor molecules were chosen for their deep IEs and EAs and degree of spectral overlap with the paired electron donor absorption, while electron donor molecules were selected to span a range of IEs and EAs to enable systematic investigation of energy level alignment effects.

Based on IE and EA values from pristine films, molecular pairs capable of supporting barrier-less charge transfer were identified. Pairs enabling both barrier-less hole and electron transfer include SubNc/DCV3T, SubPc/DCV3T, HB194/DCV3T, SubNc/FBR, and SubPc /FBR, while SubNc/HB194, DTDCTB/DCV3T, and DTDCTB/FBR support barrier-less hole transfer alone. To verify the presence of FRET, PL quenching experiments were performed on custom-designed film stacks incorporating a 3–5 nm CBP blocking layer to isolate FRET from competing CT processes. Efficient FRET was confirmed in HB194→SubNc, DCV3T→SubNc, DCV3T→DTDCTB, FBR→SubNc, FBR→DTDCTB, and FBR→SubPc, while DCV3T→SubPc and DCV3T→HB194 exhibited no measurable FRET.

These characterisations provide the selection of two sets of molecular pairs for device studies, fully evaporated and hybrid (solution-processed/evaporated), enabling systematic investigation of how FRET and energetic offsets influence device performance. In the fully evaporated set, SubNc/DCV3T, SubNc/HB194, and DTDCTB/DCV3T exhibit efficient FRET and span a range of EA offsets from large positive to negative, while SubPc/DCV3T and HB194/DCV3T show no detectable FRET but possess favourable IE and EA offsets for charge transfer. In the hybrid set, SubNc/FBR, DTDCTB/FBR, and SubPc/FBR all exhibit efficient FRET with EA offsets ranging from large positive to near-zero. Among all pairs, SubNc/DCV3T and SubNc/FBR most closely resemble high-performance solution-processed NFA OSC systems, combining high absorption coefficients, high electron acceptor PLQY, efficient FRET, and sufficiently large EA offsets (>0.4 eV), making them the most promising candidates for efficient OSCs.

5.1 Introduction

To construct a OSC with efficient exciton separation (i.e. construct Type-II heterojunction) , it is necessary to select molecular pairs with appropriate energy level alignments, where the electron donor typically exhibits shallower HOMO and LUMO levels (i.e. closer to the vacuum level) than the electron acceptor. Therefore, to construct VTE OSCs without using fullerenes as the electron acceptor, molecules with deep LUMO and HOMO levels are generally desirable as VTE NFA candidates. DCV3T is a promising option in this context. It belongs to a class of A-D-A structured oligothiophene molecules initially developed as high-performing electron donors [170,171]. However, unlike its derivatives, DCV3T possesses unusually deep HOMO and LUMO levels of -6.09 and -3.90 eV, respectively (as measured by cyclic voltammetry CV) [171], making it unsuitable as electron donor in most fullerene-based systems due to their similar energy levels. Previous attempts to use DCV3T as an acceptor with ZnPc, MeO-TPD, and 4P-TPD yielded low PCEs (maximum ∼1.63%) but confirmed that DCV3T is highly efficient at harvesting excitons [172]. Owing to its strong absorption and deep energy levels, DCV3T is selected in this thesis as the VTE NFA candidate most resembling a typical SP NFA.

For comparison, a SP NFA molecule, FBR, was selected. FBR was initially developed as a high-performance alternative to the SP fullerene $PC_{60}BM$, with a significantly higher molar extinction coefficient reported to be 3.46×10^4 M^{-1} cm^{-1}, compared to 0.49×10^4 M^{-1} cm^{-1} for $PC_{60}BM$ [173] and it has CV measured HOMO reported to be -5.70 eV and LUMO to be -3.57 eV. Similar to DCV3T, which has an absorption peak at 528 nm [171], FBR is reported to absorb strongly with peak around 509 nm [173]. These similar optical and electronic properties allow both molecules to be paired with the same electron donors, enabling comparison between VTE and SP NFAs.

Although there are many potential VTE electron donor molecules, replicating the free charge generation pathway observed in state-of-the-art SP NFA OSCs requires the donor molecules satisfying several criteria. In high-performing SP NFA OSCs, excitons which generated in the electron donor, undergo efficient FRET to the acceptor, and are subsequently followed by efficient hole transfer back to the donor [39]. However, it is challenging to find VTE electron donor molecules with both appropriate energy levels that enable FRET to the

acceptor, as this would require their emission peaks to lie around 500 nm to ensure sufficient spectral overlap with the absorption profiles of DCV3T or FBR. Instead, it is more feasible to find molecules that support the reverse FRET direction, from DCV3T or FBR to the electron donor, followed by electron transfer back to the acceptor. This reversed sequence still mirrors the key mechanism of exciton harvesting and exciton separation routes in SP NFA OSCs. In addition to spectral overlap, other optoelectronic properties such as high absorption coefficients, favourable energy level alignment, and sufficient hole mobility are also desired. With these criteria in mind, a set of VTE donor molecules with varying energy levels and differing FRET compatibility have therefore been pre-selected for detailed characterisations.

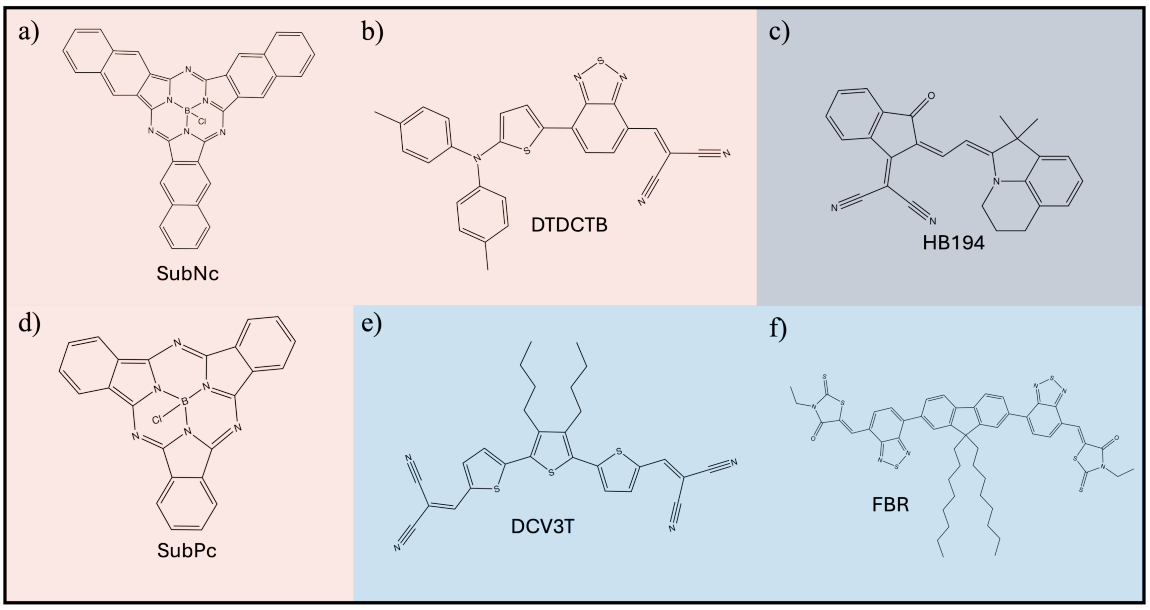


Figure 5.1: Molecular structures and name of the organic molecules investigated. Prospective electron donor molecules are shaded pink, electron donors are shaded blue. Purple shaded molecules can be used as both electron donors and acceptors. Full chemical names and material information are provided in Chapter 4.1.

In this chapter, the thin-film optical and electronic characterisations of these selected small-molecule organic semiconductors. The chemical structures of the investigated molecules are shown in Figure 5.1, with details listed in Chapter 4.1. Except for FBR, which is solution-processable, all other molecules are vacuum thermal evaporable. SubNc, SubPc, and DTDCTB are primarily considered as potential electron donors, while DCV3T and FBR are explored as electron acceptors. HB194 is capable of acting as either a donor or an acceptor, depending on its pairing counterpart.

Optical characterisations includes SE and steady-state PL spectroscopy. The measurement procedures are described in Chapters 4.3.1 and 4.3.4, respectively. The excitation laser wavelength used for each molecule was either 510 nm or 635 nm, selected based on their absorption profiles to ensure efficient excitation and strong PL signal. The specific wavelength used for each molecule is stated individually. Other optical properties, for instance the PLQY (ϕ_{PL}) of films, collected from the literature or measured using the method described in Chapter 4.3.2, are also presented. The PLQY measurements were performed on the same film samples prepared for the steady-state PL measurements, the wavelength of excitation laser was chosen to ensure strong PL.

Electronic characterisations involves UPS and IPES, which are employed to determine the IE, EA, and work function of the materials. All these measurements and analyses were conducted by Dr Nicky Evans (Oxford) at University of Cologne. Details of these measurement techniques are provided in Chapter 4.3.5. UPS and IPES measurements are conducted for SubNc, HB194, and DCV3T. For the remaining molecules, IE and EA values measured with UPS and IPES are taken from literature. Where available, we also summarise other OSC relevant electronic properties, such as charge carrier mobility.

To identify suitable FRET pairs, further PL quenching measurements on different stacked film samples are performed. The results and analyses of these measurements are discussed in detail in this chapter.

5.2 Pristine Film Optical Characteristics

5.2.1 Background Spectra

Figure 5.2 shows the background spectra of the experimental setup used in this thesis, recorded with the laser off at integration times of 0.2, 0.3, and 0.5 s. Prominent background peaks are observed at 528, 547, 613, 808, and 866 nm, with intensities increasing with integration time. For thin-film samples with low PL intensity, these peaks superimpose onto the sample film PL and manifest as bumps or shoulders in the spectra around these wavelengths. It should be noted that these features are artefacts of the setup and do not originate from vibronic

transitions of the sample.

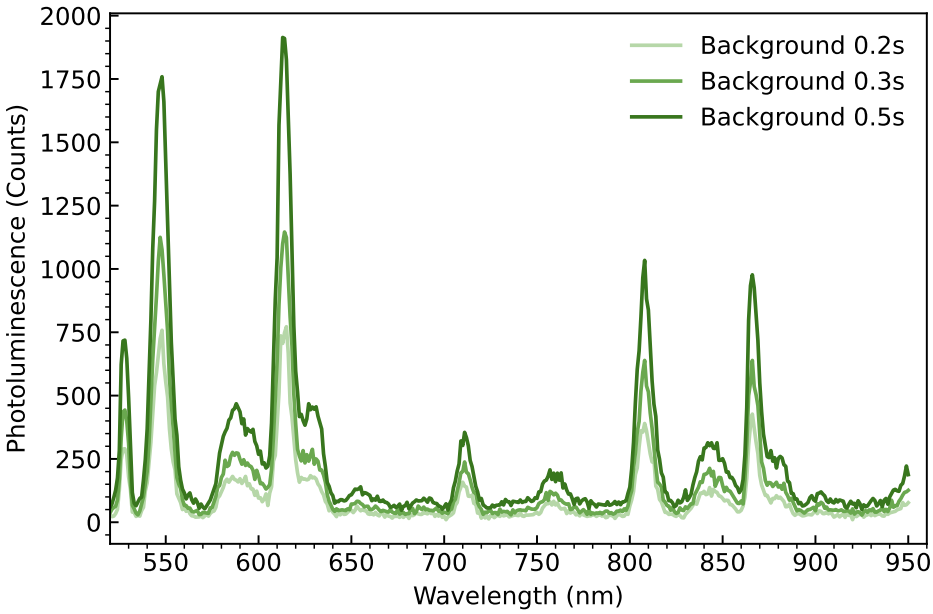


Figure 5.2: Photoluminescence (PL) background spectra recorded with the laser off at integration times of 0.2, 0.3, and 0.5 s.

5.2.2 SubNc

The films of SubNc (20 nm) for steady-state PL and SE measurements were VTE deposited (at a rate around 0.25 Å/s) onto plain glass substrates, following the procedure described in Chapter 4.2.2. Figure 5.3 presents the normalised PL spectrum (solid line) and the overall extinction coefficient, κ (dashed line). The κ spectrum was obtained by fitting the Ψ and Δ values measured by ellipsometric spectroscopy using B-spline model.

The PL measurement was performed by exciting the SubNc film with a 510 nm laser, using the methods described in Chapter 4.3.1. The film exhibits PL emission in the range of 680 to 900 nm, with a peak at approximately 740 nm, which is consistent with the literature-reported value of 743 nm at 293 K [174]. The apparent plateau between 540 and 680 nm originates from the substrate and the features around 800 and 850 nm are attributed to background noise of the measurement setup, as evidenced by background scans shown in Figure 5.2.

The κ spectrum reveals a primary absorption band spanning 500 to 760 nm, with a peak κ value of 2.10 at 688 nm. This corresponds to an absorption coefficient of approximately 3.8×10^5 cm^{-1}. The peak position and overall spectral shape are in good agreement with

previously reported absorbance spectra for SubNc films [146, 175].

ϕ_{PL} values for SubNc at room temperature have been reported as 0.09 in *o*-dichlorobenzene [176] and 0.22 in toluene solutions [177], with the discrepancy attributed to differences in sample purity (later suggested to have higher purity). In contrast, ϕ_{PL} for solid-state SubNc films has been reported to be $\leq 0.25\%$ [178]. ϕ_{PL} was attempted to be measured with our setup. However, the signal-to-noise ratio was too low to yield a physically meaningful result for this molecule.

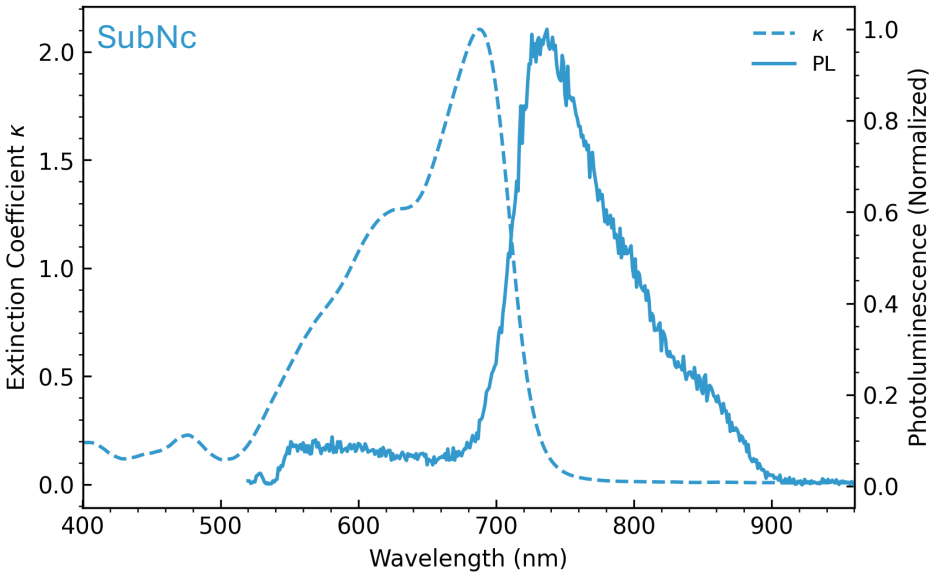


Figure 5.3: Extinction coefficient κ and normalised photoluminescence (PL) spectra of SubNc film on glass. Dashed line is κ and solid line is PL.

5.2.3 SubPc

Similarly, films of 20 nm (deposited at a rate around 0.25 Å/s) SubPc on glass were characterised. Figure 5.4 displays the normalised PL spectrum and the overall extinction coefficient κ.

PL measurements were conducted using the same 510 nm laser are for SubNc. The SubPc film exhibits PL emission over the wavelength range of 580 to 900 nm, with a primary peak at approximately 720 nm and a secondary peak around 630 nm, consistent with previously reported PL spectra [179]. Other studies have reported SubPc films with a dominant PL peak near 630 nm [180]. The red-shifted primary PL peak observed in our sample may be attributed to J-aggregate molecular stacking [181], which may be associated with enhanced ϕ_{PL} [181].

The κ spectrum reveals a main absorption range from approximately 450 to 620 nm, with a shoulder feature at around 530 nm. The peak κ value reaches 1.52 at 586 nm, corresponding to a high absorption coefficient of approximately 3.3×10^5 cm^{-1}. Both the peak position and spectral shape of the κ spectrum are in agreement with previously reported film absorbance and κ spectra for SubPc [174, 180].

Table 5.1: Reported photoluminescence quantum yields (ϕ_{PL}) of SubPc in different solvents. λ_{PL} represents the wavelength of major photoluminescence peak.

Solvent	λ_{PL} (nm)	ϕ_{PL}	Reference
Toluene	571	0.73	[182]
CH_2Cl_2	581	0.33	[183]
$CHCl_3$	571	0.25	[184]
THF	574	0.29	[185]

Table 5.1 summarises the measured ϕ_{PL} of SubPc in toluene, CH_2Cl_2, $CHCl_3$, and THF, which range from 0.25 to 0.73. These variations can be attributed to differences in solvent environment and the sensitivity of the measurement setup. Unfortunately, no reported values of ϕ_{PL} for SubPc in the solid-state were found in literature. The value for SubPc film was therefore measured in-house, yielding 0.73±0.10%, based on three repeated measurements. Although the measurement uncertainty is relatively large, the value appears reasonable, as it is significantly lower than those typically measured in solution.

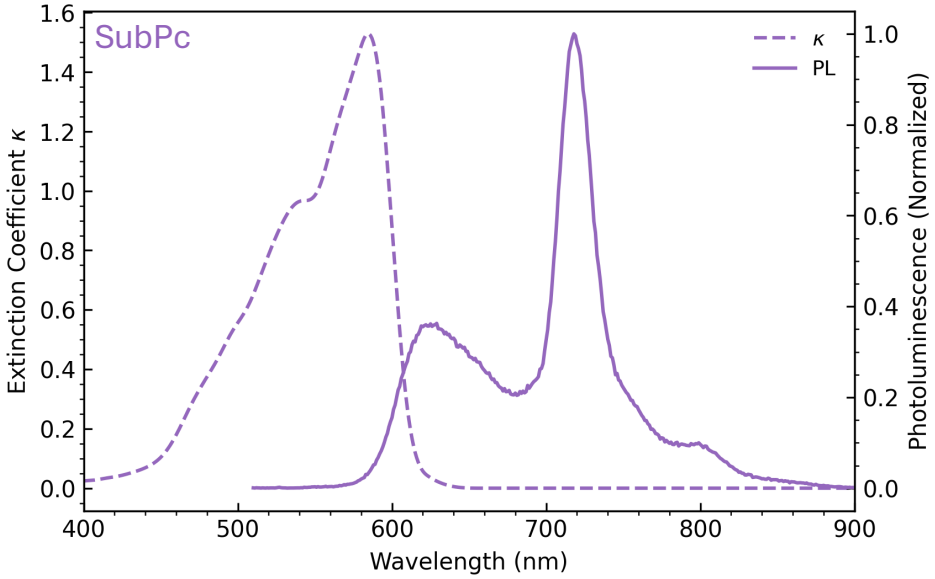


Figure 5.4: Extinction coefficient κ and normalised photoluminescence (PL) spectra of SubPc film on glass. Dashed line is κ and solid line is PL.

5.2.4 DTDCTB

Films of 30 nm (deposited at a rate around 0.20 Å/s) DTDCTB on glass were characterised. Figure 5.5 displays the normalised PL spectrum and the overall extinction coefficient κ.

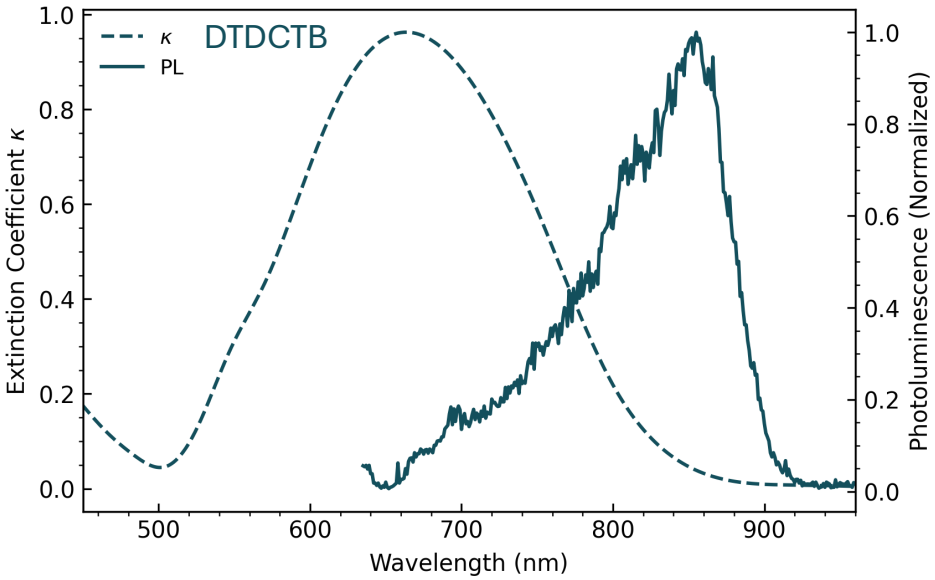


Figure 5.5: Extinction coefficient κ and normalised photoluminescence (PL) spectra of DTDCTB film on glass. Dashed line is κ and solid line is PL.

PL measurements were conducted using a 635 nm excitation laser. The DTDCTB film exhibits PL emission over the wavelength range of 660 to 920 nm, with a primary peak at approximately 880 nm. Other studies have reported three peaks at 520, 745, and 880 nm, with the 520 nm peak being the most prominent and the 880 nm peak the weakest, for DTDCTB neat films excited at 325 nm [186]. We attribute the variation in peak intensities to differences in excitation energy. In this study, the excitation wavelength was selected near its absorption maximum, thereby primarily exciting the $S_0 \rightarrow S_1$ transition and more accurately reflecting its intrinsic vibronic properties. To the best of our knowledge, there are no reported values of ϕ_{PL} for DTDCTB either in the solid state or in solution. Unfortunately, due to the extremely low signal-to-noise ratio, even under optimal excitation conditions, no physically meaningful ϕ_{PL} value for DTDCTB film could be obtained with the setup used.

The κ spectrum reveals a main absorption range from approximately 500 to 900 nm. The peak κ value reaches 0.96 at 663 nm, corresponding to a moderate absorption coefficient of approximately 1.8×10^5 cm^{-1}. Both the peak position and the spectral shape of the κ spectrum

are consistent with previously reported film absorbance and κ spectra for DTDCTB [186–188].

5.2.5 HB194

Films of 14 nm (deposited at a rate around 0.25 Å/s) HB194 on glass were characterised. Figure 5.6 displays the normalised PL spectrum and the overall extinction coefficient κ.

PL measurements were performed using a 510 nm excitation laser. The HB194 film exhibits PL emission over the wavelength range of 620 to 900 nm, with a primary peak at approximately 680 nm and a shoulder around 720 nm. To the best of our knowledge, there are no reported values of ϕ_{PL} or PL spectra for pristine HB194, either in the solid state or in solution. Therefore, the ϕ_{PL} of HB194 film was measured in-house to be 1.04±0.13%, based on the average of three repeated measurements under 532 nm laser excitation.

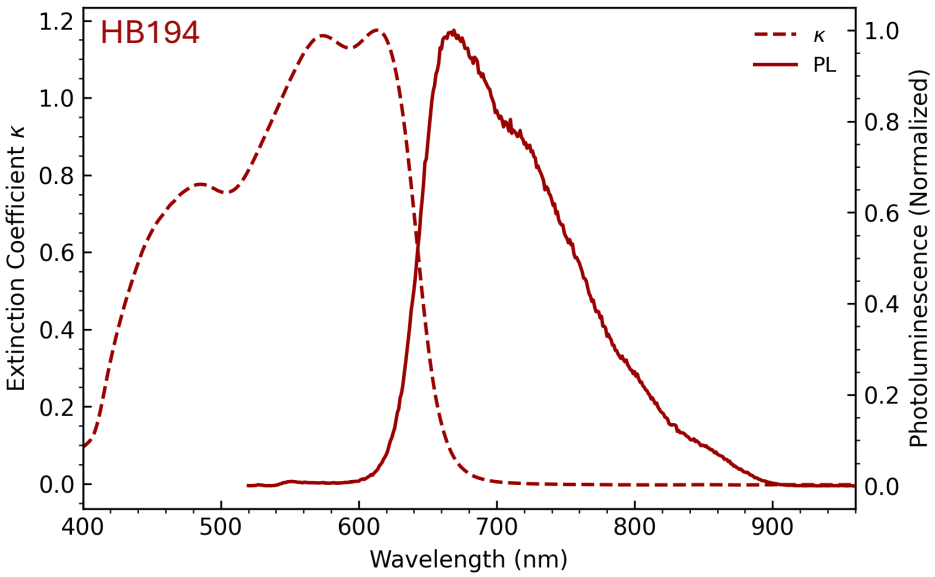


Figure 5.6: Extinction coefficient κ and normalised photoluminescence (PL) spectra of HB194 film on glass. Dashed line is κ and solid line is PL.

The κ spectrum reveals a primary absorption range spanning approximately 400 to 680 nm. Three distinct peaks are observed at 485 nm ($\kappa = 0.78$), 574 nm ($\kappa = 1.16$), and 615 nm ($\kappa = 1.17$), with the highest corresponding absorption coefficient reaching approximately 2.54×10^5 cm^{-1} at 584 nm. Both the peak positions and the overall spectral shape are in good agreement with previously reported κ spectra for HB194 films [127]. The original synthesis paper reports UV-Vis absorption peaks at around 480 nm and 578 nm for HB194

measured in CH_2Cl_2 solutions [189], and the additional peaks observed in the solid-state film are likely due to differences in the molecular environment, e.g. aggregates.

5.2.6 DCV3T

Films of 50 nm DCV3T on glass (deposited at a rate of around 0.25 Å/s) were characterised by steady-state PL, and 30 nm films were characterised by SE. Figure 5.7 presents the normalised PL spectrum and the overall extinction coefficient, κ.

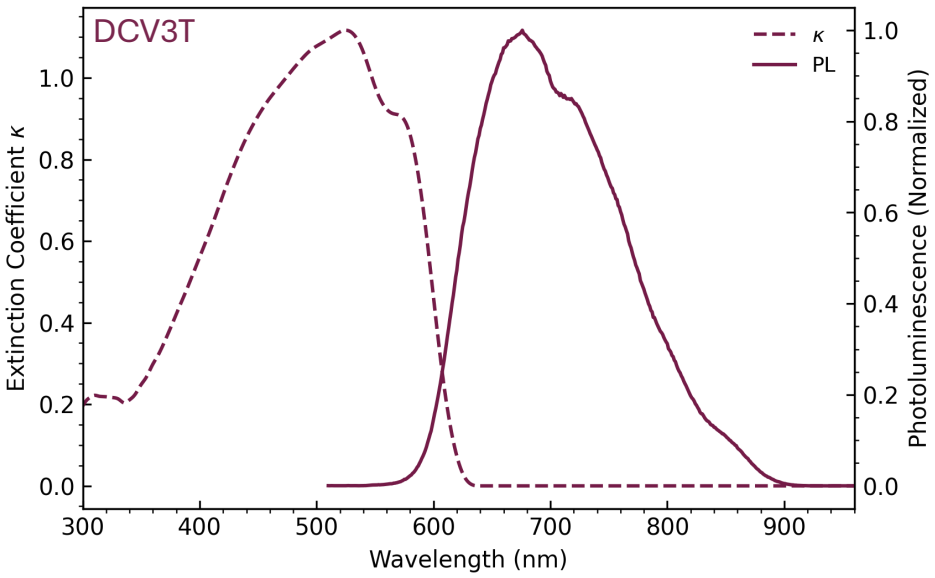


Figure 5.7: Extinction coefficient κ and normalised photoluminescence (PL) spectra of DCV3T film on glass. Dashed line is κ and solid line is PL.

PL measurements were again conducted using a 510 nm excitation laser. The DCV3T film exhibits PL emission over the wavelength range of 580 to 900 nm, with a primary peak at approximately 675 nm and a shoulder around 720 nm. Previous studies have reported dominant emission peaks for DCV3T 30 nm films at 695 nm without a shoulder [170], and others observed a shoulder at 633 nm with the main peak also at 695 nm [172]. Variations in excitation energy, measurement setup, and molecular orientation in the solid film may account for these discrepancies. For this thesis, our measured PL data are used. To the best of our knowledge, no values of ϕ_{PL} for DCV3T have been reported, either in the solid state or in solution. Again, ϕ_{PL} was measured for DCV3T film to be 7.22±0.64% with our setup, based on the average of three repeated measurements under 532 nm laser excitation.

The κ spectrum reveals a primary absorption range spanning approximately 340 to 630 nm. The main peak is located at 525 nm with a peak κ value of 1.12, corresponding to an absorption coefficient of approximately 2.7×10^5 cm^{-1}. A shoulder feature is observed around 575 nm. These results are in good agreement with previously reported absorption spectra for DCV3T solid films, which show a peak at 528 nm and a shoulder at 574 nm [172].

5.2.7 FBR

The films of FBR (20 nm) for steady-state PL and SE measurements were spin-coated onto plain glass substrates, as described in Chapter 4.2.3. Figure 5.8 presents the normalised PL spectrum and the overall extinction coefficient, κ.

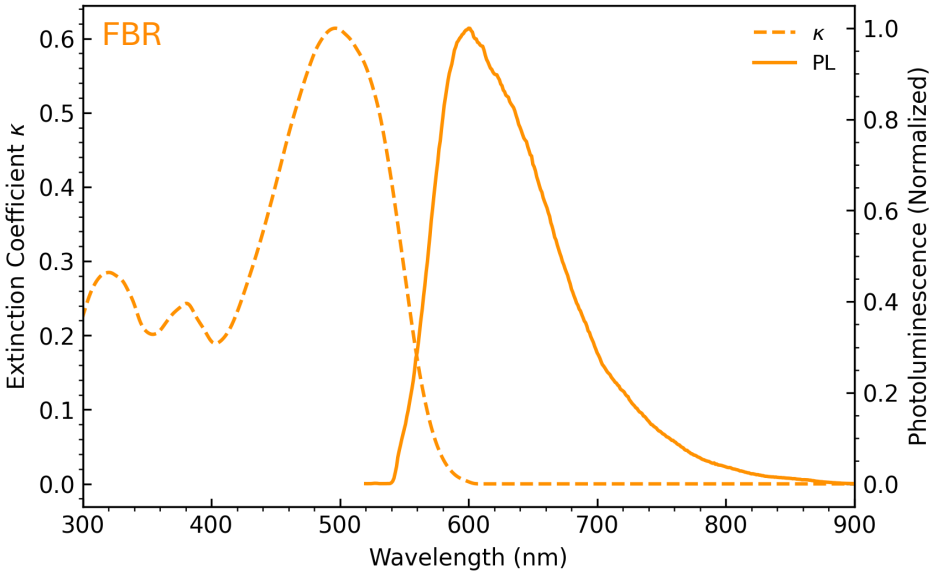


Figure 5.8: Extinction coefficient κ and normalised photoluminescence (PL) spectra of FBR film on glass. Dashed line is κ and solid line is PL.

PL measurements were carried out using a 510 nm excitation laser, following the procedure outlined in Chapter 4.3.1. The FBR film exhibits PL emission over the wavelength range of 540 to 900 nm, with a primary peak at approximately 600 nm, in good agreement with the original synthesis report of this molecule [173]. To the best of our knowledge, no values of ϕ_{PL} for FBR have been reported, either in the solid state or in solution. Similarly, the ϕ_{PL} for FBR films was measured to be 4.00±0.56%, based on the average of three repeated measurements under 532 nm laser excitation.

The κ spectrum reveals a primary absorption range spanning approximately 400 to 600 nm. The main peak is located at 496 nm, with a peak κ value of 0.61, corresponding to a moderate absorption coefficient of approximately 1.5×10^5 cm^{-1}. These results are consistent with previously reported absorption spectra for FBR solid films, which show peaks at 509 nm [173] and 508 nm [190].

5.3 Pristine Film Electronic Characteristics

5.3.1 Ionisation Energy and Electron Affinity

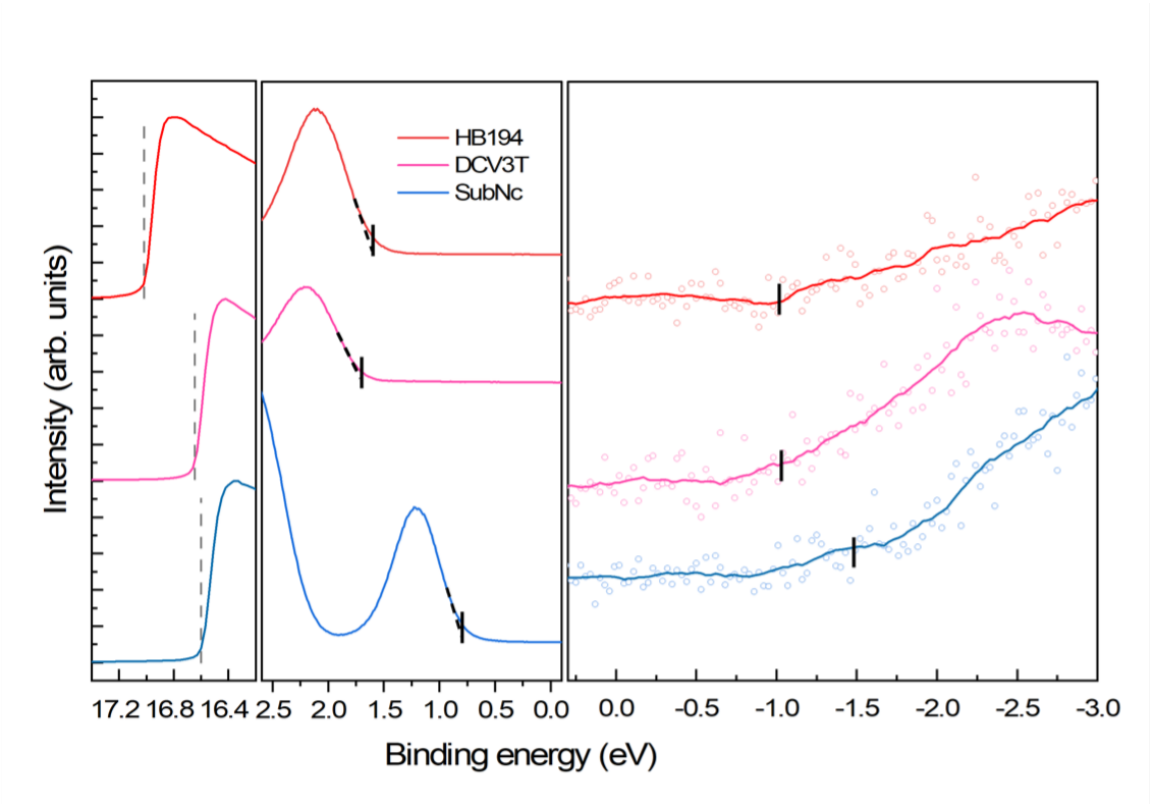


Figure 5.9: Ultraviolet photo-electron spectroscopy (UPS) and inverse photo-emission spectroscopy (IPES) spectra of HB194, DCV3T and SubNc. The left-hand panel presents the UPS data used to determine the high binding energy cut-off (HBEC), while the middle and right-hand panels show the ionisation energy (IE) onset region (from UPS data) and the electron affinity (EA) onset region (from IPES data), respectively. The grey dashed line (in left panel) indicates the HBEC position used to calculate the work function (WF), and the black dashed lines (in middle and right panel) represent the first leading edges used to extract the IE and EA onset positions. The corresponding IE and EA onset energies are denoted by solid black vertical lines. Figure is provided by Dr Nicky Evans (Oxford).

UPS and IPES measurements and analysis were conducted for HB194, DCV3T, and SubNc by Dr Nicky Evans (Oxford) at University of Cologne, whose IE and EA values have not been reported or are only partially available in the literature. These measurements were performed on pristine films with thickness of approximately 30 nm, deposited via VTE at rates of approximately 0.3 Å/s onto silicon substrates. Details of the substrates and deposition conditions can be found in Chapter 4.

Table 5.2: Work function (WF), ionisation energy (IE), electron affinity (EA), and fundamental gap (E_{fund}) determined from ultraviolet photo-electron spectroscopy (UPS) and inverse photo-emission spectroscopy (IPES) measurements on pristine films of HB194, DCV3T, and SubNc deposited on silicon wafers.

Molecule Name	**WF (eV)**	**IE (eV)**	**EA (eV)**	**E_{fund} (eV)**
HB194	4.21 ± 0.15	5.81 ± 0.26	3.19 ± 0.60	2.62 ± 0.65
DCV3T	4.57 ± 0.11	6.27 ± 0.22	3.54 ± 0.56	2.73 ± 0.60
SubNc	4.62 ± 0.11	5.42 ± 0.22	3.14 ± 0.56	2.29 ± 0.60

Table 5.3: Ionisation energy (IE), electron affinity (EA) and fundamental gap (E_{fund}) taken from literature measured[a] on solid films of SubPc, DTDCTB, and FBR.

Molecule Name	IE (eV)	EA (eV)	E_{fund} (eV)	Reference
SubPc	5.57	3.26	2.31	[191]
DTDCTB	5.27	3.65	1.62	[192]
FBR	6.16	3.70	2.46	[193]

[a] Measured with Ultraviolet photo-electron spectroscopy (UPS) and inverse photo-emission spectroscopy (IPES).

Using UPS and IPES, the work functions (WF), IE, and EA of HB194, DCV3T, and SubNc films were determined. Figure 5.9 presents the UPS (left and middle panels) and IPES (right panel) spectra acquired from the respective films deposited on silicon substrates. The UPS data were used to extract the HBEC, as indicated by the grey dashed line (Figure 5.9, left panel), and the onset energies of IE and EA, marked by solid black lines (middle and right panels, respectively). The positions of the HBEC, IE, and EA onsets were determined via linear fits to the leading-edge regions, using the initial slope as the basis for the extrapolation (black dashed line). For HB194, we included an additional uncertainty of ± 40 meV in the HBEC fit, in addition to the analyser's intrinsic energy resolution of ± 110 meV, as determined from the Fermi edge width. Due to the limited energy resolution of the IPES detector and the challenges associated with identifying the precise onset of the leading edge, the uncertainty

associated with the EA values extracted from IPES was estimated to be ± 450 meV. All extracted values are summarised in Table 5.2.

For the other molecules, SubPc, DTDCTB and FBR, their IE and EA values are available in the literature and summarised in Table 5.3. It is worth noting that the reported energy levels of SubPc [191] and FBR [193] were obtained from films deposited on silicon substrates, whereas the one for DTDCTB was measured on films deposited atop a layer of PEDOT:PSS on ITO-coated glass substrates [192]. Although the IE and EA values were measured using different setups, which may introduce some systematic differences, all values were obtained on pristine films using the same technique, thereby facilitating comparability among them. For example, SubNc has reported UPS (IPES) measured IE of 5.35 eV and EA of 3.47 eV [191], which fall within the error margins of the values measured in this thesis, indicating good comparability between datasets obtained on different setups. For ease of comparing the IE and EA values across all molecules, and to assess their suitability for application in OSCs, an energy level schematic is presented in Figure 5.10.

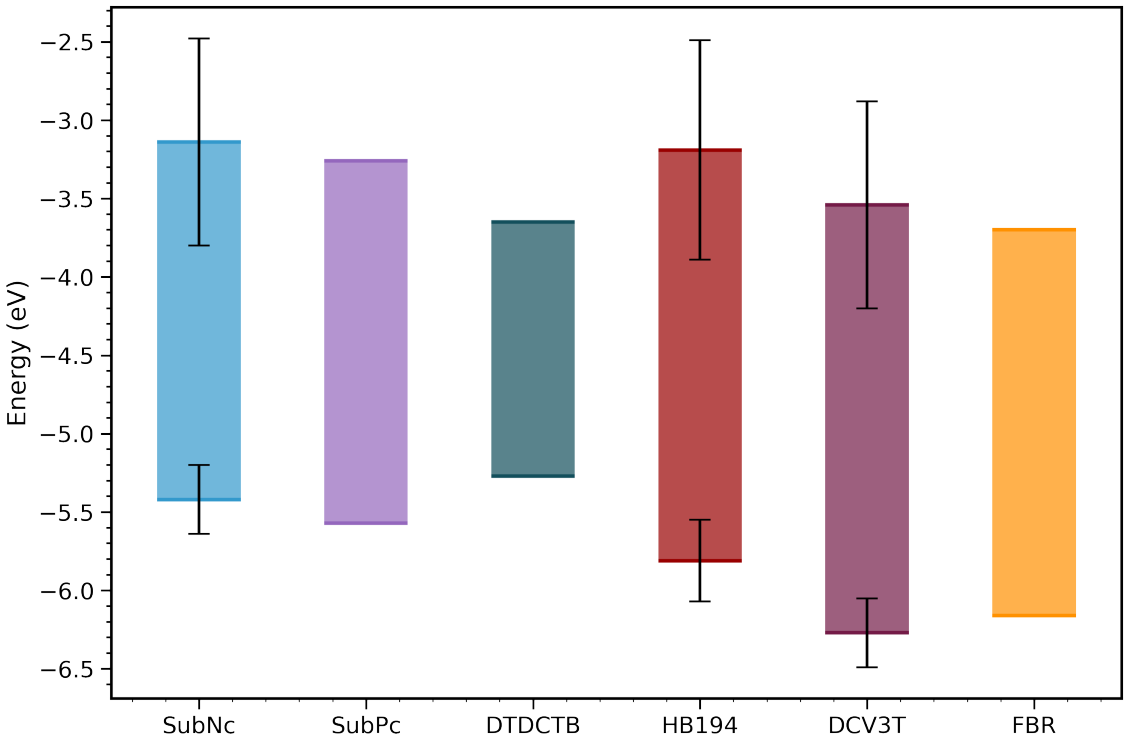


Figure 5.10: Schematic energy levels of SubNc, SubPc, DTDCTB, HB194, DCV3T, and FBR. The ionisation energy (IE) and electron affinity (EA) values, along with their associated uncertainties, are taken from Table 5.2 and Table 5.3. Uncertainties from the measurement setup are indicated by solid black error bars.

5.3.2 Charge Carrier Mobility

Charge carrier mobilities, μ_e (electron) and μ_h (hole), are important design parameters for new organic semiconducting materials. The relatively low mobilities of current organic semiconductors are often considered a limiting factor in overall device performance. Even for state-of-the-art solution-processed non-fullerene acceptors (NFAs) such as Y6 and L8-BO, their electron mobilities in pristine films are reported to be 4.1×10^{-5} and 2.5×10^{-4} cm^2 V^{-1} s^{-1}, respectively [194]. In comparison, previous-generation electron acceptors such as fullerene and its derivatives, which have long been employed in OSCs, exhibit excellent electron mobilities on the order of 10^{-2} to 10^{-3} cm^2 V^{-1} s^{-1} [195]. Moreover, it has been shown that imbalanced charge carrier mobilities can result in S-shaped J–V characteristics in PHJ solar cells [196], highlighting the importance of achieving balanced transport for optimal device operation. Consequently, evaluating these parameters is essential before integrating materials into solar cell architectures.

A widely adopted method for measuring charge carrier mobility in organic semiconductors along the direction of charge extraction (i.e. out-of-plane) is the space-charge-limited current (SCLC) technique, which requires only a thin film of approximately 100 nm in thickness [197]. Another technique,time-of-flight (TOF) measurements, offers higher accuracy, however they typically require films of micrometre-scale thickness, rendering them less practical for many organic materials, in particular for VTE materials. Due to the simplicity and practicality, SCLC method has become a standard technique for determining charge mobilities in organic semiconductors.

To perform accurate SCLC measurements, one must fabricate single-carrier devices. Under SCLC conditions, the current density J_{SCLC} can be described by Child's law [198] for materials with electric field-dependent mobility (e.g organic semiconductors) [199]:

$$J_{SCLC} = \frac{9}{8}\epsilon\epsilon_0\mu_0 \exp\left(0.89\beta\sqrt{\frac{V}{d}}\right)\frac{V^2}{d^3}, \tag{5.1}$$

where ϵ is the dielectric constant of the material, ϵ_0 is the permittivity of free space, μ_0 is the zero-field mobility, β is the field-activation parameter, which quantifies how strongly the charge-carrier mobility increases with electric field, V is the applied voltage, and d is the

film thickness. This expression can be used to extract μ_0 provided that the electrode contacts can efficiently inject charges to establish the SCLC regime [197]. When significant energy barriers exist at the contacts, the current instead follows the injection-limited current (ILC) regime [197]. More comprehensive guidance on the correct application of SCLC and ILC for mobility measurements for organic semiconductors can be found in Reference [197].

Table 5.4: Electron (μ_e) and hole (μ_h) mobilities of pristine films of SubNc, SubPc, DTDCTB, HB194, DCV3T, and FBR, as reported in the literature. For DCV3T, the reported electron mobility was measured under an applied electric field of 0.2 MV cm^{-1}, while the hole mobility was obtained from simulations and corresponds to the zero-field value. The electron mobilities of SubNc, SubPc, and DTDCTB were reported as zero-field values. A forward slash ('/') indicates that no reported values were found.

Molecule Name	μ_h (cm^2 V^{-1} s^{-1})	Reference	μ_e (cm^2 V^{-1} s^{-1})	Reference
SubNc	1.61×10^{-4} [b]	[200]	4.2×10^{-9} [b]	[146]
SubPc	$(4.5 \pm 2.3) \times 10^{-8}$ [b]	[201]	5.2×10^{-10} [b]	[201]
			4.9×10^{-6} [b]	[146]
DTDCTB	9.24×10^{-5} [b]	[186]	$\sim 3.2 \times 10^{-3}$ [b]	[186]
HB194	2×10^{-5} [a]	[189]	/	/
DCV3T	6.8×10^{-10} (simulated)	[202]	2.46×10^{-6} [b]	[203]
FBR	/	/	/	/

[a] Values were determined in organic field-effect transistor (OFETs) with pristine films of the molecule.
[b] Values were determined from space-charge-limited current (SCLC) measurements with pristine films of the molecule.

Table 5.4 presents a compilation of reported μ_e and μ_h values in pristine films of the organic semiconductors investigated in this thesis. Among these, SubNc, SubPc, and DTDCTB have their mobilities reported as zero-field values. For DCV3T, μ_e was measured under an applied electric field of 0.2 MV cm^{-1}, while μ_h was obtained through simulation at zero field. In the case of HB194, μ_h was reported from measurements organic field-effect transistor (OFET) configuration, which reflects an interface-limited transport regime in in-plane direction and typically yields lower mobility values than bulk measurements obtained via SCLC [204]. To the best of our knowledge, no mobility data for FBR has been reported in the literature. Measuring the electron mobility of FBR using the SCLC or ILC method requires knowledge of its dielectric constant, field-activation parameter, and the construction of a suitable thin-film device stack. As these steps fall beyond the scope of this thesis, the measurement was not conducted.

5.4 Photoluminescence Quenching Measurements and Candidate Selections for Solar Cells

5.4.1 Film Stacks

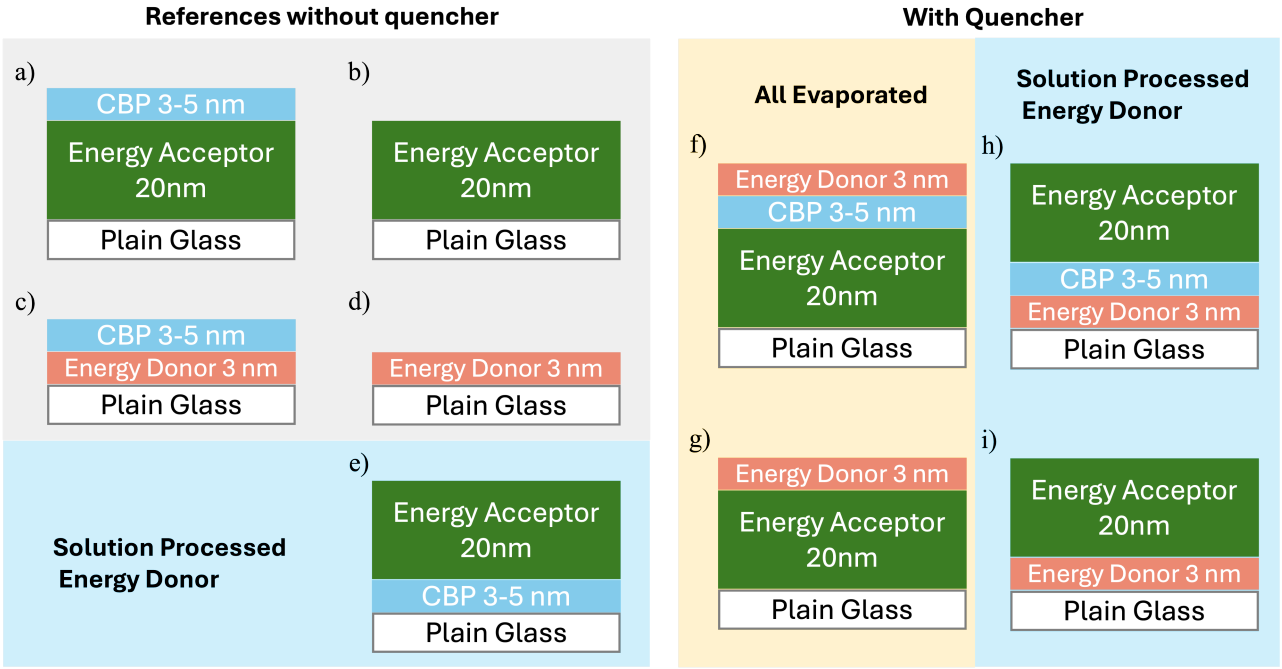


Figure 5.11: Schematic of film stacks used for photoluminescence (PL) quenching experiments to indirectly verify Förster Resonance Energy Transfer (FRET) from the energy donor to acceptor molecule. The energy acceptor acts as a quencher of the donor emission. CBP is a wide-gap (IE= 6.1 eV, EA=1.9 eV [205]) organic semiconductor used to block charge separation between the two molecular layers (chemical structure shown in Figure 4.1). (a) Energy acceptor molecule film with a CBP overlayer. (b) Energy acceptor molecule film alone. (c) Energy donor molecule film with a CBP overlayer. (d) Energy donor molecule film alone. (e) Energy acceptor film with a CBP layer underneath, used when the energy donor is solution-processed. (f) Energy donor molecule film deposited on top of an quenching acceptor film with an intermediate CBP blocking layer. (g) Energy donor molecule film directly deposited on top of the acceptor film. Stacks (f) and (g) are used for the cases when all molecules be evaporated. (h) Energy donor molecule film deposited underneath an quenching acceptor film with an intermediate CBP blocking layer. (i) Energy donor molecule film directly underneath the acceptor film. Stacks (h) and (i) are used when the energy donor is solution processed.

To indirectly verify whether two molecules can enable FRET, a series of film samples were prepared with stack configurations shown in Figure 5.11. As discussed in Chapter 3.1.3, energy transferred from excited donor molecules to acceptor molecules via FRET can be probed

through quenched PL signals of the energy donor and enhanced PL signals from the acceptor, provided that the transferred excitons do not undergo non-radiative recombination or charge dissociation. CT at electron donor–acceptor interfaces can also induce PL quenching, complicating the identification of FRET-driven effects. However, FRET can occur between molecules separated by several nanometres and does not require direct molecular contact, unlike charge transfer, which necessitates physical contact of molecules. This distinction offers an opportunity to disentangle the two processes.

To isolate FRET from CT contributions, a thin layer of a wide-gap organic semiconductor can be introduced between the energy donor and acceptor layers. This blocking layer serves to spatially separate the molecules and create energetic barriers that suppress charge transfer, and therefore needs to form a continuous and closed film. To ensure that FRET-induced PL quenching remains above the detection threshold, this layer should also be sufficiently thin, typically 3-5 nm in thickness to maintain efficient FRET.

Figure 5.11 illustrates all stack configurations used for PL quenching measurements. Here, we selected CBP as the wide-gap blocking layer, following Cnops *et al.* [146], with reported energy levels of 1.9 eV (EA) and 6.1 eV (IE) as measured by IPES and UPS, respectively [205]. Ellipsometric studies reported that CBP deposited at rate of 0.1 Å/s on quartz forms smooth films with a roughness of 1.2±0.2 nm [206], suggesting that a 3–5 nm CBP layer can act as an effective barrier against charge transfer while remaining sufficiently thin for efficient FRET.

Stack a–d in Figure 5.11 serve as reference configurations, establishing baseline PL intensities of pristine energy donor and acceptor films. Stacks a and c include an additional CBP overlayer to verify that CBP itself does not influence PL intensity of contacted layers. When the energy donor molecule is solution processed, stack a is replaced with stack e to keep consistent layer sequence with the stacks with quencher. Stack f consists of a very thin energy donor layer on top of a thick acceptor film, with a 3-5 nm CBP layer in between. The energy acceptor thickness was selected to exceed the typical FRET radius to ensure maximum FRET events, while the donor layer was kept thinner than FRET radius to minimise PL contributions from non-quenched donor molecules. When FRET occurs, a clear reduction in energy donor PL and enhancement in acceptor PL (under donor-selective excitation) should be observed in stack f compared to stacks a and c, if acceptor excitons do not fully undergo CT subsequently,

as demonstrated in Reference [146]. Stack g consists of a direct energy donor–acceptor bilayer without the CBP barrier. In this case, additional PL quenching may occur via CT if energy alignment of the two molecules is favourable. Furthermore, the absence of spatial separation enhances FRET efficiency, which may result in stronger PL quenching compared to stack e. When energy donor film is solution processed, stacks h and i are used instead of stacks f and g.

The steady-state PL setup used in this thesis does not have an integrating sphere. Therefore, absolute PL intensities cannot be compared across samples measured in different batches. This limitation arises from potential variations in laser intensity and the exclusion of scattered light from collected emissions. Nonetheless, by maintaining consistent measurement settings, relative PL intensities remain comparable among samples measured within the same batch.

5.4.2 Blocking Layer CBP

Figure 5.12 presents the PL spectra of films of the molecules under investigation, comparing samples with (in stack shown in Figure 5.11b and d) and without (in stack shown in Figure 5.11a and c) the CBP overlayer. This is to confirm that CBP does not act as a PL quencher for these molecules. Molecules (energy acceptor) with PL shown in Figure 5.12a–d were excited with a 510 nm laser from the thin-film side, while those (energy donor) in Figure 5.12e and f were excited from the glass substrate side. This directional excitation was chosen to maintain consistency with the sequence of light–material interaction in film stacks where both the energy donor and acceptor molecules are present.

Figure 5.12a shows that the PL intensity of pristine HB194 film slightly decreases upon addition of a CBP overlayer, with a reduction of approximately 7% in peak PL intensity. Since CBP absorbs primarily below 350 nm [207], this reduction is likely due to optical destructive interference or differences in sample alignment rather than true PL quenching.

Figures 5.12b and c (SubNc and DTDCTB, respectively) show no notable difference in PL intensity between pristine films and those with a CBP overlayer. In contrast, Figures 5.12d and f (SubPc and FBR) exhibit small increases in peak PL intensity, by approximately 9% for SubPc and 19% for FBR. These enhancements may be attributed to constructive optical interference, whereby the CBP overlayer modifies the local optical field experienced by the

emitting film and enhances outcoupled emission, or to roughness-induced outcoupling, whereby surface roughness at the CBP/organic interface scatters waveguided modes out of the film into the far field, increasing the detected PL intensity. This effect is more pronounced in the FBR film, which has a thickness of only ∼3 nm, where variation in thickness may also contribute.

A particularly interesting observation is found for DCV3T sample sets shown in Figure 5.12e, where the addition of CBP significantly enhances the PL intensity of DCV3T, increasing its peak PL by approximately 200%. This effect was consistently observed across repeated measurements, suggesting it is not an artefact. As CBP emits primarily in the 350–475 nm range [207], it is unlikely to directly contribute to the increased PL. It is hypothesised that, in addition to constructive interference, the bilayer structure may form an optical waveguide that enhances PL emission. If this hypothesis is correct, altering the thickness of the constituent layers should eliminate the amplification effect, which could be further explored. Surface roughness-induced variations in outcoupling efficiency may also contribute to the observed PL enhancement, though further AFM characterisation and optical modelling are needed to isolate the underlying cause. Nonetheless, for our purpose, this result confirms that CBP does not quench the PL of DCV3T.

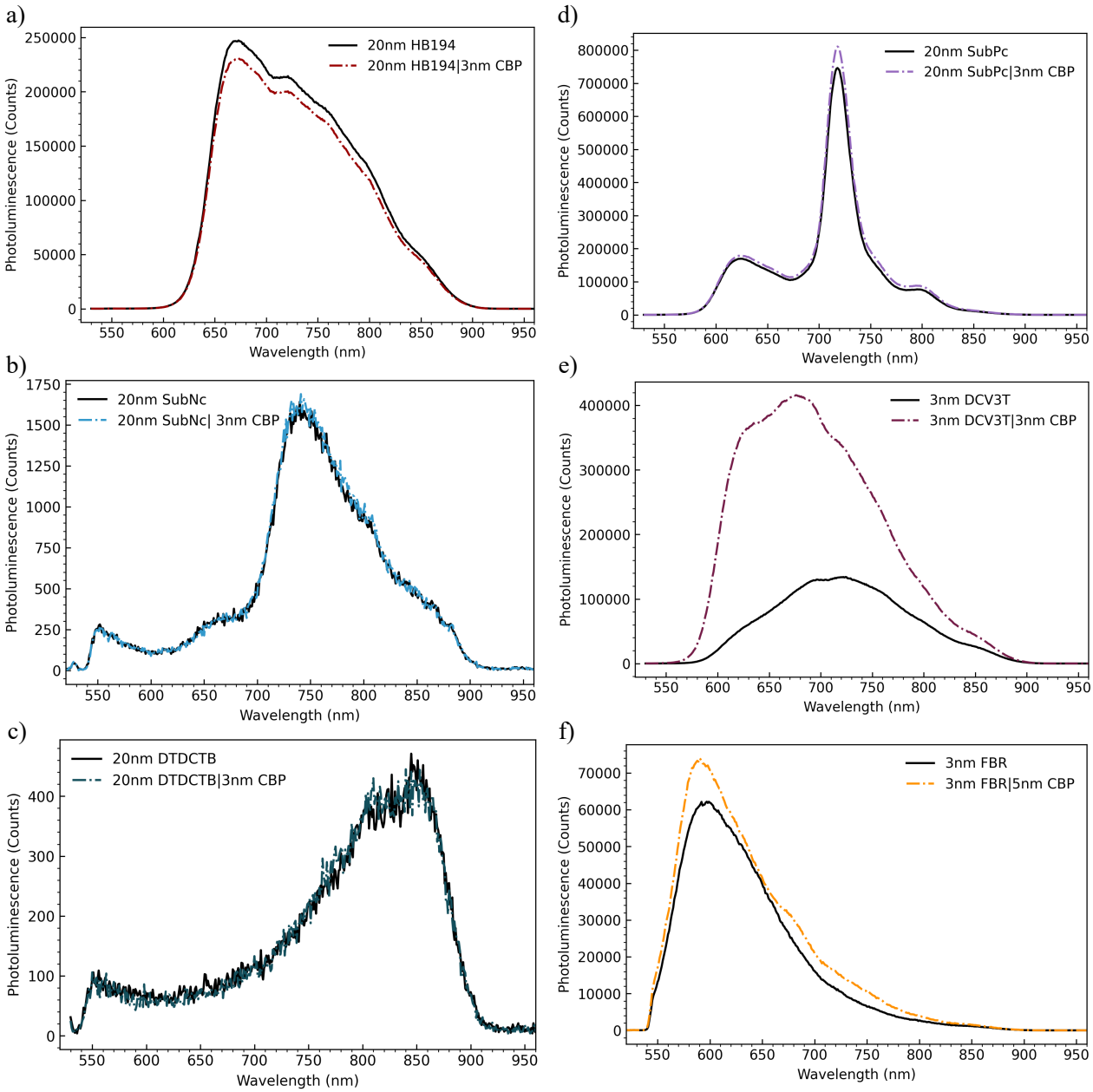


Figure 5.12: Steady-state photoluminescence (PL) spectra of multilayer thin-film samples with stack configurations shown in Figure 5.11a-d. Solid black lines represent PL spectra of 20 nm pristine films of (a) HB194 , (b) SubNc, (c) DTDCTB , (d) SubPc and 3 nm pristine film of (e) DCV3T , (f) FBR, while dot-dashed lines show the corresponding spectra with an additional 3 nm CBP layer on top. Samples for spectra (a)–(d) were excited from the film side. Samples for spectra (e) and (f) were excited from the glass substrate side so that the excitation laser first interacts with the energy donor layer. This configuration ensures that the molecules work as energy donor interacts with light prior to the CBP layer, aligning with the their light interaction sequence in film stacks where energy acceptors are also present.

5.4.3 Fully Evaporated Molecules

For energy donor and acceptor candidates that are both vacuum-evaporable, the quenched sample stacks with and without the CBP blocking layer correspond to those shown in Figure 5.11f and g, respectively. A 510 nm laser was used for these quenched samples, along with their respective reference samples in stacks shown in Figure 5.11a, b, and d, from the film side. This excitation geometry ensures that the energy donor molecule interacts with the incident light prior to any other layers, if present. All samples are excited with 510 nm laser to selectively excite the energy donor molecules.

The wide gap of CBP (EA=1.9 eV, IE=6.1 eV) provides a good energetic barrier between the candidate molecular pairs, as illustrated by the energy level diagrams in Figure 5.13a, Figure 5.14a, Figure 5.15a, Figure 5.16a, Figure 5.17a. Based on the IE and EA values measured on neat films, CBP is expected to provide large EA barriers to block electron transfer and sufficient IE barriers to significantly suppress hole transfer between the energy donor and acceptor. It should be noted that for pairs with DCV3T as the energy donor, the IE of CBP is approximately 0.2 eV lower than that of DCV3T, which may permit limited hole transfer from DCV3T to CBP. However, this effect is expected to be minor and negligible.

5.4.3.1 SubNc and HB194

As shown in Figure 5.13a, HB194 exhibits an EA comparable to that of SubNc and an IE offset of approximately 0.4 eV. It should be noted that the offsets are based on measurements of pristine films and may not accurately reflect the actual energy levels at the molecular interface, as interfacial quadrupole moment interactions can induce energy level bending, often leading to smaller effective offsets [39]. Nevertheless, these offsets remain useful approximations for comparing interfacial driving forces across different systems. This energetic configuration suggests that hole transfer from HB194 to SubNc is favourable, whereas electron transfer from SubNc to HB194 is less likely.

Figure 5.13b displays the overlay of the normalised κ spectrum of SubNc and the PL spectrum of HB194 (excited by a 510 nm laser). A strong spectral overlap is observed in the SubNc absorption region, particularly from approximately 600 nm to 760 nm. Using

Equation 3.8, the spectral overlap integral J was calculated to be 1.44×10^{16} mol^{-1} L cm^{-1} nm^4, indicating that efficient FRET is expected.

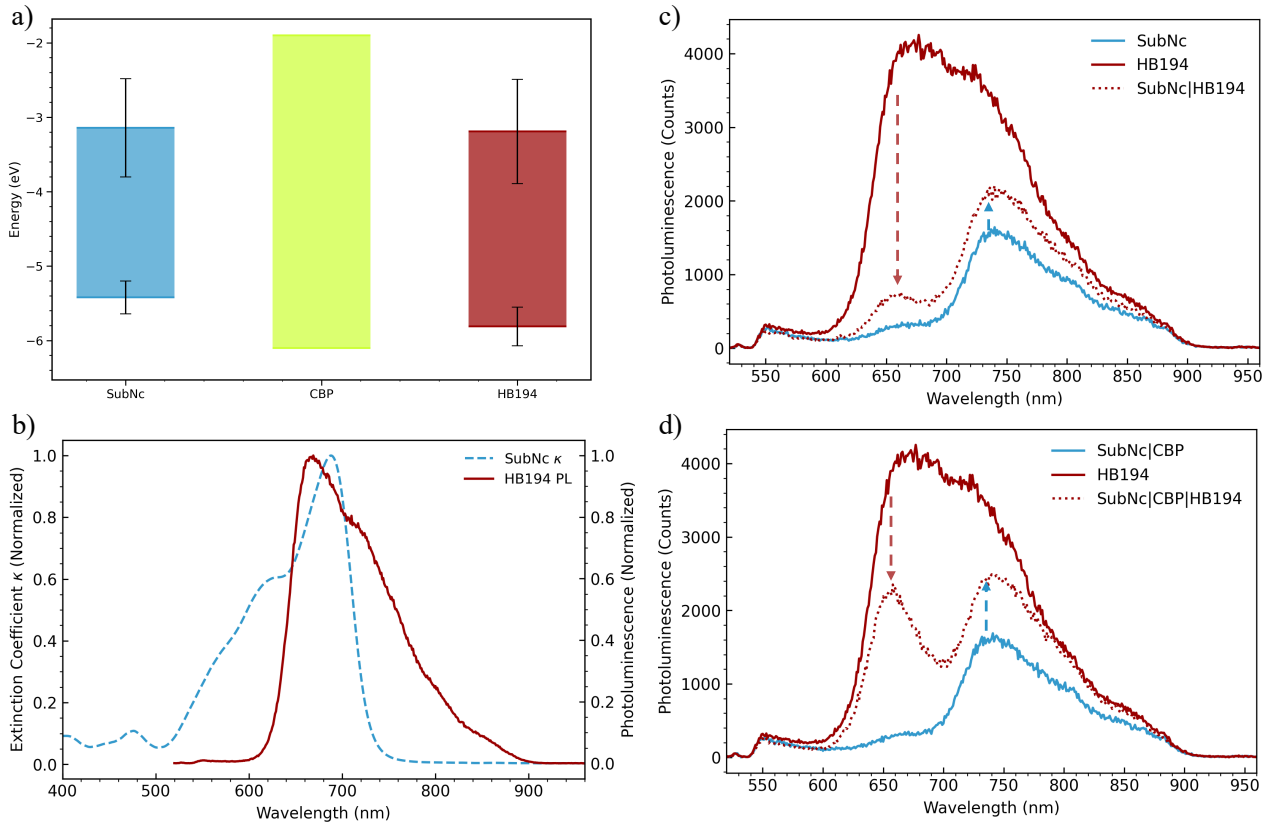


Figure 5.13: (a) Schematic energy levels of pristine SubNc, CBP, and HB194 films. (b) Extinction coefficient (κ) spectrum of SubNc (blue dashed line) and steady-state photoluminescence (PL) spectrum of HB194 (red solid line). (c) PL spectra of samples comprising 20 nm pristine SubNc (blue line), 3 nm pristine HB194 (red solid line), and 3 nm HB194 deposited on top of 20 nm SubNc (red dotted line). (d) PL spectra of samples comprising 3 nm CBP on top of 20 nm SubNc (blue line), 3 nm pristine HB194 (red solid line), and glass|20 nm SubNc|3 nm CBP|3 nm HB194 (red dotted line). All PL spectra were measured with 510 nm laser excitation from the film side.

Figure 5.13c compares the PL spectrum of the quenched sample with those of the reference pristine films, without the CBP blocking layer. Noticeable quenching (quenching ratio of 56%) of the HB194 PL signal is observed across its entire emission range, with the most pronounced quenching occurring between 600 nm and 700 nm, which is within the absorption range of SubNc. A slight enhancement of the SubNc PL signal, peaking around 740 nm, is also observed. The quenching of HB194 emission may result from FRET and hole transfer to SubNc, as suggested by the substantial IE offset. The enhancement of SubNc PL supports the presence of FRET and the inefficient electron transfer from SubNc to HB194.

To isolate FRET from hole transfer contributions, we examined the stack with a CBP blocking layer in between. The corresponding PL spectrum is shown in Figure 5.13d. Upon introducing the CBP layer, which suppresses charge transfer, the HB194 PL signal remains quenched (quenching ratio of 37%) , while a more pronounced increase in SubNc PL is observed, again peaking at 740 nm. This confirms that the observed PL quenching is induced by FRET. The reduced quenching in the 600 – 700 nm range, compared to the sample without CBP, is consistent with the increased distance of energy donor–acceptor molecule and elimination of charge transfer.

In summary, we confirm the presence of FRET from HB194 to SubNc and potentially unfavourable energetic alignment for electron transfer and favourable alignment for hole transfer between the two molecules based on IEs and EAs measured on pristine molecular films.

5.4.3.2 SubNc and DCV3T

As shown in Figure 5.14a, DCV3T exhibits an EA and IE offset of 0.40±0.66 eV and 0.85±0.22 eV, respectively, relative to SubNc. This energetic alignment indicates that both electron and hole transfer between SubNc and DCV3T are energetically favourable, with hole transfer from DCV3T to SubNc likely to be more efficient. Similar to SubNc/HB194 pair, SubNc and DCV3T also exhibit strong spectral overlap between their absorption and PL emission spectra, as shown in Figure 5.14b. And their spectral overlap integral J was calculated to be 1.37×10^{16} mol^{-1} L cm^{-1} nm^4, indicating that efficient FRET is expected.

Figure 5.14c compares the PL spectrum of the quenched sample with those of the reference pristine films, without the CBP blocking layer. The results are qualitatively similar to the SubNc/HB194 pair, but with more pronounced quenching: the DCV3T PL signal is strongly quenched (96%) across its entire emission range, with the most significant reduction between 550 and 700 nm, consistent with the SubNc absorption window. A slight SubNc PL enhancement peaking near 740 nm is also observed. The DCV3T quenching likely originates from FRET and hole transfer to SubNc, consistent with the large IE offset.

The PL spectrum of stack with a CBP blocking layer in between is shown in Figure 5.14d. The DCV3T PL signal remains strongly quenched (quenching ratio of 83%), while a more pronounced increase in SubNc PL is observed, again peaking at 740 nm. This confirms that

the observed PL quenching is primarily induced by FRET and very efficient.

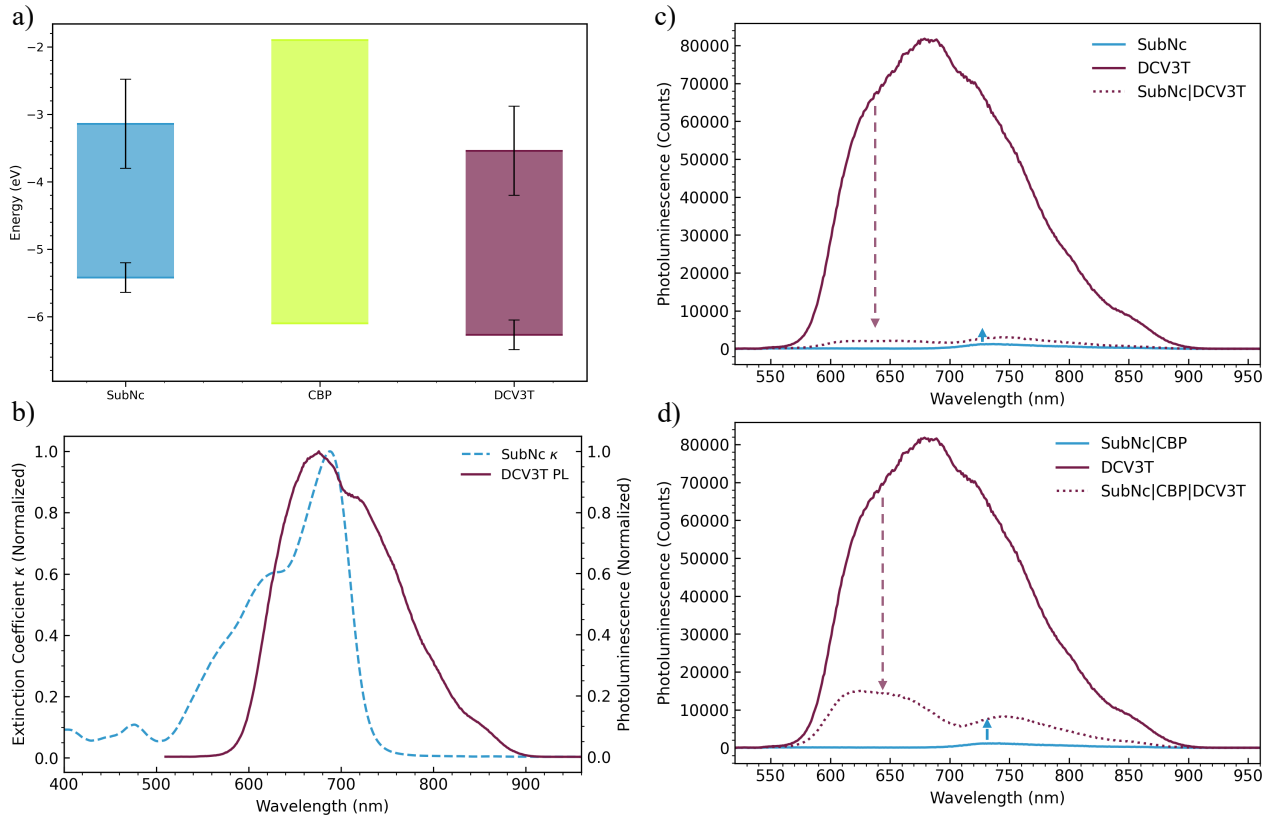


Figure 5.14: (a) Schematic energy levels of pristine SubNc, CBP, and DCV3T films. (b) Extinction coefficient (κ) spectrum of SubNc (blue dashed line) and steady-state photoluminescence (PL) spectrum of DCV3T (violet solid line). (c) PL spectra of samples comprising 20 nm pristine SubNc (blue line), 3 nm pristine DCV3T (violet solid line), and 3 nm DCV3T deposited on top of 20 nm SubNc (violet dotted line). (d) PL spectra of samples comprising 3 nm CBP on top of 20 nm SubNc (blue line), 3 nm pristine DCV3T (violet solid line), and glass|20 nm SubNc|3 nm CBP|3 nm DCV3T (violet dotted line). All PL spectra were measured with 510 nm laser excitation from the film side.

In summary, efficient FRET from DCV3T to SubNc is confirmed, with possible efficient electron and hole transfer between the two molecules based on IE and EA values measured on pristine films.

5.4.3.3 DTDCTB and DCV3T

As shown in Figure 5.15a, DTDCTB has slightly larger EA (∼0.1 eV) than DCV3T, which could create an energetic barrier for electron transfer. The IE offset between the two molecules is approximately 1 eV, which is favourable for efficient hole transfer. This energetic alignment suggests that hole transfer from DCV3T to DTDCTB is energetically favourable, while electron

transfer may be hindered. Similarly, DTDCTB and DCV3T show a broad spectral overlap between their absorption and PL emission spectra, as shown in Figure 5.15b. And their spectral overlap integral J was calculated to be 1.09×10^{16} mol^{-1} L cm^{-1} nm^4, indicating that very efficient FRET is expected.

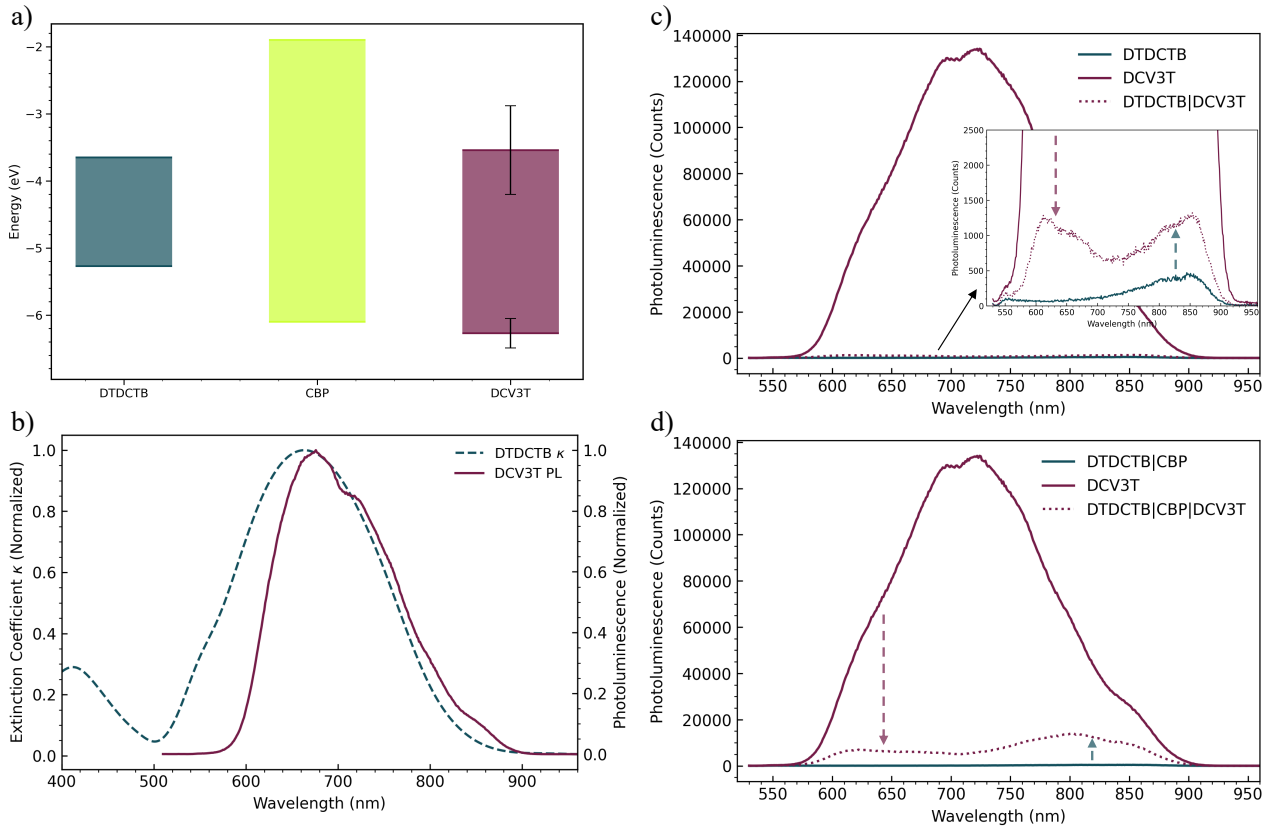


Figure 5.15: (a) Schematic energy levels of pristine DTDCTB, CBP, and DCV3T films. (b) Extinction coefficient (κ) spectrum of DTDCTB (green dashed line) and steady-state photoluminescence (PL) spectrum of DCV3T (violet solid line). (c) PL spectra of samples comprising 20 nm pristine DTDCTB (green line), 3 nm pristine DCV3T (violet solid line), and 3 nm DCV3T deposited on top of 20 nm DTDCTB (violet dotted line). (d) PL spectra of samples comprising 3 nm CBP on top of 20 nm DTDCTB (green line), 3 nm pristine DCV3T (violet solid line), and glass|20 nm DTDCTB|3 nm CBP|3 nm DCV3T (violet dotted line). All PL spectra were measured with 510 nm laser excitation from the film side.

Figure 5.15c,d shows the PL spectra for the DTDCTB/DCV3T pair without and with the CBP blocking layer, respectively. The behaviour is similar to the previous pairs: DCV3T PL is very strongly quenched (99% without CBP, 89% with CBP) across 550–750 nm, within the DTDCTB absorption window, and a slight DTDCTB PL enhancement peaking near 850 nm is observed in both cases (see close-up in Figure 5.15c). The high quenching ratio retained upon CBP insertion confirms dominant and highly efficient FRET from DCV3T to DTDCTB.

In summary, these results confirm the occurrence of efficient FRET from DCV3T to DT-DCTB, with possible efficient hole transfer and inefficient electron transfer between the two molecules based on IEs and EAs measured on pristine films.

5.4.3.4 SubPc and DCV3T

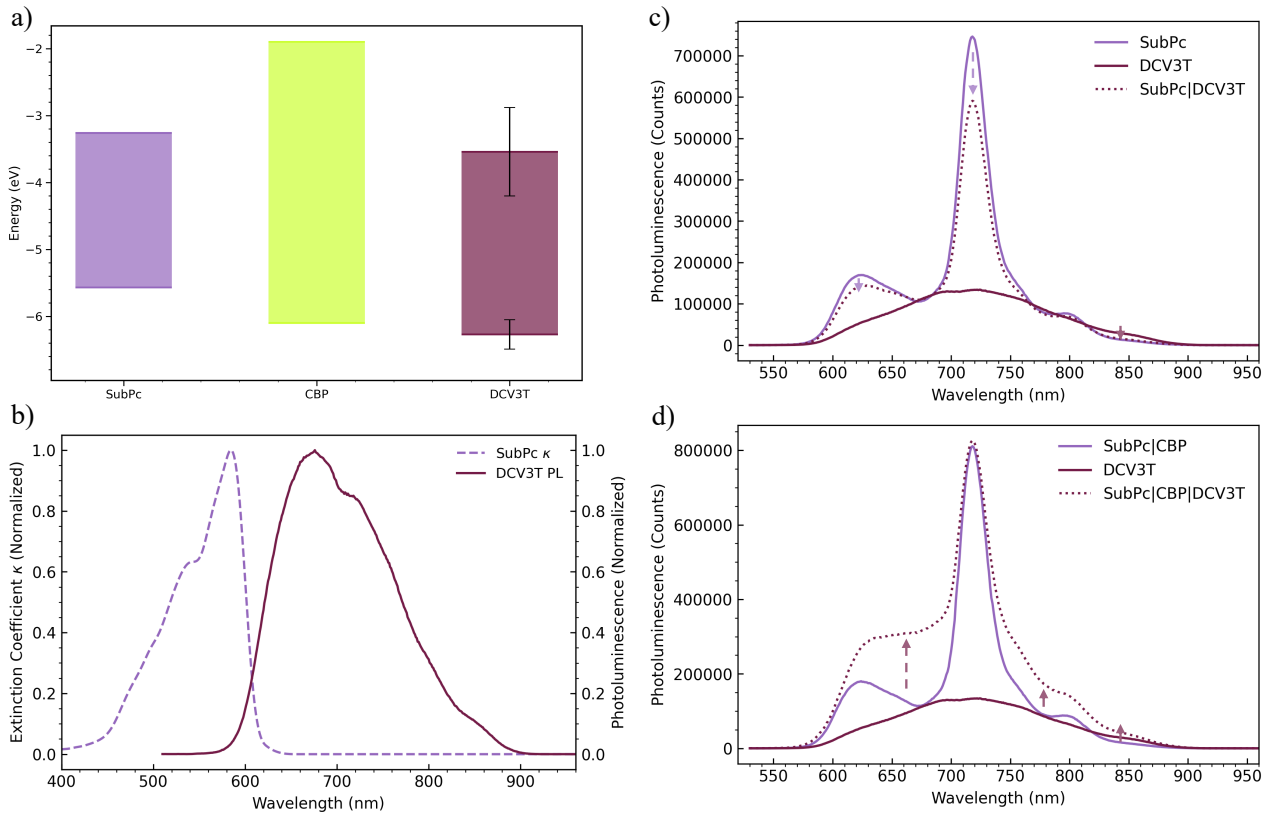


Figure 5.16: (a) Schematic energy levels of pristine SubPc, CBP, and DCV3T films. (b) Extinction coefficient (κ) spectrum of SubPc (purple dashed line) and steady-state photoluminescence (PL) spectrum of DCV3T (violet solid line). (c) PL spectra of samples comprising 20 nm pristine SubPc (purple line), 3 nm pristine DCV3T (violet solid line), and 3 nm DCV3T deposited on top of 20 nm SubPc (purple dotted line). (d) PL spectra of samples comprising 3 nm CBP on top of 20 nm SubPc (purple line), 3 nm pristine DCV3T (violet solid line), and glass|20 nm SubPc|3 nm CBP|3 nm DCV3T (violet dotted line). All PL spectra were measured with 510 nm laser excitation from the film side.

As shown in Figure 5.16a, SubPc exhibits an EA offset of approximately 0.3 eV with DCV3T, which is moderately favourable for electron transfer, though not necessarily sufficient. The IE offset between the two molecules is around 0.7 eV, which is energetically favourable for hole transfer from DCV3T to SubPc. This energetic alignment therefore suggests efficient hole transfer and moderate electron transfer. Unlike the previous pairs, SubPc and DCV3T exhibit

negligible spectral overlap (Figure 5.16b), with $J = 2.13 \times 10^{14}$ mol^{-1} L cm^{-1} nm^4, suggesting only limited FRET is expected.

Figure 5.16c shows the PL spectrum of SubPc/DCV3T pair without CBP blocking layer. Based on the absorption profiles of SubPc and DCV3T (Figures 5.4 and 5.7), excitation at 510 nm activates both molecules, leading to strong PL emissions from both molecules. A slight decrease in the SubPc PL signal is observed across its emission range, most notably around the peaks at 625 nm and 725 nm. This decrease may be attributed to electron transfer to DCV3T or to absorption competition between the two materials. The quenching of the DCV3T PL, likely due to hole transfer to SubPc, may be inferred from reduced intensity in the 815–890 nm region. However, no characteristic PL quenching of FRET, such a decrease in energy donor PL with corresponding increase in acceptor PL, was observed.

With the CBP blocking layer (Figure 5.16d), an overall PL increase between 580 and 900 nm is observed relative to the SubPc|CBP reference, with new non-SubPc features appearing between 620 and 680 nm, attributed to DCV3T emission as charge transfer is blocked by the CBP layer. These results further support the conclusion that no noticeable FRET occurs between SubPc and DCV3T.

In summary, these findings confirm the absence of detectable FRET between DCV3T and SubPc, with hole and electron transfer remaining energetically favourable based on IE and EA offsets.

5.4.3.5 HB194 and DCV3T

As shown in Figure 5.17a, HB194 exhibits an EA offset of 0.35 eV and IE offset of 0.46 eV with DCV3T. This energetic alignment is favourable for both hole and electron transfer, but may not be highly efficient. Similarly to the SubPc/DCV3T pair, HB194 and DCV3T exhibit limited spectral overlap (Figure 5.17b) with $J = 1.74 \times 10^{15}$ mol^{-1} L cm^{-1} nm^4, suggesting only limited FRET is expected.

Figure 5.17c shows the PL spectrum of HB194/DCV3T pair without the CBP blocking layer. As with the SubPc/DCV3T pair, excitation at 510 nm activates both molecules, producing strong PL from each. A slight decrease in HB194 PL is observed, attributable to electron transfer to DCV3T or absorption competition. In the 550–635 nm region, where the HB194

and DCV3T PL spectra do not overlap, quenching of DCV3T PL is observed, possibly from FRET or hole transfer to HB194.

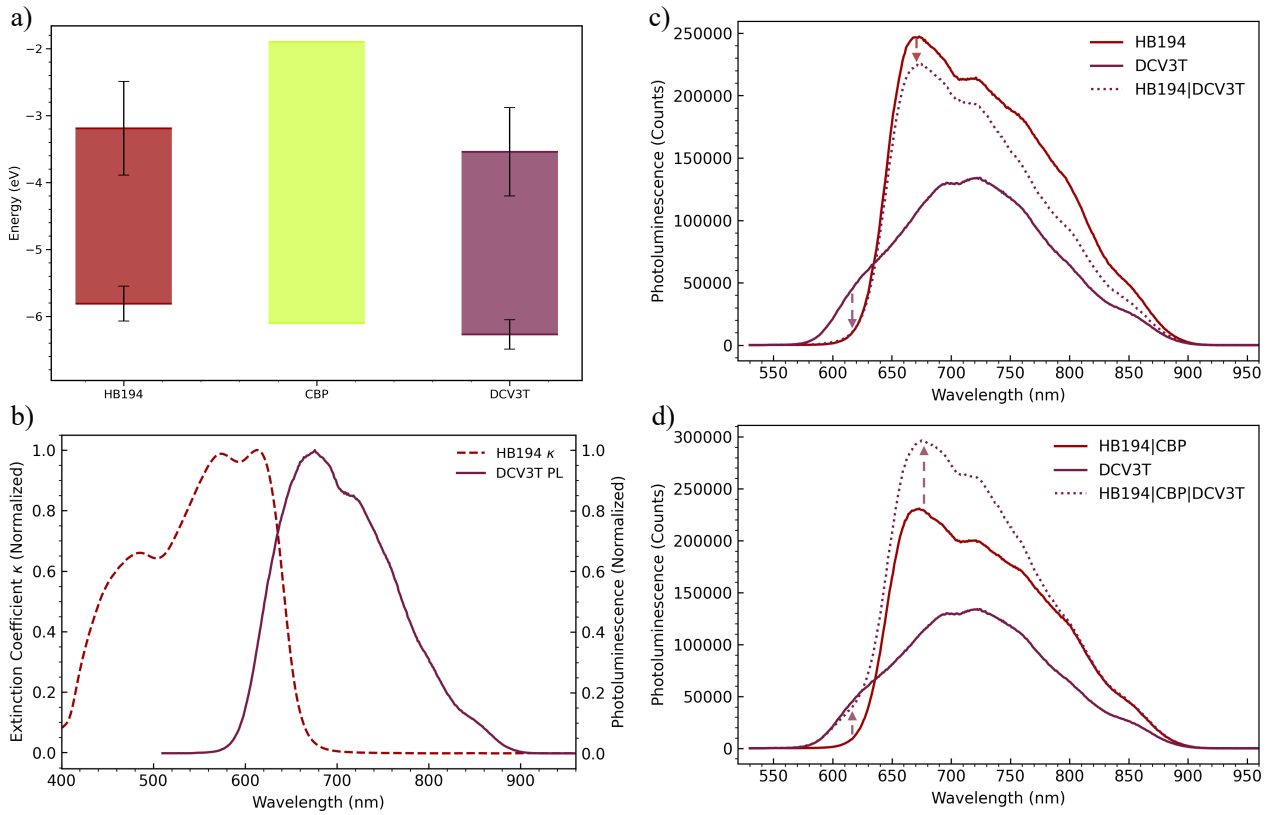


Figure 5.17: (a) Schematic energy levels of pristine HB194, CBP, and DCV3T films. (b) Extinction coefficient (κ) spectrum of HB194 (red dashed line) and steady-state photoluminescence (PL) spectrum of DCV3T (violet solid line). (c) PL spectra of samples comprising 20 nm pristine HB194 (red line), 3 nm pristine DCV3T (violet solid line), and 3 nm DCV3T deposited on top of 20 nm HB194 (violet dotted line). (d) PL spectra of samples comprising 3 nm CBP on top of 20 nm HB194 (red line), 3 nm pristine DCV3T (violet solid line), and glass|20 nm HB194|3 nm CBP|3 nm DCV3T (violet dotted line). All PL spectra were measured with 510 nm laser excitation from the film side.

With the CBP blocking layer (Figure 5.17d), an overall PL increase between 550 and 900 nm is observed relative to the HB194|CBP reference, with an additional emission feature appearing in the 550–635 nm range. This is attributed to DCV3T emission with charge transfer suppressed, indicating that the DCV3T quenching observed in Figure 5.17c arises primarily from hole transfer rather than FRET. The apparent HB194 PL enhancement in the stack with CBP is therefore attributed to addition of DCV3T PL rather than FRET.

In summary, these findings confirm the absence of detectable FRET from DCV3T to HB194, with moderately favourable conditions for hole and electron transfer based on IE and EA offsets.

5.4.4 Half Solution-Processed and Half Evaporated

For energy donor candidate that are solution processed and acceptor candidates are evaporated (hybrid), the quenched sample stacks with and without the CBP blocking layer correspond to those shown in Figure 5.11h and i, respectively. The thickness of CBP (reported roughness 1.2±0.2 nm [206]) is around 5 nm to compensate the roughness of solution processed film underneath (estimated roughness ∼2 nm [208]). A 510 nm laser was used to excite these quenched samples, along with their respective reference samples shown in Figure 5.11b, d and e, from the substrate side. This excitation geometry ensures that the energy donor molecule interacts with the incident light prior to any other layers, if present. All samples are excited with 510 nm laser to selectively excite the energy donor candidates.

Similar to the all-evaporated pairs, CBP provides an effective energetic barrier against charge transfer, as illustrated by the energy level diagrams in Figure 5.18a, 5.19a, and 5.20a. CBP is expected to provide large EA barriers to block electron transfer and significantly suppress hole transfer via its near-zero (≈0.1 eV) IE offset with FBR.

5.4.4.1 SubNc and FBR

As shown in Figure 5.18a, FBR exhibits an EA and IE offset of approximately 0.6 eV and 0.7 eV, respectively, relative to SubNc. This energetic alignment indicates that both electron and hole transfer between SubNc and FBR are energetically favourable and likely to be efficient. SubNc and FBR exhibit strong spectral overlap between their absorption and PL emission spectra, as shown in Figure 5.18b. And their spectral overlap integral J was calculated to be 1.36×10^{16} mol^{-1} L cm^{-1} nm^4, indicating that efficient FRET is expected.

Figure 5.18c compares the PL spectrum of the quenched SubNc|FBR sample with those of the reference pristine films, without the CBP blocking layer. Strong quenching of the FBR PL signal is observed across its entire emission range (quenching ratio of 93%), accompanied by only a slight SubNc PL enhancement peaking near 740 nm. The quenching of the FBR emission may arise from both FRET and hole transfer to SubNc, as suggested by the significant IE offset. Upon introducing the CBP blocking layer in between SubNc and FBR (Figure 5.18d), the FBR PL remains strongly quenched (71%), confirming that the quenching is predominantly

driven by FRET and is highly efficient.

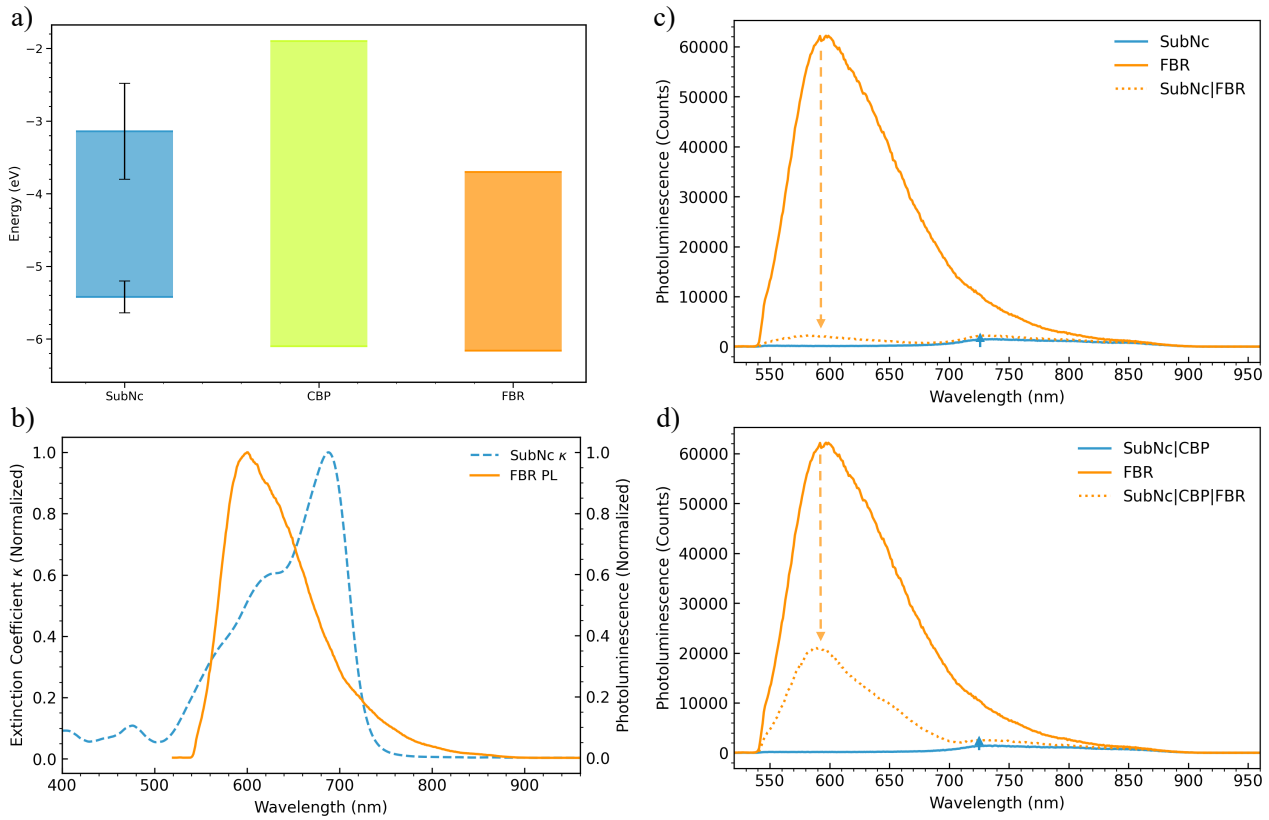


Figure 5.18: (a) Schematic energy levels of pristine SubNc, CBP, and FBR films. b Extinction coefficient (κ) spectrum of SubNc (blue dashed line) and steady-state photoluminescence (PL) spectrum of FBR (orange solid line). (c) PL spectra of samples comprising 20 nm pristine SubNc (blue line), 3 nm pristine FBR (orange solid line), and 3 nm FBR underneath 20 nm SubNc (blue dotted line). (d) PL spectra of samples comprising 5 nm CBP underneath 20 nm SubNc (blue line), 3 nm pristine FBR (orange solid line), and glass|20 nm FBR|5 nm CBP|3 nm SubNc (orange dotted line). All samples were measured with 510 nm laser excitation from the glass side.

In summary, we confirm the presence of efficient FRET from FBR to SubNc, along with a favourable energetic alignment that enables efficient electron and hole transfer between the two molecules based on IEs and EAs measured on pristine molecular films.

5.4.4.2 DTDCTB and FBR

As shown in Figure 5.19a, DTDCTB and FBR have nearly identical EA values, with an offset below 0.1 eV, and a large IE offset of approximately 0.9 eV. This energetic alignment suggests restricted electron transfer from DTDCTB to FBR, and energetically favourable hole transfer from FBR to DTDCTB. The PL emission of FBR lies entirely within the absorption region of

DTDCTB, as shown in Figure 5.19b. And their spectral overlap integral J was calculated to be 8.99×10^{15} mol^{-1} L cm^{-1} nm^4, indicating that efficient FRET is expected.

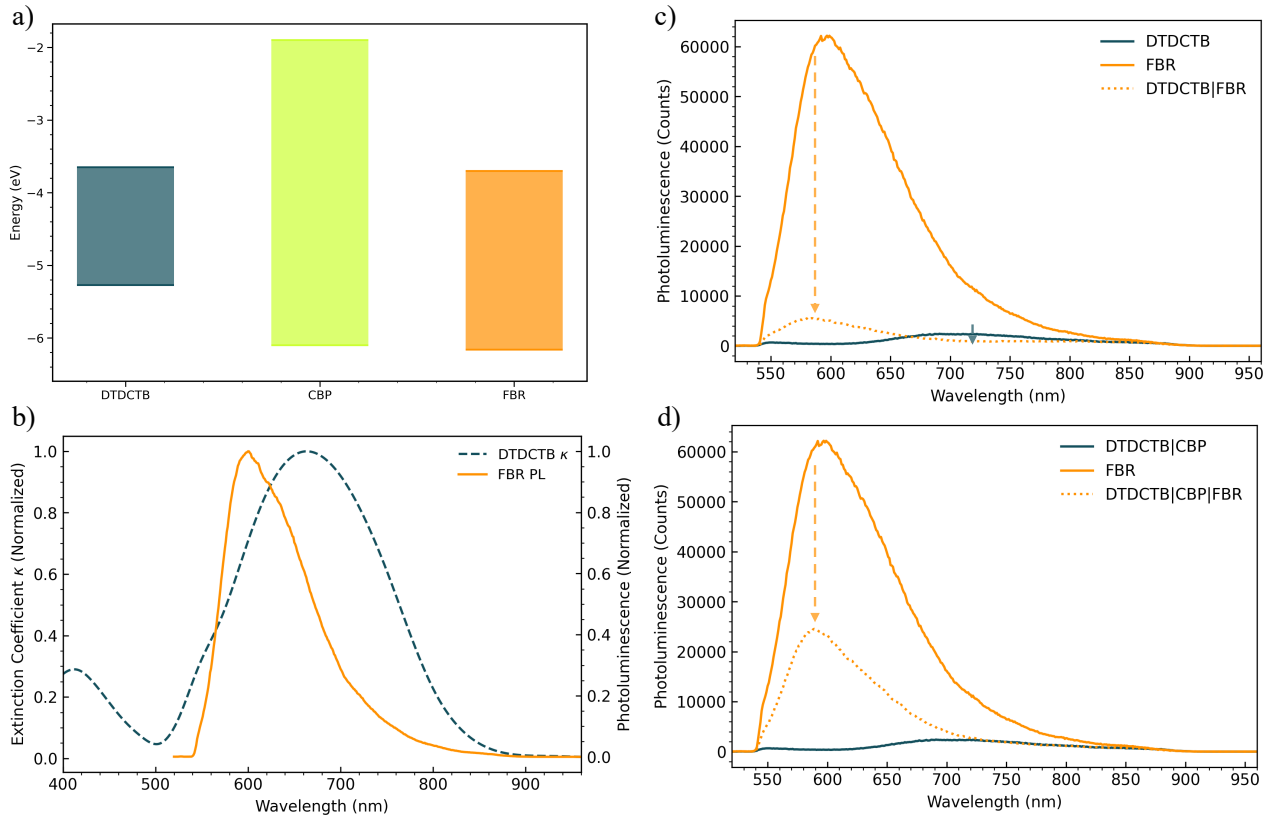


Figure 5.19: (a) Schematic energy levels of pristine DTDCTB, CBP, and FBR films. b Extinction coefficient (κ) spectrum of DTDCTB (green dashed line) and steady-state photoluminescence (PL) spectrum of FBR (orange solid line). (c) PL spectra of samples comprising 20 nm pristine DTDCTB (green line), 3 nm pristine FBR (orange solid line), and 3 nm FBR underneath 20 nm DTDCTB (green dotted line). (d) PL spectra of samples comprising 3 nm CBP underneath 20 nm DTDCTB (green line), 3 nm pristine FBR (orange solid line), and glass|20 nm FBR|3 nm CBP|3 nm DTDCTB (orange dotted line). All samples were measured with 510 nm laser excitation from the glass side.

Figure 5.19c compares the PL spectrum of the quenched DTDCTB|FBR sample with those of the reference pristine films without the CBP blocking layer. Strong quenching of the FBR PL signal is observed across its emission range, with a quenching ratio of 91%. This quenching may result from FRET and hole transfer to DTDCTB, given the substantial IE offset. Notably, a slight decrease in DTDCTB PL intensity is also observed, which is more likely due to absorption competition rather than electron transfer.

Upon introducing the CBP blocking layer in between DTDCTB and FBR (Figure 5.19d), the FBR PL remains quenched (quenching ratio of 66%). No clear increase in DTDCTB PL

was observed, likely due to the intrinsically weak emission of DTDCTB. These results confirm that the PL quenching is predominantly induced by FRET, which remains highly efficient in this configuration.

In summary, these findings confirm efficient FRET from FBR to DTDCTB, alongside energetically favourable hole transfer and restricted electron transfer between the two molecules based on IE and EA offsets.

5.4.4.3 SubPc and FBR

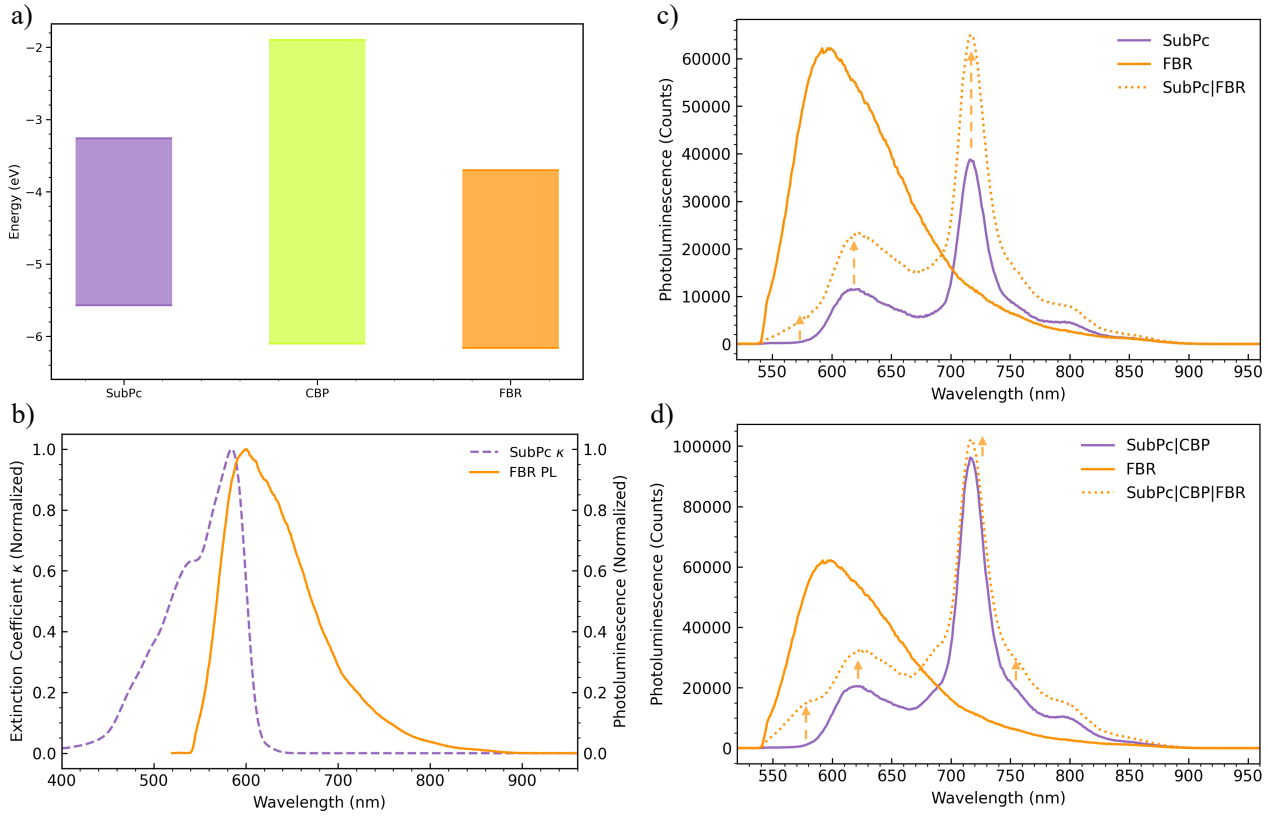


Figure 5.20: (a) Schematic energy levels of pristine SubPc, CBP, and FBR films. (b) Extinction coefficient (κ) spectrum of SubPc (purple dashed line) and steady-state photoluminescence (PL) spectrum of FBR (orange solid line). (c) PL spectra of samples comprising 20 nm pristine SubPc (purple line), 3 nm pristine FBR (orange solid line), and 3 nm FBR underneath 20 nm SubPc (purple dotted line). (d) PL spectra of samples comprising 3 nm CBP underneath 20 nm SubPc (purple line), 3 nm pristine FBR (orange solid line), and glass|20 nm FBR|3 nm CBP|3 nm SubPc (orange dotted line). All samples were measured with 510 nm laser excitation from the glass side.

As shown in Figure 5.20a, SubPc exhibits an EA offset of approximately 0.4 eV and an IE offset of approximately 0.6 eV with FBR, suggesting moderately favourable electron transfer

and highly favourable hole transfer, respectively. Some spectral overlap between the absorption spectrum of SubPc and the FBR PL emission is observed in 540-640 nm region (Figure 5.20b), with spectral overlap integral $J = 3.38 \times 10^{15}$ mol^{-1} L cm^{-1} nm^4, approximately half of the value for DTDCTB/FBR pair, suggesting weaker FRET is expected.

Figure 5.20c compares the PL spectrum of the SubPc|FBR sample with those of the reference pristine films, without a CBP blocking layer. Based on the absorption profiles of SubPc and FBR (Figures 5.4 and 5.8), excitation at 510 nm activates both molecules, resulting in strong PL emissions from both. A substantial enhancement in the SubPc PL signal is observed for the SubPc|FBR stack, particularly at the characteristic peaks near 640 nm and 740 nm, which can be attributed to FRET from FBR. Additionally, a new feature appears between 550 nm and 590 nm, likely originating from quenched FBR PL. This quenching could arise from both FRET and hole transfer.

Upon introducing the CBP blocking layer in between SubPc and FBR (Figure 5.20d), a weaker SubPc PL enhancement is observed alongside a more pronounced FBR signal between 540 and 590 nm, indicating reduced FRET efficiency relative to the quenched stack without CBP layer. Interestingly, the PL intensity of the SubPc|5 nm CBP sample is substantially higher than that of pristine SubPc, which we attribute to optical effects that enhance emission. Such enhancement is not observed in the SubPc|3 nm CBP stack, suggesting a thickness-dependent optical cavity effect.

In summary, these findings confirm the occurrence of FRET from FBR to SubPc and support energetically favourable conditions for both hole and electron transfer between the two molecules based on IE and EA offsets.

5.5 Conclusions

In summary, organic semiconducting molecules (solution-processed and vacuum-evaporated) exhibiting high absorption coefficients and, where possible, high charge carrier mobilities and PLQY were selected. These molecules were characterised thoroughly, through steady-state PL, PLQY, SE, and UPS/IPES. Additionally, their charge carrier mobilities were compiled from the literature. These molecules were further categorised into electron donor and acceptor.

The electron acceptor molecules were chosen to have deep IEs and EAs, as well as the degree of spectral overlap between their emission spectra and the absorption spectra of the pairing electron donor molecules. The electron donor molecules, in turn, were selected to span a range of IEs and EAs to facilitate systematic investigation of energy level alignment effects.

Table 5.5 summarises the ΔIE, ΔEA, spectral integral J and occurrence of FRET for the molecular pairs. Based on IE and EA values obtained from pristine films, we identified molecular pairs capable of supporting barrier-less charge transfer. The pairs enabling both barrier-less hole and electron transfer include: SubNc/DCV3T, SubPc/DCV3T, HB194/DCV3T, SubNc/FBR, and SubPc/FBR. Pairs that support barrier-less hole transfer alone include: SubNc/HB194, DTDCTB/DCV3T, and DTDCTB/FBR. SubNc/DCV3T and SubNc/FBR are most likely to form well-performing OSCs.

Table 5.5: Summary of the ionisation energy difference (IE_D–IE_A), electron affinity difference (EA_D–EA_A), spectral overlap integral J (between electron acceptor emission and donor absorption; normalised PL used for J calculation), and whether efficient FRET was observed via photoluminescence quenching for the studied electron donor–acceptor molecular pairs.

Donor	Acceptor	IE_D-IE_A (eV)	EA_D-EA_A (eV)	J (mol^{-1} L cm^{-1} nm^4)	Efficient FRET
SubNc	HB194	0.41	0.05	1.44×10^{16}	Yes
SubNc	DCV3T	0.85	0.40	1.37×10^{16}	Yes
DTDCTB	DCV3T	1.00	-0.11	1.09×10^{16}	Yes
SubPc	DCV3T	0.7	0.28	2.13×10^{14}	No
HB194	DCV3T	0.46	0.35	1.74×10^{15}	No
SubNc	FBR	0.74	0.56	1.36×10^{16}	Yes
DTDCTB	FBR	0.89	0.05	8.99×10^{15}	Yes
SubPc	FBR	0.59	0.44	3.38×10^{15}	Yes

Using the measured PL and κ spectra, donor–acceptor combinations with spectral overlap suitable for FRET were identified. To verify the presence of FRET experimentally, PL quenching studies were performed using custom-designed film stacks incorporating a 3–5 nm CBP blocking layer to isolate FRET from competing CT processes. The occurrence of FRET was confirmed by simultaneous quenching of energy donor PL and enhancement of acceptor emission upon donor excitation. Efficient FRET was observed in several systems, including HB194→SubNc, DCV3T→SubNc, DCV3T→DTDCTB, FBR→SubNc, and FBR→DTDCTB and FBR→SubPc. In contrast, DCV3T→SubPc and DCV3T→HB194 exhibited no measur-

able FRET.

These characterisations enabled the selection of two sets of molecular pairs for further solar cell device studies: fully evaporated and hybrid (half solution-processed, half evaporated). This allows a systematic investigation of how FRET and energetic offsets influence device performance. In the first (fully evaporated) set, the pairs SubNc/DCV3T, SubNc/HB194, and DTDCTB/DCV3T exhibit efficient FRET and span a range of EA offsets, from large positive (strong driving force), to near-zero, to negative (energetic barrier). By contrast, the pairs SubPc/DCV3T and HB194/DCV3T show no detectable FRET but possess favourable IE and EA offsets conducive to charge transfer. In the second (hybrid) set, where SP NFA was used directly with VTE electron donors, SubNc/FBR, DTDCTB/FBR and SubPc/FBR all exhibit efficient FRET, with EA offsets ranging from large positive to near-zero. Among these, SubNc/DCV3T and SubNc/FBR were identified as the molecular pairs that most closely resemble high-performance solution-processed NFA OSC systems. These pairs exhibit: (1) high absorption coefficients for both molecules; (2) high PLQY for the electron acceptor (ideally for both molecules); (3) efficient FRET from the high-gap to the low-gap molecule; and (4) sufficiently large EA offsets (greater than 0.4 eV, ideally above 0.5 eV), making them promising candidates for efficient OSCs.

Chapters 6 and 7 will present detailed investigations into the photovoltaic application of these molecular systems and explorations of the underlying physics.

6 | Exploiting FRET in Evaporated OSCs

Studies on fullerene-based systems have established that both radiative (ΔV_{oc}^{rad}) and non-radiative (ΔV_{oc}^{nr}) voltage losses are closely related to the energy of the charge transfer (CT) state and its offset ($\Delta E_{S1,CT}$) from the lowest singlet excited state (S_1). A smaller $\Delta E_{S1,CT}$ typically leads to reduced ΔV_{oc}^{rad} and ΔV_{oc}^{nr}, but often at the expense of efficient exciton separation. In contrast, high-performing solution-processed (SP) non-fullerene acceptor (NFA) organic solar cells (OSCs) tend to exhibit low $\Delta E_{S1,CT}$, ΔV_{oc}^{rad} and ΔV_{oc}^{nr}, while maintaining efficient exciton dissociation, resulting in significantly improved device performance compared to fullerene systems. A major area of ongoing research is therefore to assess whether the trade-off between minimising voltage losses (ΔV_{oc}) and sustaining high photocurrents still applies to NFA-based OSCs and what characteristics in these OSCs contribute to their high-performance [39, 40, 98, 134].

This chapter presents a systematic investigation of fully evaporated OSC devices incorporating NFAs, designed to emulate the beneficial characteristics of high-performing SP NFA OSCs. Molecular pairs with varying ionisation energy (IE)/electron affinity (EA) offsets and differing Förster resonance energy transfer (FRET) compatibility are selected to explore how these factors influence device performance and voltage losses. Planar heterojunction (PHJ) devices are fabricated across all selected molecular pairs, complemented by bulk heterojunction (BHJ) devices based on the best-performing system.

In the fully evaporated PHJ systems, transient absorption spectroscopy (TAS) (measured and analysed by Dr Demetra Tsokkou (Bern)) confirms efficient FRET in SubNc:DCV3T and DTDCTB:DCV3T blends, with hole transfer suppressed by the FRET process, while efficient subsequent charge generation requires a sufficiently large EA offset. Despite varying IE and EA offsets, all PHJ devices exhibit low $\Delta E_{S1,CT}$ characteristics in their external quantum efficiency (EQE) and electroluminescence (EL) (measured by Dr Zhongcheng Yuan (Oxford))

spectra, with no clearly resolvable CT emission. Voltage loss decomposition reveals consistently low ΔV_{oc}^{rad} across all systems, independent of FRET. SubNc/DCV3T achieves the best performance (power conversion efficiency (PCE) ∼3.5%), while DTDCTB/DCV3T, despite supporting FRET,exhibits extremely poor performance due to its negative EA offset, highlighting that FRET without efficient subsequent charge transfer constitutes an energy loss channel. Additionally, HB194 is investigated as an additional electron acceptor in a trilayer PHJ architecture. The trilayer α-6T|SubNc|HB194 device achieves a PCE of 5.3% with ∼30% improvements in J_{sc} and FF relative to the α-6T|SubNc reference without open-circuit voltage (V_{oc}) sacrifice. General molecular criteria for selecting a second electron acceptor to improve PHJ device performance are also proposed.

Finally, SubNc:DCV3T BHJ devices are investigated across donor:acceptor (D:A) volume ratios from 1:0.5 to 1:5. The best-performing 1:1 blend achieves an V_{oc} of 1.07 V and a total voltage loss of 0.64 V, lower than any reported value for fullerene-based evaporated BHJ OSCs, with ΔV_{oc}^{nr} comparable to state-of-art SP NFA OSCs. However, PCE remains limited by low charge carrier mobility and unfavourable edge-on molecular orientation, as confirmed by Grazing Incidence Wide-angle X-ray Scattering (GIWAXS) (analysed by Olivia Gough (Oxford)). A correlation between elevated ΔV_{oc}^{nr}, higher energetic disorder, and smaller crystallite size is proposed from comparison of the 1:1 and 1:5 blends. Overall, these results demonstrate a successful example of replicating low-$\Delta E_{S1,CT}$ CT state characteristics in a VTE BHJ OSC, while highlighting that achieving high device performance ultimately requires new evaporable NFAs with optimised optical, electronic, and morphological properties.

A manuscript based on the data presented in Sub-chapter 6.3 is in preparation and will be submitted by M. Zhu, N. Evans, P. Kaienburg, K. Meerholz, S. Olthof, M. Riede. Section 6.2.2 and Sub-chapter 6.4 are based on manuscript submitted to Journal of Physics D: Applied Physics, by M. Zhu, D. Tsokkou, O. Gough, K. Trinkaus, N. Evans, P. Kaienburg, K. Meerholz, S. Olthof, N. Banerji, M. Riede, Low-Voltage-Loss Vacuum-Deposited BHJ Organic Solar Cells with DCV3T. Text and figures were reproduced or adapted.

6.1 Introduction

Recent advances in NFA materials and refined microstructural control have successfully boosted the PCE of single-junction OSCs to 20% [20]. However, most of these achievements have been limited to SP OSCs. In contrast, VTE OSCs, despite their commercial promise, remain underrepresented in research and have largely plateaued at PCEs around 10%, typically employing fullerene-based acceptors [209]. The highest-performing evaporated bulk BHJ fullerene systems are mainly based on C_{70} [209–211], which provides strong absorption in the 300–550 nm range, complementing the spectra of common electron donors [212]. However, C_{70} currently are not commercially relevant given their cost. Nevertheless, these systems suffer from substantial V_{oc} losses, typically ranging from 0.67 to 1.1 V [126]. Fullerene-free PHJ OSCs have shown promising results, with reported PCEs up to 8.4%, but they also exhibit high voltage losses of around 0.74 V [146].

For instance, several champion devices achieving PCEs of approximately 19% report total voltage losses as low as 0.55 V while still maintaining EQE of over 80% [24]. These low losses have been thought to be attributed to small energetic offsets between E_{S1} and E_{CT}, with $\Delta E_{S1,CT}$ typically below 100 meV [39, 41, 77]. Additionally, high ϕ_{PL} of low-gap acceptor molecules in these blends have been identified as crucial [40, 41]. A hallmark of such low-$\Delta E_{S1,CT}$ systems, distinct from conventional fullerene-based devices, is the absence of discernible CT state absorption in the sub-gap region of EQE spectra. Instead, the EQE exhibits an exponential decay at the low-energy tail [39, 118]. These findings raise questions about whether the long-established trade-off between low voltage losses and high photocurrent still holds, and whether $\Delta E_{S1,CT}$ can appropriately describe the driving force for charge separation in high-performance NFA OSCs.

Due to the spectral indistinguishability between S_1 and CT states, it has become increasingly difficult to determine $\Delta E_{S1,CT}$ experimentally in NFA systems, unlike in fullerene systems, where robust methods exist. As a result, many studies resort to using the IE and EA offsets of pristine donor and acceptor molecules as proxies to quantify the interfacial driving forces for charge separation. Earlier studies claimed 'zero' IE [77, 213, 214] and EA [215–217] offsets for a few high-performing NFA OSCs based on values measured by CV. However, CV does

not reliably reflect the solid-state energy levels, particularly for polymers [59,218]. In contrast, UPS and IPES measurements have revealed that many so-called 'zero-offset' systems actually possess substantial offsets. For instance, a 0.5 eV IE offset was found in the PM6:Y6 blend via UPS, despite earlier CV measurements indicating a near-zero offset [219].

Moreover, in many high-efficiency NFA OSCs, free charge generation predominantly occurs via hole transfer from the acceptor to the donor, following ultrafast exciton FRET from donor to acceptor upon donor excitation. An IE offset of approximately 0.5 eV has been shown to be important for efficient exciton separation in such systems [39]. Furthermore, device performance, especially FF and IQE, has been found to correlate positively with larger IE offsets [39]. These insights collectively emphasise the importance of accurately determining solid-state IE and EA values in low-$\Delta E_{S1,CT}$ NFA systems and correctly identifying which offset matters, for understanding and optimising exciton separation and overall device performance.

These insights, derived from solution-processed NFA OSCs, highlight key molecular properties associated with achieving low voltage losses and high PCEs. It is therefore of interest to explore whether such design principles can be extended to VTE, fullerene-free OSC systems. Several characteristics have been identified in state-of-art SP NFA systems:

a. Strong absorption by both donor and acceptor;

b. High ϕ_{PL} for both components in pristine films;

c. Efficient FRET from the high-gap to the low-gap molecule;

d. IE or EA offsets exceeding 0.5 eV, depending on the direction of FRET;

e. High ($\sim 10^{-2}$ cm^2 V^{-1} s^{-1}) and balanced charge carrier mobilities.

Due to the limited development of VTE-compatible materials, it remains challenging to find molecular pairs that simultaneously meet all five criteria. Therefore, in this thesis, molecular pairs that support efficient FRET from one molecule to the other are selected. This enables a charge generation pathway similar to that found in NFA systems: a two-step mechanism involving efficient FRET from high-gap to low-gap molecule, followed by charge transfer from low-gap molecule back to high-gap molecule upon excitation of high-gap molecule. In such

systems, the efficiency of charge transfer from low-gap to high-gap molecule therefore becomes decisive to device performance.

In this chapter, a first step towards applying and testing the design strategies established for SP NFA OSCs to VTE systems are taken. Four highly absorbing small molecules, SubNc [174], SubPc [174], HB194 [189], and DTDCTB [187], are selected as electron donors, and DCV3T [172, 220] is selected as the primary electron acceptor. In addition, HB194 is also studied as an electron acceptor for SubNc. For comparison, the systems with SubPc and HB194 as electron donor, unlike the others, does not support efficient FRET while exhibits relatively large IE and EA offsets (>0.28 eV), enabling both hole and electron transfer. All other systems support efficient FRET from electron acceptor to donor, with measured IE offsets >0.41 eV and EA offsets ranging from –0.11 to 0.40 eV, as confirmed by photoluminescence quenching and UPS/IPES measurements explained in Chapter 5. While the charge carrier mobilities of these molecules are generally lower than those in SP NFA systems, most fall within the range of 10^{-4}–10^{-6} cm^2 V^{-1} s^{-1}.

In Sub-chapter 6.2, these selected molecular pairs are investigated in PHJ device architectures to ensure simple, well-defined D-A interfaces. TAS is used to study 1:1 (by vol) blend films of these pairs, confirming the dominant charge generation pathways and their efficiencies. SubNc|DCV3T system, with the largest EA offset and best mobilities, achieves a device with highest PCE of ∼3.5%, with low $\Delta V_{oc}^{rad} \approx 26$ mV and $\Delta V_{oc}^{nr} \approx 280$ mV. These voltage losses are comparable to those of leading NFA systems, although J_{sc} and FF remains lower. Low mobilities and potential unfavourable interfacial orientation are identified to be responsible for low J_{sc} and FF. Further analyses of EL and EQE spectra suggest the presence of low-energy emissive states, distinct from CT states, that may contribute to additional non-radiative voltage losses.

Sub-chapter 6.3 present a trilayer PHJ architecture based on the SubNc|HB194 FRET pair, which has a near-zero EA offset of 0.05 eV, identified from IPES measurements on pristine films. This system is introduced to evaluate whether HB194 can function as an second electron acceptor to replace SubPc in the trilayer PHJ structure originally proposed by Cnops *et al.* [146]. The trilayer configuration enables broader spectral harvesting via FRET transfer to the main acceptor layer, without sacrificing V_{oc}. The proposed HB194 trilayer device achieves a high PCE

of ∼5.3%, with a total voltage loss of 0.77 V, with J_{sc} and FF improved by ∼30% compared to bilayer reference without HB194. The results conclude a general guidance to enhance J_{sc} and FF without compromising V_{oc} for a functional binary PHJ OSC, a third acceptor layer should (i) possess an EA level similar to the original acceptor, (ii) support efficient FRET to the original acceptor, and (iii) exhibit comparable or superior electron mobility than the original acceptor.

In Sub-chapter 6.4, the champion device from Sub-chapter 6.2, the SubNc/DCV3T pair, is reconfigured into a BHJ device configuration to assess its performance under more practical conditions. Device SubNc:DCV3T 1:1 (by vol) blend yields a functional device with PCE of over 2.5% and a record-low total voltage loss of 0.64 V, lower than any reported value for fullerene-based BHJ OSCs. GIWAXS studies on blends with different D:A ratios is conducted to look for the connection between molecular packing and ΔV_{oc}^{nr}. The findings confirm the feasibility of achieving low-voltage-loss evaporated BHJ OSCs by adopting strategies established for solution-processed NFA systems. However, they also highlight the critical need for newly designed VTE NFAs with optimised optical, electronic, and morphological properties in order to achieve competitive PCEs.

6.2 Application of FRET in Bi-Layer Planar Heterojunction OSCs

6.2.1 Materials and Devices

The thin-film samples for TAS were deposited on quartz substrates, with each molecule evaporated at a nominal rate of 0.25 Å/s. An exception was made for the DTDCTB|DCV3T blend, where a lower rate of 0.20 Å/s per molecule was used to ensure stable evaporation.

PHJ solar cells were fabricated following methods described in Chapter 4.2 using the following electron donor and acceptor combinations in the active layer: SubNc|HB194, SubNc|DCV3T, DTDCTB|DCV3T, SubPc|DCV3T, and HB194|DCV3T. A device consists of 24 nm pristine SubNc as active layer was also fabricated in same device stack. The device stack was constructed as follows: ITO (135 nm)|PEDOT:PSS (∼25 nm)|electron donor (20 nm)|electron

acceptor (20 nm)|BPhen (8 nm)|Ag (120 nm), which was shown in Chapter 4.2.5. The nominal evaporation rate for the molecules in active layer was set to 0.25 Å/s, except for DTDCTB, which was deposited at 0.20 Å/s to maintain stable deposition. BPhen and Ag were evaporated at rates as described in Chapter 4.2.2.

6.2.2 TAS Analysis

The thin film samples for TAS were prepared by the author in Oxford. All TAS measurements and analyses presented in this section were performed by Dr Demetra Tsokkou (Bern) under the supervision of Prof Natalie Banerji. Figures of TAS spectra are provided by Dr Demetra Tsokkou, implemented by the author. The TAS results for the SubNc:DCV3T blend were rewritten based on the analyses by Dr Demetra Tsokkou for the submitted manuscript "Low-Voltage-Loss Vacuum Deposited BHJ Organic Solar Cells with DCV3T as Non-Fullerene Acceptor". The remaining systems were summarised by the author from analyses by Dr Demetra Tsokkou.

6.2.2.1 FRET Pairs

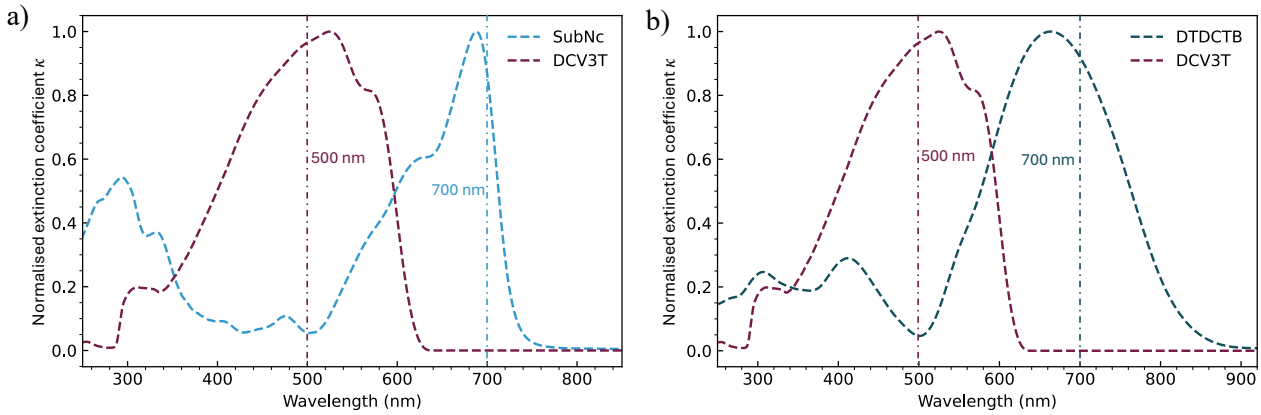


Figure 6.1: Normalised extinction coefficient spectra of (a) SubNc and DCV3T, and (b) DTDCTB and DCV3T, with the excitation wavelengths used for transient absorption spectroscopy (TAS) measurements indicated. The dot-dashed lines in each figure, labelled with corresponding wavelengths, denote the pump photon excitation energies applied to the SubNc:DCV3T and DTDCTB:DCV3T blend thin films during TAS measurements.

Previously with PL quenching measurements, efficient FRET for DCV3T→SubNc and DCV3T →DTDCTB were confirmed, with large spectral overlap integrals of 1.37×10^{16} and 1.09×10^{16} $mol^{-1}L\ cm^{-1}\ nm^4$, respectively. Based on the IE and EA values of the pristine films, it is hypothesised that the SubNc:DCV3T blend allows efficient electron and hole transfer, whereas the DTDCTB:DCV3T blend exhibits a barrier to electron transfer but allows efficient hole transfer. However, it remains unclear whether the two-step exciton separation dynamics, i.e., FRET from the electron acceptor to donor followed by electron transfer back to the acceptor, dominates over hole transfer in these two systems upon electron acceptor excitation.

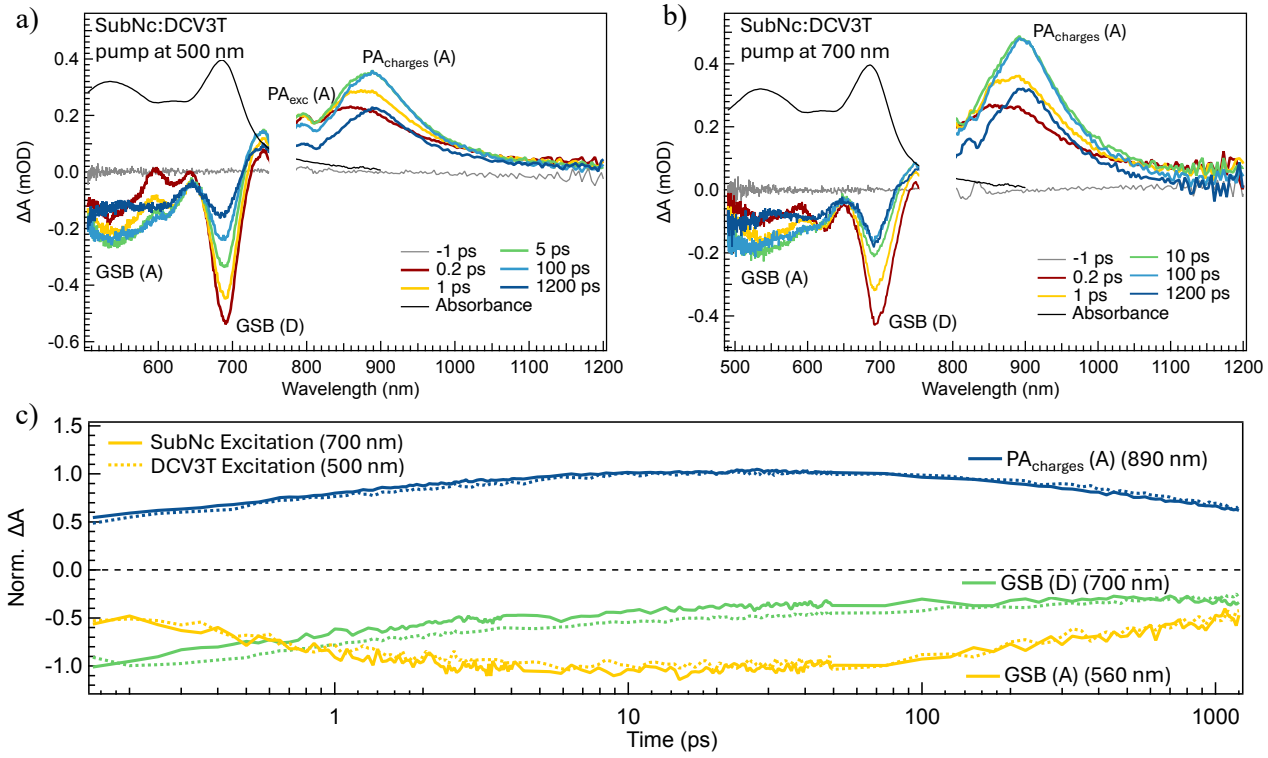


Figure 6.2: Transient absorption spectra of the SubNc(D):DCV3T(A) (1:1 by vol) blend at various time delays upon (a) DCV3T and (b) SubNc photoexcitation with 500 nm and 700 nm pulses, respectively, at an absorbed pump fluence 2.7 $\mu J/cm^2$. Negative bands at 560 nm and 700 nm correspond to ground-state bleaching (GSB) of DCV3T and SubNc, respectively, denoted as GSB (A) and GSB (D). The positive band at 800 nm is attributed to photoinduced absorption from DCV3T excitons (PA_{exc} (A)), while the band at 890 nm corresponds to photoinduced absorption from charges in DCV3T ($PA_{charges}$ (A)). (c) Comparison of normalised absorption dynamics at 560 nm (GSB (A)), 700 nm (GSB (D)), and 890 nm (PA (A)) under both SubNc and DCV3T excitation. Spectral gaps in (a) and (b) are due to pump beam scattering. The spectra were measured by Dr Demetra Tsokkou (Bern), and the figures were plotted by Dr Tsokkou with implementation contributions from the author.

To address this, TAS was employed to investigate the occurrence and timescale of FRET

from the electron acceptor to donor molecules. Figure 6.1 presents the normalised κ spectra of pristine SubNc, DTDCTB, and DCV3T films, along with the TAS pump excitation wavelengths. These show that 500 nm and 700 nm pump pulses selectively excite DCV3T and SubNc (or DTDCTB), respectively. Figures 6.2 and 6.3 show the TAS results for SubNc:DCV3T and DTDCTB:DCV3T (both 1:1 by vol) following (a) 500 nm excitation, which primarily excites the electron acceptor (DCV3T), and (b) 700 nm excitation, which selectively excites the electron donor (SubNc or DTDCTB).

In the SubNc:DCV3T blend, upon SubNc excitation (Figure 6.2b), electron transfer from SubNc to DCV3T is expected. The TAS spectra reveal a negative GSB band at 700 nm corresponding to SubNc's steady-state absorption (denoted GSB (D)), indicating direct depletion of the donor ground-state population. A delayed rise (within 10 ps) of the GSB in the 500–600 nm region, associated with DCV3T (GSB (A)), is observed along with the emergence of a positive band at 890 nm, assigned to photoinduced absorption (PA) from charges in DCV3T ($PA_{charges}$ (A)). No distinct PA features from SubNc are observed, possibly due to spectral overlap or falling outside the detection window.

Upon selective excitation of DCV3T (Figure 6.2a), it is observed that the GSB (A) is present very early, but notably the GSB (D) also rises rapidly, peaking at 0.2 ps despite minimal direct excitation. This indicates ultrafast FRET or hole transfer from DCV3T to SubNc, both of which would deplete the SubNc ground state. The slower rise of the GSB (A) and $PA_{charges}$ (A), consistent with dynamics under SubNc excitation, suggests electron transfer from FRET-generated excited SubNc to DCV3T within 10 ps. An additional positive band at 800 nm can be attributed to excitons in DCV3T (PA_{exc} (A)). This is further supported by the similar temporal profiles of GSB (D), GSB (A), and $PA_{charges}$ (A) under both excitations (Figure 6.2c). These results confirm that FRET from DCV3T to SubNc occurs within the instrument's temporal resolution (1.5 ns), followed by efficient electron transfer back to DCV3T. Hole transfer is suppressed due to the dominance of the FRET pathway.

In contrast, for the DTDCTB:DCV3T blend, electron transfer from DTDCTB to DCV3T is energetically unfavourable. Upon donor excitation (Figure 6.3b), a fast rise negative GSB (D) band at 670 nm and a PA (D) band between 550–600 nm are observed, corresponding to direct excitation and photogenerated charges in DTDCTB. However, there is no signal from

long-lived species at later times (>100 ps) and no GSB (A) and $PA_{charges}$ (A) signals from DCV3T, suggesting the absence of FRET or electron transfer.

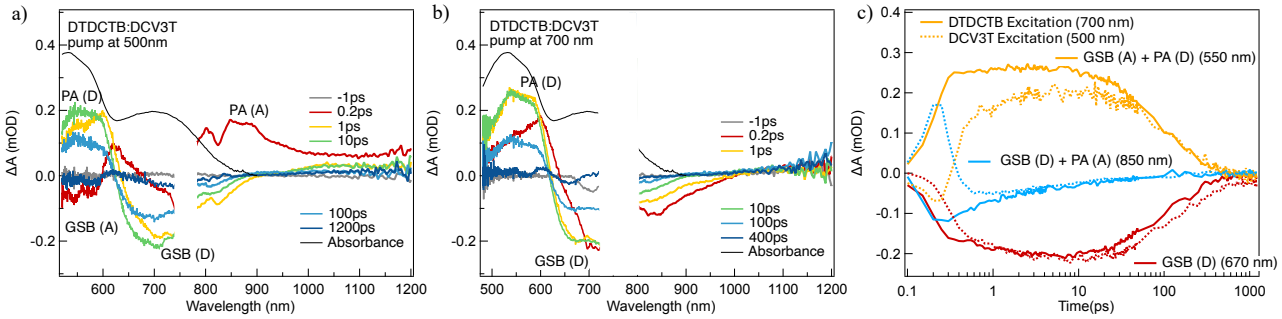


Figure 6.3: Transient absorption spectra of the DTDCTB(D):DCV3T(A) (1:1 by vol) blend at various time delays upon (a) DCV3T and (b) DTDCTB photoexcitation with 500 nm and 700 nm pulses, respectively, at an absorbed pump fluence 2.7 $\mu J/cm^2$. Negative bands at 550 nm and 700 nm correspond to ground-state bleaching (GSB) of DCV3T and DTDCTB, denoted as GSB (A) and GSB (D), respectively. The positive band at approximately 850 nm is attributed to photoinduced absorption from excitons in DCV3T (PA (A)), while the positive feature at 550 nm is assigned to photoinduced absorption from excitons in DTDCTB (PA (D)). (c) Comparison of normalised absorption dynamics at 670 nm (GSB (D)), 850 nm (GSB (D) + PA (A)), and 550 nm (GSB (A) + PA (D)) under both DTDCTB and DCV3T excitation. Spectral gaps in (a) and (b) are due to pump beam scattering.

Upon DCV3T excitation (Figure 6.3a), fast rise negative GSB (A) band around 550 nm and positive PA (A) band around 850 nm within 0.25 ps in DCV3T and fast decrease within 0.5 ps are seen. Fast rise signals are consistent with direct depletion of ground-state population in photoexcited DCV3T. Along with the fast decrease of PA (A) and GSB (A), slower rise of GSB (D) and PA (D) band from DTDCTB are observed, indicating lose of excitation in DCV3T and gain in excitation of DTDCTB. These results suggest the presence of efficient FRET from DCV3T to DTDCTB. However, there is no long-lived PA (A) signal indicative of charge formation in DCV3T, suggesting inefficient electron transfer following FRET. A weak, long-lived signal around 1150 nm may originate from charges generated by minor hole transfer. Figure 6.3c compares the dynamics at characteristic wavelengths under different excitation wavelength. Differences are most pronounced at early times (<1 ps), where FRET occurs, seen in the differences in dynamics of GSB (A)+PA (D) and GSB (D)+PA (A) at early times. After FRET, the dynamics of excitons in DTDCTB become similar, confirming that charge generation is insufficient.

In summary, only in the case of SubNc:DCV3T there is efficient charge generation in SubNc followed by fast FRET to SubNc. In the case of DTDCTB:DCV3T, where the EA offset is unfavourable and the IE offset is large, hole transfer is suppressed because of fast FRET, and electron transfer is inefficient. As a result, efficient FRET becomes a loss pathway. In contrast, in the SubNc:DCV3T blend, a favourable EA offset enables efficient electron transfer back to DCV3T, making FRET part of the dominant charge generation mechanism. These results are consistent with literature observations in PCBM-based systems, as discussed in Chapter 3.2, and suggest that a large IE offset is not apparently required for effective exciton separation in systems where efficient FRET from the electron acceptor to donor occurs.

6.2.2.2 Non-FRET Pairs

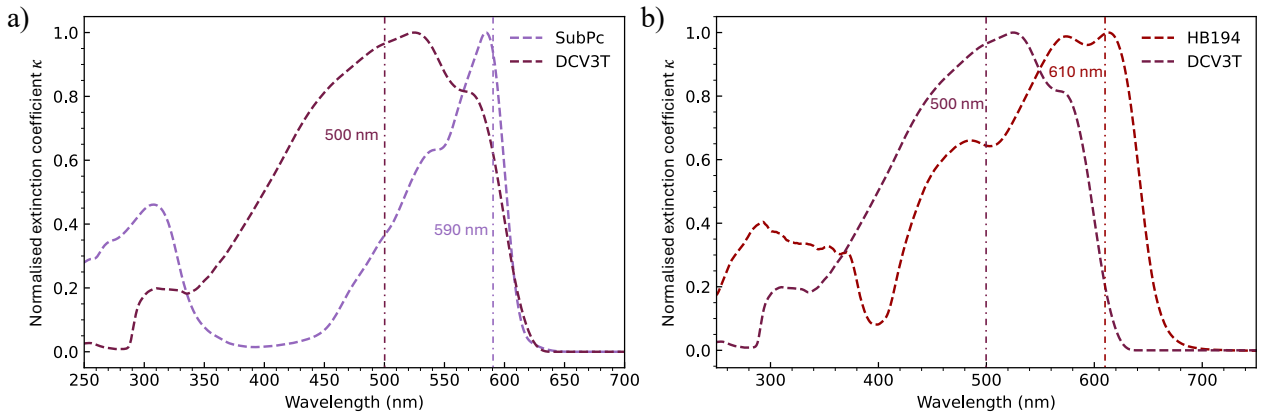


Figure 6.4: Normalised extinction coefficient spectra of (a) SubPc and DCV3T, and (b) HB194 and DCV3T, with the excitation wavelengths used for transient absorption spectroscopy (TAS) measurements indicated. The dot-dashed lines in each figure, labelled with corresponding wavelengths, denote the pump excitation energies applied to the SubPc:DCV3T and HB194:DCV3T blend thin films during TAS measurements.

The reference non-FRET pairs, SubPc:DCV3T and HB194:DCV3T, were previously shown to exhibit undetectable FRET in PL quenching measurements and possess much lower spectral overlap integrals, J, of 2.13×10^{14} and 1.74×10^{15} mol^{-1} L cm^{-1} nm^4, respectively. As reference systems for the SubNc:DCV3T blend, these two blends are not expected to support FRET from DCV3T to the electron donor, but they are anticipated to support efficient electron and hole transfer based on the IE and EA values measured on pristine films.

To better compare the exciton dynamics in these non-FRET blends with those observed

in FRET-enabled systems, TAS measurements were conducted again. However, due to the significant overlap in their absorption profiles, as shown in Figure 6.4, it is challenging to identify excitation wavelengths that can selectively excite the electron donor or acceptor molecules individually, particularly in the case of SubPc and DCV3T. The absorption strength of each molecule in the blends can be estimated from its individual κ spectrum. At 500 nm excitation, approximately 67% of the absorption is attributed to DCV3T and 33% to SubPc. Similarly, at 590 nm excitation, SubPc accounts for about 66% of the absorption and DCV3T for 37%. For the HB194:DCV3T blend, selective excitation of DCV3T is also not feasible, although HB194 can be more or less selectively excited using a 610 nm pump laser.

In the SubPc:DCV3T blend, upon excitation at 500 nm (67% DCV3T absorption), fast rise of the negative GSB band of DCV3T (GSB (A)) and SubPc (GSB (D)) is observed around 535 nm and 600 nm, respectively (Figure 6.5a), corresponding to direct excitation of both molecules. A slow rise (within 30 ps) of the long-lived $PA_{charges}$ (A) signals, appearing as a positive band around 900 nm, is attributed to charges in DCV3T, similar to observations in the SubNc:DCV3T blend. A weak positive signal at around 850 nm is attributed to DCV3T excitons (PA_{exc} (A)). Since both SubPc and DCV3T are directly excited, both hole and electron transfer processes may occur, although they cannot be clearly distinguished in the spectra. Therefore, these long-lived species are attributed to efficient charge transfer within the blend.

Upon excitation at 590 nm, Figure 6.5b shows a similar fast rise in negative GSB (A) band from DCV3T and GSB (D) band from SubPc as that with 500 nm excitation. Here, stronger GSB (D) and weaker GSB (A) are observed, consistent with SubPc-dominated absorption at this excitation wavelength. A similar slow rise in the $PA_{charges}$(A) signal is observed at around 900 nm, again attributed to DCV3T charges.

Likewise, in the HB194:DCV3T blend, upon excitation at 500 nm (where both molecules are directly excited), a fast rise of the negative GSB band of DCV3T (GSB (A)) and HB194 (GSB (D)) are observed at around 535 nm and 640 nm, respectively, as shown in Figure 6.5c. Additionally, a slow rise of positive PA (A) and GSB (A) band appears at approximately 900 nm. This signal is therefore attributed to charges formation in the molecules and indicates slow electron/hole transfer at around 100 ps. When the blend is excited at 610 nm (Figure 6.5d), where HB194 is primarily excited, a fast rise in GSB (D) from HB194 is observed due to direct

excitation. The subsequent slow rise (∼100 ps) of both GSB (A) and PA (A) from DCV3T, along with the absence of spectral shift over time, suggests that charges are formed via slow electron transfer to DCV3T.

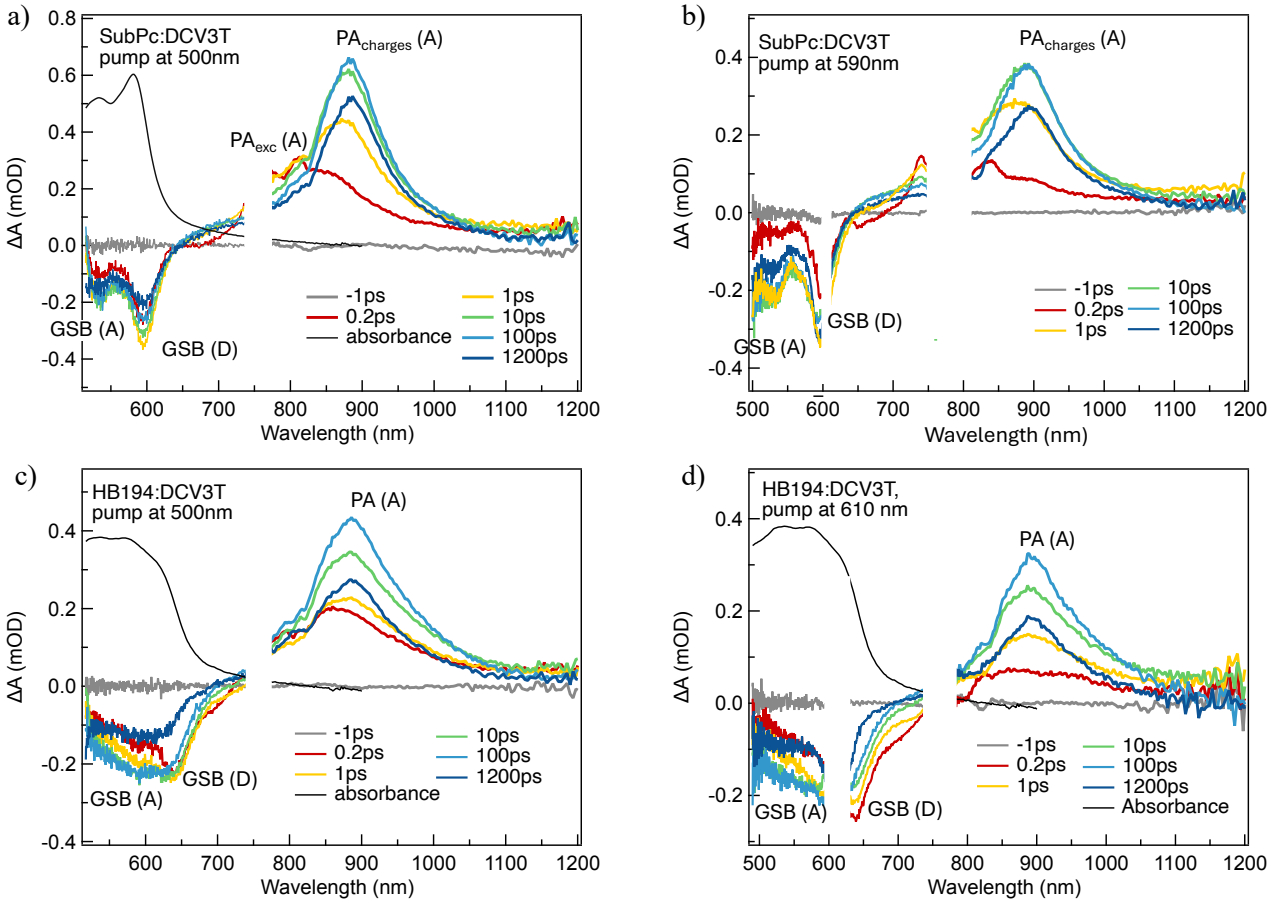


Figure 6.5: (a) and (b) show transient absorption (TA) spectra of SubPc(D):DCV3T(A) (1:1 by vol) blend at various time delays upon photexcitation at different wavelength at an absorbed pump fluence 2.7 μJ/cm^2. Negative bands at (a) 535 nm, (b) 520 nm and (a) 600 nm, (b) 580 nm correspond to ground-state bleaching (GSB) of DCV3T and SubPc, respectively, denoted as GSB (A) and GSB (D). The positive band at 850 nm arises from photoinduced absorption of DCV3T excitons (PA$_{exc}$ (A)), while the band at 900 nm corresponds to photoinduced absorption from charges in DCV3T (PA$_{charges}$ (A)). In (a), the blend is pumped at 500 nm, where DCV3T accounts for approximately 67% of the absorption and SubPc for 33%. In (b), excitation is at 590 nm, where SubPc absorbs approximately 63% and DCV3T 37%. (c) and (d) show TA spectra of an HB194 (D):DCV3T (A) (1:1 by vol) blend under identical experimental conditions. Negative bands at (c) 520 nm, (d) 535 nm and both (c), (d) at 640 nm correspond to GSB of DCV3T and HB194, respectively, denoted as GSB (A) and GSB (D). The positive band at 900 nm is attributed to photoinduced absorption from charges in DCV3T (PA (A)). In (c), the blend is pumped at 500 nm, where DCV3T dominates absorption, and in (d), excitation at 610 nm selectively excites HB194. Spectral gaps are due to pump beam scattering.

In summary, both the SubPc:DCV3T and HB194:DCV3T blends exhibit efficient charge

transfer upon photoexcitation. However, due to significant overlap in the absorption profiles of the two molecules in each blend, it is difficult to selectively excite each component to isolate their respective exciton dynamics. Furthermore, as TAS data for the individual pristine molecules are not available, it is not possible to distinguish between hole and electron transfer contributions in these blends, except for the HB194:DCV3T system, where slow electron transfer from HB194 to DCV3T was identified upon selective excitation of HB194.

6.2.3 Device Performance

Table 6.1 summarises the J-V characteristics of all PHJ devices, with values averaged over 18 devices. Outliers, such as shorted devices or those exhibiting J-V characteristics significantly different from the majority, were excluded. The parameters were extracted from reverse J-V scans, which represent the upper bound of device performance as the device is measured from a pre-accumulated charge state toward short-circuit conditions. The variations in device performance are generally small, indicating good reproducibility of devices fabricated via VTE deposition.

Table 6.1: Summary of open-circuit voltage (V_{oc}), short-circuit current density (J_{sc}), fill factor (FF), and power conversion efficiency (PCE) for 20 nm electron donor|20 nm electron acceptor planar heterojunction devices. Values are averaged over 18 devices, excluding outliers, and extracted from reverse current density-voltage scans.

Donor	Acceptor	V_{oc} (V)	J_{sc} (mA/cm^2)	FF	PCE (%)
SubNc	HB194	1.15±0.00	5.56±0.01	0.31±0.00	2.01±0.05
SubNc	DCV3T	1.09±0.01	7.43±0.03	0.42±0.02	3.39±0.19
DTDCTB	DCV3T	0.80±0.05	0.30±0.01	0.20±0.00	0.05±0.00
SubPc	DCV3T	1.23±0.03	2.91±0.03	0.42±0.01	1.51±0.06
HB194	DCV3T	1.09±0.08	1.16±0.02	0.24±0.01	0.29±0.01

Table 6.2 presents the J-V characteristics and calculated E_g^{PV} of the best PHJ devices for selected systems. The following analysis is based on the best-performing device of each system. Figure 6.6 shows the forward and reverse J-V scans for the DCV3T-based systems. In all four cases, the forward and reverse scans overlap, suggesting instantaneous charge extraction and injection, with no evidence of relaxation effects [27]. Attention is first drawn to the devices supporting efficient FRET, namely those employing SubNc and DTDCTB as the

electron donor. The SubNc|DCV3T device exhibits the best performance, with a PCE of 3.5%, moderate FF of 0.43, J_{sc} of 7.5 mA/cm^2, and V_{oc} of 1.09 V. Its performance exceeds that of the fullerene reference, for which a PCE of 2.5% (V_{oc} = 0.79 V, J_{sc} = 6.1 mA/cm^2, FF = 0.49) was reported for a PHJ comprising SubNc (13 nm) | C_{60} (40 nm) [174]. Its J-V curve shows no significant S-shape features, indicating good energetic alignment and mobility matching in active layers [196]. The FF and J-V curve shape are consistent with the relatively low but comparable hole mobility of SubNc (1.61×10^{-4} cm^2 V^{-1} s^{-1}) and the electron mobility of DCV3T (2.46×10^{-6} cm^2 V^{-1} s^{-1}) [200, 203]. The high J_{sc} is supported by the efficient electron transfer revealed by TAS and the substantial number of absorbed photons under the AM1.5 g solar spectrum (Figure 6.9a, dashed line).

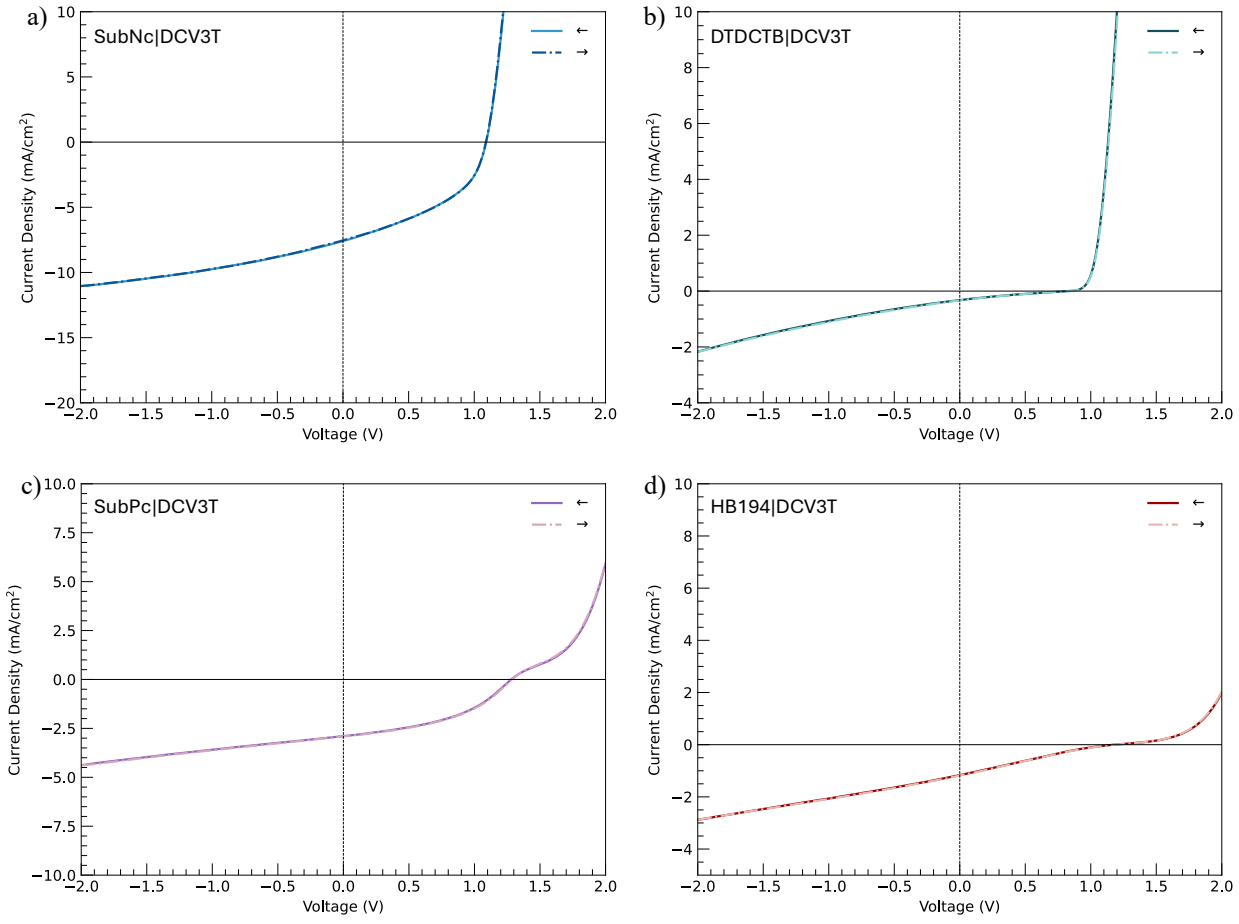


Figure 6.6: Current density–voltage characteristics of planar heterojunction devices using (a) SubNc, (b) DTDCTB, (c) SubPc, and (d) HB194 as electron donors (20 nm) and DCV3T as the electron acceptor (20 nm). Solid lines represent reverse scans, while dot-dashed lines represent forward scans.

By contrast, the DTDCTB|DCV3T device, for which TAS indicates extremely poor electron transfer and dominant FRET from DCV3T to DTDCTB (over the expected efficient hole transfer), exhibits a significantly lower J_{sc} of 0.3 mA/cm^2, as anticipated. However, the number of absorbed photons under the AM1.5 g spectrum is comparable to that of the SubNc system, with a theoretical J_{sc} (assuming IQE = 100%) of 15.0 mA/cm^2, slightly lower than that of SubNc (17.4 mA/cm^2). Given that SubNc and DTDCTB exhibit similar hole mobilities and exciton lifetime (Figure 6.7), the ultra-low J_{sc} in the DTDCTB system is attributed primarily to the energetic barrier to electron transfer. In conjunction with TAS results, this confirms that in systems with efficient FRET from electron acceptor to donor, electron transfer dominates charge carrier generation. Therefore, a sufficiently large EA offset is required for effective exciton separation, while a large IE offset does not contribute to this process.

For the systems that do not support FRET, namely those with SubPc and HB194 as electron donors, the device performance is notably worse compared to the SubNc system, despite efficient charge transfer suggested by TAS results. SubPc, like SubNc, is a bipolar molecule capable of directly generating free charge carriers upon photoexcitation with the assistance of the internal electric field of the device [221]. Devices consisting solely of 20 nm SubNc or SubPc active layers exhibit V_{oc} of 1.02 and 1.10 V, J_{sc} of 2.7 and 2.1 mA/cm^2, and FF of 0.28 and 0.23, respectively [221]. In addition, SubPc possesses a similarly high ϵ of 4.3, comparable to that of SubNc ($\epsilon = 5.8$). SubPc can therefore serve as an appropriate non-FRET reference electron donor to SubNc, offering comparable intrinsic photovoltaic properties.

As shown in Figure 6.6c, the SubPc|DCV3T PHJ device exhibits an S-shaped J-V curve and a significantly lower J_{sc}, which is indicative of low μ_h for the electron donor and high μ_e for the acceptor [196]. This S-shape behaviour is unlikely to arise from energetic barriers at other interfaces, as evidenced by the absence of such features in the SubNc|DCV3T J-V curve. The hypothesised charge transport limitations is further supported by the reported extremely low hole mobility of SubPc, measured to be $(4.5\pm2.3)\times10^{-8}$ cm^2 V^{-1} s^{-1} [201].

The V_{oc} of the SubPc|DCV3T device is higher than that of the SubNc|DCV3T device, consistent with V_{oc} of the respective pristine-layer devices and attributable to the larger energy gap of SubPc. The measured J_{sc} of the SubPc|DCV3T device is less than 40% of that of the SubNc-based device, yielding a value of approximately 2.9 mA/cm^2. However, the UV-

Vis absorptance and the calculated number of absorbed photons under AM1.5 g illumination (Figure 6.9c) suggest a theoretical J_{sc} (IQE= 100%) that is around 60% of that of the SubNc-based device. This discrepancy indicates a lower IQE for the SubPc|DCV3T device compared to the SubNc|DCV3T counterpart. Considering that TAS results have demonstrated efficient charge transfer for both SubPc:DCV3T and SubNc:DCV3T blends, the significantly reduced J_{sc} in the SubPc-based device can be primarily attributed to the poorer charge transport environment resulting from the low μ_h of SubPc, in addition to the comparatively weaker absorption.

Table 6.2: Summary of the photovoltaic gap (E_g^{PV}), open-circuit voltage (V_{oc}), total voltage loss ($\Delta V_{oc} = E_g^{PV}/e - V_{oc}$), short-circuit current (J_{sc}), fill factor (FF), and power conversion efficiency (PCE) for the best-performing planar heterojunction devices using SubNc, DTDCTB, SubPc, and HB194 as electron donors (20 nm) and DCV3T as the electron acceptor (20 nm). Values for the current density–voltage characteristics are extracted from reverse scans.

Donor	Acceptor	E_g^{PV} (eV)	V_{oc} (V)	ΔV_{oc} (V)	J_{sc} (mA/cm^2)	FF	PCE (%)
SubNc	HB194	1.69	1.16	0.53	5.7	0.31	2.07
SubNc	DCV3T	1.69	1.09	0.60	7.5	0.43	3.54
DTDCTB	DCV3T	1.58	0.85	0.73	0.3	0.20	0.05
SubPc	DCV3T	2.00	1.28	0.72	2.9	0.43	1.59
HB194	DCV3T	1.88	1.18	0.70	1.2	0.22	0.31

As for the HB194|DCV3T system, an S-shaped J-V curve is also observed, along with an even lower J_{sc} (1.2 mA/cm^2) and FF (0.22), despite the presence of efficient charge transfer demonstrated by TAS results. From the absorptance spectrum of the HB194|DCV3T device, a large theoretical J_{sc} (assuming IQE = 100%) of 14.5 mA/cm^2 is estimated, which is comparable to that of the SubNc|DCV3T device and greater than that of the SubPc|DCV3T device. Hence, the low J_{sc} cannot be attributed to weak absorption. The PEDOT:PSS/HB194 interface has also been reported to be free of energetic barriers, as demonstrated in HB194:C_{60} BHJ devices [222]. Figure 6.7 presents the time-resolved photoluminescence (TRPL) dynamics of singlet excitons in pristine films of the molecules under study. It can be observed that HB194 and DCV3T exhibit longer exciton lifetimes compared to SubNc. Additionally, HB194 may possess higher diffusivity than SubNc, which would suggest a correspondingly longer exciton diffusion length. Therefore, HB194 excitons are more likely to reach the D-A interface for dissociation than those in SubNc. These observations indicate that the S-shaped J-V and

the extremely low J_{sc} are primarily attributable to a poor charge transport environment in HB194. Interestingly, the reported μ_h of HB194 measured in OFETs suggests a value of 2×10^{-5} cm^2 V^{-1} s^{-1} [189], which is higher than that of SubPc. However, since mobilities measured in OFETs are in-plane (parallel to the substrate) and much different charge carrier densities [204], they may not reflect the out-of-plane mobility (perpendicular to the substrate), which governs current flow in OSC device. In combination with the J-V characteristics of the HB194|DCV3T device, it can therefore be concluded that the out-of-plane μ_h of HB194 is much smaller than the in-plane value. In addition to poor charge transport, unfavourable interfacial molecular orientation (e.g Edge-on orientation) may also contribute to the poor device performance observed in the HB194 system [63].

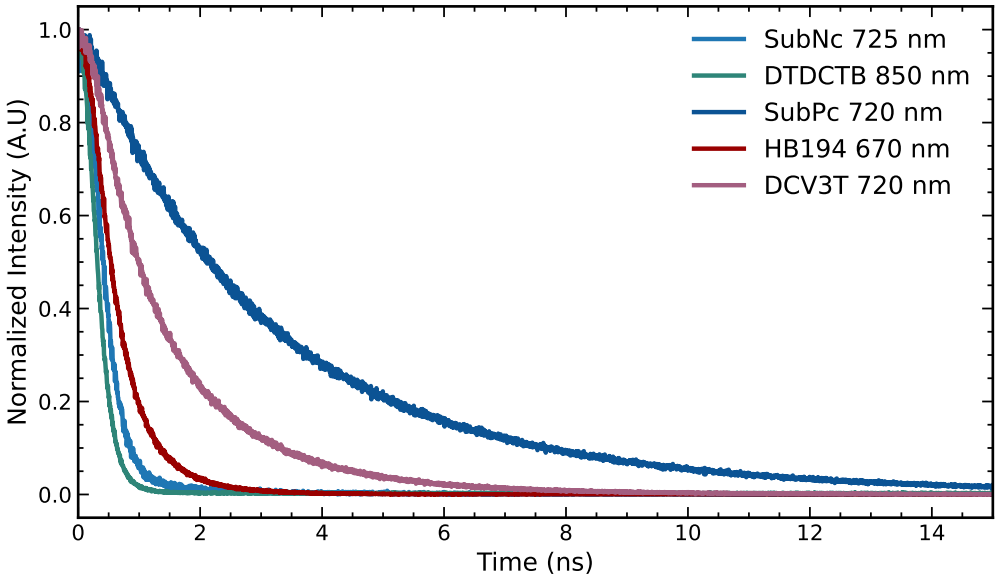


Figure 6.7: Time-resolved photoluminescence (TRPL) dynamics of SubNc, DTDCTB, SubPc, HB194, DCV3T pristine films excited by 510 nm laser (635 nm for DTDCTB) at or near the wavelength of steady-state PL peak, with intensity normalised. The monitored wavelengths are indicated in the legend.

Figure 6.8 and 6.9 present the EQE and absorptance spectra of the devices under study. The EQE spectra shown in Figure 6.8a–d are plotted on a linear scale and are consistent with measured J_{sc} values. The EQE spectral features of the active-layer molecules align well with the device absorptance spectra shown in Figure 6.9. All devices, except for the SubPc|DCV3T device, exhibit excellent absorption, resulting in high theoretical J_{sc} values (assuming IQE = 100%) of approximately 15 mA/cm^2 under AM1.5 g illumination. The two systems that support

efficient FRET, SubNc and DTDCTB, display broader absorption spectra. All molecules under study exhibit Stokes shifts ranging from 50 to 220 nm between their absorption and emission spectra, as discussed in Chapter 5.2. Consequently, molecular pairs that do not support FRET tend to exhibit considerable overlap in their individual absorption spectra. In contrast, the absorption spectra of molecular pairs that support FRET differ more significantly, resulting in a broader overall absorption profile for the device.

Interestingly, the EQE spectra plotted on a logarithmic scale for all four devices exhibit exponential tails in the sub-gap region, without observable CT state features, unlike the fullerene-based systems. With the exception of the DTDCTB|DCV3T system, the remaining three systems have been shown through TAS results to form effective charge-generating Type-II heterojunctions at D-A interfaces, and thus should be capable of forming CT states. However, no distinct CT absorption features are observed in their EQE spectra, even with extended sensitivity down to the order of 10^{-5}. This strongly suggests that the S_1 and CT states in these systems lie in close energetic proximity, similar to what has been observed in many high-performing low-$\Delta E_{S1,CT}$ NFA OSCs [39,118,223]. For the DTDCTB|DCV3T system, the exponential tail could due to the absence of CT state formation. Thus, the sub-gap absorption tail is governed by S_1 state of the system, which originates from DTDCTB. To gain further insight into the CT characteristics of these systems, EL spectra were also measured, enabling extraction of state information when used in conjunction with the EQE spectra, as discussed in the following section.

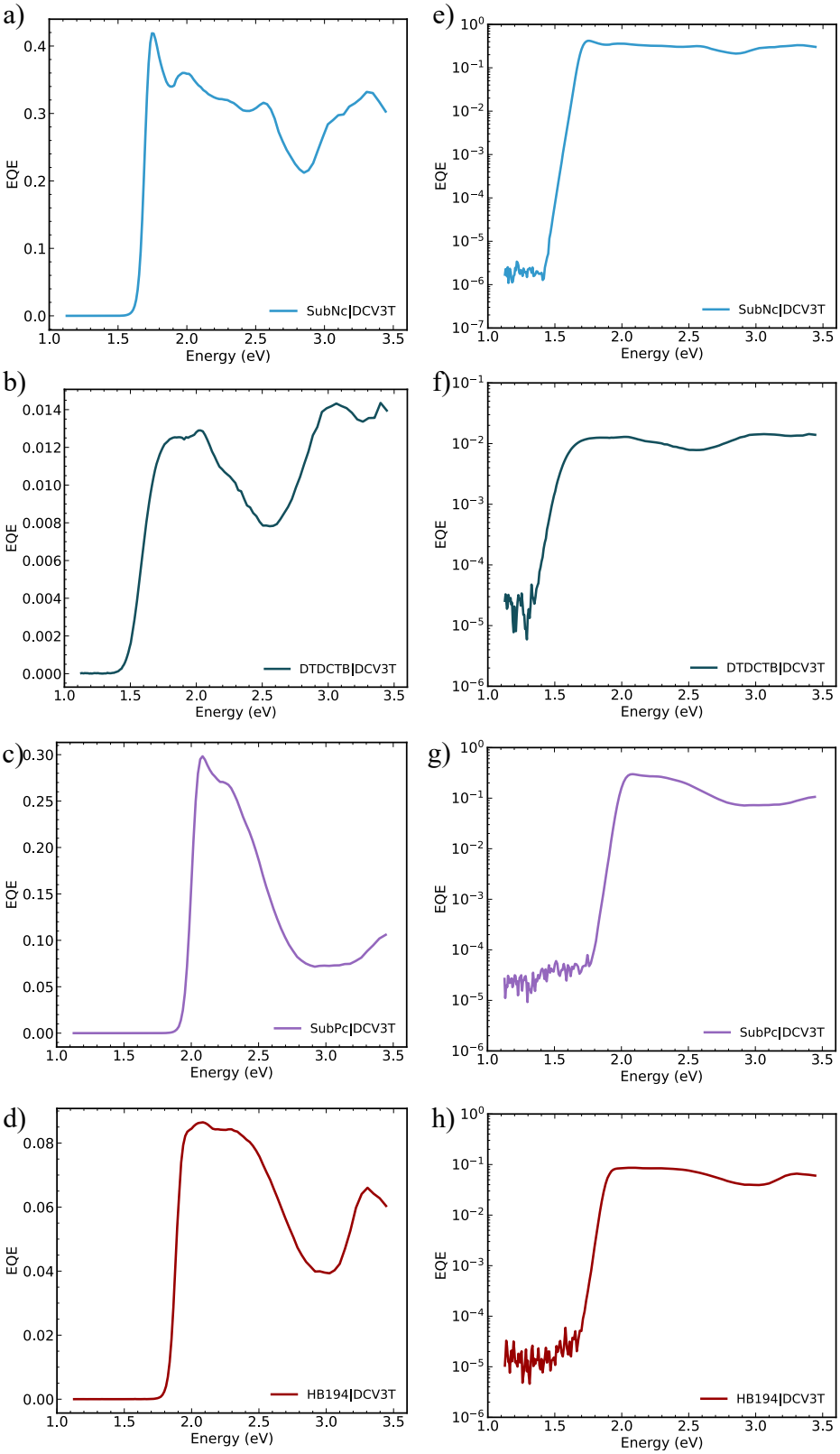


Figure 6.8: Sensitive external quantum efficiency spectra of the best performing planar heterojunction devices using SubNc (a,e) , DTDCTB (b, f), SubPc (c,g) , and HB194 (d,h) as electron donors (20 nm) and DCV3T as the electron acceptor (20 nm). Sub figures (a)–(d) show the spectra plotted on a linear scale, while (e)–(h) present the corresponding data on a logarithmic scale.

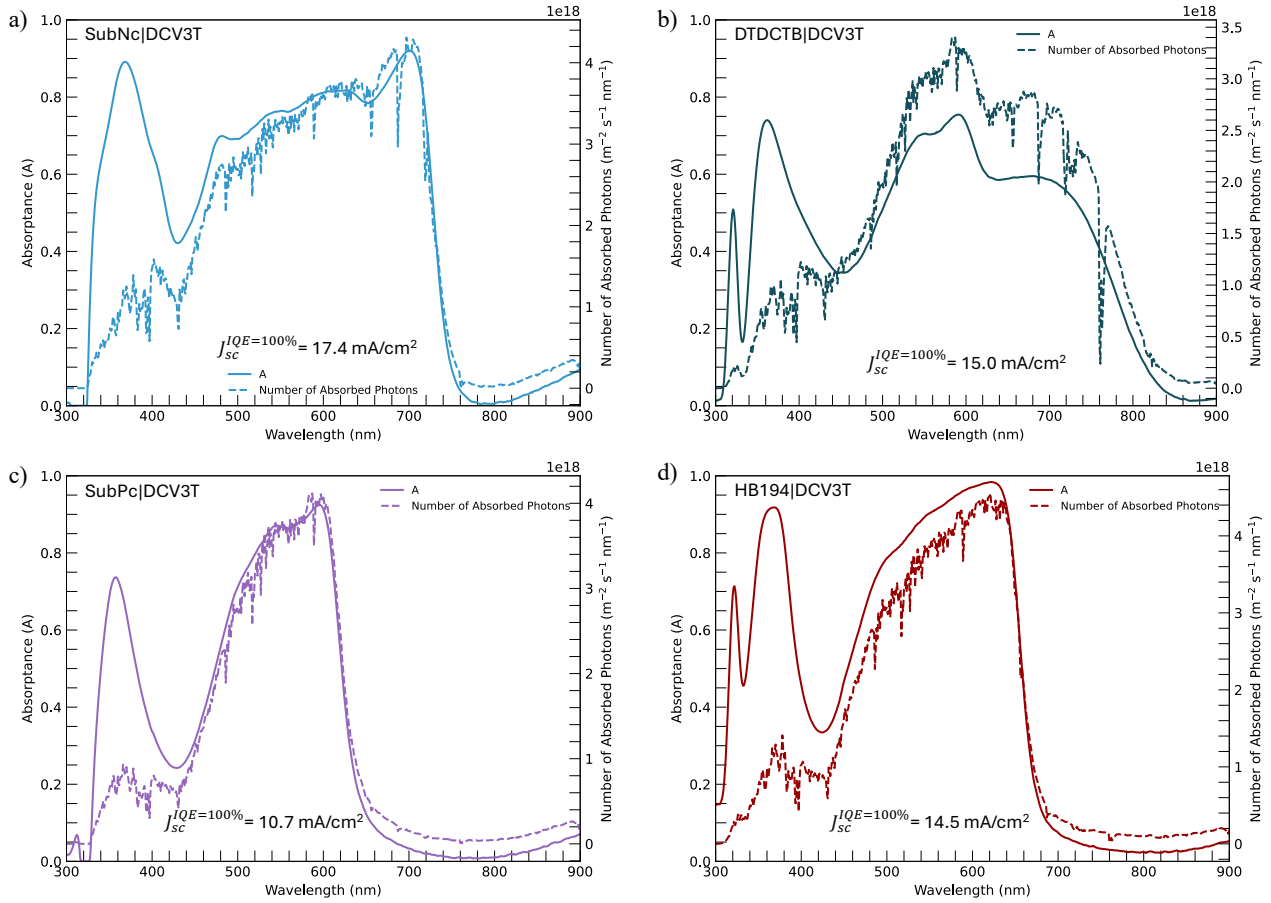


Figure 6.9: Measured absorptance and calculated number of absorbed photons (under AM1.5 g solar illumination) for the best planar heterojunction devices using (a) SubNc, (b) DTDCTB, (c) SubPc, and (d) HB194 as electron donors (20 nm) and DCV3T as the electron acceptor (20 nm). Theoretical maximum short-circuit current densities ($J_{sc}^{\mathrm{IQE=100\%}}$) calculated based on measured absorptance, assuming 100% internal quantum efficiency, are indicated in each figure. The absorptance spectra were measured by Katherine Trinkaus (Oxford).

6.2.4 Charge Transfer Characteristics

In the previous section, it was briefly mentioned that the EQE spectra of all devices under study exhibit exponential decay in the sub-gap region. As a result, probing the CT state characteristics using EQE alone becomes extremely challenging [99]. Apparent Urbach energy characteristics in the sub-gap region has been demonstrated to reveal degree of S_1-CT state energetic proximity in such systems [118]. Figure 6.10 presents the E_U^{app} curves derived from the EQE spectra of the four DCV3T-based devices, using Equation 2.28. In the S_1-dominated sub-gap absorption range, E_U^{app} reaches a broad plateau where the averaged minimum of $E_U^{\mathrm{app}} \approx k_BT$ at room temperature for all three systems: SubNc ($E_U^{\mathrm{app}} \approx 23$ meV), SubPc ($E_U^{\mathrm{app}} \approx$

24 meV), and HB194 ($E_U^{\text{app}} \approx 23$ meV). The small deviation from k_BT (<3 meV) can be attributed to the weak thickness dependence of E_U^{app} [118] and the spectral resolution limit of the EQE measurements. No narrow parabolic features are observed in the sub-gap region for all three systems, suggesting low $\Delta E_{S1,CT}$ in these systems [118]. For the DTDCTB system, due to the low signal-to-noise ratio in the spectra, the E_U^{app} features are not resolvable and are therefore excluded from further analysis.

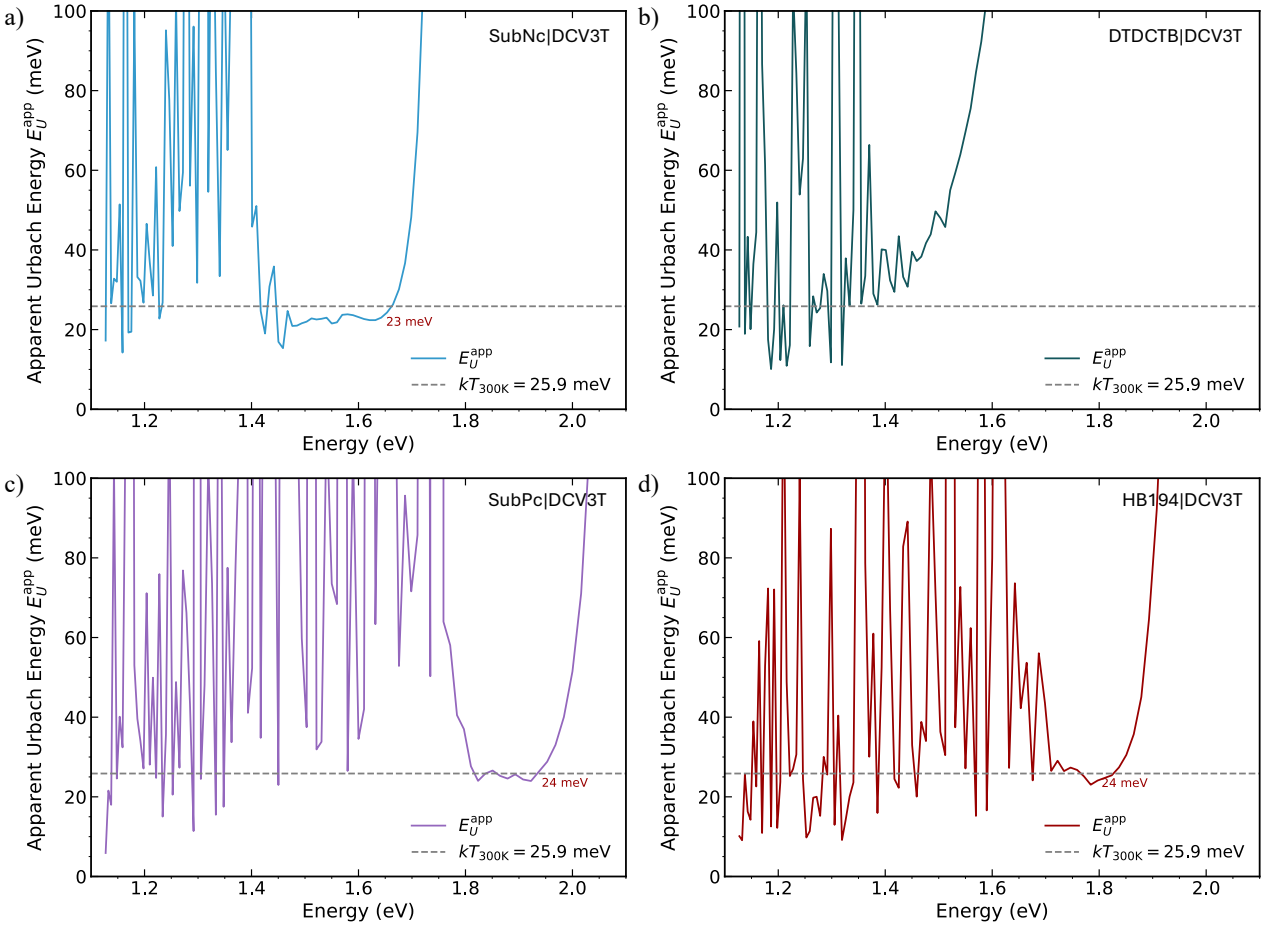


Figure 6.10: Apparent Urbach energy (E_U^{app}) spectra of the best planar heterojunction devices with (a) SubNc, (b) DTDCTB, (c) SubPc, and (d) HB194 as electron donors (20 nm) and DCV3T as the electron acceptor (20 nm). The minimum E_U^{app} values, averaged over the plateau region near the minimum point in the sub-gap region, are labelled in red in each sub figure. The value of k_BT at 300 K is indicated by a dashed horizontal line, where k is the Boltzmann constant and T is the device temperature.

In order to further probe the CT state characteristics, Dr Zhongcheng Yuan (Oxford) measured EL spectra for the SubNc|DCV3T, SubPc|DCV3T, and HB194|DCV3T PHJ devices. The EL intensity of the DTDCTB|DCV3T device was too weak to be detected by the spec-

trometer used, and therefore its EL is excluded from the following analysis. Figure 6.11a–c shows the normalised EL spectra of SubNc|DCV3T, SubPc|DCV3T, and HB194|DCV3T PHJ devices, measured at different current densities, around their J_{sc} and at higher current densities. At higher applied current densities, the spectral features of all three devices were maintained, and the EL spectra exhibited improved signal-to-noise ratios. Therefore, EL spectra measured at current densities higher than the device J_{sc} were used for further analysis. To validate the EL spectra, they were converted into EQE spectra using Equation 2.13, as described in Chapter 2.3.4.1, and reciprocity was confirmed.

Figure 6.11d–f presents the reduced EL and EQE spectra of the devices, normalised to f_{S1} of each system following the method in Chapter 2.3.4.2. By aligning the f_{S1} of the EL and EQE spectra, E_{S1} was extracted to be 1.71 eV for SubNc|DCV3T, 2.01 eV for SubPc|DCV3T, and 1.90 eV for HB194|DCV3T. The E_{S1} value determined for OSC with pristine SubNc as the active layer has been reported to be 1.73 eV in the literature [224], validating the reliability of this method. Extraction of E_{CT} from the intersection point of reduced EL and EQE spectra requires the two spectra to align at f_{CT}. However, this was not achievable for any of the three systems with no visible CT state features in EQE spectra.

For the SubNc|DCV3T device (Figure 6.11d), the EL spectrum was dominated by emission from the S_1 state at ∼1.71 eV. A subtle bump around 1.45 eV was observed, which could be attributed to weak CT state emission. The 1.71 eV peak corresponds to SubNc's PL emission at 740 nm (∼1.68 eV), not the DCV3T PL peak located at 675 nm (∼1.84 eV). Although Marcus theory allows Gaussian fitting of CT state in EL spectra, insufficient spectral data in the relevant energy range prevented reliable fitting in this case. For the SubPc|DCV3T system (Figure 6.11e), the EL emission was also dominated by the S_1 state of SubPc, with peaks at approximately 1.55, 1.74, and 1.97 eV, consistent with its PL features (800, 720, and 630 nm, respectively). A vague shoulder feature around 1.4 eV was observed and may be indicative of weak CT emission. Similarly for SubPc|DCV3T, CT emission could not be resolved through Marcus theory fitting.

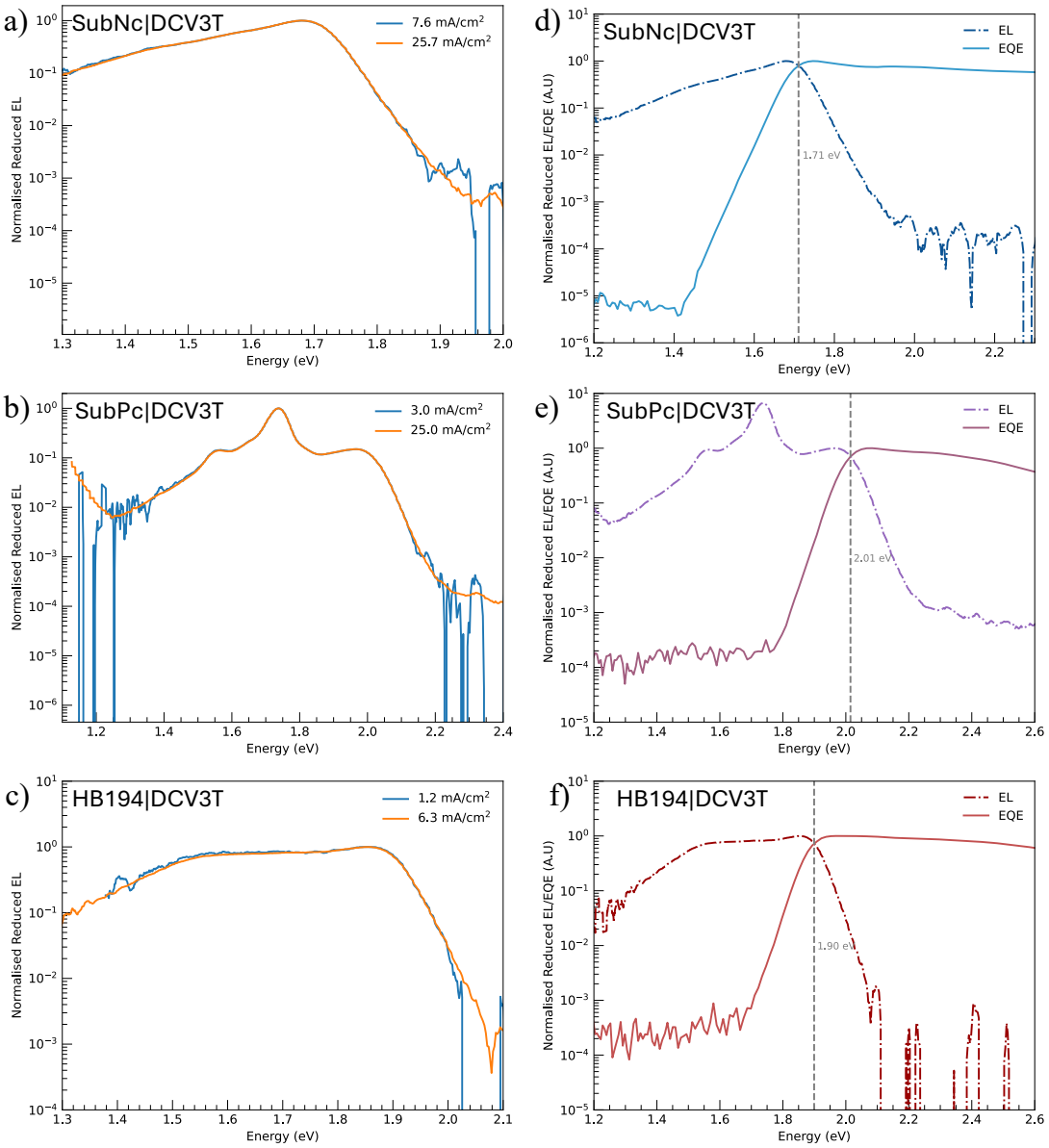


Figure 6.11: (a)–(c) Normalised reduced electroluminescence (EL) spectra of the best planar heterojunction devices using SubNc, SubPc, and HB194 as electron donors (20 nm) and DCV3T as the electron acceptor (20 nm), measured at different applied current densities, around the short-circuit current density (J_{sc}) and at higher values. (d)–(f) Reduced EL and external quantum efficiency (EQE) spectra, normalised to the oscillator strength of the system's lowest singlet state (f_{S1}). The energy of the intersection point between the EL and EQE spectra, corresponding to E_{S1}, is indicated in grey. EL spectra were measured by Dr Zhongcheng Yuan (Oxford).

In contrast, the HB194|DCV3T device exhibited a strong emission at ∼1.55 eV, comparable in magnitude to the S_1 emission. This strong low-energy emission cannot be assigned to HB194 or DCV3T, as neither molecule exhibits emission in this region according to their pristine film PL spectra (Figure 5.6 and 5.7). The S_1 emission peak around 1.85 eV is attributed

to HB194, whose major PL emission appears around 680 nm (1.82 eV). Given that DCV3T also emits at 675 nm but HB194 possesses a smaller optical gap (based on κ spectra), the S_1 state of the system is attributed to HB194. Unlike the other systems, a resolvable low-energy shoulder, likely arising from CT emission, was identified. Marcus theory fitting was performed (Figure 6.12a and b), yielding E_{CT} = 1.354±0.0002 eV, λ_{CT} = 0.248±0.003 eV, and f_{CT} = 0.000217±0.000001 eV^2. Thus, $\Delta E_{S1,CT}$ was calculated to be 0.55±0.01 eV, which is significantly larger than values in typical low-offset NFA systems with exponential EQE tails ($\Delta E_{S1,CT}$ ~0.1–0.2 eV), or fullerene-based systems with visible CT absorption features ($\Delta E_{S1,CT}$ ~0.3–0.4 eV) [51, 126, 223, 225]. This large $\Delta E_{S1,CT}$ contradicts the sub-gap E_U^{app} characteristics and may indicate that the low-energy emission originates from trap states or other emissive species, such as triplets or excimers, rather than CT states. Consequently, the assignment of CT emission for the HB194 system remains ambiguous. The subtle low-energy features seen in SubNc and SubPc devices may also be attributed to such non-CT origins.

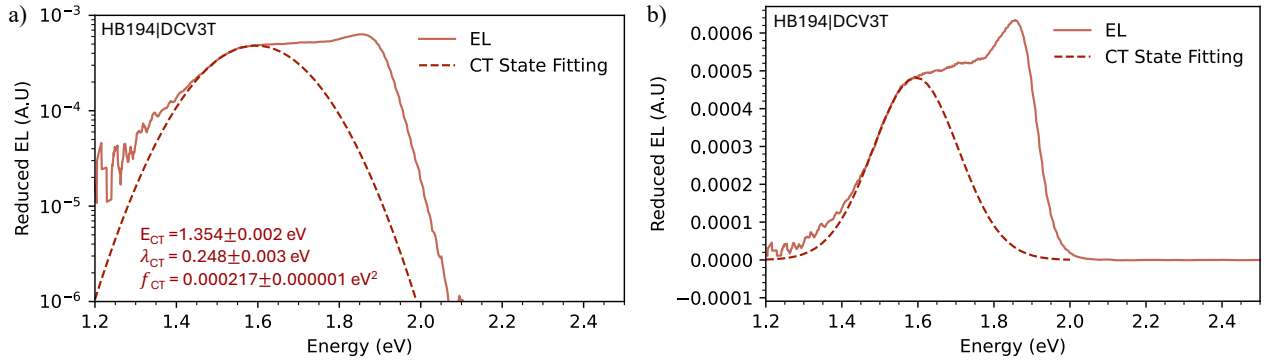


Figure 6.12: Reduced electroluminescence (EL) spectra of the HB194|DCV3T PHJ device with Marcus theory fits for a possible CT state, shown in (a) linear and (b) logarithmic scale. Dashed lines represent the fits. The fitting parameters are: $E_{CT} = 1.354 \pm 0.002$ eV, $\lambda_{CT} = 0.248 \pm 0.003$ eV, and $f_{CT} = 0.000217 \pm 0.000001$ eV^2.

In summary, both the FRET (SubNc|DCV3T) and non-FRET (SubPc|DCV3T, HB194 |DCV3T) systems exhibit S_1-dominated EL and EQE spectra with exponential tails in the sub-gap region. Due to this exponential decay, conventional Marcus theory (Gaussian) fits become unreliable, making the intersection point of reduced EL and EQE spectra a more robust method for determining E_{S1}. The plateau in E_U^{app} characteristics further supports the low $\Delta E_{S1,CT}$, suggesting that close S_1-CT state energetic proximity is possible in both FRET

and non-FRET systems. Finally, as S_1 emission dominates the EL spectra, weak CT emissions may be obscured or misinterpreted, necessitating caution in their assignment.

6.2.5 Voltage Losses

As discussed in the previous section, it is challenging to extract CT-state characteristics from EL and EQE spectra for these devices. Low-energy emissive states, distinct from CT states, were identified in the HB194|DCV3T PHJ device. Similarly, low-energy emissive features were observed in the EL spectra of SubNc and SubPc systems. These states could introduce additional energy loss channels beyond those associated with CT states. To further assess how these emissive states influence voltage loss, a detailed decomposition of ΔV_{oc} was conducted within the DB framework for all DCV3T-based systems and SubNc|HB194 system. Furthermore, the potential influence of FRET on voltage loss was examined.

Figure 6.13 summarises the voltage loss contributions: the loss relative to the S-Q limit (ΔV_{oc}^{SQ}), loss due to imperfect photocurrent collection (ΔV_{oc}^{sc}), radiative loss (ΔV_{oc}^{rad}), and non-radiative loss (ΔV_{oc}^{nr}). The value of ΔV_{oc}^{SQ} is directly related to E_g^{PV} via Equation 2.32, discussed in Chapter 2.3.5, and increases with increasing E_g^{PV} [134]. The DCV3T-based systems with DTDCTB, SubNc, HB194, and SubPc donors exhibit calculated ΔV_{oc}^{SQ} values of 0.267, 0.272, 0.286, and 0.292 V, respectively, in line with their E_g^{PV}. Regarding ΔV_{oc}^{sc}, the SubNc system shows the smallest value (∼28 mV), whereas the DTDCTB system exhibits the largest (∼111 mV), consistent with their respective J_{sc} and EQEs. The HB194 system has a slightly higher ΔV_{oc}^{sc} (∼68 mV) than SubPc (∼41 mV), again consistent with their photocurrents and EQEs.

The remaining two voltage loss components, ΔV_{oc}^{rad} and ΔV_{oc}^{nr}, are closely associated with CT state characteristics. In OSCs, $\Delta E_{S1,CT}$ has been identified as the dominant factor governing ΔV_{oc}^{rad}, particularly in fullerene-based BHJ systems [81], although the density of radiative emission sites (i.e. D-A interface density) also plays a role [99]. A smaller $\Delta E_{S1,CT}$ typically leads to a lower ΔV_{oc}^{rad}, as demonstrated for both fullerene and NFA systems [81, 126, 226]. Additionally, ΔV_{oc}^{nr} has been shown to depend on factors such as $\Delta E_{S1,CT}$ [39, 41, 132], interfacial molecular orientation and packing [63, 91], energetic disorder [121, 227], and D-A blend morphology [228, 229]. In PHJ architectures, where D-A interfaces are well-defined, $\Delta E_{S1,CT}$

and interfacial molecular orientation are expected to play a more dominant role.

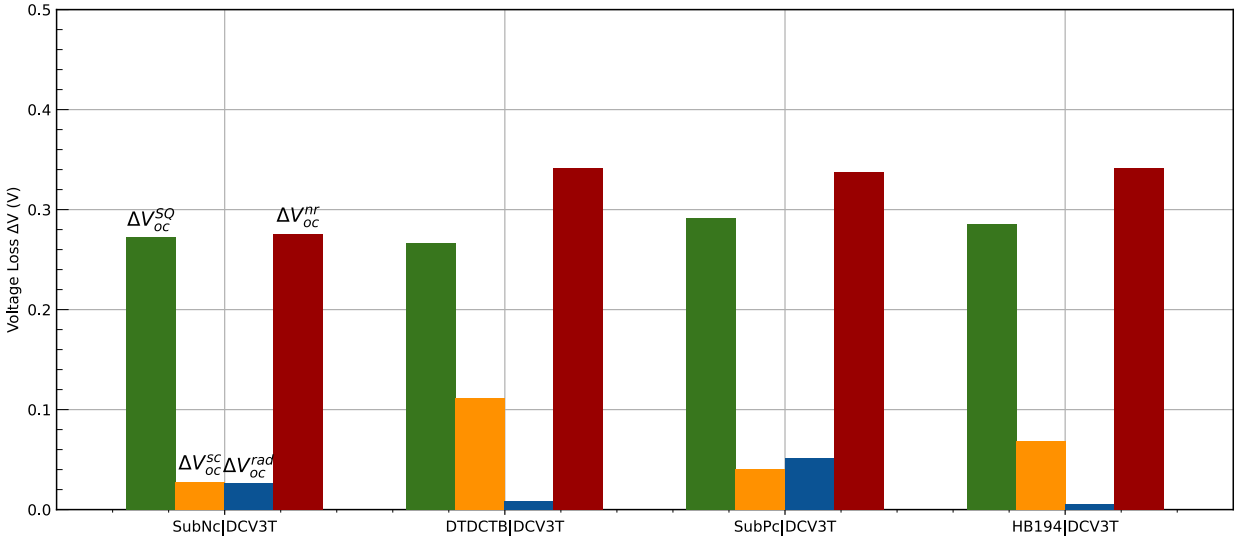


Figure 6.13: Open-circuit voltage loss decomposition for the best planar heterojunction devices using SubNc, DTDCTB, SubPc, and HB194 as electron donors (20 nm) and DCV3T as the electron acceptor (20 nm). It includes voltage loss relative to the Shockley–Queisser limit (ΔV_{oc}^{SQ}), voltage loss due to imperfect photocurrent collection (ΔV_{oc}^{sc}), radiative voltage loss (ΔV_{oc}^{rad}), and non-radiative voltage loss (ΔV_{oc}^{nr}).

In general, ΔV_{oc}^{rad} values across these devices are low. The highest, observed in the SubPc system, is approximately 52 mV. These values are significantly lower than those typically reported for fullerene-based OSCs (∼100–400 mV) [99,127], and comparable to state-of-art NFA systems (∼30–40 mV), such as D18:Y6 BHJs and PHJs using Y6 with evaporated donors [40, 126]. The DTDCTB device shows ultra-low ΔV_{oc}^{rad} (<10 mV), consistent with its lack of efficient charge transfer due to a negligible or negative $\Delta E_{S1,CT}$. Interestingly, the HB194 system exhibits an even lower ΔV_{oc}^{rad} (∼5 mV), suggesting an extremely small $\Delta E_{S1,CT}$. Prior TAS results indicated efficient charge transfer in HB194:DCV3T blends (1:1 by vol), likely enabled by a sufficiently large $\Delta E_{S1,CT}$. The discrepancy observed here may therefore arise from other factors, such as an overestimation of V_{oc}^{rad} due to a low FF [51,82], which could lead to an underestimation of ΔV_{oc}^{rad} of up to 17.5 mV. Nevertheless, a clear explanation remains elusive. Further investigation using alternative architectures with higher density of CT states such as BHJs may help clarify this. The SubPc system shows a ΔV_{oc}^{rad} (∼52 mV) higher than that of SubNc (∼26 mV), reflecting a marginally larger $\Delta E_{S1,CT}$. However, direct extraction

of E_{CT} and E_{S1} for this system was not possible, therefore it is not possible to confirm if the positive correlation between ΔV_{oc}^{rad} and $\Delta E_{S1,CT}$ holds. Additionally, there is no clear evidence that the ability to support FRET either benefits or hinders ΔV_{oc}^{rad}.

Table 6.3: Summary of voltage loss relative to Shockley-Queisser limit (ΔV_{oc}^{SQ}), voltage loss due to imperfect photocurrent collection (ΔV_{oc}^{sc}), radiative voltage loss (ΔV_{oc}^{rad}), and non-radiative voltage loss (ΔV_{oc}^{nr}) for the best 20 nm SubNc|20 nm HB194 (DCV3T) planar heterojunction devices.

Donor	Acceptor	ΔV_{oc}^{SQ} (mV)	ΔV_{oc}^{sc} (mV)	ΔV_{oc}^{rad} (mV)	ΔV_{oc}^{nr} (mV)
SubNc	HB194	274	35	24	196
SubNc	DCV3T	272	28	26	276

Turning to ΔV_{oc}^{nr}, the SubNc device shows a relatively low value of approximately 0.28 V, comparable to leading NFA systems such as PM6:D18:L8-BO (∼0.24 V) [19]. However, for the other three systems, which show S-shaped J-V curves, the calculated ΔV_{oc}^{nr} values may be unreliable within the DB framework. In such cases, the measured V_{oc} may no longer reflect the intrinsic D-A junction properties. It has been demonstrated that while Schottky barriers at electrode/active layer interfaces do not influence V_{oc}, other transport limitations or interfacial barriers can cause underestimation of V_{oc} [230, 231]. This may explain the nearly identical ΔV_{oc}^{nr} values observed for DTDCTB (∼0.341 V), SubPc (∼0.337 V), and HB194 (∼0.342 V), despite differences in their energetic alignments. According to Equation 2.32, ΔV_{oc}^{nr} can also be independently determined from the EL quantum efficiency measured at V_{oc}. Unfortunately, signs of degradation were observed for devices under study by the time EL measurements were performed (slightly reduced V_{oc} and J_{sc}), making this approach unreliable. As a result, comparison of ΔV_{oc}^{nr} between FRET and non-FRET devices could not be carried out, and the impact of FRET on ΔV_{oc}^{nr} remains inconclusive.

However, the SubNc|HB194 device, which exhibits a normal J-V curve, provides a useful comparison point for the SubNc|DCV3T system. Table 6.3 summarises the voltage loss components for these two PHJ systems. These two devices exhibit efficient FRET from DCV3T or HB194 (electron acceptor) to SubNc under electron acceptor excitation. TAS results support a two-step charge generation mechanism: FRET from DCV3T or HB194 to SubNc, followed by either electron transfer back to DCV3T or field-assisted dissociation of SubNc excitons.

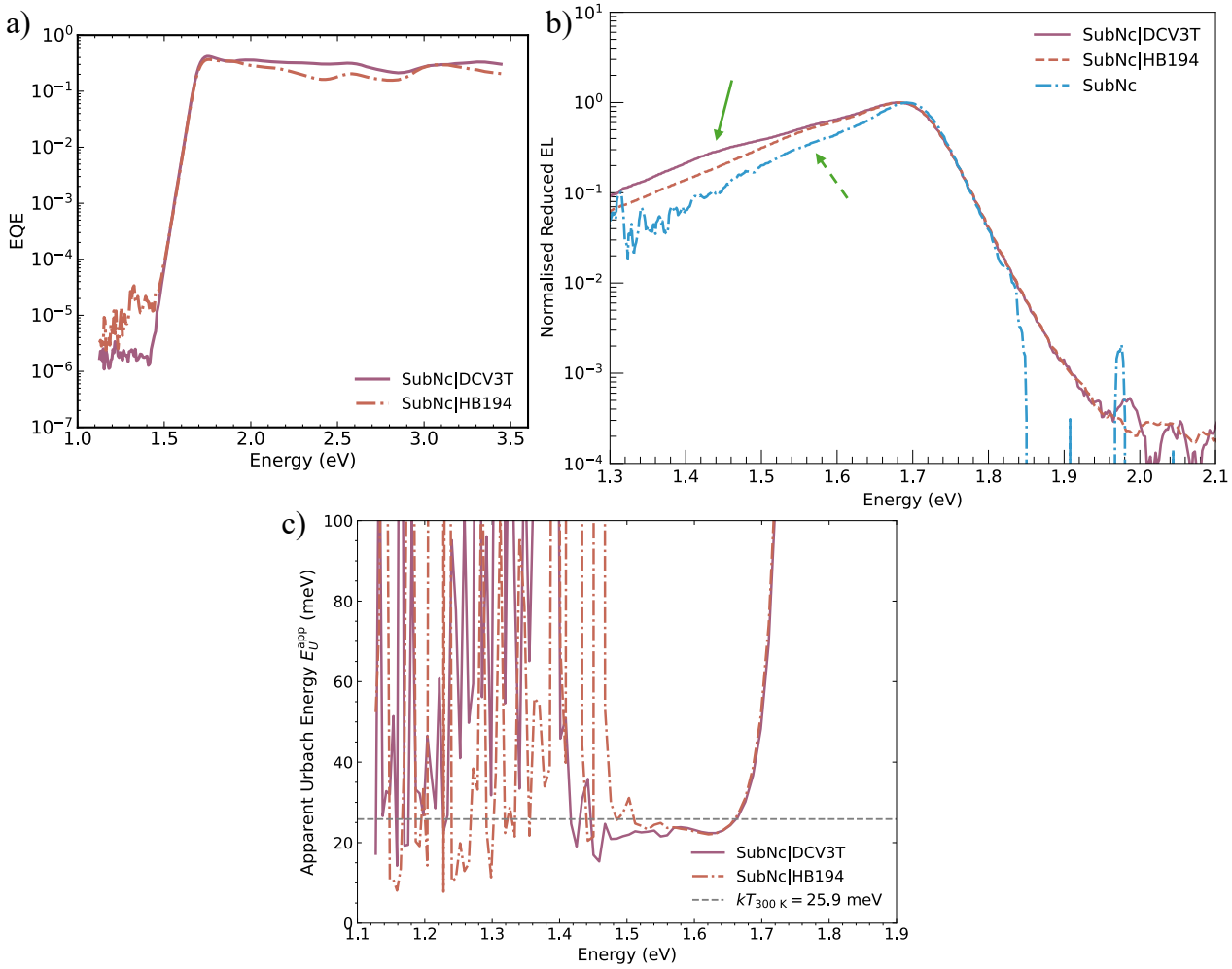


Figure 6.14: (a) External quantum efficiency spectra of the best planar heterojunction (PHJ) 20 nm SubNc|20 nm DCV3T and 20 nm HB194|20 nm DCV3T devices plotted on a logarithmic scale. (b) Reduced electroluminescence spectra of the same two devices and a 24 nm SubNc reference, normalised to their respective maxima. (c) Apparent Urbach energy (E_U^{app}) spectra of the two PHJ devices. The value of k_BT at 300 K is shown as a dashed horizontal line, where k is the Boltzmann constant and T is the device temperature.

The key difference lies in their EA offsets: SubNc exhibits negligible EA offset (∼0.05 eV) with HB194 but a significant offset (∼0.40 eV) with DCV3T. In both systems, the lowest singlet state is associated with SubNc, and their EQE spectra exhibit identical exponential tails dominated by S_1 absorption (Figure 6.14a). Their overlapping E_U^{app} spectra (Figure 6.14c) confirm similar energetic disorder characteristics in sub-gap region. ΔV_{oc}^{sc} is identical for both devices due to their matched E_g^{PV}. The small difference in ΔV_{oc}^{rad} (∼2 mV higher for SubNc|DCV3T) suggests only minor differences in $\Delta E_{S1,CT}$. However, a significant difference of ∼80 mV is observed in ΔV_{oc}^{nr}, with SubNc|DCV3T showing the larger loss. The EL spectra may help

explain this difference. Figure 6.14b presents reduced EL spectra for the SubNc|DCV3T, SubNc|HB194, and pristine SubNc devices, normalised to their f_{S1} values. The pristine SubNc device shows a weak emission shoulder at ∼1.55 eV, consistent with a similar PL emission bump around 800 nm, both attributable to SubNc S_1 emission. Both PHJ devices show enhanced low-energy EL emission compared to pristine SubNc, with the DCV3T device exhibiting stronger sub-1.55 eV emission (highlighted by the green arrow in Figure 6.14b). As previously discussed, these emissions cannot simply be attributed to CT states and therefore may relate to intrinsic molecular properties, such as triplet or excimer emission. Future investigations using custom-designed molecular series will be required to elucidate the molecular or optoelectronic origins of ΔV_{oc}^{nr}.

6.2.6 Conclusions

In this section, the photovoltaic performance of five VTE OSC systems, four using DCV3T as the electron acceptor and one with HB194 as the electron acceptor, were systematically investigated, with a focus on how FRET, IE/EA offsets, and low-energy emissive states influence device performance and voltage losses. Exciton dynamics were investigated via TAS, for the four systems with DCV3T as electron acceptors. OSC device characteristics, CT state characteristics and voltage losses of systems supporting efficient FRET (SubNc|DCV3T and DTDCTB|DCV3T) were compared with non-FRET systems (SubPc|DCV3T and HB194|DCV3T). Among FRET-supported systems, SubNc|DCV3T was also compared with other systems exhibiting smaller EA offsets, SubNc|HB194 and DTDCTB|DCV3T.

Exciton dynamics of the four DCV3T-based systems were probed on 1:1 (by vol) blends via TAS by Dr Demetra Tsokkou at University of Bern. TAS results confirmed that both DTDCTB and SubNc systems undergo efficient FRET, with hole transfer suppressed by the FRET process. However, only the system with large EA offset of 0.4 eV demonstrated following efficient electron transfer, while the system with negative EA offset of -0.11 eV did not. Efficient charge generation following donor or acceptor excitation was observed in non-FRET systems with large EA and IE offsets (ΔEA>0.28 eV, ΔIE>0.46 eV). These findings suggest that exciton separation efficiency is strongly influenced by the IE and EA offsets, with EA offsets playing a dominant role in systems that support FRET from the electron acceptor to the donor.

All PHJ devices with non-fullerene molecules as electron acceptor exhibited exponential decay in their EQE spectra at low energies, suggesting small $\Delta E_{S1,CT}$, despite varying IE (∼0.46-1 eV) and EA (∼-0.1-0.46 eV) offsets. SubNc|DCV3T showed the best device performance, achieving a PCE of ∼3.5%, attributed to efficient electron transfer, moderate but balanced mobility, and strong light-absorption. In contrast, FRET-supported system with negative ΔEA, DTDCTB|DCV3T, exhibited extremely poor performance. This comparison highlighted that FRET without subsequent efficient charge transfer becomes energy loss channel. Although the role of FRET in directly improving device performance could not be conclusively determined, the broader absorption observed in FRET systems appeared to stem from their little-overlapping electron donor and acceptor absorption spectra.

Further investigation into CT state characteristics via EQE and EL (measured by Dr Zhongcheng Yuan in Oxford) confirms small $\Delta E_{S1,CT}$ in systems SubNc|DCV3T, SubPc|DCV3T, and HB194|DCV3T. It was shown that FRET is not a prerequisite for small $\Delta E_{S1,CT}$. EL spectra of all three analysed systems were dominated by S_1 emission with no clearly resolvable CT emission. Instead, some low-energy emissive states were observed in their EL spectra.

With further exploration on whether and how FRET and these low-energy emissive states contribute to energy loss, voltage loss decomposition was carried out for all five systems in DB picture. ΔV_{oc}^{rad} was found to be low across all systems and did not correlate with FRET. By comparing the two systems with same E_{S1}, it was possible to identify the contributions of low-energy EL emissions observed to ΔV_{oc}^{nr}. The origin of these low-energy EL emissions could not be determined, however it is plausible that this is related to intrinsic molecular properties.

Overall, these results demonstrate that intentionally designing electron donor and acceptor molecules to support FRET does not necessarily lead to high-performing devices. Instead, sufficient interfacial energy level offsets (IE/EA), along with balanced and high charge carrier mobilities, play a more decisive role. Notably, molecular pairs that support FRET tend to exhibit broader absorption spectra, due to their little-overlapping absorption spectra. One of the most interesting findings in this study is the consistent observation of S_1-donimated EQE and EL spectra across all systems, regardless of the varying energetic offsets of dominating CT. It raise the question what determines $\Delta E_{S1,CT}$ and could be an interesting topic to explore in the future. Moreover, the low-energy emissive states, distinct from CT states, warrant further

investigations to understand their origin and role in device energy loss.

6.3 Application of FRET in Tri-Layer Planar Heterojunction OSCs

6.3.1 Materials and Devices

As demonstrated in Chapter 5, HB194 and SubNc have a sizeable ΔIE of 0.39 eV and an almost zero offset in EA. Also HB194 are proved to be able to undergo efficient FRET to SubNc. Therefore HB194 can effectively harvest additional light and transfer energy to SubNc.

To investigate whether the FRET from HB194 to SubNc can be utilised for improving existing binary OSC systems, PHJ solar cells with the active layer being SubNc|HB194 bilayer and α-6T|SubNc|HB194 were fabricated. The PHJ devices were constructed using the following layer stack: ITO (135 nm)|PEDOT:PSS (25 nm)|(α-6T 20 nm)|SubNc|HB194|BPhen (8 nm)|Ag (120 nm), which were also shown in Figure 4.4b. Single-component reference devices based on pristine SubNc (24 nm) and reference devices with α-6T|SubNc (24 nm), α-6T|SubNc (12 nm)|SubPc (18 nm) were also fabricated in same device stack. The evaporation rate for molecules in active layer was set nominally to be 0.25 Å/s. The optimal thickness for SubNc and HB194 layer in trilayer PHJ are 10 nm and 14 nm, respectively.

6.3.2 Device Performance

6.3.2.1 SubNc|HB194 Bilayer PHJ

We first investigated bilayer PHJ devices in which HB194 served as the electron acceptor and SubNc as the donor. For comparison, single-component reference devices based on pristine SubNc (24 nm) were fabricated, maintaining the same total active layer thickness as that of the bilayer devices.

Figure 6.15a, b and Table 6.4 show the J-V characteristics, EQE spectra (in log scale) and device parameters of the HB194 bilayer and pristine SubNc reference devices. The pristine SubNc device exhibits a considerable J_{sc} of 4.3 mA/cm^2, which can be attributed to field-

assisted exciton dissociation [175]. The HB194 bilayer device displays increased FF (from 0.28 to 0.37) and J_{sc} (from 4.3 to 6.0 mA/cm^2) compared with the neat SubNc device. We attribute these improvements partly to the improved electron transport environment introduced by HB194. The increase in the calculated IQE (Figure 6.19a) at the SubNc absorption peak around 700 nm suggests that HB194 facilitates the extraction of free charge carriers generated from SubNc excitons. Reported values for SubNc indicate a hole mobility of 1.61×10^{-4} cm^2 V^{-1} s^{-1} [200] and a significantly lower electron mobility of 4.2×10^{-9} cm^2 V^{-1} s^{-1} [146], suggesting poor electron transport in SubNc. Although no reported electron mobility for HB194 was found, the absence of an S-shape in the J-V curve of the bilayer device suggests that HB194 possesses an electron mobility comparable to the hole mobility of SubNc [196], which is more favourable for electron transport.

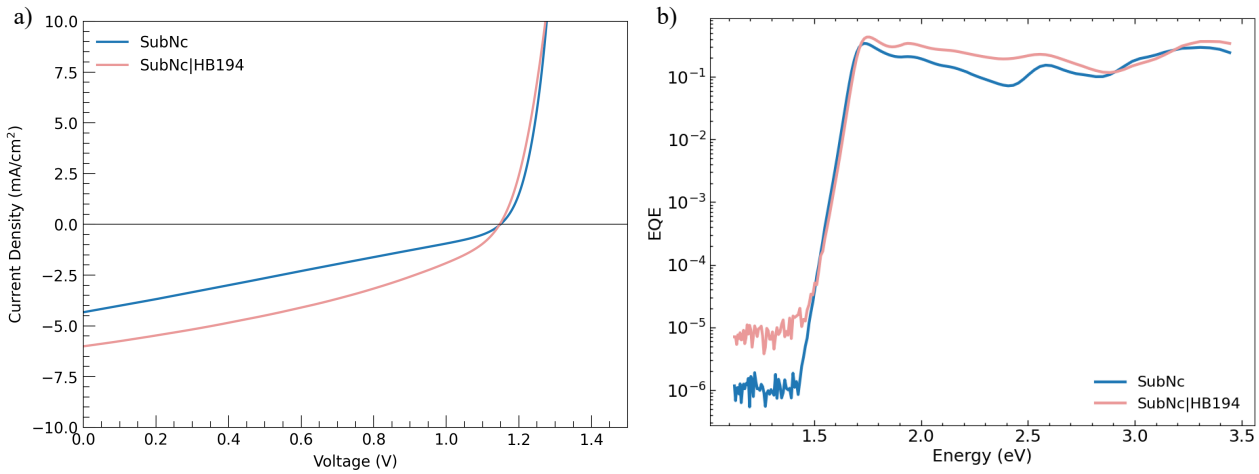


Figure 6.15: (a) Current density-Voltage characteristics of the best SubNc|HB194 bilayer PHJ device along with its single-component reference SubNc. (b) Sensitive external quantum efficiency spectra of these devices in logarithm scale. The thickness of each active layer and device performance can be found in Table 6.4.

An increase in both IQE and EQE is also observed between 500 and 650 nm, corresponding to the main absorption band of HB194, indicating that excitons generated in HB194 contribute to the photocurrent. We attribute the generation of free charges to three possible pathways: (1) hole transfer from HB194 excitons to SubNc, (2) field-assisted dissociation of FRET-generated SubNc excitons, and (3) electron transfer from FRET-generated SubNc excitons to HB194. The third mechanism likely contributes the least owing to the near-zero EA offset. The relative contributions of mechanisms (1) and (2) could not be determined using the characterisation

methods employed in this thesis and can be an topic for future investigation. An example of a suitable approach is demonstrated in Reference [138].

Table 6.4: Active layer thickness, device photovoltaic gap (E_g^{PV}), open-circuit voltage (V_{oc}), total voltage loss ($\Delta V_{oc} = E_g^{PV}$/e - V_{oc}), short-circuit current (J_{sc}), fill factor (FF) and power conversion efficiency (PCE) for the reported devices.

Donor	Acceptor	E_g^{PV} (eV)	V_{oc} (V)	ΔV_{oc} (V)	J_{sc} (mA/cm^2)	FF	PCE (%)
24 nm SubNc	N/A	1.69	1.15	0.54	4.3	0.28	1.38
10 nm SubNc	14 nm HB194	1.71	1.15	0.56	6.0	0.37	2.57
20 nm α-6T	24 nm SubNc	1.69	0.94	0.75	7.9	0.43	3.21
20 nm α-6T	12 nm SubNc |18 nm SubPc	1.70	0.93	0.77	10.3	0.53	5.03
20 nm α-6T	10 nm SubNc |14 nm HB194	1.71	0.94	0.77	10.2	0.56	5.31

The logarithmic EQE spectra of both devices (Figure 6.15b) exhibit nearly identical exponential tails without visible sub-gap CT-state absorption features. This suggests that the HB194|SubNc device contains very few CT states or that CT states are very close to S_1 states of the system. This tail feature is very similar to that reported for the SubNc|SubPc PHJ device by Nikolis *et al.* [175]. SubPc possesses a similar intrinsic EA to HB194 and higher IE. They attributed the absence of CT features in the SubNc|SubPc PHJ to the lack of a charge-generating Type-II heterojunction due to very small EA and IE offsets between SubNc and SubPc, i.e., the absence of effective CT interfaces between SubNc and SubPc. Interestingly, although our HB194/SubNc system exhibits a larger IE offset, which should enable CT formation via hole transfer, no CT feature is observed in the sEQE sub-gap region. This may indicate that hole transfer in our system is less competitive than FRET. Given the near-zero EA offset, the system likely fails to form a Type-II heterojunction, resulting in sub-gap features in the EQE that closely resemble those of the pristine SubNc device.

Overall, HB194 introduces additional light absorption in the spectral region where SubNc absorbs weakly, enhances the electron transport environment in the device. However, the improvements in J_{sc} and FF remain limited. Nevertheless, V_{oc} is maintained in the HB194|SubNc device compared with the neat SubNc device, suggesting that HB194 functions effectively as an additional light absorber adjacent to the SubNc layer without compromising V_{oc}, rather than as an electron acceptor to provide efficient driving force for CT.

6.3.2.2 α-6T|SubNc|HB194 Trilayer PHJ

From the bilayer PHJ devices, we demonstrated that HB194 can act as an additional light absorber adjacent to the SubNc layer, boosting J_{sc} and FF without sacrificing V_{oc}. Building on this, we adopted the device stack proposed by Cnops *et al.*, in which a third layer, α-6T, is introduced as the electron donor to a double-acceptor system comprising SubNc and SubPc [146]. For reference, we reproduced a similar stack to that of Cnops's and α-6T|SubNc binary PHJ as reference devices. To maintain consistency, the α-6T thickness was kept at 20 nm for both reference and target devices.

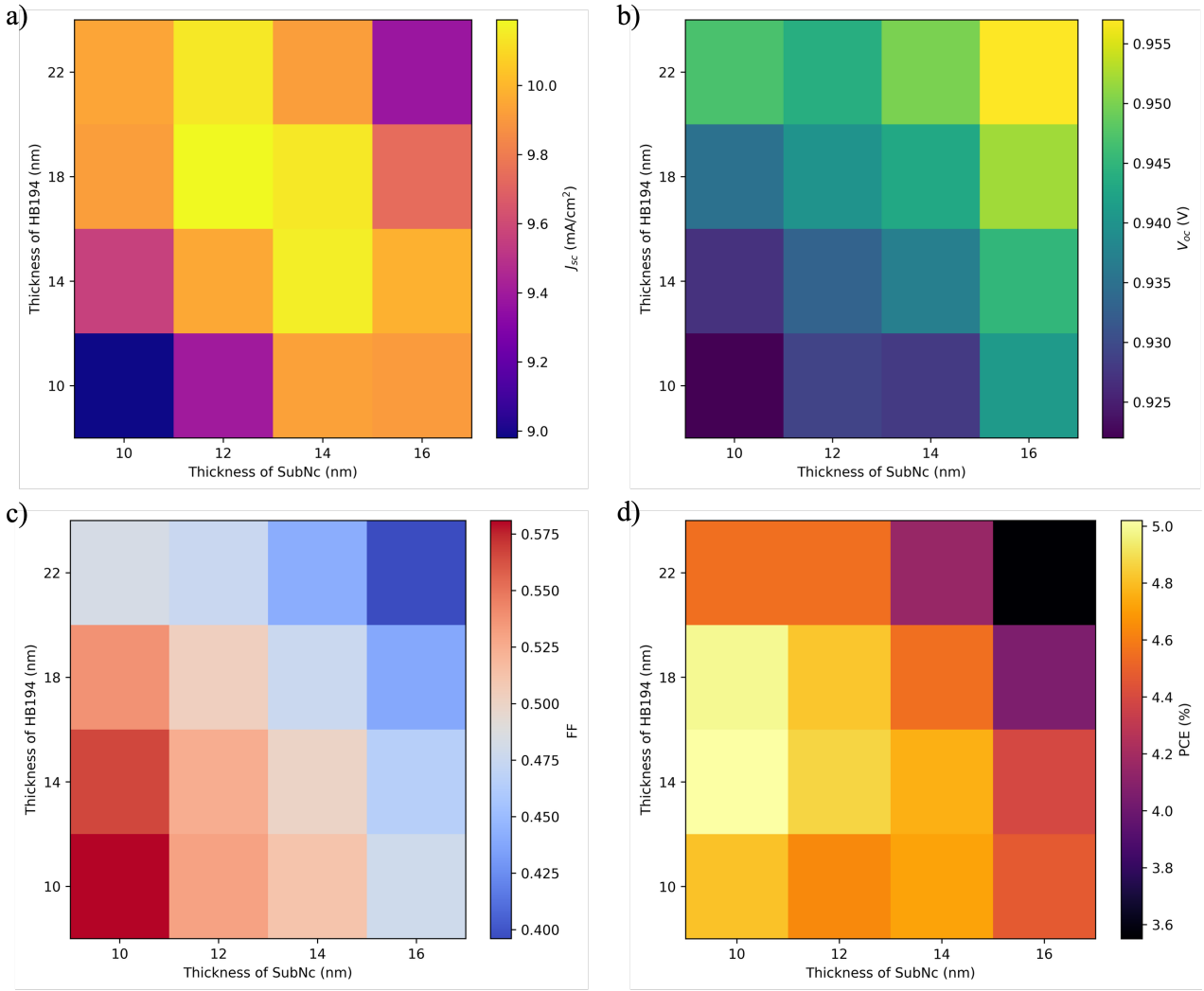


Figure 6.16: Heat maps showing the dependence of (a) short-circuit current, J_{sc}, (b) open-circuit voltage, V_{oc}, (c) fill factor, FF, and (d) power conversion efficiency, PCE, on the thicknesses of SubNc (10, 12, 14, and 16 nm) and HB194 (10, 14, 18, and 22 nm). The values were extracted from the current density–voltage curves of the best-performing devices for each thickness combination.

As discussed in Chapter 2.3.1, the efficiency of PHJ devices is limited by the exciton diffusion length owing to limited D-A interfaces. In addition, given the overall low charge carrier mobilities of the materials under investigation, thickness also has a pronounced effect on the FF. To enable a fair comparison of the photovoltaic potential of HB194 in the stack of Cnops *et al.*, we carried out a thickness optimisation in which SubNc was varied from 10 to 16 nm and HB194 from 10 to 22 nm, while the α-6T thickness was fixed at 20 nm.

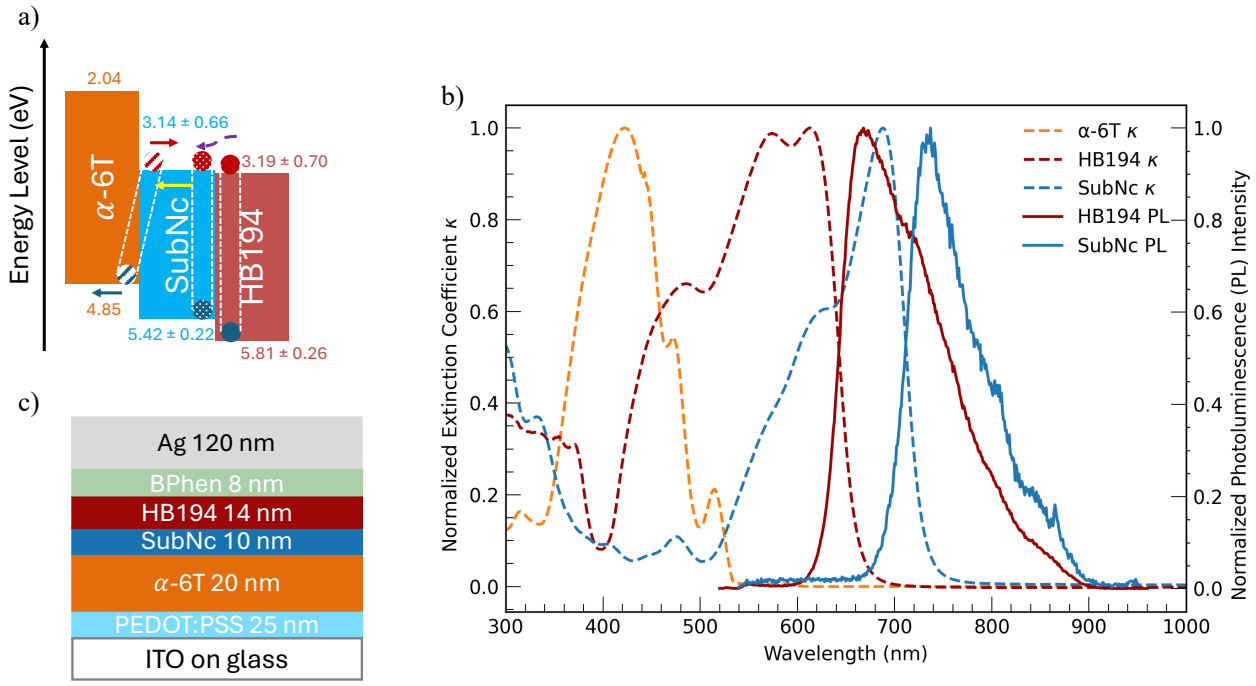


Figure 6.17: (a) Schematic showing the respective highest occupied molecular orbital (HOMO) and lowest unoccupied molecular orbital (LUMO) levels of the molecules. The values of these energy level for SubNc and HB194 are based on Ultraviolet Photoelectron Spectroscopy and Inverse Photoelectron Spectroscopy measurements measured by Dr Nicky Evans (Oxford) and α-6T from Reference [191]. The dashed purple arrow indicates the *Förster* Resonance Energy Transfer (FRET) process from HB194 to SubNc. The solid yellow arrow shows the exciton transport in SubNc layer to the interface with α-6T. Solid red and blue arrows show the exciton dissociation via hole transfer at the respective interfaces. (b) Normalized extinction coefficient spectra of all the molecules (dashed lines) and steady-state photoluminescence spectra of HB194 and SubNc (solid lines). (c) Schematic of the stacking of α-6T|SubNc|HB194 triplelayer PHJ device.

Figure 6.16 shows the dependence of J_{sc}, V_{oc}, FF, and PCE on the thicknesses of SubNc (10, 12, 14, and 16 nm) and HB194 (10, 14, 18, and 22 nm), i.e. 16 thickness combinations. J_{sc} does not vary linearly with SubNc and HB194 thicknesses, with lower values observed at the thinnest and thickest total active-layer thicknesses and a maximum occurs for the thickness

combination (12 nm SubNc, 18 nm HB194). By contrast, V_{oc} increases with thickness, ranging from approximately 0.92 to 0.96 V. FF shows the opposite trend, decreasing for thicker SubNc and HB194, which is consistent with relatively poor charge-carrier mobilities reported for these materials [200]. Overall, the best PCE was obtained for 10 nm SubNc and 14 nm HB194 and these thicknesses were selected for further investigations.

The resulting best-performing trilayer PHJ device, with an active layer of α-6T (20 nm)|SubNc (10 nm)|HB194 (14 nm), is shown in Figure 6.17c. The three molecules exhibit absorption spectra covering 340–720 nm (Figure 6.17b), effectively covering most of the visible solar spectrum. The α-6T/SubNc interface is expected to provide efficient charge separation, with both EA and IE offsets exceeding 0.4 eV (Figure 6.17a).

Figure 6.18a and b show the J-V characteristics and the EQE on a log scale for the HB194 trilayer device alongside its references. The device performance parameters are listed in Table 6.4. The HB194 trilayer device achieved a PCE of 5.3% with $V_{oc} = 0.94$ V, comparable to our Cnops-like stack (PCE 5.0%, $V_{oc} = 0.93$ V). Relative to the α-6T|SubNc device (same total acceptor thickness), the HB194 trilayer maintains V_{oc} while improving J_{sc} and FF by nearly 30%. The calculated IQE and EQE (Figure 6.19b) again show an increased SubNc contribution to photocurrent, together with contributions from HB194 and α-6T between 400 and 650 nm.

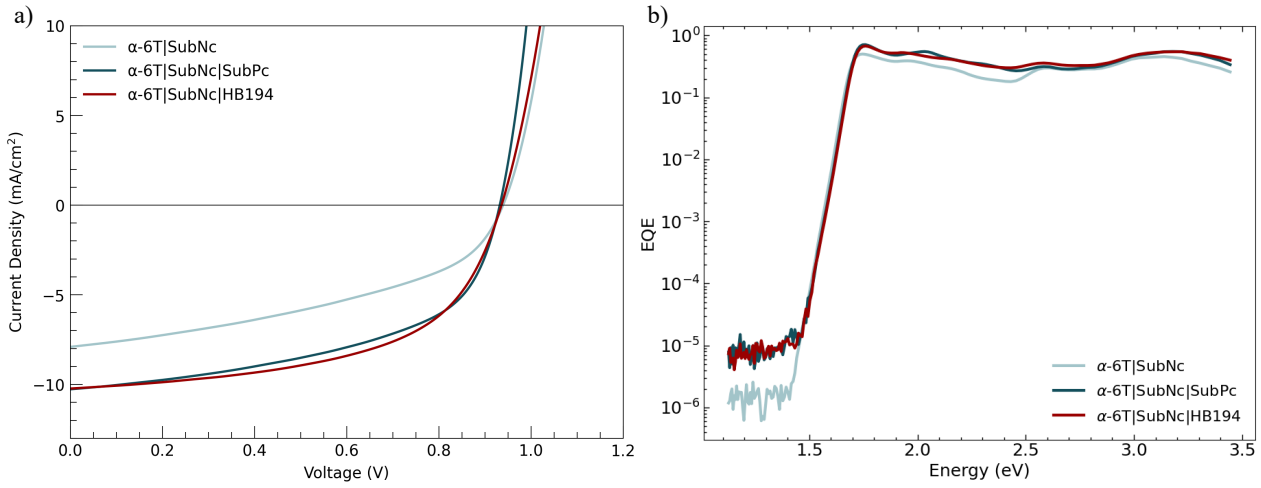


Figure 6.18: (a) Current density-Voltage characterization of α-6T|SubNc|HB194 triple-layer PHJ devices along with its references. (b) Sensitive external quantum efficiency spectra of these devices in logarithm scale. Results from best devices are shown. The thickness of each active layer and device performance can be found in Table 6.4.

Notably, the logarithmic EQE of the HB194 trilayer exhibits essentially overlapping sub-gap tail as the α-6T|SubNc and α-6T|SubNc|SubPc references, suggesting same S_1 state (assigned to SubNc) and low $\Delta E_{S1,CT}$. Despite large ΔIE and ΔEA offsets at the α-6T/SubNc interface that should allow a Type-II heterojunction, no distinct CT-state features are observed in the sub-gap range, unlike fullerene-based systems with similar large energetic offsets. Karuthedath *et al.* proposed a model in which charge–quadrupole electrostatic interactions induce energy-level bending at the donor–acceptor interface [39]. Fullerenes possess zero quadrupole moments (Q) along any axis, leading to weak interfacial bending and therefore E_{CT} well below E_{S1}. This may also account for the indistinguishable CT and S_1 state features observed in our trilayer device. Density functional theory (DFT) calculations report quadrupole moments in the π-π stacking direction (Q_π) of -66.5 and -86.8 $ea_0{}^2$ for α-6T and SubNc, respectively [232]. Their large quadrupole moments can induce strong energy level bending at the D-A interface, thereby increasing the E_{CT} close to E_{S1}.

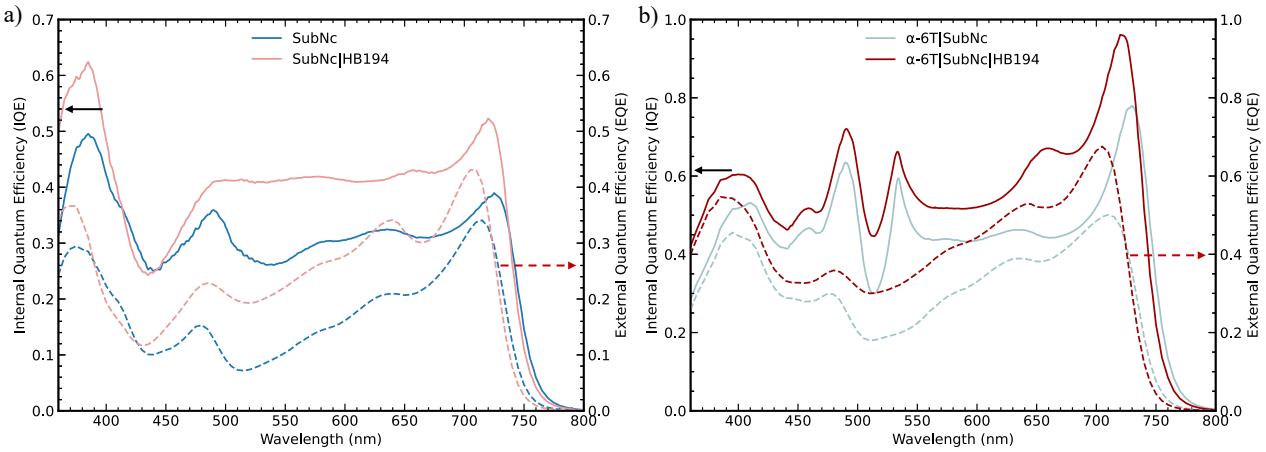


Figure 6.19: Measured sensitive external quantum efficiency and calculated internal quantum efficiency spectra based on TMM simulated device absorptance. Solid lines are IQEs and dashed lines are sEQEs. (a)Spectra for active layer being SubNc and SubNc|HB194 devices. (b) Spectra for active layer being α-6T|SubNc and α-6T|SubNc|HB194 devices.

The performance enhancement introduced by HB194 mirrors the bilayer results and suggests that incorporating HB194 can mitigate the FF drop typically observed for thick SubNc layers, as also seen in work by Cnops *et al.* [146]. We therefore demonstrate that the strategy of introducing a third absorbing layer into a bilayer PHJ can preserve V_{oc} while enhancing FF and J_{sc} in an trilayer PHJ stack, and that this is not limited to molecules from the SubPc

family [233, 234]. Specifically, if the third layer is added as an additional electron acceptor, it should (i) possess an EA similar to that of the original acceptor, (ii) enable efficient FRET to the original acceptor, and (iii) exhibit electron mobility comparable to, or greater than, that of the original acceptor.

6.3.3 Voltage Losses

The application of HB194 in bilayer and trilayer devices has helped maintain their V_{oc}, compared to their single-component and bilayer references. Therefore, we further investigate the composition of their V_{oc} losses to better understand how they are maintained.

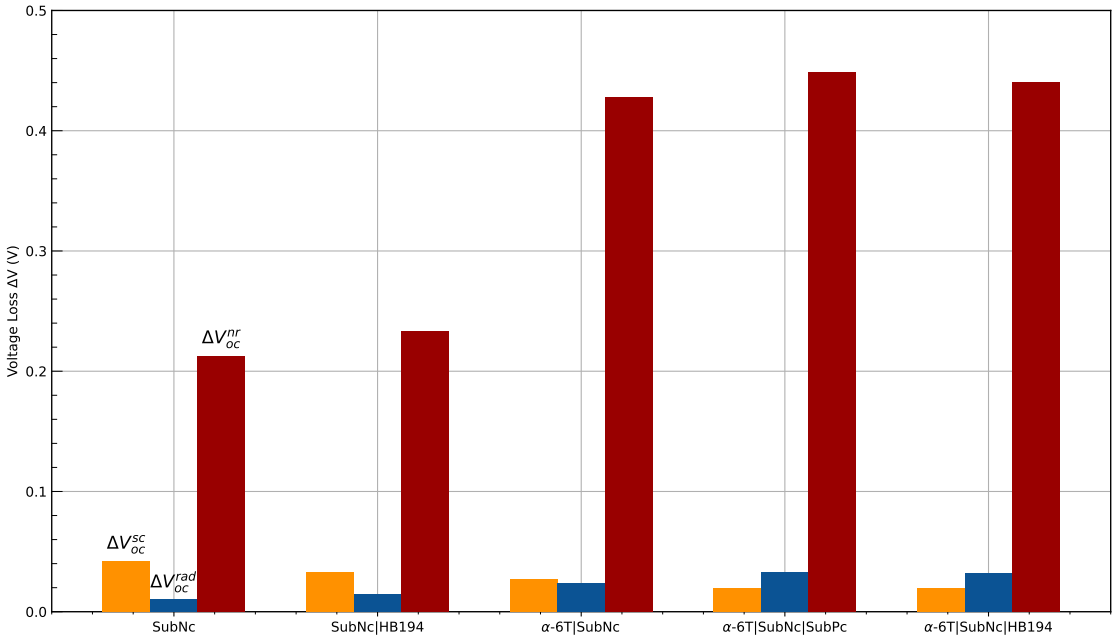


Figure 6.20: Voltage loss breakdown showing ΔV_{oc}^{sc} (orange), ΔV_{oc}^{rad} (blue), ΔV_{oc}^{nr} (red) of devices with active layer being pristine SubNc (24 nm), SubNc (10 nm)|HB194 (14 nm), α-6T (20 nm)|SubNc (24 nm), α-6T (20 nm)|SubNc (12 nm)|SubPc (18 nm), and α-6T (20 nm)|SubNc (10 nm)|HB194 (14 nm). Calculations were done follow the method described in Chapter 2.3.5.3

Table 6.4 lists the total voltage loss, ΔV_{oc}, and Figure 6.20 shows the major contributions, ΔV_{oc}^{sc}, ΔV_{oc}^{rad}, and ΔV_{oc}^{nr}, for the bilayer and trilayer PHJ devices discussed above. Owing to S_1 state dominance, the sub-gap EQE tails appear as exponential decays. Consequently, reliable E_{CT} values could not be extracted via Gaussian tail fitting within a Marcus-theory framework, limiting voltage loss comparison under that approach. Nonetheless, we employed

the DB model of Rau *et al.* to decompose ΔV_{oc} into individual loss terms [46]. To refine the voltage loss calculation, the low-energy region of the EQE was extrapolated down to 0.5 eV (beyond our measurement limit) using an exponential approximation, and each term was then evaluated using the equations and methods introduced in Chapter 2.3.5.3.

For the pristine SubNc device, the overall voltage loss is 0.54 V, of which ∼210 mV arises from non-radiative loss (ΔV_{oc}^{nr}). The SubNc|HB194 device exhibits a larger ΔV_{oc} with ∼230 mV comes from ΔV_{oc}^{nr}. Thus, adding HB194 as an acceptor in the bilayer introduces an additional ∼20 mV of ΔV_{oc}^{nr}. According to the energy-gap law, a smaller gap between electronic states increases the non-radiative decay rate. CT states, which typically lie below the S_1 states, therefore show increased non-radiative decay to the ground state [26]. Hence, we attribute the increase in the bilayer PHJ to the formation of CT states at the donor–acceptor interfaces. A similar increase in ΔV_{oc}^{nr} is observed for the α-6T|SubNc|HB194 device relative to the α-6T|SubNc reference. Overall, the increase in ΔV_{oc}^{nr} is small, suggesting that the CT states introduced by the SubNc/HB194 interfaces lie relatively close to S_1 states (i.e. small $\Delta E_{S_1,CT}$).

The radiative voltage loss, ΔV_{oc}^{rad}, is only ∼10 mV for SubNc|HB194, comparable to non-fullerene acceptor systems such as D18:Y6 BHJs [40] and PHJ solar cells employing Y6 with evaporated donors [126], where ΔV_{oc}^{rad} are around 30–40 mV. In OSCs, ΔV_{oc}^{rad} is strongly influenced by the $\Delta E_{S_1,CT}$. For fullerene-based systems that display distinct CT features in the sub-gap EQE, ΔV_{oc}^{rad} often ranges from 100 to 400 mV [99,126,127], and can be substantially larger in BHJs than in PHJs (by up to a factor of five in some fullerene studies). Despite the low voltage losses observed here, the near-zero offset in the bilayer imposes the usual trade-off of reduced driving force and hence inefficient exciton separation, so performance remains below that of solution-processed counterparts.

Upon introducing α-6T to the SubNc|HB194 bilayer, the trilayer α-6T|SubNc|HB194 exhibited an increased ΔV_{oc} of 0.77 V. The non-radiative component, ΔV_{oc}^{nr}, accounts for ∼440 mV, nearly double that of the SubNc|HB194 device. We attribute this increase to additional CT states formed at the α-6T/SubNc interface, although no distinct CT state feature is observed in the EQE spectrum due to low $\Delta E_{S_1,CT}$. While large EA and IE offsets at this interface facilitate efficient exciton separation, they also open further non-radiative decay pathways via low-energy CT states. An increase in ΔV_{oc}^{rad} and a decrease in ΔV_{oc}^{sc} are again observed for

the HB194 trilayer relative to the α-6T|SubNc reference, mirroring the bilayer results. The former is consistent with a larger $\Delta E_{S_1,CT}$, and the latter with improved photocurrent. Compared with the Cnops-like trilayer employing SubPc, our HB194 trilayer shows almost identical voltage loss terms, plausibly because HB194 and SubPc have similar EA, contributing similar ΔV_{oc}^{nr} at their interface with SubNc. The reduced ΔV_{oc}^{sc} in both HB194-containing bilayer and trilayer devices offsets their higher ΔV_{oc}^{rad} and ΔV_{oc}^{nr} relative to HB194-free references, thereby preserving the overall V_{oc}.

In summary, the HB194 bilayer PHJ exhibits a relatively low $\Delta V_{oc} \approx 550$ mV and an exceptionally low $\Delta V_{oc}^{nr} \approx 230$ mV, comparable to top solution-processed NFA OSCs with PCE of 19.6% ($\Delta V_{oc} \approx 560$ mV, $\Delta V_{oc}^{nr} \approx 240$ mV) [19]. The well-performing HB194 trilayer demonstrates a total V_{oc} loss of ~770 mV. In the literature, evaporated fullerene devices often report total voltage losses in the range 670–1100 mV [126], placing our HB194 trilayer among evaporated OSCs with relatively low losses. Overall, HB194 enhances the performance of the α-6T|SubNc device without sacrificing V_{oc}, as a lower ΔV_{oc}^{sc} compensates for increases in ΔV_{oc}^{rad} and ΔV_{oc}^{nr}, similar to SubPc.

6.3.4 Conclusions

In this section, we systematically investigated the integration of HB194 as a VTE non-fullerene acceptor in simple bilayer and trilayer PHJ organic solar cell architectures. IE and EA characterised by UPS and IPES (Chapter 5.3.1) on pristine films of SubNc and HB194, suggest a near-zero EA offset and a large IE offset of ~0.39 eV. Efficient FRET from HB194 to SubNc was verified via PL-quenching measurements (Chapter 5.4.3.1).

Bilayer PHJ devices incorporating HB194 exhibited improved J_{sc} and FF relative to neat SubNc references, while maintaining a low total voltage loss of ~550 mV, an exceptionally low ΔV_{oc}^{rad} of ~10 mV and ΔV_{oc}^{nr} of ~230 mV. These values are comparable to state-of-the-art solution-processed NFA systems. We attribute the device improvements to two main factors: HB194 (i) introduces additional light absorption in the spectral region where SubNc absorbs weakly, (ii) enhances the electron-transport environment within the device.

The trilayer device, α-6T|SubNc|HB194, further confirms HB194's potential as a secondary acceptor that enhances light harvesting without compromising voltage. It achieves a PCE

of 5.3% and a relatively low ΔV_{oc} of 770 mV. These are ∼30% improvements in J_{sc} and FF relative to the α-6T|SubNc reference. While HB194-based bilayer and trilayer devices show slightly increased ΔV_{oc}^{rad} and ΔV_{oc}^{nr}, these increases are offset by a lower ΔV_{oc}^{sc}, thereby retaining V_{oc}. This voltage preservation and enhanced charge extraction resemble trends observed in the SubPc-based trilayer PHJ devices proposed by Cnops *et al.*, demonstrating that HB194 is a viable alternative to SubPc and its derivatives. For adding a third layer as an additional electron acceptor with these benefits, the layer should (i) possess an EA similar to that of the original acceptor, (ii) enable efficient FRET to the original acceptor, and (iii) exhibit electron mobility comparable to, or greater than, that of the original acceptor.

Overall, these results prove HB194 as a viable electron acceptor to replace SubPc in trilayer PHJ OSCs. Further performance improvement could be achieved through interfacial and morphological optimisation, or by transitioning to ternary bulk heterojunctions. In parallel, extracting E_{CT} and E_{S1} will help understand the correlation between ΔV_{oc}^{nr} and $\Delta E_{S1,CT}$ in these bilayer and trilayer PHJ systems, which exhibit exponential tails in the low-energy region of the EQE spectra. Developing a methodology to extract CT state information from these low-$\Delta E_{S1,CT}$ systems could be a meaningful direction for future investigation.

6.4 Application of FRET in Bulk Heterojunction OSCs

6.4.1 Materials and Devices

Solar cells comprising SubNc and DCV3T in a PHJ configuration have demonstrated promising device performance, as discussed in Chapter 6.2. However, the limited D-A interfacial area in PHJ restricts efficient free charge carrier generation, particularly for DCV3T, which has an exciton diffusion length of approximately 6 nm [138]. As the efficiency of FRET from DCV3T to SubNc is constrained by the R_0, not all DCV3T molecules within PHJ configuration lie within the effective energy transfer range and can therefore participate in FRET.

To further investigate the photovoltaic potential of these two molecules in a more widely adopted device architecture, we fabricated SubNc:DCV3T BHJ solar cells. The BHJ devices were constructed using the following layer stack: ITO (135 nm)/PEDOT:PSS (25 nm)/SubNc:

DCV3T (40 nm)/BPhen (8 nm)/Ag (120 nm). The PEDOT:PSS HTL was employed to maximise device performance.

Donor-to-acceptor (D:A) volume ratios of 1:0.5, 1:1, 1:1.5, 1:3, and 1:5 were selected based on previous reports of analogous fullerene-based systems (SubNc:$PC_{70}BM$) [200]. For the SubNc:DCV3T (1:0.5 by vol) devices, the evaporation rates were 0.2 Å/s for SubNc and 0.1 Å/s for DCV3T. For the 1:5 blend, SubNc was deposited at 0.2 Å/s and DCV3T at 1 Å/s.

6.4.2 Device Performance

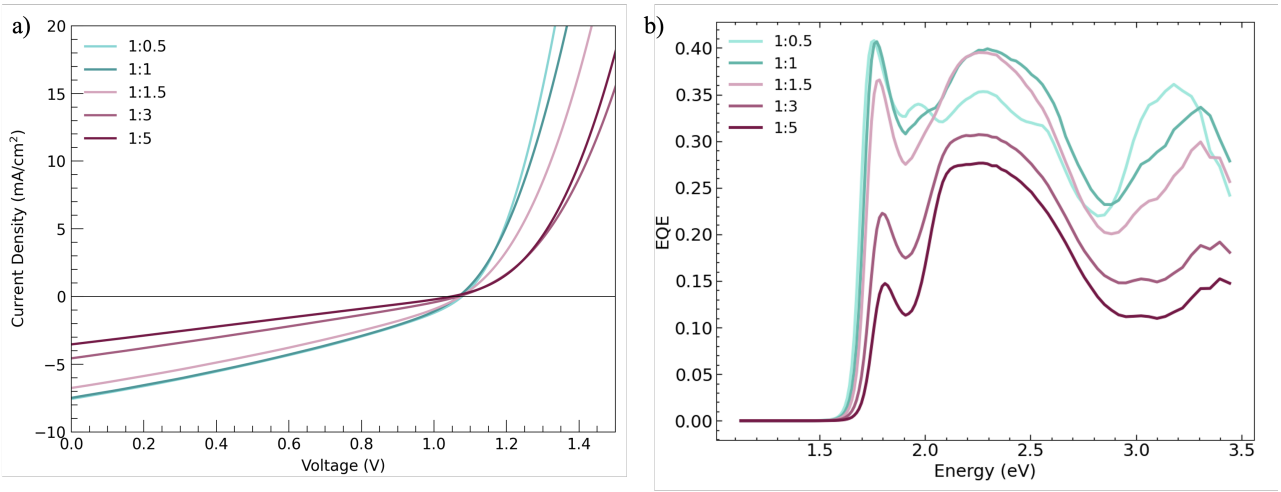


Figure 6.21: (a) Current density-voltage characteristics and (b) external quantum efficiency of SubNc:DCV3T bulk heterojunction (BHJ) devices with 1:0.5, 1:1, 1:1.5, 1:3, 1:5 donor-to-acceptor ratios by vol.

Figure 6.21 shows the J–V characteristics and EQE spectra of the best-performing devices from each blend, with the key photovoltaic parameters summarised in Table 6.5. Overall, these blends exhibit significantly lower FF than previous SubNc|DCV3T PHJ devices (FF=0.43), suggesting unfavourable microstructure and charge carrier transport environment in the blend films. As the concentration of DCV3T increases, the J_{sc}, FF, and PCE decrease approximately linearly, while the photovoltaic bandgap (E_g^{PV}) and the voltage loss in the DB picture (ΔV_{oc}^{DB}) increase approximately linearly, except for the SubNc:DCV3T 1:0.5 blend, as shown in Figure 6.22. This continuous decline in performance suggests the accumulation of detrimental characteristics in the blends with increasing DCV3T content. Additionally, contributions from DCV3T (in the range of 1.9–2.8 eV, i.e., 442–652 nm) and SubNc (1.6–1.9 eV, i.e., 652–775 nm)

to the EQE spectrum maximise at D:A ratio of 1:1. The EQE contributions from both SubNc and DCV3T are the lowest in the 1:5 blend. To further explore the mechanisms underlying this performance decline, the 1:1 and 1:5 blends are therefore chosen as representative cases.

Table 6.5: Performance characteristics of the best-performing pixels for solar cell devices with 40 nm SubNc:DCV3T active layers in 1:0.5, 1:1, 1:1.5, 1:3 and 1:5 donor-to-acceptor ratios (by vol).

D:A Ratio	J_{sc} (mA/cm^2)	V_{oc} (V)	E_g^{PV} (eV)	$\Delta V_{oc-loss}$ (V)	FF	PCE (%)
1:0.5	7.6	1.08	1.70	0.62	0.32	2.61
1:1	7.5	1.07	1.71	0.64	0.32	2.58
1:1.5	6.8	1.07	1.72	0.65	0.31	2.27
1:3	4.6	1.07	1.74	0.67	0.27	1.33
1:5	3.5	1.05	1.75	0.70	0.26	0.95

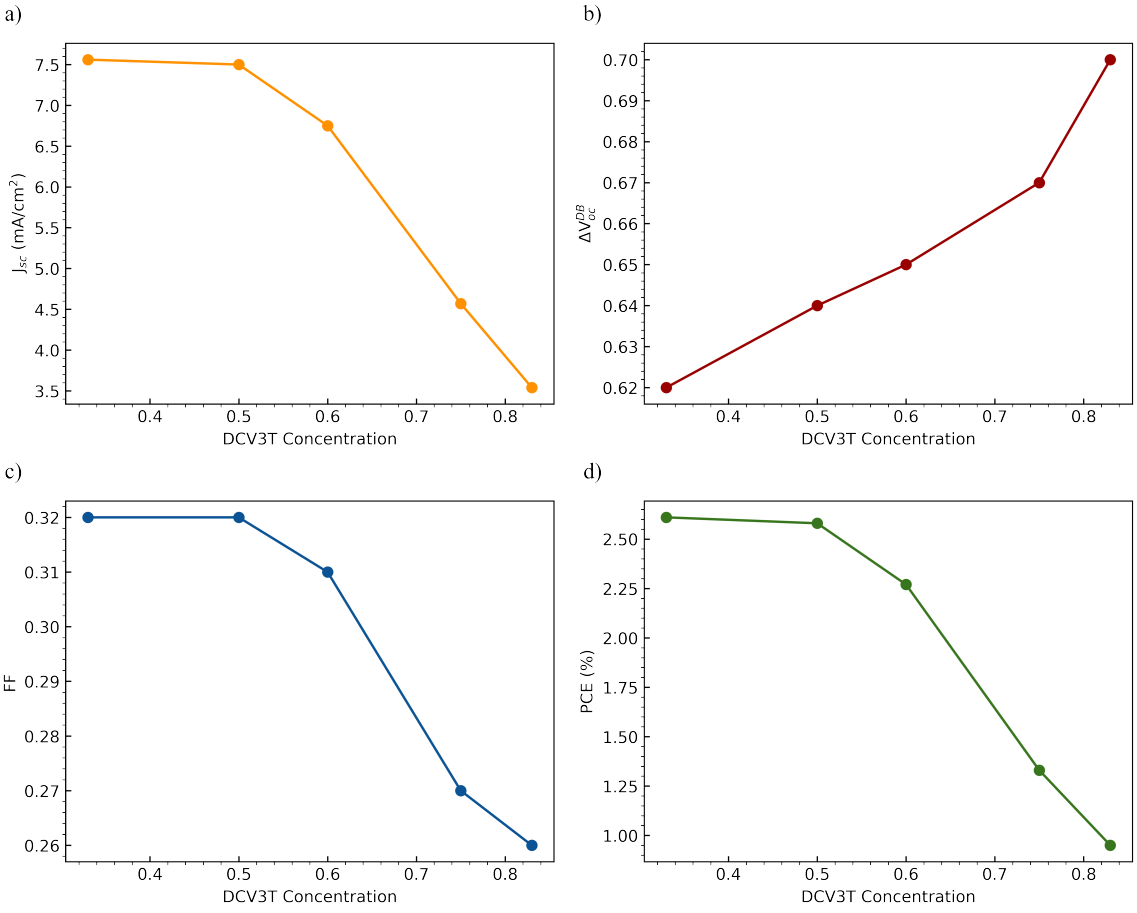


Figure 6.22: The dependence of (a) short-circuit current (J_{sc}), (b) voltage loss in Detail Balance picture ΔV_{oc}^{DB}, (c) fill factor (FF) and (d) power conversion efficiency (PCE) on DCV3T concentration in SubNc:DCV3T BHJ devices.

The V_{oc} values for the 1:1 and 1:5 SubNc:DCV3T blends are 1.07 V and 1.05 V respectively, significantly higher than those reported for their fullerene-based analogue (SubNc:$PC_{70}BM$,

V_{oc}=0.9 V) [200], indicating improved energy level alignments and reduced voltage losses. The SubNc:DCV3T 1:1 device achieved a J_{sc} of 7.5 mA cm^{-2}, a FF of 0.32, and a PCE of 2.6%. These figures are not better than the fullerene-based analogue (SubNc:$PC_{70}BM$ (1:5) BHJ) with optimised D:A ratio and a similar active layer thickness of 50 nm (J_{sc} = 8.1 mA cm^{-2}, FF = 0.45, PCE = 3.2%) [200]. However, when compared to other evaporated OSCs using non-fullerene acceptors (NFAs), for instance, the SubNc|BTIC-H PHJ device (J_{sc} = 3.5 mA cm^{-2}, FF = 0.43, PCE = 1.2%) [127], this device outperforms. TAS measurements previously confirmed efficient electron transfer in this blend. The absorptance spectra in Figure 6.25b also show good photon collection across the visible region for the SubNc:DCV3T 1:1 device, with peak absorptance approaching unity. Hence, the relatively low J_{sc} may be attributed primarily to issues in free charge carrier collection, for example due to low charge carrier mobility in the blend [196, 235]. Low charge carrier mobilities have been reported for pristine SubNc (μ_h=1.61×10^{-4} cm^2 V^{-1} s^{-1}) [200] and DCV3T (μ_e=2.46×10^{-6} cm^2 V^{-1} s^{-1}) [203] films, which suggests an overall low mobility in the blended films. The low FF may further indicate that the device relies on field-assisted charge generation and morphology issues, and the latter will be investigated in the following section.

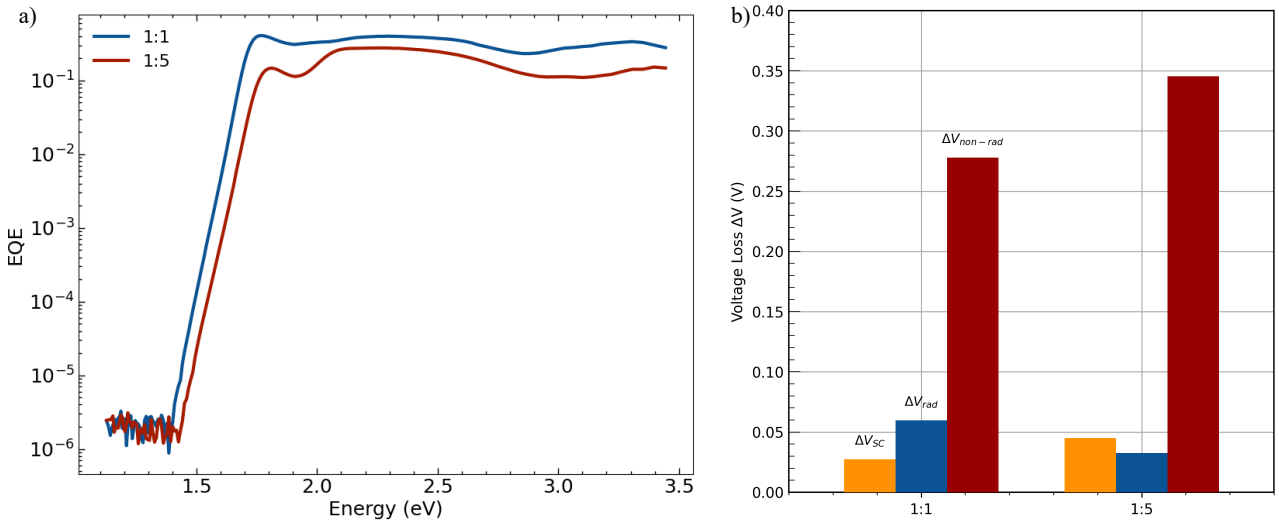


Figure 6.23: (a) Sensitive External Quantum Efficiency spectra of SubNc:DCV3T 1:1 by vol (blue) and 1:5 by vol (red) BHJ devices in logarithm scale. (b) Breakdown of voltage losses for the corresponding devices, showing ΔV_{oc}^{sc} (orange), ΔV_{oc}^{rad} (blue), and ΔV_{oc}^{nr} (red).

Notably, the SubNc:DCV3T 1:1 device exhibits an exceptionally low total voltage loss of

0.64 V (Table 6.5), comparable to that of state-of-the-art solution-processed NFA OSCs such as PM6:D18:L8-BO, which reports 0.56 V [19]. Further decomposition of the voltage losses under DB model reveals that the SubNc:DCV3T 1:1 blend has ΔV_{oc}^{nr} of 280 meV (Figure 6.23b), which is close to the 240 meV observed in PM6:D18:L8-BO devices [19]. The EQE spectrum of the blend, when plotted on a logarithmic scale, displays an exponential tail where features associated with the CT and S_1 states are indistinguishable (Figure 6.23a). This spectral profile closely resembles that of low-offset NFA systems and suggests a small energetic offset between CT and S_1 states ($\Delta E_{S1,CT}$) in the blend, potentially accounting for its low ΔV_{oc}^{nr} [99, 134].

Compared with the SubNc:DCV3T 1:1 blend, the 1:5 blend exhibits overall poorer device performance, with the most significant reduction observed in J_{sc}. According to TMM simulations under the assumption of IQE=100%, the SubNc:DCV3T 1:1 blend is projected to have a maximum theoretical J_{sc} of approximately 16.2 mA/cm^2, while the 1:5 blend is projected to reach 14.5 mA/cm^2. This is consistent with the overall lower absorptance of the 1:5 blend, as shown by the solid lines in Figure 6.25b, as well as the lower total number of absorbed photons compared with the 1:1 blend, shown by the dashed lines in the same figure. For the 1:5 blend, the increased DCV3T concentration does not enhance light absorptance, but instead caused reduction of SubNc absorptance. However, as indicated by the TMM simulations, the difference in absorptance has a limited influence on J_{sc}. Experimentally, the J_{sc} of the SubNc:DCV3T 1:1 blend is more than twice that of the 1:5 blend, which therefore suggests that the efficiency of free charge carrier collection may be significantly lower in the 1:5 blend. It is primarily attributed to an unfavourable charge transport environment caused by the high DCV3T concentration. The pronounced π-stacking of DCV3T results in strong electronic couplings that hinder three-dimensional transport, as demonstrated in the work by Schrader *et al.* [236]. Hence, DCV3T can be bad at charge transport if molecules are not stacked in transport-favourable direction i.e. face-on.

Figure 6.23b shows the major voltage losses ΔV_{oc}^{sc}, ΔV_{oc}^{rad}, and ΔV_{oc}^{nr} of the two blends. It is also worth noting that the V_{oc} values of the two blends differ, in contrast to their fullerene analogue (SubNc:$PC_{70}BM$ BHJ), where V_{oc} remains unchanged with varying D:A ratios from 1:1 to 1:7 [200]. This suggests that variations in the concentration of DCV3T within the blend may affect the interfacial energetics and morphology, leading to changes in V_{oc}.

As shown in Figure 6.23b, the SubNc:DCV3T 1:5 blend has ΔV_{oc}^{sc} from imperfect J_{sc} of 45 meV, which is higher than the 27 meV observed in the 1:1 blend. This result is consistent with the lower J_{sc} measured for the 1:5 blend, indicating inefficient charge extraction and reduced absorption. A decrease in ΔV_{oc}^{rad} is observed for the 1:5 blend, suggesting a lower density of radiative emission sites, namely fewer D-A interfaces, within the blend [81, 99].

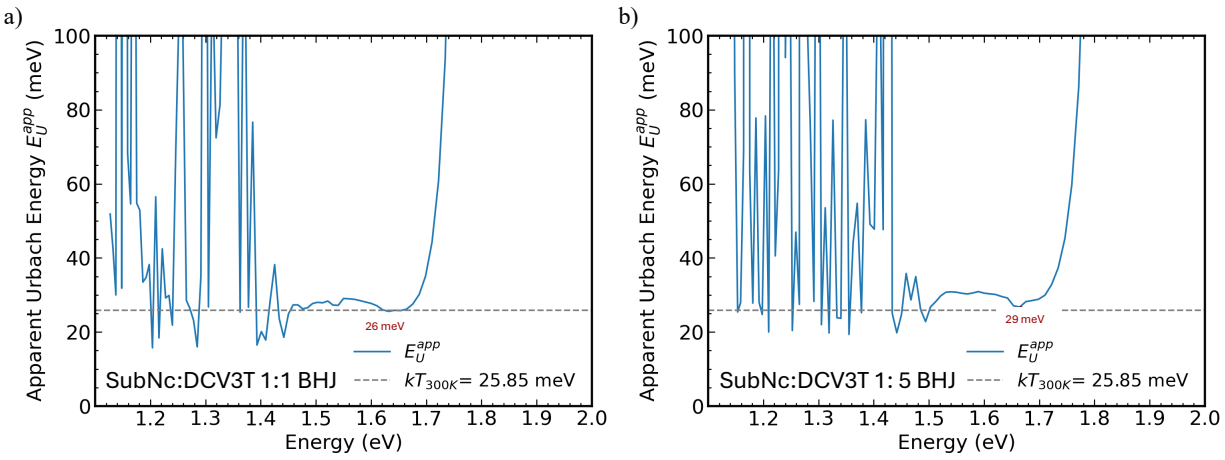


Figure 6.24: Apparent Urbach energy (E_U^{app}) of (a) SubNc:DCV3T bulk heterojunction (BHJ) 1:1 (b) 1:5 by vol solar cell devices. The minimum value of E_U^{app} in the sub-gap region is labelled in the plot with red text.

Interestingly, the ΔV_{oc}^{nr} of the SubNc:DCV3T 1:5 blend is approximately 67 meV higher than that of the 1:1 blend. It has been reported that ΔV_{oc}^{nr} can be influenced by several factors, including the $\Delta E_{S1,CT}$ [39, 41, 132], D-A blend morphology [228, 229], interfacial molecular orientation and packing [63, 91], and energetic disorder [121, 227]. In the present study, $\Delta E_{S1,CT}$ of both blends cannot be determined from the EQE spectra alone due to the S_1-state dominance. Therefore, $\Delta E_{S1,CT}$ may differ between the two blends, contributing to ΔV_{oc}^{nr} difference. As neither blend underwent microstructural tuning during fabrication, their molecular packing and orientations can be assumed to reflect unimplemented configuration. The SubNc:DCV3T 1:5 blend may therefore exhibit unfavourable microstructural characteristics, such as an edge-on molecular orientation, which are investigated by GIWAXS in the following section. Furthermore, the minimum E_U^{app} values in the sub-gap region were determined from their EQE to be 26 meV for the SubNc:DCV3T 1:1 blend and 29 meV for the 1:5 blend (Figure 6.24). This indicates a slightly higher energetic disorder in the sub-gap states of the SubNc:DCV3T 1:5

blend [119,120]. Consequently, the observed difference in energetic disorder, and thus in ΔV_{oc}^{nr}, is possible to be related to variations in the blend morphology.

6.4.3 GIWAXS Study on Molecular Orientation and Packing

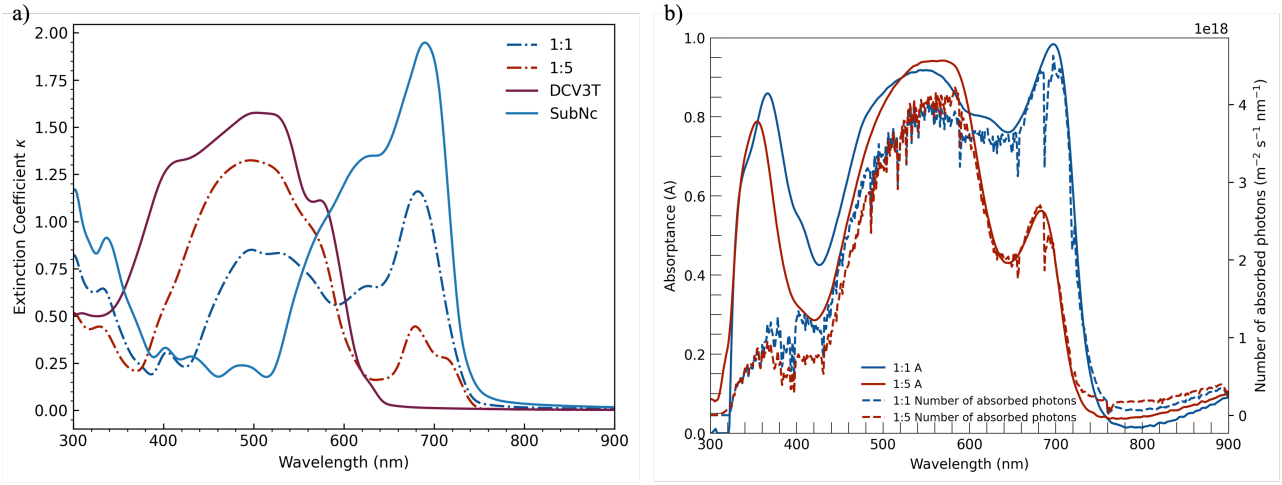


Figure 6.25: (a) Extinction coefficients of SubNc (solid blue), DCV3T (solid purple), SubNc:DCV3T (1:1 by vol, dash-dot blue), and SubNc:DCV3T (1:5 by vol, dash-dot red). (b) Absorptance (A) and numbers of absorbed photons spectra of SubNc:DCV3T 1:1 by vol (blue) and 1:5 by vol (red) bulk heterojunction solar cell devices. Absorptance spectra measured by Katherine Trinkaus (Oxford).

To further evaluate the origin of the difference in ΔV_{oc}^{nr}, κ and the complex spatial arrangements of the pure D/A films and D:A blends using ellipsometric spectroscopy and GIWAXS were determined. The analysis of ellipsometric spectroscopy and measurement of device absorptance spectra were done by Katherine Trinkaus (Oxford) and GIWAXS by Olivia Gough (Oxford). Figure 6.25a presents the ordinary component of κ spectra of the blends and the individual molecules. The κ spectrum of the pure DCV3T film exhibits shoulders at around 400 nm, 500 nm, 540 nm, and 580 nm. In the SubNc:DCV3T 1:1 blend, the spectral features of DCV3T are less pronounced and more hybridised with SubNc features from 400 to 600 nm, due to its lower concentration. In the SubNc:DCV3T 1:5 blend, stronger broadening was observed for DCV3T features, suggesting higher disorder [27,237].

Figure 6.26b and c shows the GIWAXS 2D images of pristine DCV3T and SubNc film on silicon substrates. It can be seen that DCV3T exhibits a preference for edge-on orientation,

as the prominent lamellar feature appears OoP while the higher q-space feature, attributed to π–π stacking, is in-plane (IP). This indicates that the π–π orbital overlap occurs predominantly perpendicular to the substrate, with the long edge of the DCV3T molecule lying parallel to the surface it adsorbs onto.

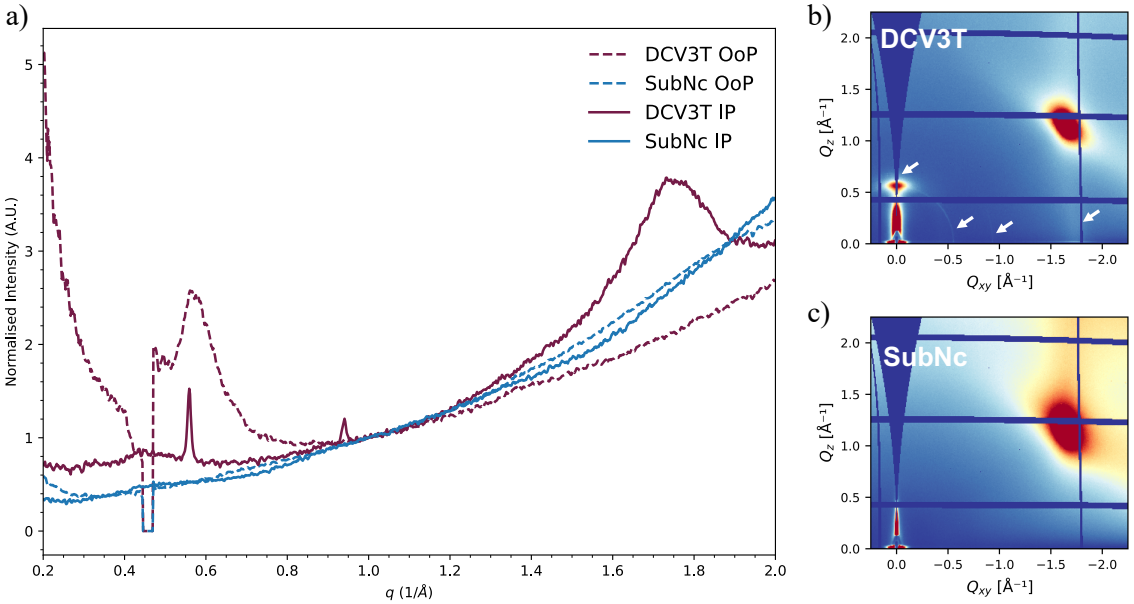


Figure 6.26: (a) Normalised integrated in-plane (IP) and out-of-plane (OoP) GIWAXS profiles of pure DCV3T (green) and SubNc (yellow) films over the azimuthal ranges 0–15° and 65–80°, respectively. Solid lines represent the IP integrations, and dashed lines correspond to the OoP integrations. GIWAXS 2D images of 40 nm films of (b) DCV3T (c) SubNc, deposited on Si substrates held at room temperature. White arrows (from left to right) show the lamellar OoP peak, lamellar isotropic (IP) peak, and π–π stacking (IP) features in DCV3T film. The intensity range plotted for (b) and (c) is 0-1800. Integrated IP and OoP GIWAXS profiles and 2D images are provided by Olivia Gough (Oxford).

Table 6.6: Morphology parameters extracted from the GIWAXS measurements (2D GIWAXS images shown in Figure 6.26) of 40 nm films of DCV3T pristine films deposited on Si wafers.

Materials	Direction	Peak Position (1/Å)	Crystalline Coherence Length (Å)	Peak origin
	OoP	0.572±0.010	50.7±4.3	Lamellar
	OoP	0.478±0.016	196±50	Lamellar
DCV3T	IP	0.574±0.003	48.9±3.1	Lamellar (isotropic)
	IP	0.940±0.001	527±36	Lamellar (isotropic)
	IP	1.74±0.13	20.9±0.2	$\pi - \pi$ Stacking

As shown in Figure 6.26c, SubNc appears amorphous, with no observable Bragg peaks in the pure film under X-ray. The peaks observed in the pure DCV3T sample (Figure 6.26a) occur at similar positions to those in the blend, although the blend peaks are significantly

broadened (Figure 6.27a). This suggests that mixing DCV3T with amorphous SubNc reduces the crystallinity of DCV3T and disrupts its molecular order, which is reported in literature when an analogous molecule DCV5T is blended with another acceptor molecule [238]. It is also worth noting that the SubNc:DCV3T 1:5 blend exhibits higher Bragg peak amplitudes (Figure 6.27a), which is likely a consequence of its higher DCV3T content. It should also be noted that the bright feature at an azimuthal angle ∼45° is from the silicon substrate and is not from the DCV3T:SubNc blend.

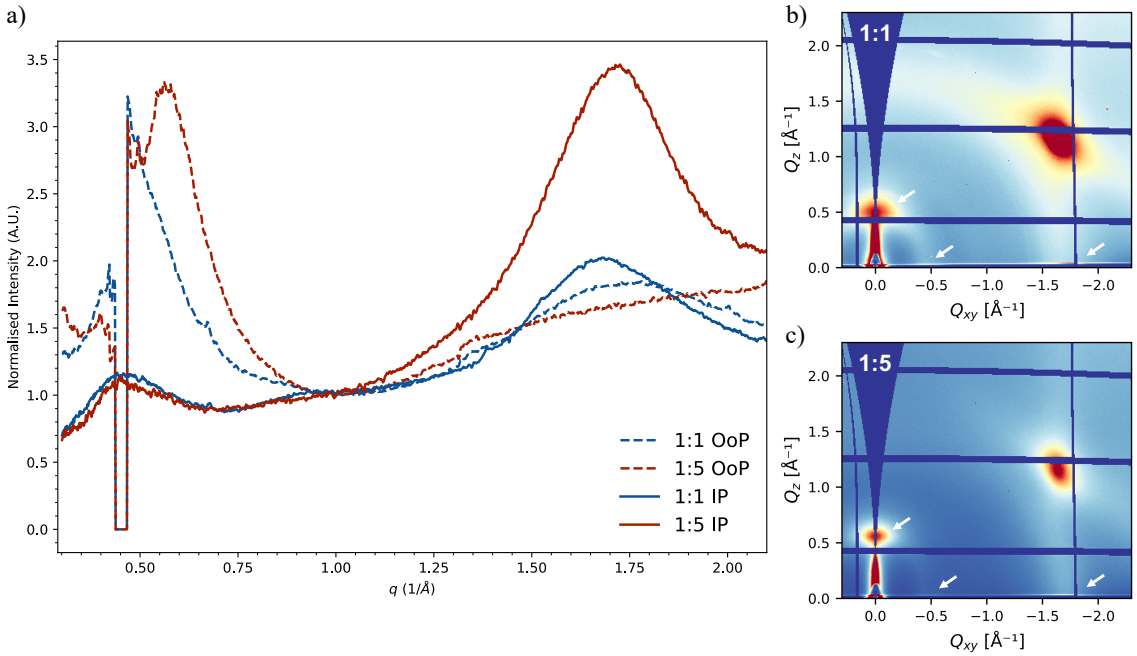


Figure 6.27: (a) Normalised integrated in-plane (IP) and out-of-plane (OoP) GIWAXS profiles of SubNc:DCV3T blend films at 1:1 (red) and 1:5 (blue) (by vol) over the azimuthal ranges 0–15°and 65-80°, respectively. Solid lines represent the IP integrations, and dashed lines correspond to the OoP integrations. The peak positions of the pure materials (SubNc and DCV3T) are provided in Figure 6.26 and Table 6.6. (b) and (c) are GIWAXS 2D images of 40 nm SubNc:DCV3T blend films at 1:1 and 1:5 (by vol), respectively, deposited on Si wafers. The intensity range plotted for (b) and (c) is 0-1800. White arrows shows the lamellar OoP peak, lamellar isotropic (IP) peak, and π–π stacking (IP) DCV3T features observed in both blends. Integrated IP and OoP GIWAXS profiles and 2D images are provided by Olivia Gough (Oxford).

A relative comparison based on Scherrer analysis was performed on the blend peaks to determine the crystallite coherence length (L), as summarised in Table 6.7. As the content of DCV3T increases, the lamellar stacking distance decreases, from 12.5±0.1 Å to 11.1±0.1 Å. However, notably the L of the prominent OoP lamellar feature in the SubNc:DCV3T 1:1 blend is ∼28% larger than that of the analogous feature in the 1:5 blend, calculated to be 29.9±1.4 Å

and 23.4±1.2 Å, respectively. It is somewhat surprising that the lower DCV3T concentration in the SubNc:DCV3T 1:1 blend results in a longer L compared to the higher DCV3T content in the 1:5 blend. A shorter L suggests the formation of smaller crystallites, which could be correlated with reduced phase separation, thereby leading to higher ΔV_{oc}^{nr} [228]. Whilst the lamellar stacking seems to worsen with increased DCV3T content, the $\pi - \pi$ stacking sees a slight increase in L, from 10.3±0.1 Å in the SubNc:DCV3T 1:1 blend, to 11.1±0.1 Å. This could suggest higher DCV3T content, whilst promoting tighter molecular packing, suppresses lamellar crystallinity, consistent with the observed increase in non-radiative losses. Furthermore, the fact that there is higher crystallite coherence in the OoP direction than in the IP direction reflects that lamellar ordering is the dominant long-range structural motif in the blend, indicating crystalline anisotropy. The $\pi - \pi$ stacking is usually considered to be locally ordered but less extended laterally. All data were normalised around $q \sim 1.1$ Å^{-1}, where only background scattering is present.

Table 6.7: Morphology parameters extracted from the GIWAXS measurements (2D GIWAXS images shown in Figure 6.27) of 40 nm films of SubNc:DCV3T blend 1:1 (by vol) and 1:5 (by vol) deposited on Si substrates.

Materials	Direction	Peak Position (1/Å)	Stacking Distance (Å)	Crystalline Coherence Length (Å)	Peak origin
1:1	OoP	0.501 ± 0.004	12.5 ± 0.1	29.9 ± 1.4	Lamellar
	IP	0.445 ± 0.004	14.1 ± 0.1	15.2 ± 0.3	Lamellar (isotropic)
	IP	1.676 ± 0.002	3.75 ± 0.01	10.3 ± 0.1	$\pi - \pi$ Stacking
1:5	OoP	0.556 ± 0.005	11.1 ± 0.1	23.4 ± 1.2	Lamellar
	IP	0.458 ± 0.004	13.7 ± 1.3	18.1 ± 0.6	Lamellar (isotropic)
	IP	1.705 ± 0.001	3.68 ± 0.00	11.1 ± 0.1	$\pi - \pi$ Stacking

The strongest lamellar peaks are observed OoP, but the 2D GIWAXS images also reveal a faint isotropic ring around $q \sim 0.45$ Å^{-1} (Figure 6.27b and c), as confirmed by the IP integrations. This was assigned as scattering of DCV3T based on the reference samples of pure DCV3T and SubNc given in Figure 6.26.

Since charge transport is generally more efficient along the direction of π–π orbital overlap, a face-on orientation is usually more favourable in OSCs [239]. Face-on orientation also has been shown to contribute to better absorption in OSCs [240, 241]. In particular, for edge-on oriented DCV3T in the blends, the strong electronic coupling arising from π-stacking further contributes to reduced charge transport efficiency. The lack of face-on orientation preference

in both blends may therefore further contribute to their relatively low FF values [63, 91].

6.4.4 Conclusions

In this section, the molecular pair SubNc and DCV3T was employed, which exhibits FRET, in a BHJ device configuration, varying their D:A volume ratio from 1:0.5 to 1:5. An approximately linear decrease in J_{sc} from 7.6 to 3.5 mA/cm^2, FF from 0.32 to 0.23, and PCE from 2.6% to 1.0% was observed as the DCV3T volume fraction increased from 50% to 83%. To investigate the origins of this performance change, the analyses are focused on two representative blends: 1:1 and 1:5.

The best-performing SubNc:DCV3T 1:1 blend device exhibited a high V_{oc} of 1.07 V and an exceptionally low total voltage loss of 0.64 V, which is lower than any reported value for fullerene-based evaporated OSCs [126], while still achieving a working PCE of 2.6%. Its non-radiative voltage loss ΔV_{oc}^{nr} is comparable to that of state-of-art NFA based OSCs, and its EQE spectrum shown similarly indistinguishable CT and S_1 state features. However, the PCE of the SubNc:DCV3T system remains significantly lower than that of NFA systems, likely due to low charge carrier mobility, unfavourable molecular orientation and packing. A higher ΔV_{oc}^{nr} was observed in the SubNc:DCV3T 1:5 blend compared to the 1:1 blend, which was hypothesised to originate from increased energetic disorder relating to differences in blend morphology. Extinction coefficient profiles and GIWAXS measurements of the two blends revealed higher disorder and a potentially reduced out-of-plane lamellar crystalline coherence length for DCV3T, i.e. smaller crystallite size, in the SubNc:DCV3T 1:5 blend, supporting this hypothesis. Additionally, a preferential edge-on orientation of DCV3T molecules in both blends were identified, which likely hinders efficient charge transport in the direction perpendicular to the substrate and may contribute to the low FF (0.32 and 0.26) observed in the both blends.

These findings present a successful example of employing evaporated molecules to replicate the CT state characteristics in low-$\Delta E_{S1,CT}$ state-of-art SP NFA-based OSCs, achieving a functional VTE OSC with comparable low voltage-loss and $\Delta E_{S1,CT}$. A correlation between high ΔV_{oc}^{nr} and elevated sub-gap energetic disorder, higher disorder, and smaller crystallite size are proposed. To improve the performance of this system, it may be worthwhile to explore the use of a templating layer beneath the photoactive layers to promote IP molecular orientation [239],

thereby enhancing charge transport. However, the intrinsically low charge carrier mobilities of the photoactive molecules remain a limiting factor and would require targeted molecular engineering to overcome. Ultimately, achieving high device performance in VTE OSCs continues to be challenging without the development of new evaporable NFAs that possess optimised optical, electronic, and morphological properties.

7 | Exploiting FRET in Half-solution Processed Half-evaporated OSCs

Accompanied by the reduced energy losses enabled by the development of non-fullerene acceptors (NFAs), the energy difference $\Delta E_{S1,CT}$ between the charge transfer (CT) state and the lowest excited singlet state (S_1) in organic solar cells has been reduced to approximately 0.1 eV [39,41,77–79]. At such low $\Delta E_{S1,CT}$ values, spectral features associated with S_1 dominate over those of the CT state in both external quantum efficiency (EQE) and electroluminescence (EL) spectra. Consequently, extracting the energies of the S_1 and CT states using conventional methods, typically effective in fullerene-based systems with large $\Delta E_{S1,CT}$ and clearly resolved CT features, becomes increasingly challenging. In this chapter, three hybrid systems comprising a solution-processed NFA and an evaporated electron donor, along with their C_{60} reference systems exhibiting a range of $\Delta E_{S1,CT}$ values, are systematically investigated. A linear correlation between $\Delta E_{S1,CT}$ and radiative voltage loss is found, offering a complementary approach for probing CT state energies in PHJ systems with low $\Delta E_{S1,CT}$.

A manuscript based on the data presented in Sub-chapter 6.2 and this chapter is in preparation and will be submitted by M. Zhu, D. Tsokkou, K. Trinkaus, N. Evans, P. Kaienburg, K. Meerholz, S. Olthof, N. Banerji, M. Riede.

7.1 Introduction

For fullerene-based OSCs, the sub-gap EQE tail typically exhibits clear CT absorption features, enabling robust modelling using classical Marcus theory [113–115] and Marcus–Levich–Jortner theory [242], which incorporates quantum effects. These models have been widely used to extract E_{CT} and E_{S1}, offering valuable insights into the relationship between voltage losses and charge transfer processes [81, 82, 99, 116]. It has been demonstrated that lowering the energy gap between the lowest excited singlet state S_1 and CT state in OSC systems, i.e. reducing $\Delta E_{S1,CT}$, effectively minimises voltage losses [99]. However, a trade-off between achieving high V_{oc} and maintaining high photocurrents was observed. A driving force $\Delta E_{S1,CT}$ of several hundred meV, with an empirical lower limit of ∼300 meV, was found necessary for efficient charge generation [100, 243]. Consequently, fullerene-based systems typically show $\Delta E_{S1,CT}$ values above 0.25 eV when CT state shoulders are clearly present in EQE spectra. As $\Delta E_{S1,CT}$ is further reduced to optimise voltage loss, the CT state increasingly overlaps with the S_1 state, complicating reliable extraction of E_{CT}, even in C_{60} systems [61, 99].

With the emergence of high-performance NFAs, numerous solution-processed NFA OSCs have demonstrated low voltage losses below 0.6 eV while simultaneously maintaining high peak EQE of over 80% [19, 134], despite showing indistinguishable S_1-CT features in their sub-gap EQE, i.e., lacking clear CT shoulders. In these systems, the estimated driving forces are often below 100 meV and in some cases approaching zero [39, 41, 77–79]. This raises the question of whether the driving force for exciton separation can still be described by $\Delta E_{S1,CT}$. Many NFA systems display exponential decay in sub-gap EQE, rendering Gaussian fits from Marcus-type models invalid. As a result, even with highly sensitive measurements (down to 10^{-8}), E_{CT} cannot be reliably extracted from EQE (e.g., for PM6:Y6) [118].

EL spectra are been proven useful for probing CT emissions in fullerene systems, however many NFA systems also exhibit strong S_1 emission, sometimes overriding the CT emission, complicating interpretation [39]. Consequently, the definition and determination of the driving force for exciton dissociation in the literature vary. Some studies define the driving force as $|\,\mathrm{HOMO}_A\,| - |\,\mathrm{HOMO}_D\,|$ based on cyclic voltammetry [243], while others subtract the exciton binding energy difference, defining it as $|\,\mathrm{HOMO}_A\,| - |\,\mathrm{HOMO}_D\,| - \Delta E_B$, where ΔE_B is the

difference in binding energies between the acceptor exciton and charge-pair state [79]. These definitions, however, are based on the energetics of pristine materials and therefore cannot represent the interfacial energetics in heterojunctions. As a result, many studies continue to define the driving force as $\Delta E_{S1,CT}$, using reduced EL and EQE spectra to determine E_{CT} from the intersection point of CT emission and absorption curves [78]. However, correct assignment of CT emissions is challenging in S_1-dominated systems, and fitting CT emission in EL with Gaussian Marcus models may suffer from misassignment of CT state emission [39]. Failure to correctly determine $\Delta E_{S1,CT}$ could lead to a misleading interpretation of efficient exciton separation in NFA OSCs. While computational modelling of excitonic and CT states can provide reasonably accurate $\Delta E_{S1,CT}$ values (resolution down to 10 meV) [41], experimental approaches remain highly challenging. A simple and reliable experimental method for determining E_{CT} in low-$\Delta E_{S1,CT}$ systems remains elusive.

In this chapter, PHJ devices with varying CT state features in EQE (ranging from no visible CT signal to strong CT shoulders) are studied. The aim is to estimate $\Delta E_{S1,CT}$ indirectly via its correlation with ΔV_{oc}^{rad} calculated under the DB framework. The investigated systems consisted of VTE electron donors paired with either FBR (a NFA) or C_{60}, to maximise the compatibility of this correlation. The chosen donors, SubNc, DTDCTB, and SubPc, exhibited a range of IE, EA, and E_{S1}, enabling a broad variation in CT and S_1 characteristics. Moreover, these systems under study support FRET from the electron acceptor to the donor, possessing similar free-charge generation routes of those high-performing, all-solution-processed NFA OSCs [39].

A strong linear correlation was found between ΔV_{oc}^{rad} and $\Delta E_{S1,CT}$, with the best fit yielding: slope=1.16±0.17, intercept=–0.11±0.05, and R^2=0.92. This empirical relationship was used to estimate $\Delta E_{S1,CT}$ in a system with indistinguishable CT and S_1 states, where direct extraction was not possible. For example, $\Delta E_{S1,CT}$ was estimated as 0.10±0.05 eV for the SubNc|FBR device, where its sub-gap EQE exhibits exponential tail feature. Additionally, an inverse relationship between $\Delta E_{S1,CT}$ and $\Delta Q_{\pi,D-A}$ was identified in systems with the same S_1 state. Together, these findings provide a practical framework for approximating $\Delta E_{S1,CT}$ from experimentally determined quantities like ΔV_{oc}^{rad}, in both NFA and fullerene PHJ systems where conventional approaches fail.

7.2 Materials and Devices

In Chapter 5, it was demonstrated that hybrid molecular pairs SubNc/FBR, SubPc/FBR could support barrier-less hole and electron transfer, based on their IE and EA measured on pristine films. The pair DTDCTB/FBR was found likely only support barrier-less hole transfer. Also, efficient FRET was observed for FBR→SubNc and FBR→DTDCTB, moderate FRET was observed for FBR→SubPc. This selection of hybrid molecular pairs provides a foundation for investigating how energetic alignments influence the performance of solar cell devices based on FRET-supported systems comprising VTE electron donors and solution-processed NFAs, with particular focus on their CT state characteristics.

Inverted-stack PHJ solar cells were fabricated using the following electron donor and acceptor combination in the active layer (SP electron acceptor deposited on substrate first): SubNc|FBR (C_{60}), DTDCTB|FBR (C_{60}) and SubPc|FBR (C_{60}). To maintain consistency with the system naming convention used in previous chapters, the systems below are still named in the format of 'electron donor|electron acceptor'. Where electron acceptor is C_{60}, are reference devices that do not support efficient FRET. It should be noted that though C_{60} has PL emission partially overlap with DTDCTB absorption spectrum, their PHJ devices are not expected to support efficient FRET from C_{60} to the electron donor. This is due to the extremely low ϕ_{PL} of C_{60}, which is on the order of 10^{-4} in room-temperature solutions and lower in solid films [244]. The device stack was constructed as follows: ITO (135 nm)|ZnO (30 nm)|electron acceptor (20 nm)|electron donor (20 nm)|MoO_3 (10 nm)|Ag (100 nm), which was also shown in Figure 4.6. FBR layer was spin-coated with the method and conditions discussed in Chapter 4.2.3. The evaporation rate for the molecules in the active layer was set nominally to 0.25 Å/s, except for DTDCTB, which was deposited at 0.20 Å/s to maintain stable deposition. MoO_3 and Ag were evaporated as described in Chapter 4.2.2. The FBR and C_{60} devices were fabricated in two separate evaporations. However, the common layers were deposited following the same procedure, and the evaporation chamber conditions were maintained consistently to ensure a reliable comparison.

7.3 Device Performance

7.3.1 Current Density-Voltage

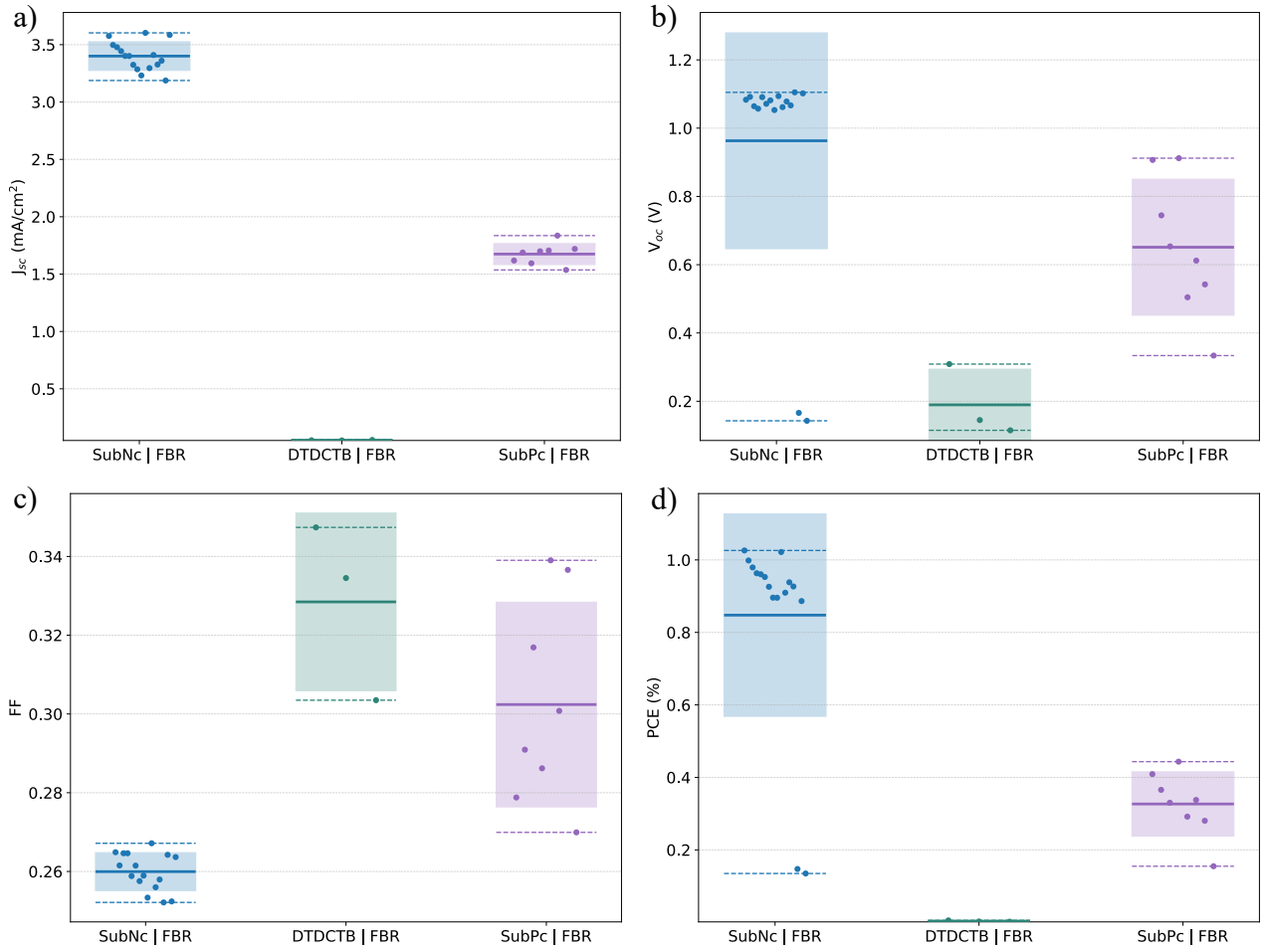


Figure 7.1: Summary of device performance parameters: (a) short-circuit current J_{sc}, (b) open-circuit voltage V_{oc}, (c) fill factor FF, (d) power conversion efficiency PCE for planar heterojunction devices in inverted stack using SubNc, DTDCTB and SubPc as electron donors (20 nm) and FBR as electron acceptor (20 nm).

Figure 7.1 and Figure 7.2 present the photovoltaic performance parameters of the hybrid PHJ devices employing SubNc, DTDCTB, and SubPc as electron donors with FBR as the electron acceptor, alongside their all-evaporated C_{60} reference devices. Overall, the hybrid systems exhibit significantly lower reproducibility compared to the all-evaporated references, highlighting a key advantage of VTE for the stable fabrication of organic solar cells. Among the systems studied, SubNc shows the best compatibility with FBR, yielding 16 functional devices out of

18 fabricated. The average V_{oc}, J_{sc}, FF, and PCE of SubNc|FBR devices are 0.96±0.32 V, 3.40±0.12 mA/cm^2, 0.260±0.005, and 0.85±0.28%, respectively. In contrast, DTDCTB|FBR devices exhibit the worst performance, with only 3 marginally working devices out of 18. The averaged V_{oc} is 0.19±0.10 V, J_{sc} is 0.052±0.002 mA/cm^2, FF is 0.33±0.02, and PCE is just 0.003±0.002%. SubPc|FBR devices perform slightly better, with 8 out of 18 devices functioning. Their average V_{oc}, J_{sc}, FF, and PCE are 0.65±0.20 V, 1.67±0.09 mA/cm^2, 0.30±0.03, and 0.33±0.09%, respectively.

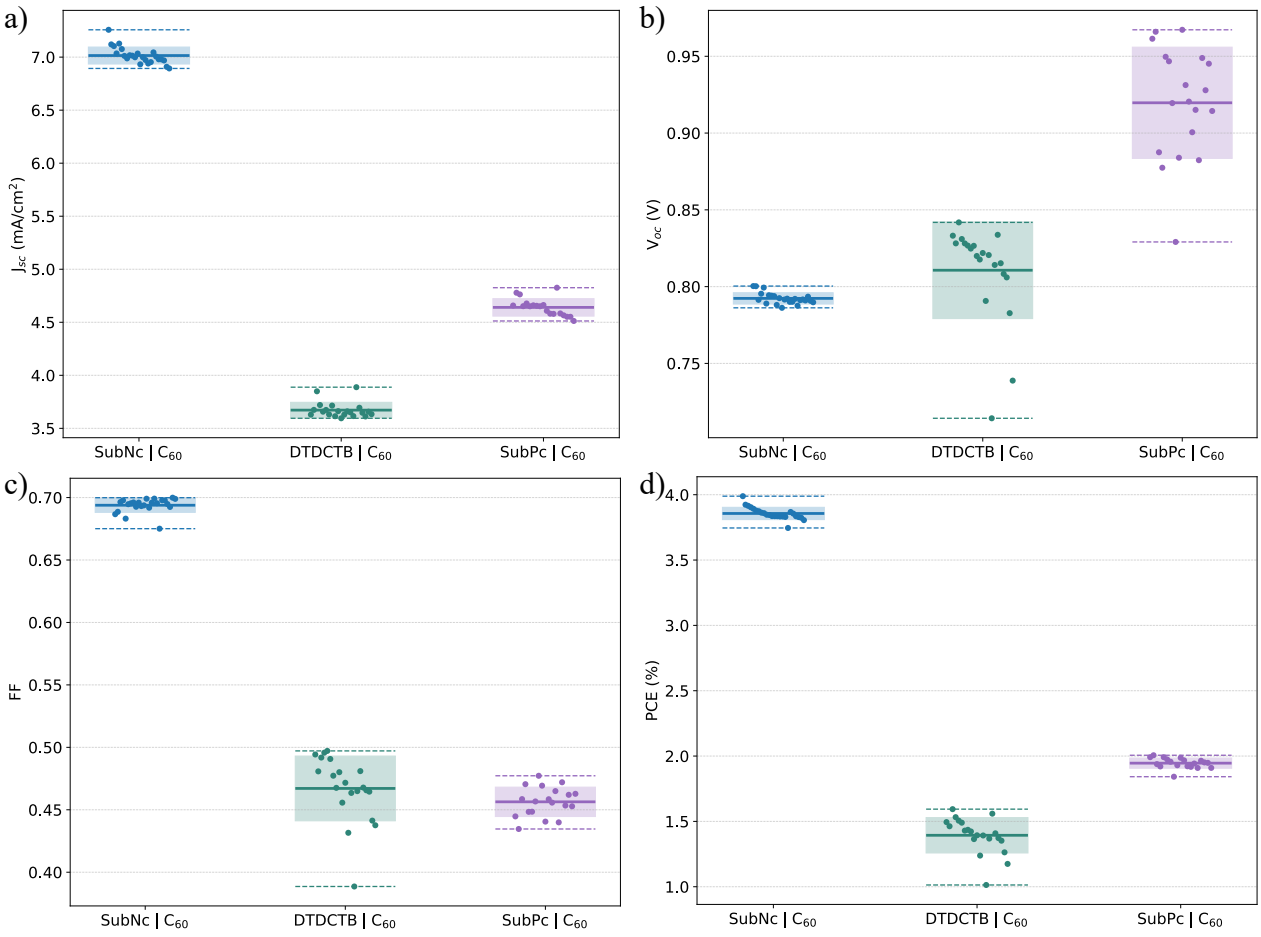


Figure 7.2: Summary of device performance parameters: (a) short-circuit current J_{sc}, (b) open-circuit voltage V_{oc}, (c) fill factor FF, (d) power conversion efficiency PCE for planar heterojunction devices (C_{60} reference devices) in inverted stack using SubNc, DTDCTB and SubPc as electron donors (20 nm) and C_{60} as electron acceptor (20 nm).

SubPc and DTDCTB devices exhibited unexpectedly low V_{oc}. To rule out fabrication-related artefacts, control devices were fabricated using FBR layers that were intentionally exposed to air prior to electron donor deposition. These devices showed similarly poor per-

formance, suggesting that the low V_{oc} was not due to fabrication uncertainties. Notably, P3HT:FBR BHJ devices with PCE of up to 4.1% with good J-V characteristics have been reported in the same inverted device architecture using ZnO as the electron transport layer [173], suggesting that the ZnO/FBR interface does not have energetic barriers. Therefore, the poor V_{oc} is more likely attributable to unfavourable interfacial contacts between FBR and the evaporated donor layer in the PHJ configuration. Since FBR was originally developed as a NFA for BHJ systems, the processing conditions employed here, based on BHJ-optimised recipes [173, 245], may not be suitable for SubPc and DTDCTB in PHJ architectures. Consequently, additional energy loss channels at the electron donor–acceptor interface may contribute to the observed low V_{oc}, which could be unfavourable molecular orientation and packing [63, 91, 239]. Further characterisation by atomic force microscopy (AFM) or X-ray photoelectron spectroscopy (XPS) would be valuable to confirm the surface morphology of FBR films and rule out film quality or morphology-related issues.

Table 7.1: Summary of open-circuit voltage (V_{oc}), short-circuit current (J_{sc}), fill factor (FF), and power conversion efficiency (PCE) for the best-performing planar heterojunction devices using SubNc, DTDCTB, SubPc as electron donors (20 nm) and FBR (C_{60}) as the electron acceptor (20 nm). Values for the current density–voltage characteristics are extracted from reverse scans.

Donor	Acceptor	V_{oc} (V)	J_{sc} (mA/cm^2)	FF	PCE (%)
SubNc	FBR	1.08	3.58	0.26	1.03
DTDCTB	FBR	0.31	0.05	0.35	0.006
SubPc	FBR	0.61	1.84	0.30	0.34
SubNc	C_{60}	0.80	7.26	0.69	4.01
DTDCTB	C_{60}	0.84	3.85	0.49	1.60
SubPc	C_{60}	0.97	4.78	0.43	2.01

Figure 7.3 presents the J-V characteristics of the best-performing devices from the FBR-based hybrid systems and their C_{60} references. Reverse scans (from +V to -V) are shown as solid lines, while forward scans are plotted as dash-dot lines. The corresponding parameters are summarised in Table 7.1. Overall, the hybrid devices incorporating FBR exhibit more compromised J-V characteristics compared to their C_{60}-based counterparts. Although FBR has slightly shallower HOMO and LUMO levels than C_{60}, with reported values for C_{60} in the range of 6.2-6.35 eV (IE) and 3.97-4.3 eV (EA) [192, 246], the difference in device performance

is much more pronounced.

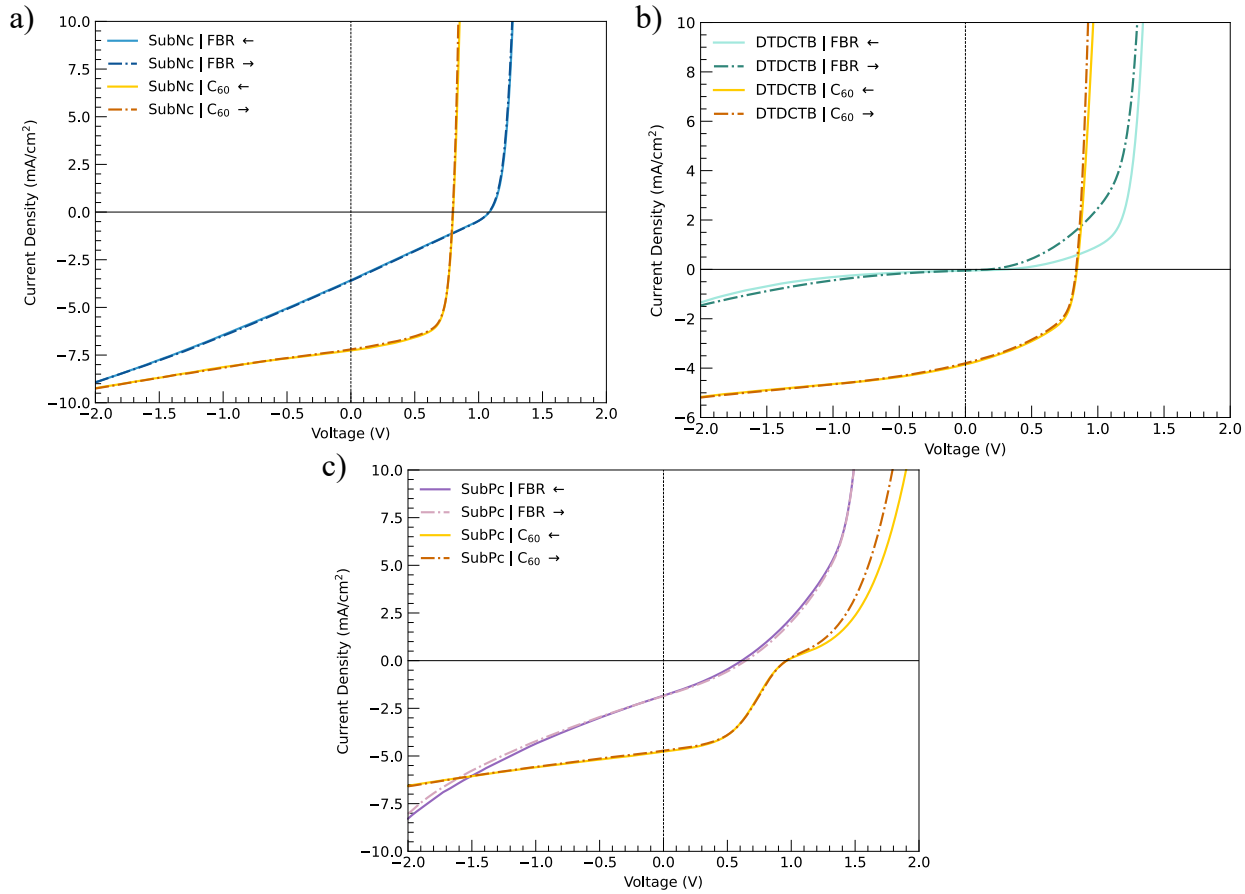


Figure 7.3: Current density-voltage characteristics of planar heterojunction devices using (a) SubNc, (b) DTDCTB and (c) SubPc as electron donors (20 nm) and FBR (C_{60}) as electron acceptor (20 nm). Solid lines represent reverse scans, while dot-dashed lines represent forward scans.

The SubNc|FBR device exhibits a linear trend J-V under reverse bias, indicating strong field-dependent charge extraction [27]. This behaviour suggests non-ideal charge transport, likely due to low electron mobility in the FBR layer and potentially insufficient $\Delta E_{S1,CT}$ [247]. The J_{sc} of the SubNc|FBR device is less than half of its C_{60} counterpart, further supporting the hypothesis of unfavourable electron transport properties of FBR layer.

For the DTDCTB|FBR device, a clear discrepancy is observed between forward and reverse scans, indicating slow relaxation effects and possible charge accumulation [27]. Additionally, the device exhibits field-dependent extraction in the reverse-biased region, again pointing to a combination of energetic barriers at electron donor-acceptor interface and low electron mobility of the FBR layer. Its extremely low J_{sc} may be attributed to a near-zero EA offset (0.05 eV),

which likely hinders efficient electron transfer following FRET from FBR to DTDCTB. Notably, its C_{60} reference device shows normal-shaped J-V and good device performance, agreeing with literature [187, 248].

The SubPc|FBR system, which also supports FRET, unexpectedly displays abnormal J-V characteristics and performs even worse than the pristine 20 nm SubPc device, which was previously reported to achieve J_{sc} = 2.1 mA/cm^2, V_{oc} = 1.1 V, FF = 0.23, and PCE = 0.6% [221]. This suggests that the presence of FBR negatively affects device performance, likely due to unfavourable electron D-A interfacial properties and low electron mobility of the FBR layer. Its C_{60} reference device exhibits an S-shaped J-V curve, likely stemming from mobility mismatch between C_{60} and SubPc. This is supported by previous reports showing normal-shaped J-V curves for SubPc|C_{60} PHJ devices with reduced SubPc layer thickness of 13 nm and below [249, 250].

In summary, except for the SubNc|C_{60} and DTDCTB|C_{60} devices, all other systems show impacted J-V behaviour. These results are also consistent with observations in FRET-supported all-VTE systems discussed in Chapter 6.2, as the J_{sc}, FF, and overall J–V shape in these hybrid systems appear to be primarily governed by EA offsets, interfacial molecular properties, and charge carrier mobilities.

7.3.2 External Quantum Efficiency

Figure 7.4 and 7.5 present their simulated and measured absorptance spectra and measured EQE of the devices under investigation. The J_{sc} values calculated from the measured EQE spectra are slightly lower but close to the experimentally measured J_{sc}. Although the measured EQE was obtained without bias light and therefore cannot fully represent the device under operational conditions, the minimal difference between the measured and EQE-calculated J_{sc} suggests that the EQE spectra still reliably capture the spectral dependence of free charge carrier extraction in the devices. The absorptance spectra were measured by Katherine Trinkaus (Oxford) and reflect relative values only, owing to the difficulty of spectrometer calibration for 100% reflectance on pristine Ag electrode with probing light incident from the side of glass substrate. This limitation, inherent to the fibre-based UV-Vis setup used, resulted in non-physical measured absorptance values (e.g. absorptance < 0) in certain wavelength regions.

Although the absolute absorptance values may be inaccurate, the overall spectral shape and relative intensities remain physically meaningful.

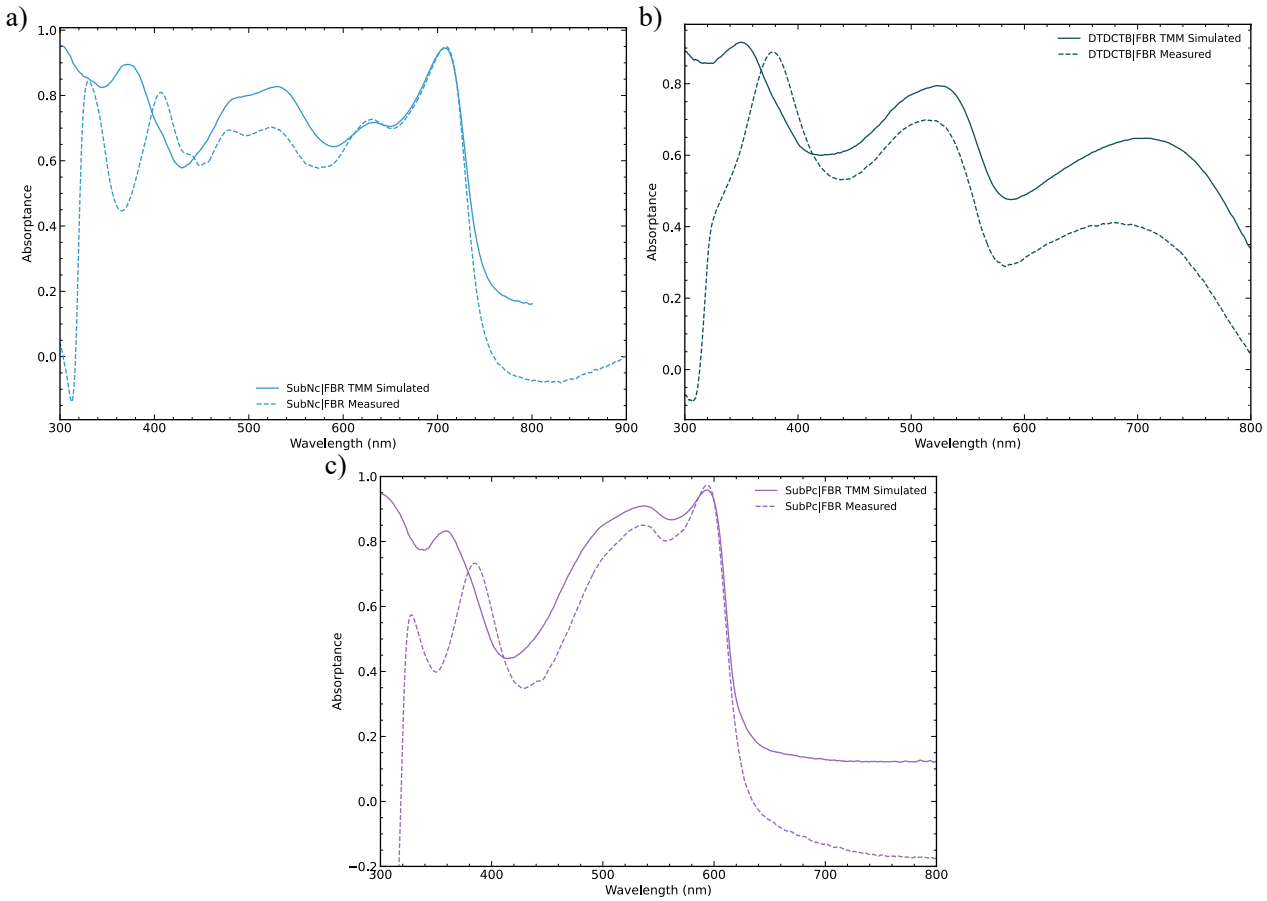


Figure 7.4: Transfer-Matrix simulated (solid lines) and measured (dashed lines) device absorptance spectra for best performing planar heterojunction devices using (a) SubNc, (b) DTDCTB, (c) SubPc as electron donors (20 nm) and FBR as the electron acceptor (20 nm). The measured absorptance are relative values. The absorptance spectra were measured by Katherine Trinkaus (Oxford) and only represent relative values.

As shown in Figure 7.4, the simulated absorptance spectra from TMM generally agree with the measured spectra, indicating that the simulations provide a good approximation of the real devices. All FBR-based devices exhibit strong simulated absorptance, with peak values approaching unity, suggesting excellent photon harvesting. However, the calculated IQE, derived from measured EQE (EQE_{meas}) and simulated absorptance (A_{TMM}), are extremely low. The peak IQE values for the SubNc, DTDCTB, and SubPc systems are approximately 0.25, 0.009, and 0.20, respectively, indicating substantial limitations in free charge carrier generation. These findings support the hypothesis of poor electron mobility within the FBR layer and/or

unfavourable D-A interfacial properties.

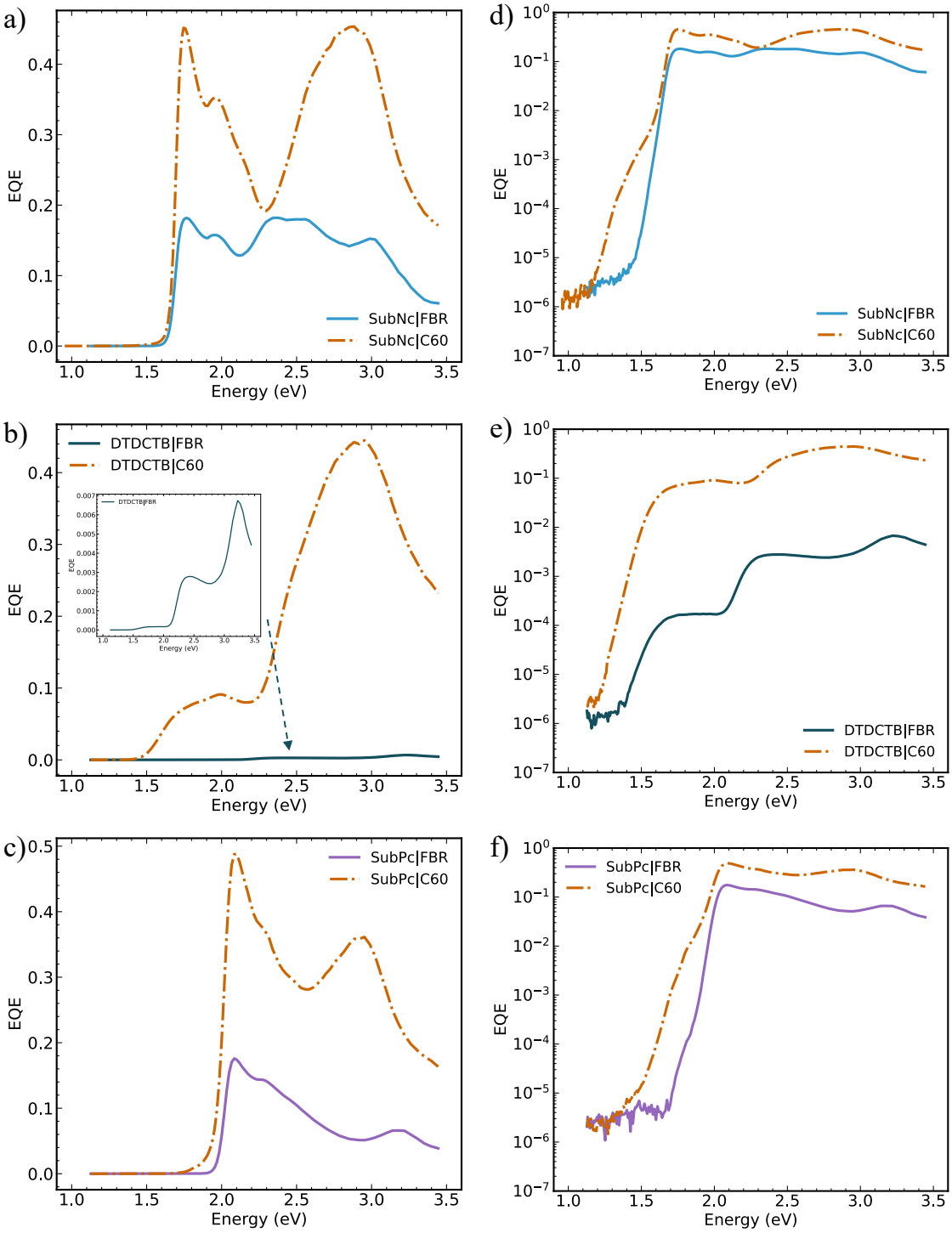


Figure 7.5: Sensitive external quantum efficiency (EQE) spectra of the best performing planar heterojunction devices using SubNc, DTDCTB, SubPc as electron donors (20 nm) and FBR (C_{60}) as the electron acceptor (20 nm). (a)–(c) show the spectra plotted on a linear scale, while (d)–(f) present the corresponding data on a logarithmic scale. The insert in (b) is a EQE close-up for device DTDCTB|FBR.

The EQE spectra plotted on a logarithmic scale (Figure 7.5d–f) are particularly informative,

as they provide insight into both CT and S_1 state absorption features, especially valuable in devices exhibiting abnormal J-V characteristics. For both DTDCTB|FBR and DTDCTB|C_{60} systems, no discernible CT state shoulders are visible, indicating small driving forces (i.e. low $\Delta E_{S1,CT}$) or very few CT states. Previous studies have shown that hot CT states dominate exciton dissociation at the DTDCTB/C_{60} interface and are effective in generating free charge carriers [103], which may explain the absence of low-energy CT absorption in the EQE spectrum of DTDCTB|C_{60}, despite its reasonably good performance.

Similarly, SubNc|FBR system also exhibits exponential decay in the sub-gap region, suggesting low $\Delta E_{S1,CT}$ and hence a higher E_{CT} relative to its C_{60} reference system. Interestingly, the SubPc|FBR system shows weak but visible CT state shoulder features, like its C_{60} reference. To further explore the factors influencing $\Delta E_{S1,CT}$, robust extraction of both E_{CT} and E_{S1} for SubNc|FBR (C_{60}) and SubPc|FBR (C_{60}) systems is required, and this will be addressed in the next section.

7.4 Charge Transfer Characteristics and Voltage Loss

Figure 7.6a, b, and d show the logarithmic EQE spectra of SubNc|C_{60}, SubPc|C_{60}, and SubPc|FBR devices, respectively, with the CT and S_1 state contributions fitted separately under the Marcus theory framework. Figure 7.6c presents E_U^{app} characteristics in the sub-gap region for the SubNc|FBR system. A clear plateau is observed with E_U^{app} = 22±0.4 meV $\approx k_B T_{300K}$, suggesting low $\Delta E_{S1,CT}$ in the system [118]. Consequently, it is not possible to extract E_{CT} and E_{S1} from its EQE spectrum. From the Marcus fits, $\Delta E_{S1,CT}$ is determined to be 0.39±0.00 eV for SubNc|C_{60}, 0.29±0.01 eV for SubPc|C_{60}, and 0.22±0.01 eV for SubPc|FBR. For SubNc|FBR, fitting was not possible. However, $\Delta E_{S1,CT}$ has been demonstrated to be related to ΔV_{oc}^{rad} from studies based on fullerene systems [81, 126], it may be able to be estimated if empirical correlation between the two can be found.

Figure 7.7a shows the V_{oc} loss decomposition based in DB picture, and Table 7.2 summarises the E_g^{PV}, V_{oc}, and each voltage loss term. Due to impacted J-V characteristics in the FBR-based devices, the calculated ΔV_{oc}^{nr} values may be over- or underestimated depending on the their J-V characteristics, and are therefore not comparable across different systems. An overestimation

of ΔV_{oc}^{nr} and underestimation of ΔV_{oc}^{rad} can occur when the photocurrent density drops by 50% between J_{sc} and V_{oc}, potentially leading to an overestimation of V_{oc}^{rad} by up to 17.5 mV [51,82]. It is noted that E_g^{PV} remains nearly identical between SubNc|FBR and SubNc|C_{60}, as well as between SubPc|FBR and SubPc|C_{60}, leading to equivalent ΔV_{oc}^{SQ} values. Both FBR-based devices show larger ΔV_{oc}^{sc} than their C_{60} references, consistent with their J-V characteristics.

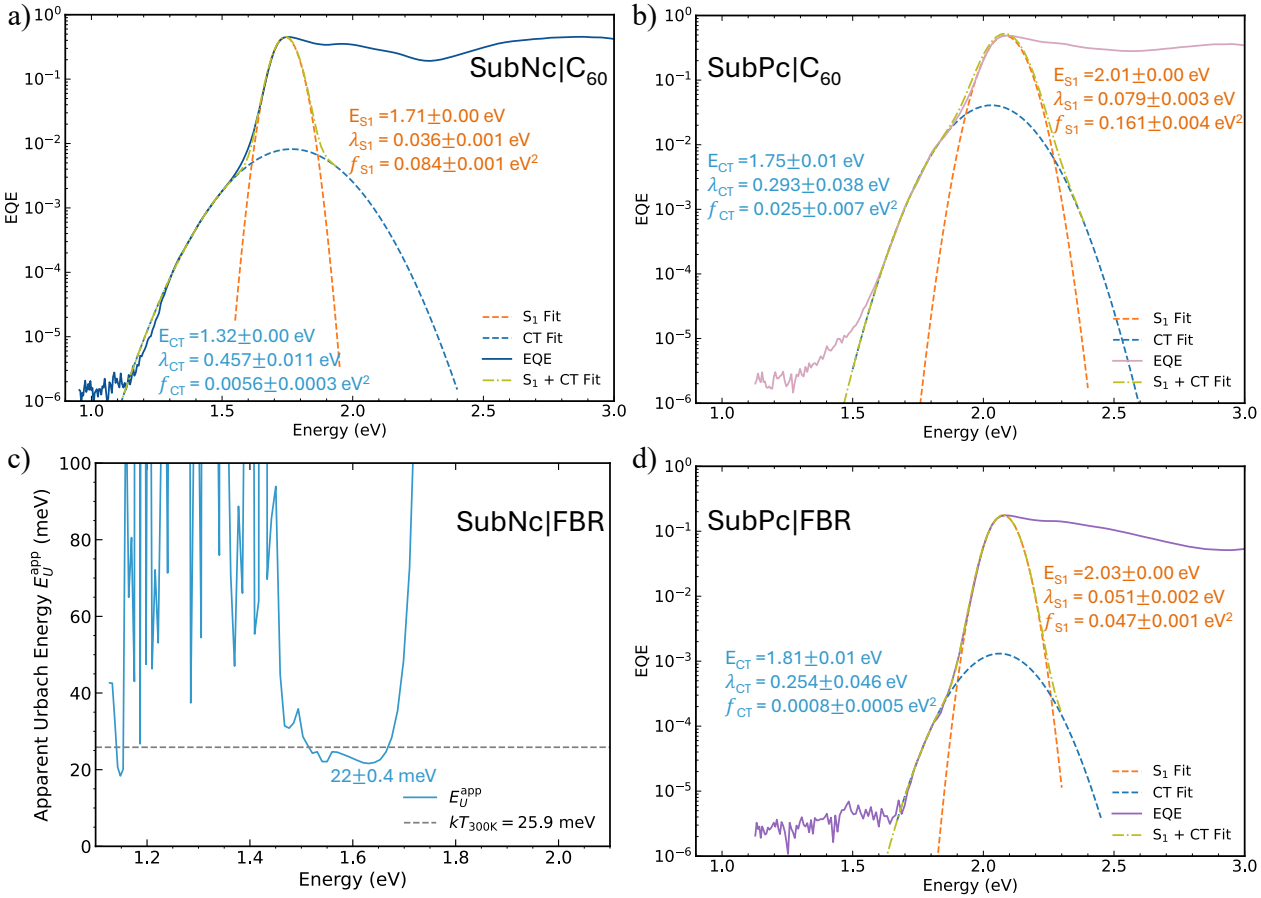


Figure 7.6: (a), (b), (d) Sensitive external quantum efficiency (EQE) spectra of the best performing planar heterojunction (PHJ) devices using SubNc, SubPc as electron donors (20 nm) and FBR (C_{60}) as the electron acceptor (20 nm) with Marcus theory fits for S_1 and CT states, shown in logarithmic scale. Dashed lines represent the fits. The fitting parameters are labelled in figures. (c) Apparent Urbach energy (E_U^{app}) spectra of PHJ device with SubNc|FBR as active layer. The minimum E_U^{app} values, averaged over the plateau region near the minimum point in the sub-gap region, are labelled in blue. The value of k_BT at 300 K is indicated by a dashed horizontal line, where k is the Boltzmann constant and T is the device temperature.

Plotting ΔV_{oc}^{rad} versus $\Delta E_{S1,CT}$ of PHJ devices from this study and literature [126] yields an approximately linear correlation, as shown in Figure 7.7b. The literature data were obtained from devices with identical configurations to those used in this study, and can therefore be

considered a valid extension of the present dataset. The linear model was adopted for simplicity based on experimental observation. Its physical basis warrants further theoretical investigation and represents an interesting direction for future work.

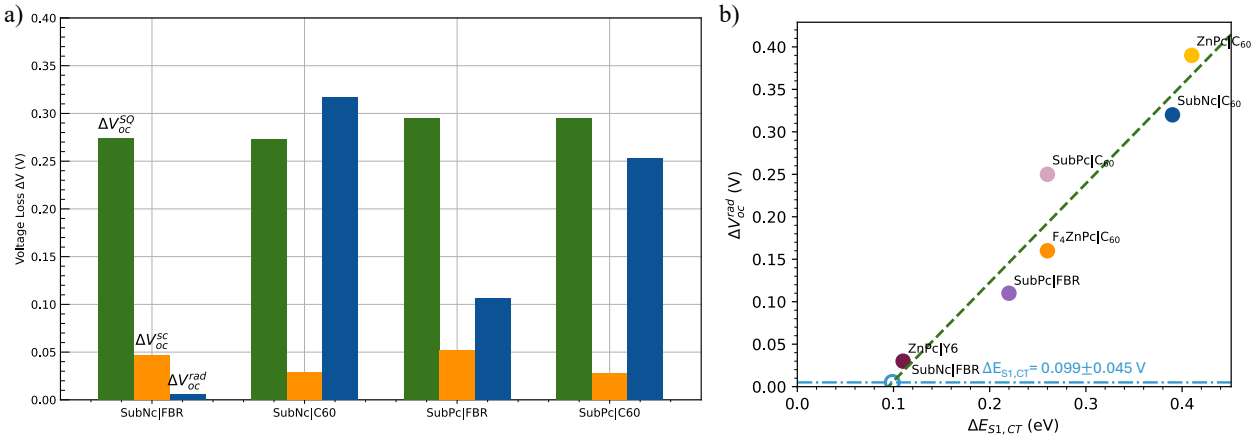


Figure 7.7: (a) Open-circuit voltage loss decomposition in DB picture for the best planar heterojunction devices using SubNc and SubPc as electron donors (20 nm) and FBR (C_{60}) as the electron acceptor (20 nm). The breakdown includes the voltage loss relative to the Shockley–Queisser limit (ΔVoc^{SQ}), voltage loss due to imperfect photocurrent collection (ΔV_{oc}^{sc}), and radiative voltage loss (ΔV_{oc}^{rad}). (b) Radiative voltage loss (ΔV_{oc}^{rad}) plotted as a function of the energy difference between the S_1 and CT states ($\Delta E_{S1,CT}$), shown as solid circles. The data for ZnPc|Y6, F_4ZnPc|C_{60} and ZnPc|C_{60} were taken from literature [126]. A linear fit (green dashed line) yields a slope of 1.16±0.17 and an intercept of -0.11±0.05, with $R^2 = 0.92$. The blue hollow circle indicates the estimated $\Delta E_{S1,CT}$ value of 0.10±0.05 eV for the SubNc|FBR device, based on $\Delta V_{oc}^{rad} = 0.005$ V.

Table 7.2: Summary of device photovoltaic gap (E_g^{PV}), open-circuit voltage (V_{oc}), voltage loss relative to Shockley-Queisser limit (ΔV_{oc}^{SQ}), voltage loss due to imperfect photocurrent collection (ΔV_{oc}^{sc}), radiative voltage loss (ΔV_{oc}^{rad}) and ΔV_{oc}^{nr} (V) for the best 20 nm SubNc (SubPc)|20 nm FBR (C_{60}) planar heterojunction devices.

Donor	Acceptor	E_g^{PV} (eV)	V_{oc} (V)	ΔV_{oc}^{SQ} (V)	ΔV_{oc}^{sc} (V)	ΔV_{oc}^{rad} (V)	ΔV_{oc}^{nr} (V)
SubNc	FBR	1.69	1.08	0.27	0.05	0.005	N/A
SubNc	C_{60}	1.70	0.80	0.27	0.03	0.32	0.28
SubPc	FBR	2.02	0.61	0.29	0.05	0.11	N/A
SubPc	C_{60}	2.02	0.97	0.29	0.03	0.25	0.48

A best-fit line with $R^2 = 0.92$ gives a slope of 1.16±0.17 and an intercept of –0.11±0.05. Although the limited number of data points results in relatively large uncertainty, this fit allows estimation of $\Delta E_{S1,CT}$ for SubNc|FBR as 0.10±0.05 eV with its $V_{oc}^{rad} = 0.005$ eV. Considering the possible underestimation of V_{oc}^{rad} by up to 17.5 mV due to the extremely low FF, $\Delta E_{S1,CT}$

can be estimated to lie within the range of 0.10–0.11±0.05 eV. This estimate is consistent with the observed indistinguishable S_1-CT state features. Due to the multiple contributing factors behind the poor device performance of SubNc|FBR, it remains unclear whether its poor performance is related to small $\Delta E_{S1,CT}$. Further systems with confirmed small $\Delta E_{S1,CT}$, but featuring optimised molecular and device designs, are needed to verify this.

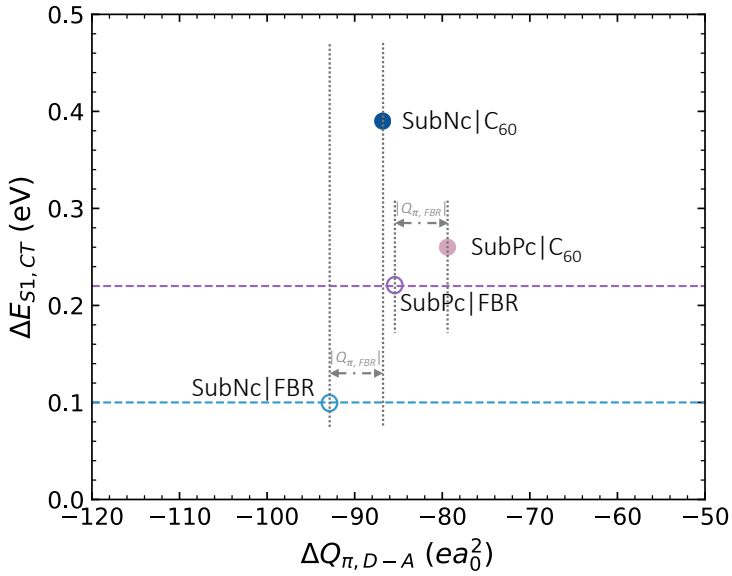


Figure 7.8: $\Delta E_{S1,CT}$ as a function of $\Delta Q_{\pi,D-A}$ for SubNc|FBR (C_{60}) and SubPc|FBR (C_{60}) material systems. Solid circles are drawn based on measured data, while hollow circles indicate possible $\Delta Q_{\pi,D-A}$ for SubNc|FBR and SubPc|FBR systems, assuming $Q_{\pi,FBR} > 0$. The magnitude of $|Q_{\pi,\mathrm{FBR}}|$ is not drawn to scale and is shown only for demonstration purposes. The purple horizontal line denotes the value of $\Delta E_{S1,CT}$ for the SubPc|FBR system, and the blue line corresponds to that of the SubNc|FBR system.

SubNc and SubPc has reported Q_π of –86.8 $ea_0{}^2$ [232] and –79.4 $ea_0{}^2$ [251], respectively, while C_{60} has reported Q_π of 0 $ea_0{}^2$. Using these values, $\Delta E_{S1,CT}$ is plotted against $\Delta Q_{\pi,D-A}$ for the four material systems, as shown in Figure 7.8. No reported Q_π for FBR was found in literature. However, as an AA-D-AA type NFA, FBR is likely to possess a positive Q_π due to the strong push-pull effect across its conjugated backbone, analogous to A-D-A and A-D-A'-D-A structured NFAs such as Y6 [63]. In Figure 7.8, $Q_{\pi,FBR}$ is therefore assumed to be positive.

The plot reveals that, for systems sharing the same E_{S1} (e.g. SubNc|FBR and SubNc|C_{60}), a more negative $\Delta Q_{\pi,D-A}$ corresponds to a smaller $\Delta E_{S1,CT}$, i.e., higher E_{CT}. This appears to contradict the trend proposed in the literature [63, 232], where a positive Q_π would shift the IE

and EA away from vacuum level while a negative Q_π shifts them towards it. Consequently, for a donor–acceptor pair in which $Q_{\pi,D}$ is negative and $Q_{\pi,A}$ is positive, a more negative quadrupole moment difference $Q_{\pi,D-A}$ (=$Q_{\pi,D}$-$Q_{\pi,A}$) is expected to lower E_{CT} and hence increase $\Delta E_{S1,CT}$, the opposite of what is observed here. Theoretical calculation of Q_π for FBR is therefore essential to resolve this contradiction. As a result, a definitive relationship between $Q_{\pi,D-A}$ and $\Delta E_{S1,CT}$ cannot be established for the four systems studied here. A more comprehensive investigation will require additional data from devices with either shared or varied E_{S1} values and known Q_π, which is proposed for future work.

In summary, for PHJ systems, ΔV_{oc}^{rad} exhibits a positive linear correlation with $\Delta E_{S1,CT}$, i.e. larger $\Delta E_{S1,CT}$ leads to greater radiative voltage losses. For BHJ systems, this correlation will need to be verified separately, as additional factors related to blend microstructure can influence voltage loss and CT characteristics, which may vary across different material systems.

7.5 Conclusions

In this chapter, three FRET-supported hybrid OSC systems, comprising VTE electron donors (SubNc, DTDCTB, and SubPc) and a SP NFA (FBR), were examined, along with their C_{60} references. The EA offsets with FBR of three donor molecules vary from 0.05 to 0.56 eV for varying D-A interfacial energetics, i.e different $\Delta E_{S1,CT}$. The aim was to find the correlation between $\Delta E_{S1,CT}$ and ΔV_{oc}^{rad} for an simple and universal method to estimate $\Delta E_{S1,CT}$ for low-$\Delta E_{S1,CT}$ systems. Additionally, how the quadrupole moment between electron donor and acceptor relates to $\Delta E_{S1,CT}$, and whether these relationships differ from those established in fullerene systems were explored.

Hybrid PHJ devices were fabricated in an inverted architecture consisting of 20 nm electron donor|20 nm electron acceptor. FBR-based systems consistently showed poorer performance than their C_{60} references, which was primarily attributed to poor electron transport in the FBR layer and unoptimised D-A interfacial properties. Notably, SubNc|FBR and SubPc|FBR devices exhibited distinct CT-state features although their EA offset with FBR only differs by 0.12 eV: the former showed an exponential tail in the low-energy region of EQE, while the latter displayed a clear CT absorption shoulder. Both of their C_{60} references showed clear

CT features. With extracted E_{S1} and E_{CT} from systems with clear CT features, a linear correlation between $\Delta E_{S1,CT}$ and the radiative voltage loss ΔV_{oc}^{rad} was found, with a fitted slope of 1.16±0.17 and an intercept of -0.11±0.05. This linear fit managed to estimate $\Delta E_{S1,CT}$ for SubNc|FBR system, for which E_{CT} could not be directly extracted. The estimated value was 0.10±0.05 eV, which was a reasonable value for low-$\Delta E_{S1,CT}$ systems. Therefore, it was concluded that this linear relationship can be used to as a simple method to estimate $\Delta E_{S1,CT}$ when ΔV_{oc}^{rad} is known.

Overall, these results extend the positive relationship between $\Delta E_{S1,CT}$ and ΔV_{oc}^{rad}, confirming a linear correlation that can be used to estimate $\Delta E_{S1,CT}$ from ΔV_{oc}^{rad} in PHJ systems where E_{CT} cannot be directly extracted. Due to the limited number of devices studied, the relationship between $\Delta Q_{\pi,D-A}$ and $\Delta E_{S1,CT}$ across systems with different S_1 remains inconclusive. Further studies involving additional material systems with both matched and varied E_{S1} are proposed.

8 | Conclusion and Outlook

Overall, this thesis investigated a series of all-VTE and hybrid OSC systems with non-fullerene electron acceptors, the latter comprising VTE electron donors and SP acceptor molecules. The molecular pairs of interest were selected based on design strategies established from high-performing SP NFA OSCs and exhibit several key characteristics identified in those systems. A central design feature in the studied OSC systems is the presence of efficient FRET between the electron donor and acceptor. The experimental work in this thesis can be broadly categorised into two parts: (1) the identification of molecular pairs that support FRET and are suitable for OSC applications (Chapter 5), and (2) in-depth studies of the selected molecular pairs in various OSC device configurations (Chapter 6 and 7). To summarise the main takeaways, this thesis expands the current understanding of the field in the following ways:

- Confirmed that several design strategies identified in high-efficiency SP NFA OSCs also apply to the development of high-efficiency VTE NFA OSCs.
- Identified the key molecular criteria for introducing a second electron acceptor to enhance bilayer PHJ OSC performance without compromising V_{oc}.
- Found a linear correlation between $\Delta E_{S1,CT}$ and ΔV_{oc}^{rad} in PHJ OSCs employing C_{60} or SP non-fullerene acceptors, enabling $\Delta E_{S1,CT}$ estimation in systems where CT state features are unresolvable due to S_1 state dominance.

In Chapter 5, a comprehensive study was conducted on six candidate molecules and their combinations, including both SP and VTE molecules: SubNc, SubPc, DTDCTB, HB194, DCV3T, and FBR, with DCV3T and FBR being the main electron acceptor candidates. Optical characterisations (steady-state PL, PLQY, SE) and electronic characterisations (UPS,

IPES) were carried out on pristine films. Charge carrier mobilities (μ_e and μ_h), and UPS/IPES measured IE and EA values were compiled from literature. All molecules demonstrated high peak absorption coefficients exceeding 1×10^5 cm^{-1} in the visible region (400-700 nm). Based on these characterisations, DCV3T (VTE) and FBR (SP) were identified as strong candidates for FRET energy donors, showing the highest PLQY values of 7.22±0.65% and 4.00±0.56%, respectively, with PL emission peaks around 600–700 nm (higher wavelengths than the other molecules). Due to their deep IE (>6 eV) and EA (>3.5 eV), both molecules are also suitable as electron acceptors. PL quenching experiments confirmed efficient FRET in the following all-VTE molecular pairs: SubNc/HB194, SubNc/DCV3T, and DTDCTB/DCV3T. These pairs feature EA_D–EA_A ranging from –0.11 to 0.40 eV, and IE_D–IE_A offsets above 0.4 eV. In contrast, SubPc/DCV3T and HB194/DCV3T did not support efficient FRET, mainly due to their limited absorption-emission spectral overlap. However, they shown large IE offsets and EA_D–EA_A of 0.28-0.35 eV, which are indications for efficient electron and hole charge transfers. FRET-supporting hybrid systems comprising VTE donors and SP acceptors were identified as SubNc/FBR, SubPc/FBR, and DTDCTB/FBR, with EA_D–EA_A ranging from 0.05 to 0.56 eV and IE_D–IE_A exceeding 0.5 eV. Among these, SubNc/DCV3T and SubNc/FBR most closely resembled high-performance SP NFA OSC systems, exhibiting: (1) high absorption coefficients, (2) high PLQY for the electron acceptor (ideally also the electron donor), (3) efficient FRET from high-gap to low-gap molecules, and (4) sufficiently large EA offsets (>0.4 eV, ideally >0.5 eV).

Chapter 6 evaluated all-VTE molecular pairs in multiple device architectures: bilayer PHJs (Chapter 6.2), trilayer PHJs (Chapter 6.3), and BHJs (Chapter 6.4). In Chapter 6.2, exciton dynamics, device performance, and CT characteristics were studied in bilayer PHJs. TAS measurements confirmed a two-step free charge generation process in FRET-supporting systems: FRET from high-gap electron acceptor to low-gap donor dominates over direct hole transfer, followed by electron transfer back to the acceptor. EA offset was found to be the key determinant for exciton dissociation efficiency, with offsets of around 0.4 eV enough promoting efficient charge separation. FRET was not found to be a prerequisite for small $\Delta E_{S1,CT}$ or low voltage losses. Instead, sufficient energetic offsets of dominating CT and high, balanced charge mobilities remain essential. SubNc/DCV3T emerged as a high-performing pair, achieving a

PHJ PCE of 3.5%, suggesting that design strategies from SP NFA OSCs can be successfully extended to VTE systems. Further analyses of EQE and EL revealed the presence of low-energy emissive states in EL unrelated to CT states, which may contribute to additional ΔV_{ov}^{nr}. The dominance of S_1 emission and absorption features in low-$\Delta E_{S1,CT}$ systems makes the correct assignment of E_{CT} challenging, and misidentification can lead to incorrect interpretations. Future studies regarding the determination of E_{CT} in systems with unresolvable CT states, and the origin of these low-energy emissive states observed in EL should be explored, as these may uncover fundamental reasons for the higher intrinsic ΔV_{ov}^{nr} in organic semiconductors compared to inorganic ones.

In Chapter 6.3, the FRET pair SubNc/HB194, characterised by near-zero EA offset, was studied in trilayer PHJ OSCs. The goal was to generalise FRET's use in enhancing bilayer PHJ OSC performance without compromising voltage. The added third acceptor layer must: (i) have a similar EA as the original electron acceptor, (ii) allow efficient FRET to it, and (iii) exhibit comparable or higher electron mobility. The trilayer device α-6T|SubNc|HB194 achieved a PCE of 5.3% and a total voltage loss of 770 mV, representing a ~30% improvement in J_{sc} and FF over the α-6T|SubNc reference, while preserving V_{oc}. This was attributed to HB194's complementary absorption and improved electron transport. Further investigation reveals the voltage retention was actually a result of trade-off between different losses: small increases in ΔV_{oc}^{rad} and ΔV_{oc}^{nr} were offset by a reduced ΔV_{oc}^{sc}. Future improvements to this ternary systems may focus on interface and morphology engineering or transition to ternary BHJ configurations.

Chapter 6.4 investigated the champion SubNc/DCV3T pair in BHJ architecture, focusing on morphology and molecular orientation. A 1:1 blend achieved a V_{oc} of 1.07 V and a record-low voltage loss of 0.64 V among evaporated BHJs, with ΔV_{oc}^{nr} of 280 meV, approaching the 240 meV benchmark of SP NFA systems. However, PCE remained limited due to poor charge transport and edge-on molecular orientation, as revealed by GIWAXS. A correlation was proposed between increased energetic disorder, reduced OoP lamellar crystalline coherence length of DCV3T, and higher ΔV_{oc}^{nr}. These findings successfully replicate CT-state characteristics of low-$\Delta E_{S1,CT}$ SP NFA OSCs using fully evaporated molecules. Nonetheless, limited charge carrier mobility and unfavourable orientations continue to constrain performance. Face-on

favoured underlying templating layer may improve orientation of active-layer molecules, but increased intrinsic mobility requires tailored molecular engineering. High-efficiency VTE OSCs will likely depend on the development of new evaporable NFAs with optimised optoelectronic and morphological properties.

Finally, Chapter 7 studied three FRET-enabled hybrid PHJ systems (DTDCTB|FBR, SubPc|FBR, and SubNc|FBR) with EA offsets ranging from 0.05 to 0.56 eV, alongside their C_{60} references. A linear correlation between $\Delta E_{S1,CT}$ and ΔV_{oc}^{rad} was confirmed for PHJ OSCs with C_{60} or SP non-fullerene molecules as electron acceptors, enabling $\Delta E_{S1,CT}$ estimation even when CT state features are unresolvable due to S_1 state dominance. The fitted relationship (slope: 1.16±0.17, intercept: -0.11±0.05) successfully estimated the $\Delta E_{S1,CT}$ for SubNc|FBR system, which has indistinguishable S_1-CT states, to be 0.10±0.05 eV. These results offer a simple, generalisable estimate to characterising CT states in low-$\Delta E_{S1,CT}$ systems. Future work could include DFT simulations to validate this empirical relationship and studies involving more diverse materials to further probe the $\Delta Q_{\pi,D-A^-}$–$\Delta E_{S1,CT}$ correlation.

Bibliography

[1] H. Ritchie and M. Roser, "CO_2 emissions." https://archive.ourworldindata.org/20251204-133459/co2-emissions.html, 2020. Accessed: 5 December 2025.

[2] NOAA National Centers for Environmental Information, "Climate at a glance: Global time series." https://www.ncei.noaa.gov/access/monitoring/climate-at-a-glance/global/time-series, 2025. Accessed: 5 December 2025.

[3] V. Masson-Delmotte, P. Zhai, A. Pirani, S. L. Connors, C. Péan, S. Berger, N. Caud, Y. Chen, L. Goldfarb, M. Gomis, *et al.*, "Climate change 2021: the physical science basis," *Contribution of working group I to the sixth assessment report of the intergovernmental panel on climate change*, vol. 2, no. 1, p. 2391, 2021.

[4] R. K. Pachauri, M. R. Allen, V. R. Barros, J. Broome, W. Cramer, R. Christ, J. A. Church, L. Clarke, Q. Dahe, P. Dasgupta, *et al.*, *Climate change 2014: synthesis report. Contribution of Working Groups I, II and III to the fifth assessment report of the Intergovernmental Panel on Climate Change*. Ipcc, 2014.

[5] P. M. Forster, C. Smith, T. Walsh, W. F. Lamb, R. Lamboll, B. Hall, M. Hauser, A. Ribes, D. Rosen, N. P. Gillett, *et al.*, "Indicators of global climate change 2023: annual update of key indicators of the state of the climate system and human influence," *Earth System Science Data*, vol. 16, no. 6, pp. 2625–2658, 2024.

[6] Q. Hassan, P. Viktor, T. J. Al-Musawi, B. M. Ali, S. Algburi, H. M. Alzoubi, A. K. Al-Jiboory, A. Z. Sameen, H. M. Salman, and M. Jaszczur, "The renewable energy role in the global energy transformations," *Renewable Energy Focus*, vol. 48, p. 100545, 2024.

[7] P. IEA, "World energy outlook 2022," *Paris, France: International Energy Agency (IEA)*, 2022.

[8] L. Hammarstrom, "Overview: Capturing the sun for energy production," *Ambio*, vol. 41, no. Suppl 2, pp. 103–107, 2012.

[9] D. A. Baharoon, H. A. Rahman, W. Z. W. Omar, and S. O. Fadhl, "Historical development of concentrating solar power technologies to generate clean electricity efficiently-a review," *Renewable and Sustainable Energy Reviews*, vol. 41, pp. 996–1027, 2015.

[10] The Renewable Energy Hub UK, "History of solar pv." https://www.renewableenergyhub.co.uk/main/solar-panels/history-of-solar-pv/, 2025. Accessed: 5 December 2025.

[11] A. Goetzberger, C. Hebling, and H.-W. Schock, "Photovoltaic materials, history, status and outlook," *Materials science and engineering: R: Reports*, vol. 40, no. 1, pp. 1–46, 2003.

[12] REN21 Secretariat, "Renewables 2025 global status report." https://www.ren21.net/gsr-2025/downloads/pdf/supply/GSR_2025_Factsheet_Supply_SolarPV.pdf, 2025. Accessed: 5 December 2025.

[13] H. Tong, S. Tan, Y. Zhang, Y. He, C. Ding, H. Zhang, J. He, J. Cao, H. Liu, Y. Li, *et al.*, "Total-area world-record efficiency of 27.03% for 350.0 cm2 commercial-sized single-junction silicon solar cells," *Nature Communications*, vol. 16, no. 1, p. 5920, 2025.

[14] IRENA, "Renewable power generation costs in 2024," tech. rep., International Renewable Energy Agency, Abu Dhabi, 2025. Accessed: 8 December 2025.

[15] G. Sævarsdottir, H. Kvande, and T. Magnusson, "Greenhouse gas emissions from silicon production-development of carbon footprint with changing energy systems," in *Proceedings of the 16th International Ferro-Alloys Congress (INFACON XVI)*, 2021.

[16] M. Riede, D. Spoltore, and K. Leo, "Organic solar cells—the path to commercial success," *Advanced Energy Materials*, vol. 11, no. 1, p. 2002653, 2021.

[17] Heliatek, "Whitepaper: Organic photovoltaics — truly green energy: Ultra-low carbon footprint." https://www.heliatek.com/de/blog/whitepaper-organic-photovoltaics-truly-green-energy-ultra-low-carbon-footprint, 2025. Accessed: 8 December 2025.

[18] S. Yang, X. Chen, Y. Pan, J. Fang, Y. Han, Z. Wang, F. Qian, W. Qi, K. Shui, Q. Zhang, *et al.*, "High Cell to Module Efficiency Remaining Ratio of 90% for the 100 cm2 Fully Roll-to-Roll Gravure Printed Flexible Organic Solar Cells From Non-Halogenated Solvent," *Advanced Materials*, vol. 37, no. 17, p. 2500115, 2025.

[19] L. Zhu, M. Zhang, J. Xu, C. Li, J. Yan, G. Zhou, W. Zhong, T. Hao, J. Song, X. Xue, Z. Zhou, R. Zeng, H. Zhu, C.-C. Chen, R. C. I. MacKenzie, Y. Zou, J. Nelson, Y. Zhang, Y. Sun, and F. Liu, "Single-junction organic solar cells with over 19% efficiency enabled by a refined double-fibril network morphology," *Nature materials*, vol. 21, no. 6, pp. 656–663, 2022.

[20] H. Chen, Y. Huang, R. Zhang, H. Mou, J. Ding, J. Zhou, Z. Wang, H. Li, W. Chen, J. Zhu, Q. Cheng, H. Gu, X. Wu, T. Zhang, Y. Wang, H. Zhu, Z. Xie, F. Gao, Y. Li, and Y. Li, "Organic solar cells with 20.82% efficiency and high tolerance of active layer thickness through crystallization sequence manipulation," *Nature materials*, vol. 24, no. 3, pp. 444–453, 2025.

[21] N. Liu, M. Liu, J. Dai, X. Cheng, and Z. Chen, "Nucleation engineering to strengthen interface contacts in single-crystal perovskite photovoltaics," *Angewandte Chemie*, vol. 137, no. 20, p. e202500947, 2025.

[22] B. M. Kayes, H. Nie, R. Twist, S. G. Spruytte, F. Reinhardt, I. C. Kizilyalli, and G. S. Higashi, "27.6% conversion efficiency, a new record for single-junction solar cells under 1 sun illumination," in *2011 37th IEEE photovoltaic specialists conference*, pp. 000004–000008, IEEE, 2011.

[23] National Renewable Energy Laboratory, "Best research-cell efficiency chart." https://www.nrel.gov/pv/cell-efficiency, 2025. Accessed: 5 December 2025.

[24] Y. Cui, Y. Xu, H. Yao, P. Bi, L. Hong, J. Zhang, Y. Zu, T. Zhang, J. Qin, J. Ren, Z. Chen, C. He, X. Hao, Z. Wei, and J. Hou, "Single-junction organic photovoltaic cell with 19% efficiency," *Advanced materials (Weinheim)*, vol. 33, no. 41, pp. e2102420–n/a, 2021.

[25] K. Yoshikawa, H. Kawasaki, W. Yoshida, T. Irie, K. Konishi, K. Nakano, T. Uto, D. Adachi, M. Kanematsu, H. Uzu, *et al.*, "Silicon heterojunction solar cell with interdigitated back contacts for a photoconversion efficiency over 26%," *Nature energy*, vol. 2, no. 5, pp. 1–8, 2017.

[26] J. Benduhn, K. Tvingstedt, F. Piersimoni, S. Ullbrich, Y. Fan, M. Tropiano, K. A. McGarry, O. Zeika, M. K. Riede, C. J. Douglas, S. Barlow, S. R. Marder, D. Neher, D. Spoltore, and K. Vandewal, "Intrinsic non-radiative voltage losses in fullerene-based organic solar cells," *Nature energy*, vol. 2, no. 6, pp. 17053–, 2017.

[27] W. Tress, *Organic solar cells : theory, experiment, and device simulation*. Springer series in materials science, volume 208, Cham: Springer, 2014.

[28] M. Knupfer, "Exciton binding energies in organic semiconductors," *Applied Physics A*, vol. 77, no. 5, pp. 623–626, 2003.

[29] J. Brebels, J. V. Manca, L. Lutsen, D. Vanderzande, and W. Maes, "High dielectric constant conjugated materials for organic photovoltaics," *Journal of Materials Chemistry A*, vol. 5, no. 46, pp. 24037–24050, 2017.

[30] N. Karl, "Studies of organic semiconductors for 40 years—iii," *Molecular Crystals and Liquid Crystals*, vol. 171, no. 1, pp. 31–51, 1989.

[31] P. Friederich, V. Meded, A. Poschlad, T. Neumann, V. Rodin, V. Stehr, F. Symalla, D. Danilov, G. Lüdemann, R. F. Fink, *et al.*, "Molecular origin of the charge carrier mobility in small molecule organic semiconductors," *Advanced Functional Materials*, vol. 26, no. 31, pp. 5757–5763, 2016.

[32] T. B. Singh, N. Marjanović, G. Matt, S. Günes, N. Sariciftci, A. M. Ramil, A. Andreev, H. Sitter, R. Schwödiauer, and S. Bauer, "High-mobility n-channel organic field-effect

transistors based on epitaxially grown c60 films," *Organic Electronics*, vol. 6, no. 3, pp. 105–110, 2005.

[33] J. Zhao, Y. Li, G. Yang, K. Jiang, H. Lin, H. Ade, W. Ma, and H. Yan, "Efficient organic solar cells processed from hydrocarbon solvents," *Nature Energy*, vol. 1, no. 2, pp. 1–7, 2016.

[34] B.-W. Chen, M.-W. An, Y.-F. Li, X. Wang, Z.-L. Qiu, L.-S. Dai, K. Cao, K.-Y. Yang, D.-Q. Yun, L.-L. Deng, *et al.*, "Vacuum-deposited organic solar cells with over 10% efficiency and device lifetime over 2 years enabled by fluorinated donor," *Advanced Functional Materials*, p. e09380, 2025.

[35] J. Yuan and Y. Zou, "The history and development of y6," *Organic Electronics*, vol. 102, p. 106436, 2022.

[36] J. Yuan, Y. Zhang, L. Zhou, G. Zhang, H.-L. Yip, T.-K. Lau, X. Lu, C. Zhu, H. Peng, P. A. Johnson, *et al.*, "Single-junction organic solar cell with over 15% efficiency using fused-ring acceptor with electron-deficient core," *Joule*, vol. 3, no. 4, pp. 1140–1151, 2019.

[37] Q. Burlingame, X. Huang, X. Liu, C. Jeong, C. Coburn, and S. R. Forrest, "Intrinsically stable organic solar cells under high-intensity illumination," *Nature*, vol. 573, no. 7774, pp. 394–397, 2019.

[38] H. Liu, M.-H. Yu, C.-C. Lee, X. Yu, Y. Li, Z. Zhu, C.-C. Chueh, Z. Li, and A. K.-Y. Jen, "Technical challenges and perspectives for the commercialization of solution-processable solar cells," *Advanced Materials Technologies*, vol. 6, no. 6, p. 2000960, 2021.

[39] S. Karuthedath, J. Gorenflot, Y. Firdaus, N. Chaturvedi, C. S. P. De Castro, G. T. Harrison, J. I. Khan, A. Markina, A. H. Balawi, T. A. D. Peña, W. Liu, R.-Z. Liang, A. Sharma, S. H. K. Paleti, W. Zhang, Y. Lin, E. Alarousu, S. Lopatin, D. H. Anjum, P. M. Beaujuge, S. De Wolf, I. McCulloch, T. D. Anthopoulos, D. Baran, D. Andrienko, and F. Laquai, "Intrinsic efficiency limits in low-bandgap non-fullerene acceptor organic solar cells," *Nature materials*, vol. 20, no. 3, pp. 378–384, 2021.

[40] J. Hofinger, C. Putz, F. Mayr, K. Gugujonovic, D. Wielend, and M. C. Scharber, "Understanding the low voltage losses in high-performance non-fullerene acceptor-based organic solar cells," *Materials advances*, vol. 2, no. 13, pp. 4291–432, 2021.

[41] D. Qian, Z. Zheng, H. Yao, W. Tress, T. R. Hopper, S. Chen, S. Li, J. Liu, S. Chen, J. Zhang, X.-K. Liu, B. Gao, L. Ouyang, Y. Jin, G. Pozina, I. A. Buyanova, W. M. Chen, O. Inganäs, V. Coropceanu, J.-L. Bredas, H. Yan, J. Hou, F. Zhang, A. A. Bakulin, and F. Gao, "Design rules for minimizing voltage losses in high-efficiency organic solar cells," *Nature materials*, vol. 17, no. 8, pp. 703–709, 2018.

[42] A. Armin, W. Li, O. J. Sandberg, Z. Xiao, L. Ding, J. Nelson, D. Neher, K. Vandewal, S. Shoaee, T. Wang, H. Ade, T. Heumüller, C. Brabec, and P. Meredith, "A history and perspective of non-fullerene electron acceptors for organic solar cells," *Advanced energy materials*, vol. 11, no. 15, 2021.

[43] L. Ma, S. Zhang, J. Wang, Y. Xu, and J. Hou, "Recent advances in non-fullerene organic solar cells: from lab to fab," *Chemical communications (Cambridge, England)*, vol. 56, no. 92, pp. 14337–14352, 2020.

[44] A. Köhler and H. Bässler, *Electronic processes in organic semiconductors : an introduction*. Weinheim, Germany: Wiley-VCH, 2015.

[45] U. Rau, "Reciprocity relation between photovoltaic quantum efficiency and electroluminescent emission of solar cells," *Physical review. B, Condensed matter and materials physics*, vol. 76, no. 8, 2007.

[46] U. Rau, B. Blank, T. C. Müller, and T. Kirchartz, "Efficiency potential of photovoltaic materials and devices unveiled by detailed-balance analysis," *Physical review applied*, vol. 7, no. 4, 2017.

[47] P. Friederich, V. Meded, A. Poschlad, T. Neumann, V. Rodin, V. Stehr, F. Symalla, D. Danilov, G. Lüdemann, R. F. Fink, I. Kondov, F. von Wrochem, and W. Wenzel, "Molecular origin of the charge carrier mobility in small molecule organic semiconductors," *Advanced functional materials*, vol. 26, no. 31, pp. 5757–5763, 2016.

[48] J. Cornil, S. Verlaak, N. Martinelli, A. Mityashin, Y. Olivier, T. Van Regemorter, G. D'Avino, L. Muccioli, C. Zannoni, F. Castet, D. Beljonne, and P. Heremans, "Exploring the energy landscape of the charge transport levels in organic semiconductors at the molecular scale," *Accounts of chemical research*, vol. 46, no. 2, pp. 434–443, 2013.

[49] P. Cheng and Y. Yang, "Narrowing the band gap: The key to high-performance organic photovoltaics," *Accounts of chemical research*, vol. 53, no. 6, pp. 1218–1228, 2020.

[50] C. M. Marian, "Understanding and controlling intersystem crossing in molecules," *Annual review of physical chemistry*, vol. 72, no. 1, pp. 617–640, 2021.

[51] A. Jungbluth, *Sensitive External Quantum Efficiency Measurements for Studying Charge Transfer in Organic Solar Cells*. PhD thesis, University of Oxford, 2022.

[52] E. U. Condon, "Nuclear motions associated with electron transitions in diatomic molecules," *Physical review*, vol. 32, no. 6, pp. 858–872, 1928.

[53] I. R. Gould, D. Noukakis, L. Gomez-Jahn, R. H. Young, J. L. Goodman, and S. Farid, "Radiative and nonradiative electron transfer in contact radical-ion pairs: Electron transfer," *Chemical physics*, vol. 176, no. 2-3, pp. 439–456, 1993.

[54] T. Koopmans, "Ü̈ber die zuordnung von wellenfunktionen und eigenwerten zu den einzelnen elektronen eines atoms," *Physica*, vol. 1, no. 1, pp. 104–113, 1934.

[55] R. Warren, *Energy Levels in Organic Semiconductors : Tuning and Doping*. PhD thesis, University of Oxford, 2020.

[56] M. Schwarze, W. Tress, B. Beyer, F. Gao, R. Scholz, C. Poelking, K. Ortstein, A. A. Günther, D. Kasemann, D. Andrienko, and K. Leo, "Band structure engineering in organic semiconductors," *Science (American Association for the Advancement of Science)*, vol. 352, no. 6292, pp. 1446–1449, 2016.

[57] H. Yoshida, K. Yamada, J. Tsutsumi, and N. Sato, "Complete description of ionization energy and electron affinity in organic solids: Determining contributions from electronic polarization, energy band dispersion, and molecular orientation," *Physical review. B, Condensed matter and materials physics*, vol. 92, no. 7, 2015.

[58] N. Sato, K. Seki, and H. Inokuchi, "Polarization energies of organic solids determined by ultraviolet photoelectron spectroscopy," *Journal of the Chemical Society, Faraday Transactions 2*, vol. 77, no. 9, pp. 1621–, 1981.

[59] J. Sworakowski, "How accurate are energies of homo and lumo levels in small-molecule organic semiconductors determined from cyclic voltammetry or optical spectroscopy?," *Synthetic Metals*, vol. 235, pp. 125–130, 2018.

[60] G. C. La Rocca, "Wannier–mott excitons in semiconductors," *Thin films and nanostructures*, vol. 31, pp. 97–128, 2003.

[61] K. Vandewal, J. Benduhn, and V. C. Nikolis, "How to determine optical gaps and voltage losses in organic photovoltaic materials," *Sustainable energy & fuels*, vol. 2, no. 3, pp. 538–544, 2018.

[62] Y. Dong, V. C. Nikolis, F. Talnack, Y.-C. Chin, J. Benduhn, G. Londi, J. Kublitski, X. Zheng, S. C. B. Mannsfeld, D. Spoltore, L. Muccioli, J. Li, X. Blase, D. Beljonne, J.-S. Kim, A. A. Bakulin, G. D'Avino, J. R. Durrant, and K. Vandewal, "Orientation dependent molecular electrostatics drives efficient charge generation in homojunction organic solar cells," *Nature communications*, vol. 11, no. 1, pp. 4617–9, 2020.

[63] Y. Fu, T. H. Lee, Y.-C. Chin, R. A. Pacalaj, C. Labanti, S. Y. Park, Y. Dong, H. W. Cho, J. Y. Kim, D. Minami, J. R. Durrant, and J.-S. Kim, "Molecular orientation-dependent energetic shifts in solution-processed non-fullerene acceptors and their impact on organic photovoltaic performance," *Nature communications*, vol. 14, no. 1, pp. 1870–12, 2023.

[64] Y. Yan, S. Zhao, Y. Zhang, T. Wang, Y. Shi, D. Qiu, J. Zhang, L. Zhu, M. Wang, J. Qiao, *et al.*, "Molecular orientation-dependent exciton separation in optimized single-component y6 organic solar cells," *Solar RRL*, vol. 7, no. 18, p. 2300342, 2023.

[65] S. Y. Park, C. Labanti, R. A. Pacalaj, T. H. Lee, Y. Dong, Y.-C. Chin, J. Luke, G. Ryu, D. Minami, S. Yun, *et al.*, "The state-of-the-art solution-processed single component organic photodetectors achieved by strong quenching of intermolecular emissive state

and high quadrupole moment in non-fullerene acceptors," *Advanced Materials*, vol. 35, no. 49, p. 2306655, 2023.

[66] O. V. Mikhnenko, P. W. M. Blom, and T.-Q. Nguyen, "Exciton diffusion in organic semiconductors," *Energy & environmental science*, vol. 8, no. 7, pp. 1867–1888, 2015.

[67] Y. Firdaus, V. M. Le Corre, S. Karuthedath, W. Liu, A. Markina, W. Huang, S. Chattopadhyay, M. M. Nahid, M. I. Nugraha, Y. Lin, A. Seitkhan, A. Basu, W. Zhang, I. McCulloch, H. Ade, J. Labram, F. Laquai, D. Andrienko, L. J. A. Koster, and T. D. Anthopoulos, "Long-range exciton diffusion in molecular non-fullerene acceptors," *Nature communications*, vol. 11, no. 1, pp. 5220–10, 2020.

[68] D. L. Dexter, "A theory of sensitized luminescence in solids," *The Journal of chemical physics*, vol. 21, no. 5, pp. 836–850, 1953.

[69] D. L. Dexter, R. S. Knox, and T. Förster, "The radiationless transfer of energy of electronic excitation between impurity molecules in crystals," *Physica Status Solidi (b)*, vol. 34, no. 2, pp. K159–K162, 1969.

[70] I. Medintz and N. Hildebrandt, *FRET - Förster resonance energy transfer : from theory to applications*. Weinheim: Wiley-VCH Verlag GmbH & Co. KGaA, 1st ed. ed., 2014.

[71] V. Cleave, G. Yahioglu, P. L. Barny, R. H. Friend, and N. Tessler, "Harvesting singlet and triplet energy in polymer leds," *Advanced materials (Weinheim)*, vol. 11, no. 4, pp. 285–288, 1999.

[72] Y. Kawamura, S. Yanagida, and S. R. Forrest, "Energy transfer in polymer electrophosphorescent light emitting devices with single and multiple doped luminescent layers," *Journal of applied physics*, vol. 92, no. 1, pp. 87–93, 2002.

[73] A. Köhler and H. Bässler, "Triplet states in organic semiconductors," *Materials science & engineering. R, Reports : a review journal*, vol. 66, no. 4, pp. 71–109, 2009.

[74] G. Chamberlain, "Organic solar cells: A review," *Solar cells*, vol. 8, no. 1, pp. 47–83, 1983.

[75] C. W. Tang, "Two-layer organic photovoltaic cell," *Applied physics letters*, vol. 48, no. 2, pp. 183–185, 1986.

[76] J. J. Benson-Smith, L. Goris, K. Vandewal, K. Haenen, J. V. Manca, D. Vanderzande, D. D. C. Bradley, and J. Nelson, "Formation of a ground-state charge-transfer complex in polyfluorene//[6,6]-phenyl-c61 butyric acid methyl ester (pcbm) blend films and its role in the function of polymer/pcbm solar cells," *Advanced functional materials*, vol. 17, no. 3, pp. 451–457, 2007.

[77] S. Li, L. Zhan, C. Sun, H. Zhu, G. Zhou, W. Yang, M. Shi, C.-Z. Li, J. Hou, Y. Li, *et al.*, "Highly efficient fullerene-free organic solar cells operate at near zero highest occupied molecular orbital offsets," *Journal of the American Chemical Society*, vol. 141, no. 7, pp. 3073–3082, 2019.

[78] L. Perdigón-Toro, H. Zhang, A. Markina, J. Yuan, S. M. Hosseini, C. M. Wolff, G. Zuo, M. Stolterfoht, Y. Zou, F. Gao, *et al.*, "Barrierless free charge generation in the high-performance pm6: Y6 bulk heterojunction non-fullerene solar cell," *Advanced Materials*, vol. 32, no. 9, p. 1906763, 2020.

[79] R. Wang, J. Yuan, R. Wang, G. Han, T. Huang, W. Huang, J. Xue, H.-C. Wang, C. Zhang, C. Zhu, *et al.*, "Rational tuning of molecular interaction and energy level alignment enables high-performance organic photovoltaics," *Advanced Materials*, vol. 31, no. 43, p. 1904215, 2019.

[80] K. Vandewal, K. Tvingstedt, A. Gadisa, O. Inganäs, and J. V. Manca, "On the origin of the open-circuit voltage of polymer–fullerene solar cells," *Nature materials*, vol. 8, no. 11, pp. 904–909, 2009.

[81] K. Vandewal, K. Tvingstedt, A. Gadisa, O. Inganäs, and J. V. Manca, "Relating the open-circuit voltage to interface molecular properties of donor:acceptor bulk heterojunction solar cells," *Physical review. B, Condensed matter and materials physics*, vol. 81, no. 12, pp. 125204–, 2010.

[82] A. Jungbluth, P. Kaienburg, and M. Riede, "Charge transfer state characterization and voltage losses of organic solar cells," *Journal of Physics: Materials*, vol. 5, no. 2, p. 024002, 2022.

[83] J. A. Bartelt, D. Lam, T. M. Burke, S. M. Sweetnam, and M. D. McGehee, "Charge-Carrier Mobility Requirements for Bulk Heterojunction Solar Cells with High Fill Factor and External Quantum Efficiency exceeding 90," *Advanced Energy Materials*, vol. 5, no. 15, pp. np–n/a, 2015.

[84] R. R. Lunt, N. C. Giebink, A. A. Belak, J. B. Benziger, and S. R. Forrest, "Exciton diffusion lengths of organic semiconductor thin films measured by spectrally resolved photoluminescence quenching," *Journal of applied physics*, vol. 105, no. 5, pp. 053711–053711–7, 2009.

[85] H. Tamura and Y. Matsuo, "Exciton diffusion length and charge mobility in donor and acceptor materials in organic photovoltaics: Tetrabenzoporphyrin and silylmethyl [60] fullerene," *Chemical physics letters*, vol. 598, pp. 81–85, 2014.

[86] M. Hiramoto, H. Fujiwara, and M. Yokoyama, "Three-layered organic solar cell with a photoactive interlayer of codeposited pigments," *Applied physics letters*, vol. 58, no. 10, pp. 1062–1064, 1991.

[87] G. Yu, J. Gao, J. C. Hummelen, F. Wudl, and A. J. Heeger, "Polymer photovoltaic cells: Enhanced efficiencies via a network of internal donor-acceptor heterojunctions," *Science (American Association for the Advancement of Science)*, vol. 270, no. 5243, pp. 1789–1791, 1995.

[88] J. J. M. Halls, C. A. Walsh, N. C. Greenham, E. A. Marseglia, R. H. Friend, S. C. Moratti, and A. B. Holmes, "Efficient photodiodes from interpenetrating polymer networks," *Nature (London)*, vol. 376, no. 6540, pp. 498–500, 1995.

[89] D. Zhang, B. Fan, L. Ying, N. Li, C. J. Brabec, F. Huang, and Y. Cao, "Recent progress in thick-film organic photovoltaic devices: Materials, devices, and processing," *SusMat (Online)*, vol. 1, no. 1, pp. 4–23, 2021.

[90] K. R. Graham, G. O. N. Ndjawa, S. M. Conron, R. Munir, K. Vandewal, J. J. Chen, S. Sweetnam, M. E. Thompson, A. Salleo, M. D. McGehee, and A. Amassian, "Organic electronics: The roles of structural order and intermolecular interactions in determining ionization energies and charge-transfer state energies in organic semiconductors (adv. energy mater. 22/2016)," *Advanced energy materials*, vol. 6, no. 22, 2016.

[91] Y. Ma, M. Zhang, S. Wan, P. Yin, P. Wang, D. Cai, F. Liu, and Q. Zheng, "Efficient organic solar cells from molecular orientation control of m-series acceptors," *Joule*, vol. 5, no. 1, pp. 197–209, 2021.

[92] C. Schunemann, D. Wynands, L. Wilde, M. P. Hein, S. Pfutzner, C. Elschner, K.-J. Eichhorn, K. Leo, and M. Riede, "Phase separation analysis of bulk heterojunctions in small-molecule organic solar cells using zinc-phthalocyanine and C_{60}," *Physical review. B, Condensed matter and materials physics*, vol. 85, no. 24, 2012.

[93] M. Zhang, H. Wang, H. Tian, Y. Geng, and C. W. Tang, "Bulk heterojunction photovoltaic cells with low donor concentration," *Advanced materials (Weinheim)*, vol. 23, no. 42, pp. 4960–4964, 2011.

[94] K. Vandewal, J. Widmer, T. Heumueller, C. J. Brabec, M. D. McGehee, K. Leo, M. Riede, and A. Salleo, "Increased open-circuit voltage of organic solar cells by reduced donor-acceptor interface area," *Advanced materials (Weinheim)*, vol. 26, no. 23, pp. 3839–3843, 2014.

[95] C. Zhang, J. Li, W. Deng, J. Dai, J. Yu, G. Lu, H. Hu, and K. Wang, "18.9% efficiency ternary organic solar cells enabled by isomerization engineering of chlorine-substitution on small molecule donors," 2023.

[96] Y. Wang, J. Yu, R. Zhang, J. Yuan, S. Hultmark, C. E. Johnson, N. P. Gallop, B. Siegmund, D. Qian, H. Zhang, Y. Zou, M. Kemerink, A. A. Bakulin, C. Müller, K. Vandewal, X.-K. Chen, and F. Gao, "Origins of the open-circuit voltage in ternary organic solar cells and design rules for minimized voltage losses," *Nature energy*, vol. 8, no. 9, pp. 978–988, 2023.

[97] G. J. Moore, M. Causa', J. F. Martinez Hardigree, S. Karuthedath, I. Ramirez, A. Jungbluth, F. Laquai, M. Riede, and N. Banerji, "Ultrafast charge dynamics in dilute-donor versus highly intermixed tapc:c60 organic solar cell blends," *The journal of physical chemistry letters*, vol. 11, no. 14, pp. 5610–5617, 2020.

[98] S. M. Menke, N. A. Ran, G. C. Bazan, and R. H. Friend, "Understanding energy loss in organic solar cells: Toward a new efficiency regime," *Joule*, vol. 2, no. 1, pp. 25–35, 2018.

[99] A. Jungbluth, E. Cho, A. Privitera, K. M. Yallum, P. Kaienburg, A. E. Lauritzen, T. Derrien, S. V. Kesava, I. Habib, S. M. Pratik, *et al.*, "Limiting factors for charge generation in low-offset fullerene-based organic solar cells," *Nature Communications*, vol. 15, no. 1, p. 5488, 2024.

[100] I. Ramirez, M. Causa', Y. Zhong, N. Banerji, and M. Riede, "Key tradeoffs limiting the performance of organic photovoltaics," *Advanced Energy Materials*, vol. 8, no. 28, p. 1703551, 2018.

[101] H. Bässler and A. Köhler, ""hot or cold": how do charge transfer states at the donor–acceptor interface of an organic solar cell dissociate?," *Physical Chemistry Chemical Physics*, vol. 17, no. 43, pp. 28451–28462, 2015.

[102] K. Vandewal, S. Albrecht, E. T. Hoke, K. R. Graham, J. Widmer, J. D. Douglas, M. Schubert, W. R. Mateker, J. T. Bloking, G. F. Burkhard, *et al.*, "Efficient charge generation by relaxed charge-transfer states at organic interfaces," *Nature materials*, vol. 13, no. 1, pp. 63–68, 2014.

[103] X. Shen, G. Han, D. Fan, Y. Xie, and Y. Yi, "Hot charge-transfer states determine exciton dissociation in the DTDCTB/C_{60} complex for organic solar cells: A theoretical insight," *The Journal of Physical Chemistry C*, vol. 119, no. 21, pp. 11320–11326, 2015.

[104] C. J. Brabec, G. Zerza, G. Cerullo, S. De Silvestri, S. Luzzati, J. C. Hummelen, and S. Sariciftci, "Tracing photoinduced electron transfer process in conjugated polymer/fullerene bulk heterojunctions in real time," *Chemical physics letters*, vol. 340, no. 3, pp. 232–236, 2001.

[105] J. L. Langentepe-Kong, M. Pranav, S. Shoaee, and D. Neher, "Dark side of organic solar cells: How triplet excitons shape charge recombination and efficiency limits," *PRX Energy*, vol. 5, no. 1, p. 013003, 2026.

[106] A. Rao, P. C. Y. Chow, S. Gélinas, C. W. Schlenker, C.-Z. Li, H.-L. Yip, A. K.-Y. Jen, D. S. Ginger, and R. H. Friend, "The role of spin in the kinetic control of recombination in organic photovoltaics," *Nature (London)*, vol. 500, no. 7463, pp. 435–439, 2013.

[107] A. J. Gillett, A. Privitera, R. Dilmurat, A. Karki, D. Qian, A. Pershin, G. Londi, W. K. Myers, J. Lee, J. Yuan, S.-J. Ko, M. K. Riede, F. Gao, G. C. Bazan, A. Rao, T.-Q. Nguyen, D. Beljonne, and R. H. Friend, "The role of charge recombination to triplet excitons in organic solar cells," *Nature (London)*, vol. 597, no. 7878, pp. 666–671, 2021.

[108] W. Shockley and H. J. Queisser, "Detailed balance limit of efficiency of p-n junction solar cells," *Journal of applied physics*, vol. 32, no. 3, pp. 510–519, 1961.

[109] W. Shockley, "The theory of p-n junctions in semiconductors and p-n junction transistors," *Bell System Technical Journal*, vol. 28, no. 3, pp. 435–489, 1949.

[110] T. Kirchartz, J. Nelson, and U. Rau, "Reciprocity between charge injection and extraction and its influence on the interpretation of electroluminescence spectra in organic solar cells," *Physical review applied*, vol. 5, no. 5, 2016.

[111] A. Armin, N. Zarrabi, O. J. Sandberg, C. Kaiser, S. Zeiske, W. Li, and P. Meredith, "Limitations of charge transfer state parameterization using photovoltaic external quantum efficiency," *Advanced energy materials*, vol. 10, no. 41, 2020.

[112] M. List, T. Sarkar, P. Perkhun, J. Ackermann, C. Luo, and U. Würfel, "Correct determination of charge transfer state energy from luminescence spectra in organic solar cells," *Nature communications*, vol. 9, no. 1, pp. 3631–8, 2018.

[113] R. A. Marcus, "On the theory of oxidation-reduction reactions involving electron transfer. i," *The Journal of chemical physics*, vol. 24, no. 5, pp. 966–978, 1956.

[114] R. A. Marcus, "On the theory of oxidation-reduction reactions involving electron transfer. ii. applications to data on the rates of isotopic exchange reactions," *The Journal of chemical physics*, vol. 26, no. 4, pp. 867–871, 1957.

[115] R. A. Marcus, "Electron transfer reactions in chemistry theory and experiment," *Journal of electroanalytical chemistry (Lausanne, Switzerland)*, vol. 438, no. 1-2, pp. 251–259, 1997.

[116] K. Vandewal, A. Gadisa, W. D. Oosterbaan, S. Bertho, F. Banishoeib, I. Van Severen, L. Lutsen, T. J. Cleij, D. Vanderzande, and J. V. Manca, "The relation between open-circuit voltage and the onset of photocurrent generation by charge-transfer absorption in polymer: fullerene bulk heterojunction solar cells," *Advanced Functional Materials*, vol. 18, no. 14, pp. 2064–2070, 2008.

[117] K. Tvingstedt, K. Vandewal, A. Gadisa, F. Zhang, J. Manca, and O. Inganäs, "Electroluminescence from charge transfer states in polymer solar cells," *Journal of the American Chemical Society*, vol. 131, no. 33, pp. 11819–11824, 2009.

[118] C. Kaiser, O. J. Sandberg, N. Zarrabi, W. Li, P. Meredith, and A. Armin, "A universal urbach rule for disordered organic semiconductors," *Nature Communications*, vol. 12, no. 1, p. 3988, 2021.

[119] N. A. Ran, J. A. Love, C. J. Takacs, A. Sadhanala, J. K. Beavers, S. D. Collins, Y. Huang, M. Wang, R. H. Friend, G. C. Bazan, *et al.*, "Harvesting the full potential of photons with organic solar cells.," *Advanced Materials (Deerfield Beach, Fla.)*, vol. 28, no. 7, pp. 1482–1488, 2015.

[120] Q. Liu, Y. Jiang, K. Jin, J. Qin, J. Xu, W. Li, J. Xiong, J. Liu, Z. Xiao, K. Sun, S. Yang, X. Zhang, and L. Ding, "18% efficiency organic solar cells," *Science bulletin*, vol. 65, no. 4, pp. 272–275, 2020.

[121] S.-U.-Z. Khan, J. Bertrandie, M. Gui, A. Sharma, W. Alsufyani, J. F. Gorenflot, F. Laquai, D. Baran, and B. P. Rand, "Quantifying the effect of energetic disorder on organic solar cell energy loss," *Joule*, vol. 6, no. 12, pp. 2821–2834, 2022.

[122] C. Kaiser, S. Zeiske, P. Meredith, and A. Armin, "Determining ultralow absorption coefficients of organic semiconductors from the sub-bandgap photovoltaic external quantum efficiency," *Advanced optical materials*, vol. 8, no. 1, 2020.

[123] W. Li, K. H. Hendriks, A. Furlan, M. M. Wienk, and R. A. J. Janssen, "High quantum efficiencies in polymer solar cells at energy losses below 0.6 ev," *Journal of the American Chemical Society*, vol. 137, no. 6, pp. 2231–2234, 2015.

[124] R. Carron, C. Andres, E. Avancini, T. Feurer, S. Nishiwaki, S. Pisoni, F. Fu, M. Lingg, Y. E. Romanyuk, S. Buecheler, and A. N. Tiwari, "Bandgap of thin film solar cell absorbers: A comparison of various determination methods," *Thin solid films*, vol. 669, pp. 482–486, 2019.

[125] P. Makuła, M. Pacia, and W. Macyk, "How to correctly determine the band gap energy of modified semiconductor photocatalysts based on uv–vis spectra," *The journal of physical chemistry letters*, vol. 9, no. 23, pp. 6814–6817, 2018.

[126] P. Kaienburg, H. Bristow, A. Jungbluth, I. Habib, I. McCulloch, D. Beljonne, and M. Riede, "Vacuum-deposited donors for low-voltage-loss nonfullerene organic solar cells," *ACS Applied Materials & Interfaces*, vol. 15, no. 26, pp. 31684–31691, 2023.

[127] I. Habib, P. Kaienburg, D. Xia, O. Gough, M. Zhu, J. Spruce, W. Li, and M. Riede, "Vacuum deposited organic solar cells with btic-h as a–d–a non-fullerene acceptor," *APL materials*, vol. 11, no. 6, pp. 061128–061128–11, 2023.

[128] O. Almora, C. I. Cabrera, J. Garcia-Cerrillo, T. Kirchartz, U. Rau, and C. J. Brabec, "Quantifying the absorption onset in the quantum efficiency of emerging photovoltaic devices," *Advanced energy materials*, vol. 11, no. 16, 2021.

[129] M. Azzouzi, J. Yan, T. Kirchartz, K. Liu, J. Wang, H. Wu, and J. Nelson, "Nonradiative energy losses in bulk-heterojunction organic photovoltaics," *Physical review. X*, vol. 8, no. 3, pp. 031055–, 2018.

[130] R. T. Ross, "Some thermodynamics of photochemical systems," *The Journal of chemical physics*, vol. 46, no. 12, pp. 4590–4593, 1967.

[131] S. Liu, J. Yuan, W. Deng, M. Luo, Y. Xie, Q. Liang, Y. Zou, Z. He, H. Wu, and Y. Cao, "High-efficiency organic solar cells with low non-radiative recombination loss and low energetic disorder," *Nature photonics*, vol. 14, no. 5, pp. 300–305, 2020.

[132] M. Azzouzi, T. Kirchartz, and J. Nelson, "Factors controlling open-circuit voltage losses in organic solar cells," *Trends in chemistry*, vol. 1, no. 1, pp. 49–62, 2019.

[133] X.-K. Chen, D. Qian, Y. Wang, T. Kirchartz, W. Tress, H. Yao, J. Yuan, M. Hülsbeck, M. Zhang, Y. Zou, Y. Sun, Y. Li, J. Hou, O. Inganäs, V. Coropceanu, J.-L. Bredas, and F. Gao, "A unified description of non-radiative voltage losses in organic solar cells," *Nature energy*, vol. 6, no. 8, pp. 799–806, 2021.

[134] Q. Liu and K. Vandewal, "Understanding and suppressing non-radiative recombination losses in non-fullerene organic solar cells," *Advanced materials (Weinheim)*, vol. 35, no. 35, pp. e2302452–n/a, 2023.

[135] A. Classen, C. L. Chochos, L. Lüer, V. G. Gregoriou, J. Wortmann, A. Osvet, K. Forberich, I. McCulloch, T. Heumüller, and C. J. Brabec, "The role of exciton lifetime for charge generation in organic solar cells at negligible energy-level offsets," *Nature energy*, vol. 5, no. 9, pp. 711–719, 2020.

[136] T. Főrster, "10th spiers memorial lecture. transfer mechanisms of electronic excitation," *Discussions of the Faraday Society*, vol. 27, pp. 7–17, 1959.

[137] A. R. Clapp, I. L. Medintz, and H. Mattoussi, "Förster resonance energy transfer investigations using quantum-dot fluorophores," *ChemPhysChem*, vol. 7, no. 1, pp. 47–57, 2006.

[138] A. Holzhey, C. Uhrich, E. Brier, E. Reinhold, P. Bäuerle, K. Leo, and M. Hoffmann, "Exciton diffusion and energy transfer in organic solar cells based on dicyanovinylterthiophene," *Journal of applied physics*, vol. 104, no. 6, pp. 064510–064510–8, 2008.

[139] Y. J. Jang, D. Kawaguchi, S. Yamaguchi, S. Lee, J. W. Lim, H. Kim, K. Tanaka, and D. H. Kim, "Enhancing the organic solar cell efficiency by combining plasmonic and förster

resonance energy transfer (fret) effects," *Journal of Power Sources*, vol. 438, p. 227031, 2019.

[140] G. K. Mor, J. Basham, M. Paulose, S. Kim, O. K. Varghese, A. Vaish, S. Yoriya, and C. A. Grimes, "High-efficiency forster resonance energy transfer in solid-state dye sensitized solar cells," *Nano Letters*, vol. 10, no. 7, pp. 2387–2394, 2010.

[141] J.-S. Huang, T. Goh, X. Li, M. Y. Sfeir, E. A. Bielinski, S. Tomasulo, M. L. Lee, N. Hazari, and A. D. Taylor, "Polymer bulk heterojunction solar cells employing förster resonance energy transfer," *Nature Photonics*, vol. 7, no. 6, pp. 479–485, 2013.

[142] R. Narayanan, M. Deepa, and A. K. Srivastava, "Förster resonance energy transfer and carbon dots enhance light harvesting in a solid-state quantum dot solar cell," *Journal of Materials Chemistry A*, vol. 1, no. 12, pp. 3907–3918, 2013.

[143] L. Mishra, R. K. Behera, A. Panigrahi, and M. K. Sarangi, "Förster resonance energy transfer assisted enhancement in optoelectronic properties of metal halide perovskite nanocrystals," *The Journal of Physical Chemistry Letters*, vol. 13, no. 19, pp. 4357–4364, 2022.

[144] M. H. Stewart, A. L. Huston, A. M. Scott, E. Oh, W. R. Algar, J. R. Deschamps, K. Susumu, V. Jain, D. E. Prasuhn, J. Blanco-Canosa, *et al.*, "Competition between förster resonance energy transfer and electron transfer in stoichiometrically assembled semiconductor quantum dot-fullerene conjugates," *Acs Nano*, vol. 7, no. 10, pp. 9489–9505, 2013.

[145] M. Zhou, K. Zhang, X. Li, Y. Ge, W. Zhang, P. Lu, and X. Hao, "Improved exciton diffusion through modulating förster resonance energy transfer for efficient organic solar cells," *Solar RRL*, vol. 8, no. 13, p. 2400136, 2024.

[146] K. Cnops, B. P. Rand, D. Cheyns, B. Verreet, M. A. Empl, and P. Heremans, "8.4% efficient fullerene-free organic solar cells exploiting long-range exciton energy transfer," *Nature communications*, vol. 5, no. 1, pp. 3406–, 2014.

[147] J.-H. Lee, C.-C. Teng, J.-H. Lin, T.-C. Lin, and C. Yang, "Direct observations of energy transfer and quenching dynamics between alq3 and c545t in thin films with different doping concentrations," in *Light-Emitting Diode Materials and Devices*, vol. 5632, pp. 66–71, SPIE, 2005.

[148] E. A. Kovrigina, B. Pattengale, C. Xia, A. R. Galiakhmetov, J. Huang, J.-J. P. Kim, and E. L. Kovrigin, "Conformational states of cytochrome p450 oxidoreductase evaluated by fret using ultrafast transient absorption spectroscopy," *Biochemistry*, vol. 55, no. 43, p. 5973, 2016.

[149] K. Sreenath, C. Yi, K. L. Knappenberger, and L. Zhu, "Distinguishing förster resonance energy transfer and solvent-mediated charge-transfer relaxation dynamics in a zinc (ii) indicator: a femtosecond time-resolved transient absorption spectroscopic study," *Physical Chemistry Chemical Physics*, vol. 16, no. 11, pp. 5088–5092, 2014.

[150] A. A. Mohapatra, R. Shivanna, S. Podapangi, A. Hinderhofer, M. I. Dar, N. Maity, F. Schreiber, A. Sadhanala, R. H. Friend, and S. Patil, "Role of morphology and förster resonance energy transfer in ternary blend organic solar cells," *ACS Applied Energy Materials*, vol. 3, no. 12, pp. 12025–12036, 2020.

[151] L. J. Patalag, J. Hoche, M. Holzapfel, A. Schmiedel, R. Mitric, C. Lambert, and D. B. Werz, "Ultrafast resonance energy transfer in ethylene-bridged bodipy heterooligomers: From frenkel to förster coupling limit," *Journal of the American Chemical Society*, vol. 143, no. 19, pp. 7414–7425, 2021.

[152] H. Wang, D. Yang, P. Ding, L. Xie, Z. Chen, S. Yang, P. Yan, Y. Meng, J. Zhang, Z. Wei, *et al.*, "Dual förster resonance energy transfer effects enables high photocurrent density and high fill factor in ternary organic solar cells," *Chemical Engineering Journal*, vol. 474, p. 145395, 2023.

[153] R. Hamburger, C. Rumble, and E. R. Young, "An introduction to processing, fitting, and interpreting transient absorption data," *Journal of Visualized Experiments*, no. 204, 2024.

[154] D. C. Coffey, A. J. Ferguson, N. Kopidakis, and G. Rumbles, "Photovoltaic charge generation in organic semiconductors based on long-range energy transfer," *ACS nano*, vol. 4, no. 9, pp. 5437–5445, 2010.

[155] X. Gong, S.-H. Lim, J. C. Ostrowski, D. Moses, C. J. Bardeen, and G. C. Bazan, "Phosphorescence from iridium complexes doped into polymer blends," *Journal of Applied Physics*, vol. 95, no. 3, pp. 948–953, 2004.

[156] Y. W. Soon, T. M. Clarke, W. Zhang, T. Agostinelli, J. Kirkpatrick, C. Dyer-Smith, I. McCulloch, J. Nelson, and J. R. Durrant, "Energy versus electron transfer in organic solar cells: a comparison of the photophysics of two indenofluorene: fullerene blend films," *Chemical Science*, vol. 2, no. 6, pp. 1111–1120, 2011.

[157] S. Honda, S. Yokoya, H. Ohkita, H. Benten, and S. Ito, "Light-harvesting mechanism in polymer/fullerene/dye ternary blends studied by transient absorption spectroscopy," *The Journal of Physical Chemistry C*, vol. 115, no. 22, pp. 11306–11317, 2011.

[158] K. Harun, F. Hussain, A. Purwanto, B. Sahraoui, A. Zawadzka, and A. A. Mohamad, "Sol-gel synthesized zno for optoelectronics applications: a characterization review," *Materials research express*, vol. 4, no. 12, pp. 122001–, 2017.

[159] D. Baran, T. Kirchartz, S. Wheeler, S. Dimitrov, M. Abdelsamie, J. Gorman, R. S. Ashraf, S. Holliday, A. Wadsworth, N. Gasparini, *et al.*, "Reduced voltage losses yield 10% efficient fullerene free organic solar cells with exceeding 1 V open circuit voltages," *Energy & environmental science*, vol. 9, no. 12, pp. 3783–3793, 2016.

[160] N. Evans, *Investigating electron transport layers in organic solar cells and the effects of doping, through electronic and spectroscopic characterisation techniques.* PhD thesis, University of Oxford, 2024.

[161] Ossila Ltd., "Spin coating: A guide to theory and techniques," n.d. Accessed: 25 June 2025.

[162] J. C. de Mello, H. F. Wittmann, and R. H. Friend, "An improved experimental determination of external photoluminescence quantum efficiency," *Advanced materials*, vol. 9, no. 3, pp. 230–232, 1997.

[163] N. Greenham, I. Samuel, G. Hayes, R. Phillips, Y. Kessener, S. Moratti, A. Holmes, and R. Friend, "Measurement of absolute photoluminescence quantum efficiencies in conjugated polymers," *Chemical physics letters*, vol. 241, no. 1-2, pp. 89–96, 1995.

[164] J. Kieffer, V. Valls, N. Blanc, and C. Hennig, "New tools for calibrating diffraction setups," *Journal of Synchrotron Radiation*, vol. 27, pp. 558–566, Mar 2020.

[165] J. Filik, A. W. Ashton, P. C. Y. Chang, P. Chater, S. Day, M. Drakopoulos, M. Gerring, M. Hart, O. Magdysyuk, S. Michalik, *et al.*, "Processing two-dimensional x-ray diffraction and small-angle scattering data in dawn 2," *Applied Crystallography*, vol. 50, no. 3, pp. 959–966, 2017.

[166] D.-M. Smilgies, "Scherrer grain-size analysis adapted to grazing-incidence scattering with area detectors," *Journal of applied crystallography*, vol. 42, no. 6, pp. 1030–1034, 2009.

[167] J. I. Langford and A. J. C. Wilson, "Scherrer after sixty years: A survey and some new results in the determination of crystallite size," *Journal of applied crystallography*, vol. 11, no. 2, pp. 102–113, 1978.

[168] A. Jungbluth, L. M. Hanauske, M. Zhu, G. Christoforo, P. Kaienburg, and M. Riede, "An open source sensitive external quantum efficiency setup for characterising optoelectronic devices," *Journal of Open Hardware*, vol. 9, no. 1, 2025.

[169] G. F. Burkhard, E. T. Hoke, and M. D. McGehee, "Accounting for interference, scattering, and electrode absorption to make accurate internal quantum efficiency measurements in organic and other thin solar cells," *Advanced materials (Weinheim)*, vol. 22, no. 30, pp. 3293–3297, 2010.

[170] R. Fitzner, E. Reinold, A. Mishra, E. Mena-Osteritz, H. Ziehlke, C. Körner, K. Leo, M. Riede, M. Weil, O. Tsaryova, A. Weiß, C. Uhrich, M. Pfeiffer, and P. Bäuerle,

"Dicyanovinyl-substituted oligothiophenes: Structure-property relationships and application in vacuum-processed small molecule organic solar cells," *Advanced functional materials*, vol. 21, no. 5, pp. 897–910, 2011.

[171] A. Mishra, D. Popovic, A. Vogt, H. Kast, T. Leitner, K. Walzer, M. Pfeiffer, E. Mena-Osteritz, and P. Bäuerle, "A–d–a-type s, n-heteropentacenes: next-generation molecular donor materials for efficient vacuum-processed organic solar cells," *Adv Mater*, vol. 26, no. 42, pp. 7217–7223, 2014.

[172] C. Uhrich, R. Schueppel, A. Petrich, M. Pfeiffer, K. Leo, E. Brier, P. Kilickiran, and P. Baeuerle, "Organic thin-film photovoltaic cells based on oligothiophenes with reduced bandgap," *Advanced functional materials*, vol. 17, no. 15, pp. 2991–2999, 2007.

[173] S. Holliday, R. S. Ashraf, C. B. Nielsen, M. Kirkus, J. A. Röhr, C.-H. Tan, E. Collado-Fregoso, A.-C. Knall, J. R. Durrant, J. Nelson, and I. McCulloch, "A rhodanine flanked nonfullerene acceptor for solution-processed organic photovoltaics," *Journal of the American Chemical Society*, vol. 137, no. 2, pp. 898–904, 2015.

[174] B. Verreet, S. Schols, D. Cheyns, B. P. Rand, H. Gommans, T. Aernouts, P. Heremans, and J. Genoe, "The characterization of chloroboron (iii) subnaphthalocyanine thin films and their application as a donor material for organic solar cells," *Journal of materials chemistry*, vol. 19, no. 30, pp. 5295–5297, 2009.

[175] V. C. Nikolis, Y. Dong, J. Kublitski, J. Benduhn, X. Zheng, C. Huang, A. C. Yüzer, M. Ince, D. Spoltore, J. R. Durrant, A. A. Bakulin, and K. Vandewal, "Field effect versus driving force: Charge generation in small-molecule organic solar cells," *Advanced energy materials*, vol. 10, no. 47, 2020.

[176] N. Kobayashi, T. Ishizaki, K. Ishii, and H. Konami, "Synthesis, spectroscopy, and molecular orbital calculations of subazaporphyrins, subphthalocyanines, subnaphthalocyanines, and compounds derived therefrom by ring expansion 1," *Journal of the American Chemical Society*, vol. 121, no. 39, pp. 9096–9110, 1999.

[177] S. Nonell, N. Rubio, B. del Rey, and T. Torres, "Synthesis, optical absorption and photophysical properties of cone-shaped subnaphthalocyanine," *Perkin 2 : an international journal of physical organic chemistry*, no. 6, pp. 1091–1094, 2000.

[178] S. M. Menke and R. J. Holmes, "Energy-cascade organic photovoltaic devices incorporating a host–guest architecture," *ACS applied materials & interfaces*, vol. 7, no. 4, pp. 2912–2918, 2015.

[179] H. Ye, S. V. Kesava, J. F. M. Hardigree, R. E. Brown, G. Mazzotta, R. Warren, P. J. Skabara, and M. Riede, "Efficiency enhancement of small molecule organic solar cells using hexapropyltruxene as an interface layer," *Journal of Materials Chemistry C*, vol. 8, no. 14, pp. 4909–4918, 2020.

[180] H. Gommans, S. Schols, A. Kadashchuk, P. Heremans, and S. C. J. Meskers, "Exciton diffusion length and lifetime in subphthalocyanine films," *Journal of physical chemistry. C*, vol. 113, no. 7, pp. 2974–2979, 2009.

[181] S. Ma, S. Du, G. Pan, S. Dai, B. Xu, and W. Tian, "Organic molecular aggregates: From aggregation structure to emission property," *Aggregate (Hoboken)*, vol. 2, no. 4, 2021.

[182] M. V. Fulford, D. Jaidka, A. S. Paton, G. E. Morse, E. R. L. Brisson, A. J. Lough, and T. P. Bender, "Crystal structures, reaction rates, and selected physical properties of halo-boronsubphthalocyanines (halo = fluoride, chloride, and bromide)," *Journal of chemical and engineering data*, vol. 57, no. 10, pp. 2756–2765, 2012.

[183] E. Maligaspe, M. R. Hauwiller, Y. V. Zatsikha, J. A. Hinke, P. V. Solntsev, D. A. Blank, and V. N. Nemykin, "Redox and photoinduced electron-transfer properties in short distance organoboryl ferrocene-subphthalocyanine dyads," *Inorganic chemistry*, vol. 53, no. 17, pp. 9336–9347, 2014.

[184] Y. Bernhard, E. Gigot, V. Goncalves, M. Moreau, N. Sok, P. Richard, and R. A. Decréau, "Direct subphthalocyanine conjugation to bombesin vs. indirect conjugation to its lipidic nanocarrier," *Organic & biomolecular chemistry*, vol. 14, no. 19, pp. 4511–4518, 2016.

[185] K. McAuliffe, M. Kaster, R. Szlag, and E. Trivedi, "Low-symmetry mixed fluorinated subphthalocyanines as fluorescence imaging probes in mda-mb-231 breast tumor cells," *International journal of molecular sciences*, vol. 18, no. 6, pp. 1177–, 2017.

[186] H.-S. Shim, C.-K. Moon, J. Kim, C.-K. Wang, B. Sim, F. Lin, K.-T. Wong, Y. Seo, and J.-J. Kim, "Efficient vacuum-deposited ternary organic solar cells with broad absorption, energy transfer, and enhanced hole mobility," *ACS applied materials & interfaces*, vol. 8, no. 2, pp. 1214–1219, 2016.

[187] L.-Y. Lin, Y.-H. Chen, Z.-Y. Huang, H.-W. Lin, S.-H. Chou, F. Lin, C.-W. Chen, Y.-H. Liu, and K.-T. Wong, "A low-energy-gap organic dye for high-performance small-molecule organic solar cells," *Journal of the American Chemical Society*, vol. 133, no. 40, pp. 15822–15825, 2011.

[188] K.-i. Nakayama, T. Okura, Y. Okuda, J. Matsui, A. Masuhara, T. Yoshida, M. S. White, C. Yumusak, P. Stadler, M. Scharber, and N. S. Sariciftci, "Single-component organic solar cells based on intramolecular charge transfer photoabsorption," *Materials*, vol. 14, no. 5, pp. 1200–, 2021.

[189] H. Buerckstuemmer, N. M. Kronenberg, M. Gsaenger, M. Stolte, K. Meerholz, and F. Wuerthner, "Tailored merocyanine dyes for solution-processed bhj solar cells," *Journal of materials chemistry*, vol. 20, no. 2, pp. 240–243, 2010.

[190] I. Sudakov, M. Van Landeghem, R. Lenaerts, W. Maes, S. Van Doorslaer, and E. Goovaerts, "The interplay of stability between donor and acceptor materials in a fullerene-free bulk heterojunction solar cell blend," *Advanced energy materials*, vol. 10, no. 46, 2020.

[191] J. Endres, I. Pelczer, B. P. Rand, and A. Kahn, "Determination of energy level alignment within an energy cascade organic solar cell," *Chemistry of materials*, vol. 28, no. 3, pp. 794–801, 2016.

[192] J. Yoo, K. Jung, J. Jeong, G. Hyun, H. Lee, and Y. Yi, "Energy level alignment at C_{60}/DTDCTB/PEDOT:PSS interfaces in organic photovoltaics," *Applied surface science*, vol. 402, pp. 41–46, 2017.

[193] J. Bertrandie, J. Han, C. S. P. De Castro, E. Yengel, J. Gorenflot, T. Anthopoulos, F. Laquai, A. Sharma, and D. Baran, "The energy level conundrum of organic semiconductors in solar cells," *Advanced materials (Weinheim)*, vol. 34, no. 35, pp. e2202575–n/a, 2022.

[194] D. Jiang, J. Sun, R. Ma, V. K. Wong, J. Yuan, K. Gao, F. Chen, S. K. So, X. Hao, G. Li, and H. Yin, "Extracting charge carrier mobility in organic solar cells through space-charge-limited current measurements," *Materials science & engineering. R, Reports : a review journal*, vol. 157, pp. 100772–, 2024.

[195] B. P. Rand, J. Xue, S. Uchida, and S. R. Forrest, "Mixed donor-acceptor molecular heterojunctions for photovoltaic applications. i. material properties," *Journal of applied physics*, vol. 98, no. 12, pp. 124902–124902–7, 2005.

[196] W. Tress, A. Petrich, M. Hummert, M. Hein, K. Leo, and M. Riede, "Imbalanced mobilities causing s-shaped iv curves in planar heterojunction organic solar cells," *Applied Physics Letters*, vol. 98, no. 6, 2011.

[197] Z. B. Wang, M. G. Helander, M. T. Greiner, J. Qiu, and Z. H. Lu, "Carrier mobility of organic semiconductors based on current-voltage characteristics," *Journal of applied physics*, vol. 107, no. 3, pp. 034506–034506–4, 2010.

[198] C. Child, "Discharge from hot cao," *Physical Review (Series I)*, vol. 32, no. 5, p. 492, 1911.

[199] P. N. Murgatroyd, "Theory of space-charge-limited current enhanced by frenkel effect," *Journal of physics. D, Applied physics*, vol. 3, no. 2, pp. 151–156, 1970.

[200] G. Chen, H. Sasabe, T. Sano, X.-F. Wang, Z. Hong, J. Kido, and Y. Yang, "Chloroboron (iii) subnaphthalocyanine as an electron donor in bulk heterojunction photovoltaic cells," *Nanotechnology*, vol. 24, no. 48, pp. 484007–9, 2013.

[201] R. Pandey, A. A. Gunawan, K. A. Mkhoyan, and R. J. Holmes, "Efficient Organic Photovoltaic Cells Based on Nanocrystalline Mixtures of Boron Subphthalocyanine Chloride and C_{60}," *Advanced functional materials*, vol. 22, no. 3, pp. 617–624, 2012.

[202] M. Schrader, C. Körner, C. Elschner, and D. Andrienko, "Charge transport in amorphous and smectic mesophases of dicyanovinyl-substituted oligothiophenes," *Journal of materials chemistry*, vol. 22, no. 41, pp. 22258–22264, 2012.

[203] K.-H. Lee, D.-S. Leem, S. Sul, K.-B. Park, S.-J. Lim, H. Han, K.-S. Kim, Y. W. Jin, S. Lee, and S. Y. Park, "A high performance green-sensitive organic photodiode comprising a bulk heterojunction of dimethyl-quinacridone and dicyanovinyl terthiophene," *Journal of materials chemistry. C, Materials for optical and electronic devices*, vol. 1, no. 15, pp. 2666–2671, 2013.

[204] B. Domercq, J. Yu, B. R. Kaafarani, T. Kondo, S. Yoo, J. N. Haddock, S. Barlow, S. R. Marder, and B. Kippelen, "A comparative study of charge mobility measurements in a diamine and in a hexaazatrinaphthylene using different techniques," *Molecular crystals and liquid crystals (Philadelphia, Pa. : 2003)*, vol. 481, no. 1, pp. 80–93, 2008.

[205] M. E. Kondakova, T. D. Pawlik, R. H. Young, D. J. Giesen, D. Y. Kondakov, C. T. Brown, J. C. Deaton, J. R. Lenhard, and K. P. Klubek, "High-efficiency, low-voltage phosphorescent organic light-emitting diode devices with mixed host," *Journal of applied physics*, vol. 104, no. 9, pp. 094501–094501–17, 2008.

[206] I. Aulika, P. Paulsone, J. Butikova, K. Štucere, and A. Vembris, "Comprehensive optical characterization of organic thin films for oled applications via spectroscopic ellipsometry," *Optical materials. X*, vol. 27, pp. 100419–, 2025.

[207] L.-S. Cui, S.-C. Dong, Y. Liu, Q. Li, Z.-Q. Jiang, and L.-S. Liao, "A simple systematic design of phenylcarbazole derivatives for host materials to high-efficiency phosphorescent organic light-emitting diodes," *Journal of materials chemistry. C, Materials for optical and electronic devices*, vol. 1, no. 25, pp. 3967–3975, 2013.

[208] H. Cha, S. Wheeler, S. Holliday, S. D. Dimitrov, A. Wadsworth, H. H. Lee, D. Baran, I. McCulloch, and J. R. Durrant, "Influence of blend morphology and energetics on charge separation and recombination dynamics in organic solar cells incorporating a nonfullerene acceptor," *Advanced Functional Materials*, vol. 28, no. 3, p. 1704389, 2018.

[209] O. L. Griffith, X. Liu, J. A. Amonoo, P. I. Djurovich, M. E. Thompson, P. F. Green, and S. R. Forrest, "Charge transport and exciton dissociation in organic solar cells consisting of dipolar donors mixed with C_{70}," *Physical review. B, Condensed matter and materials physics*, vol. 92, no. 8, 2015.

[210] X. Che, C. Chung, C. Hsu, F. Liu, K. Wong, and S. R. Forrest, "Donor–acceptor–acceptor's molecules for vacuum-deposited organic photovoltaics with efficiency exceeding 9%," *Advanced energy materials*, vol. 8, no. 19, 2018.

[211] B. Chen, M. An, Y. Li, X. Wang, Z. Qiu, L. Dai, K. Cao, K. Yang, D. Yun, L. Deng, S. Xie, and L. Zheng, "Vacuum-deposited organic solar cells with over 10% efficiency and device lifetime over 2 years enabled by fluorinated donor," *Advanced functional materials*, 2025.

[212] L. Benatto, C. Marchiori, T. Talka, M. Aramini, N. Yamamoto, S. Huotari, L. Roman, and M. Koehler, "Comparing C_{60} and C_{70} as acceptor in organic solar cells: Influence of the electronic structure and aggregation size on the photovoltaic characteristics," *Thin solid films*, vol. 697, p. 137827, 2020.

[213] S. Chen, Y. Liu, L. Zhang, P. C. Chow, Z. Wang, G. Zhang, W. Ma, and H. Yan, "A wide-bandgap donor polymer for highly efficient non-fullerene organic solar cells with a small voltage loss," *Journal of the American Chemical Society*, vol. 139, no. 18, pp. 6298–6301, 2017.

[214] Y. Li, D. Qian, L. Zhong, J.-D. Lin, Z.-Q. Jiang, Z.-G. Zhang, Z. Zhang, Y. Li, L.-S. Liao, and F. Zhang, "A fused-ring based electron acceptor for efficient non-fullerene polymer solar cells with small homo offset," *Nano Energy*, vol. 27, pp. 430–438, 2016.

[215] C. Yan, S. Barlow, Z. Wang, H. Yan, A. K.-Y. Jen, S. R. Marder, and X. Zhan, "Non-fullerene acceptors for organic solar cells," *Nature Reviews Materials*, vol. 3, no. 3, pp. 1–19, 2018.

[216] S. Chen, Y. Wang, L. Zhang, J. Zhao, Y. Chen, D. Zhu, H. Yao, G. Zhang, W. Ma, R. H. Friend, *et al.*, "Efficient nonfullerene organic solar cells with small driving forces for both hole and electron transfer," *Advanced Materials*, vol. 30, no. 45, p. 1804215, 2018.

[217] D. Baran, T. Kirchartz, S. Wheeler, S. Dimitrov, M. Abdelsamie, J. Gorman, R. S. Ashraf, S. Holliday, A. Wadsworth, N. Gasparini, *et al.*, "Reduced voltage losses yield 10% efficient fullerene free organic solar cells with exceeding 1 V open circuit voltages," *Energy & environmental science*, vol. 9, no. 12, pp. 3783–3793, 2016.

[218] J. Bertrandie, J. Han, C. S. De Castro, E. Yengel, J. Gorenflot, T. Anthopoulos, F. Laquai, A. Sharma, and D. Baran, "The energy level conundrum of organic semiconductors in solar cells," *Advanced Materials*, vol. 34, no. 35, p. 2202575, 2022.

[219] J. Zhang, W. Liu, G. Zhou, Y. Yi, S. Xu, F. Liu, H. Zhu, and X. Zhu, "Accurate determination of the minimum homo offset for efficient charge generation using organic semiconducting alloys," *Advanced Energy Materials*, vol. 10, no. 5, p. 1903298, 2020.

[220] R. Schueppel, C. Uhrich, M. Pfeiffer, K. Leo, E. Brier, E. Reinold, and P. Baeuerle, "Enhanced photogeneration of triplet excitons in an oligothiophene-fullerene blend," *Chemphyschem*, vol. 8, no. 10, pp. 1497–1503, 2007.

[221] H. T. Chandran, T.-W. Ng, Y. Foo, H.-W. Li, J. Qing, X.-K. Liu, C.-Y. Chan, F.-L. Wong, J. A. Zapien, S.-W. Tsang, *et al.*, "Direct free carrier photogeneration in single layer and stacked organic photovoltaic devices," *Advanced Materials*, vol. 29, no. 22, p. 1606909, 2017.

[222] V. Steinmann, N. M. Kronenberg, M. R. Lenze, S. M. Graf, D. Hertel, K. Meerholz, H. Bürckstümmer, E. V. Tulyakova, and F. Würthner, "Simple, highly efficient vacuum-processed bulk heterojunction solar cells based on merocyanine dyes," *Advanced Energy Materials*, vol. 1, no. 5, pp. 888–893, 2011.

[223] A. Karki, J. Vollbrecht, A. J. Gillett, P. Selter, J. Lee, Z. Peng, N. Schopp, A. L. Dixon, M. Schrock, V. Nádaždy, *et al.*, "Unifying charge generation, recombination, and extraction in low-offset non-fullerene acceptor organic solar cells," *Advanced Energy Materials*, vol. 10, no. 29, p. 2001203, 2020.

[224] V. C. Nikolis, A. Mischok, B. Siegmund, J. Kublitski, X. Jia, J. Benduhn, U. Hörmann, D. Neher, M. C. Gather, D. Spoltore, *et al.*, "Strong light-matter coupling for reduced photon energy losses in organic photovoltaics," *Nature communications*, vol. 10, no. 1, p. 3706, 2019.

[225] A. Jungbluth, P. Kaienburg, A. E. Lauritzen, T. Derrien, and M. Riede, "Probing the energy levels of organic bulk heterojunctions by varying the donor content," *APL Materials*, vol. 11, no. 6, 2023.

[226] T. Fritsch, J. Kurpiers, S. Roland, N. Tokmoldin, S. Shoaee, T. Ferron, B. A. Collins, S. Janietz, K. Vandewal, and D. Neher, "On the interplay between ct and singlet exciton emission in organic solar cells with small driving force and its impact on voltage loss," *Advanced Energy Materials*, vol. 12, no. 31, p. 2200641, 2022.

[227] S. Xie, Y. Xia, Z. Zheng, X. Zhang, J. Yuan, H. Zhou, and Y. Zhang, "Effects of nonradiative losses at charge transfer states and energetic disorder on the open-circuit voltage in nonfullerene organic solar cells," *Advanced functional materials*, vol. 28, no. 5, 2018.

[228] Z. Tang, J. Wang, A. Melianas, Y. Wu, R. Kroon, W. Li, W. Ma, M. R. Andersson, Z. Ma, W. Cai, W. Tress, and O. Inganäs, "Relating open-circuit voltage losses to the active layer morphology and contact selectivity in organic solar cells," *Journal of materials chemistry. A, Materials for energy and sustainability*, vol. 6, no. 26, pp. 12574–12581, 2018.

[229] L. Perdigón-Toro, L. Q. Phuong, F. Eller, G. Freychet, E. Saglamkaya, J. I. Khan, Q. Wei, S. Zeiske, D. Kroh, S. Wedler, A. Köhler, A. Armin, F. Laquai, E. M. Herzig, Y. Zou, S. Shoaee, and D. Neher, "Understanding the role of order in y-series non-fullerene solar cells to realize high open-circuit voltages," *Advanced energy materials*, vol. 12, no. 12, 2022.

[230] L. Zuo, J. Yao, H. Li, and H. Chen, "Assessing the origin of the s-shaped i–v curve in organic solar cells: An improved equivalent circuit model," *Solar energy materials and solar cells*, vol. 122, pp. 88–93, 2014.

[231] R. Saive, "S-shaped current–voltage characteristics in solar cells: a review," *IEEE Journal of Photovoltaics*, vol. 9, no. 6, pp. 1477–1484, 2019.

[232] M. Schwarze, K. S. Schellhammer, K. Ortstein, J. Benduhn, C. Gaul, A. Hinderhofer, L. Perdigón Toro, R. Scholz, J. Kublitski, S. Roland, M. Lau, C. Poelking, D. Andrienko, G. Cuniberti, F. Schreiber, D. Neher, K. Vandewal, F. Ortmann, and K. Leo, "Impact of molecular quadrupole moments on the energy levels at organic heterojunctions," *Nature communications*, vol. 10, no. 1, pp. 2466–9, 2019.

[233] P.-H. Huang, Y.-H. Wang, and C.-J. Huang, "Enhancement of light harvesting for organic solar cells via halogenated (sub-)phthalocyanines and fullerene," in *2019 IEEE International Conference on Electron Devices and Solid-State Circuits (EDSSC)*, pp. 1–2, IEEE, 2019.

[234] B. Verreet, K. Cnops, D. Cheyns, P. Heremans, A. Stesmans, G. Zango, C. G. Claessens, T. Torres, and B. P. Rand, "Decreased recombination through the use of a non-fullerene acceptor in a 6.4% efficient organic planar heterojunction solar cell," *Advanced energy materials*, vol. 4, no. 8, pp. np–n/a, 2014.

[235] S. M. Arnab and M. Kabir, "An analytical model for analyzing the current-voltage characteristics of bulk heterojunction organic solar cells," *Journal of applied physics*, vol. 115, no. 3, 2014.

[236] M. Schrader, R. Fitzner, M. Hein, C. Elschner, B. Baumeier, K. Leo, M. Riede, P. Bäuerle, and D. Andrienko, "Comparative study of microscopic charge dynamics in crystalline acceptor-substituted oligothiophenes," *Journal of the American Chemical Society*, vol. 134, no. 13, pp. 6052–6056, 2012.

[237] P. PETELENZ, M. ANDRZEJAK, and A. EILMES, "Spectral effects of microscopic and mesoscopic disorder in organic films — model calculations," *International Journal of Modern Physics B*, vol. 15, no. 28n30, pp. 3651–3655, 2001.

[238] R. Fitzner, E. Mena-Osteritz, A. Mishra, G. Schulz, E. Reinold, M. Weil, C. Körner, H. Ziehlke, C. Elschner, K. Leo, M. Riede, M. Pfeiffer, C. Uhrich, and P. Bäuerle, "Correlation of pi-Conjugated Oligomer Structure with Film Morphology and Organic Solar Cell Performance," *Journal of the American Chemical Society*, vol. 134, no. 27, pp. 11064–11067, 2012.

[239] E. Bittrich, J. Domke, M. Levichkova, D. Jehnichen, L. Bittrich, A. Janke, P. Formanek, R. Hübner, P. Uhlmann, K. Eichhorn, R. Forker, M. Gruenewald, M. Al-Hussein, T. Fritz, and K. Walzer, "Structural templating of an organic solar cell absorber by ellagic acid to tune its aggregation, molecular orientation, and optical properties," *ACS Applied Energy Materials*, vol. 4, no. 12, pp. 14273–14286, 2021.

[240] O. Guskova, C. Schünemann, K. Eichhorn, K. Walzer, M. Levichkova, S. Grundmann, and J. Sommer, "Light absorption in organic thin films: The importance of oriented molecules," *The Journal of Physical Chemistry C*, vol. 117, no. 33, pp. 17285–17293, 2013.

[241] C. Schünemann, D. Wynands, K. Eichhorn, M. Stamm, K. Leo, and M. Riede, "Evaluation and control of the orientation of small molecules for strongly absorbing organic thin films," *The Journal of Physical Chemistry C*, vol. 117, no. 22, pp. 11600–11609, 2013.

[242] J. Jortner, "Temperature dependent activation energy for electron transfer between biological molecules," *The Journal of Chemical Physics*, vol. 64, no. 12, pp. 4860–4867, 1976.

[243] K. Kawashima, Y. Tamai, H. Ohkita, I. Osaka, and K. Takimiya, "High-efficiency polymer solar cells with small photon energy loss," *Nature communications*, vol. 6, no. 1, p. 10085, 2015.

[244] Y. P. Sun, P. Wang, and N. B. Hamilton, "Fluorescence spectra and quantum yields of buckminsterfullerene (C_{60}) in room-temperature solutions. No excitation wavelength dependence," *Journal of the American Chemical Society*, vol. 115, no. 14, pp. 6378–6381, 1993.

[245] M. Ren, G. Zhang, Z. Chen, J. Xiao, X. Jiao, Y. Zou, H.-L. Yip, and Y. Cao, "High-performance ternary organic solar cells with controllable morphology via sequential layer-by-layer deposition," *ACS applied materials & interfaces*, vol. 12, no. 11, pp. 13077–13086, 2020.

[246] A. K. Pandey, "Highly efficient spin-conversion effect leading to energy up-converted electroluminescence in singlet fission photovoltaics," *Scientific reports*, vol. 5, no. 1, p. 7787, 2015.

[247] K. Nakano, Y. Kaji, and K. Tajima, "Origin of electric field-dependent charge generation in organic photovoltaics with planar and bulk heterojunctions," *Journal of Materials Chemistry A*, vol. 11, no. 48, pp. 26499–26507, 2023.

[248] Y.-H. Chen, L.-Y. Lin, C.-W. Lu, F. Lin, Z.-Y. Huang, H.-W. Lin, P.-H. Wang, Y.-H. Liu, K.-T. Wong, J. Wen, *et al.*, "Vacuum-deposited small-molecule organic solar cells with high power conversion efficiencies by judicious molecular design and device optimization," *Journal of the American Chemical Society*, vol. 134, no. 33, pp. 13616–13623, 2012.

[249] J. Kim and S. Yim, "Influence of surface morphology evolution of SubPc layers on the performance of SubPc/C_{60} organic photovoltaic cells," *Applied Physics Letters*, vol. 99, no. 19, 2011.

[250] K. L. Mutolo, E. I. Mayo, B. P. Rand, S. R. Forrest, and M. E. Thompson, "Enhanced open-circuit voltage in subphthalocyanine/C_{60} organic photovoltaic cells," *Journal of the American Chemical Society*, vol. 128, no. 25, pp. 8108–8109, 2006.

[251] R.-R. Bai, C.-R. Zhang, Y.-Z. Wu, Y.-L. Shen, Z.-J. Liu, and H.-S. Chen, "Donor Halogenation Effects on Electronic Structures and Electron Process Rates of Donor/C_{60} Het-

erojunction Interface: A Theoretical Study on F_nZnPc (n= 0, 4, 8, 16) and Cl_nSubPc (n= 0, 6)," *The Journal of Physical Chemistry A*, vol. 123, no. 18, pp. 4034–4047, 2019.

A | Computation Code

A.1 Spectral Overlap Integral J Calculation

The code used for spectral overlap integral J calculation can be found on GitHub via https://github.com/mzjswjz/FRET_spectral_overlap_integral.git

A.2 Spectroscopic Ellipsometry Fitting

Fitting details and raw data can be found on GitHub via: https://github.com/mzjswjz/Ellipsometry_Data_and_Fits.git

A.3 Voltage Loss Calculation

The code used for voltage loss calculation under DB framework can be found on GitHub via https://github.com/mzjswjz/Voltage_Loss_Calculations.git.

A.4 Parameters Extracted from EQE

A.4.1 Determination of E_g^{PV}

The code used to determine E_g^{PV} from EQE spectra can be found on GitHub via https://github.com/mzjswjz/Voltage_Loss_Analysis_Tools.git.

A.4.2 Determination of E_U^{app}

The code used to determine E_U^{app} from EQE spectra can be found on GitHub via https://github.com/mzjswjz/Voltage_Loss_Analysis_Tools.git.

A.5 Reduced EL and EQE

The code used to validate EL and convert measured EL and EQE spectra to reduced EL and EQE spectra can be found on GitHub via https://github.com/mzjswjz/Reduced_EL_EQE.git.